UNIVERSITY OF LJUBLJANA
FACULTY OF MATHEMATICS AND PHYSICS
DEPARTMENT OF PHYSICS

Luka Debenjak

Construction and calibration of the Čerenkov radiation detector for high-countrate hypernuclear experiments

Doctoral thesis

ADVISER: assoc. prof. dr. Simon Širca
CO-ADVISER: dr. Patrick Achenbach

Ljubljana, 2012

UNIVERZA V LJUBLJANI
FAKULTETA ZA MATEMATIKO IN FIZIKO
ODDELEK ZA FIZIKO

Luka Debenjak

Izgradnja in umeritev detektorja sevanja Čerenkova za hiperjedrske poskuse pri visokih števnih hitrostih

Doktorska disertacija

MENTOR: izred. prof. dr. Simon Širca
SOMENTOR: dr. Patrick Achenbach

Ljubljana, 2012

To my grandfather, Nono.

Povzetek

Z novo pospeševalno enoto pospeševalnika elektronov v Mainzu (MAMI) na Institutu za jedrsko fiziko je mogoče doseč energijo žarka do 1.6 GeV, kar je nad pragom za produkcijo kaonov.

Za učinkovito identifikacijo kaonov sem izgradil, namestil in kalibriral detektor sevanja Čerenkova. Za sevalec smo izbrali silicijev aerogel z lomnim količnikom $n = 1.055$. Izmerili smo vse njegove optične lastnosti, (svetlobna prepustnost, absorbcijska dolžina, sipalna dolžina) ki imajo neposreden vpliv na izkoristek detektorja.

Podrobne simulacije optičnih procesov in zmogljivost pri različnih geometrijah detektorja sem izvedel v programskem okolju `SLitrani`. V simulacijah je bil detektor optimiziran (geometrija, lastnosti fotopomnoževalk, odbojne ploskve, debelina sevalca) v smislu največjega stevila fotoelektronov in obenem najkrajšega časa preleta detektiranih fotonov. Na podlagi rezultatov simulacije in serije testov s predhodnjima prototipoma sem določil karakteristike končne oblike detektorja.

Čerenkov detektor sem testiral s kozmičnimi žarki in v seriji hiperjedrskih poskusov pri različnih gibalnih količinah vpadnih delcev in njihovo števnostjo ter energijah vpadnih elektronov. Z detekcijskim pragom nastavljenim na 0.5 fotoelektrona je bil dosežen izkoristek $\gtrsim 95\%$ s kozmičnimi žarki in pozitroni.

Na koncu sem identificiral dogodke iz $p(e, e'K^+)\Lambda$ reakcije in naredil približen izračun sipalnega preseka elektroprodukcije kaonov pri nizkem Q^2.

Ključne besede: Pragovni Čerenkov števec; Silicijev aerogel; Identifikacija delcev; Monte Carlo; Difuziven odboj; Detektorji; Hiperjedra; Magnetni spektrometri

PACS: 29.40.Ka; 25.80.Nv

Abstract

With the upgrade of the electron accelerator in Mainz (MAMI) at the Institute for nuclear physics the energy of the beam has increased to 1.6 GeV, which is above the kaon production threshold.

For efficient kaon identification a new Čerenkov detector system has been designed, constructed, installed and calibrated . For the radiator media silica aerogel has been chosen with refractive index of $n = 1.055$. All its optical properties have been measured (transmittance, absorption length, scattering length), which have direct impact to the detector efficiency.

A detailed simulations of the optical processes and performance at various geometries of the detector have been performed using the program package `SLitrani`. In the simulations the detector has been optimized (geometry, properties of photomultipliers, reflective surfaces, radiator thickness) in order to increase the number of photo-electrons and simultaneously decrease the time distribution of the detected photons. Upon my simulation results and a series of tests with two prototypes the detector has been designed in its final form.

The Čerenkov counter has been tested with cosmic-rays and in a series of hypernuclear experiments at different particle momenta, their flux and energy of incoming electron. With the threshold set to 0.5 photo-electrons the efficiency of $\gtrsim 95\%$ with cosmics and positrons has been achieved.

At the end I have identified events from $p(e, e'K^+)\Lambda$ reaction and made a rough calculation for kaon electro-production cross-section at low Q^2.

Keywords: Threshold Čerenkov counters; Silica aerogel; Particle identification; Monte Carlo; Diffusion box; Detectors; Hypernuclei; Magnetic spectrometers

PACS: 29.40.Ka; 25.80.Nv

Contents

CHAPTER 1

Introduction

Strangeness nuclear physics bears a broad impact on contemporary physics since it lies at the intersection of nuclear and elementary particle physics. Information on baryon-baryon interactions is mainly obtained from nuclear experiments with projectiles and targets with ordinary nucleons, addressing interactions in flavor SU(2) only. Unfortunately it is very difficult to study the hyperon-nucleon (YN) and hyperon-hyperon (YY) interactions by reaction experiments, because of the difficulties of the preparation of low energy hyperon beams and because no hyperon targets are available due to the short lifetimes of hyperons. However, hypernuclei can be used as a micro-laboratory to study YN and YY interactions. In a hypernucleus, a hyperon can also serve as a unique probe for the structure of the nucleus and its change due to the hyperon presence and thus makes it possible to study and test different nuclear models.

On the other hand, the properties of the hyperon can change when it is bound inside the nucleus. Atomic nuclei can serve as a laboratory for studying the basic properties of hyperons. The added strange hadron introduces an SU(3)-flavor dimension to traditional nuclear physics, see Fig. 1.1.

Kaons can be produced by photo-production mechanism, where real photon interacts with a proton, which is changed into Λ hyperon:

$$\gamma + p \longrightarrow K^+ + \Lambda. \tag{1.1}$$

Production of kaons is also possible with electron beams. Such process can be well described by a first order of perturbation calculation as the exchange of one virtual photon between the electron and the proton:

$$e + p \longrightarrow e' + K^+ + \Lambda. \tag{1.2}$$

This production mechanics is more general, because the four-momentum transfer of the virtual photon is non-zero, $Q^2 \neq 0$, while the real photons in photo-production reaction lie on the mass-shell with $Q^2 = 0$. Thus the photo-production can be treated as a special case of electro-production process with low, essentially zero, four-momentum transfer of the photon. The electro-production has another contribution,

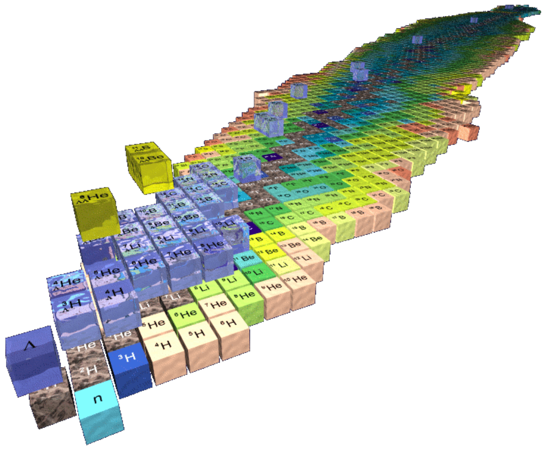

Figure 1.1: Two-dimensional nuclear chart extended to third dimension with ordinary nuclei at the ground level with $S = 0$ and hypernuclei at higher levels with $S \neq 0$. Black boxes represent stable nuclei.

that does not exist in photo-production: the longitudinal cross-section contribution of the virtual photons.

First kaon electro-production data comes from experiments carried out in the 1970s at CEA (Cambridge Electron Accelerator), the Wilson Synchrotron Laboratory at Cornell University and DESY (Deutsches Elektronen-Synchrotron), but is of limited precision. The first experiment was done at CEA at $Q^2 < 1.2$ (GeV/c)^2, $W \approx 1.8 - 2.6$ GeV and forward kaon angles: $\theta_K^{\rm cm} < 28°$. They found out that the $K^+\Lambda$ channel dominates over the $K^+\Sigma^0$ channel [1]. Results from Cornell at $Q^2 < 2.0$ (GeV/c)^2 and $W = 2.15$ and 2.67 GeV have confirmed this result [2]. A Rosenbluth separation was first applied to kaon electro-production data at Harvard in 1977 [3]. The separation was poor due to large systematic uncertainties and the results were not useful for available theories and models. The first low-statistics experiment to separate interference terms, σ_{LT} and σ_{TT}, was done at DESY at $1.9 < W < 2.8$ GeV and $0.1 < Q^2 < 0.6$ (GeV/c)^2, but the error bars were too large to separate them. Another experiment was carried out at DESY at $W = 2.2$ GeV and $0.06 < Q^2 < 1.35$ GeV^2 with measurements on differential cross-sections for the $K^+\Lambda$ and $K^+\Sigma^0$ final states [4]. Most electro-production data before 1980 were taken at low energies and low kaon counting rates.

The first precise separation of cross sections into longitudinal σ_L and transverse terms σ_T and comes from quite recent kaon electro-production experiment carried out at Jefferson Laboratory (Thomas Jefferson National Accelerator Facility, also known as the Continuous Electron Beam Accelerator Facility, CEBAF) by the Hall C collaboration [5, 6]. The experiment was performed at different values of virtual photon transverse linear polarization, ϵ, for different momentum transfers $Q^2 = 0.52, 0.75, 1.00$ and 2.0 (GeV/c)^2. In another experiment at Jefferson Lab Hall A more data has been measured in a kinematical region of higher $Q^2 = 2.35$ (GeV/c)^2

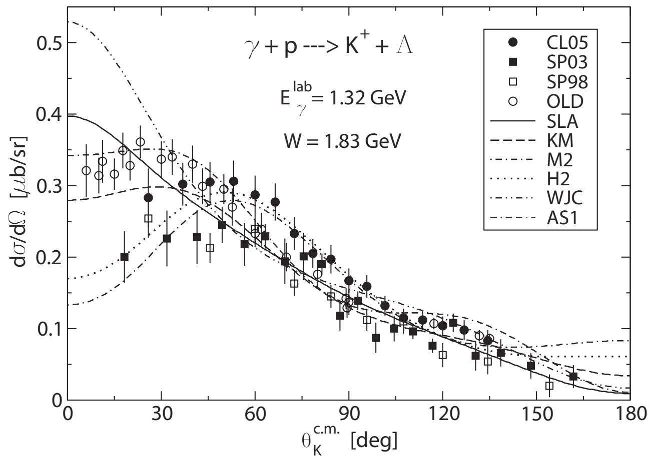

Figure 1.2: Comparison of various differential cross-sections for kaon photo-production and the results of various effective Lagrangian models. Data points were measured by CLAS collaboration from Jefferson Lab Hall B (CL05) and SAPHIR collaboration from ELSA in Bonn (SP98), (SP03). Models are: Saclay-Lyon A (SLA), Kaon-Maid (KM), M2, H2, Williams-Ji-Cotanch (WJC), and Adelseck-Saghai (AS1) [11].

and $W \geq 1.80$ [7]. The most recent measurements have been performed in Jefferson Lab Hall A [8] and in Hall C, which is now under analysis [9].

Several measurements have been performed at Jefferson Lab Hall B by the CLAS collaboration with improved statistics and wider energy range compared to previous measurements. They found out that in $K^+\Lambda$ channel the longitudinal coupling is important only at forward angles and higher W [10]. However, the detector used in this experiment can not be positioned at small forward angles and has a limited acceptance for four-vector momentum transfers $Q^2 < 0.5$ (GeV/c)^2.

Even though there is a lot of data from Jefferson Lab there are still many open questions in the interpretation of kaon photo- and electro-production data and the description of the process. In Fig. 1.2 we can see differential cross sections for kaon photo-production measured at different laboratories, together with the results of various effective Lagrangian models. At small kaon angles even the most precise results are inconsistent and the effective models differ strongly between each other. This clearly means that additional, independent measurements under forward kaon angles are needed for reliable results about differential cross-section and determination of the parameters of the effective Lagrangian models.

All measurements done so far reached a number of conclusions about the production mechanisms, but still additional measurements are needed to improve the world data-base and to resolve the remaining uncertainties about the cross-section. There is a lack of good data on kaon electro-production in the threshold region, compared to photo-production, where a good set of upolarized and polarized cross-section data exist. In Fig. 1.3 we can see data points on the reaction (1.2) published so far in

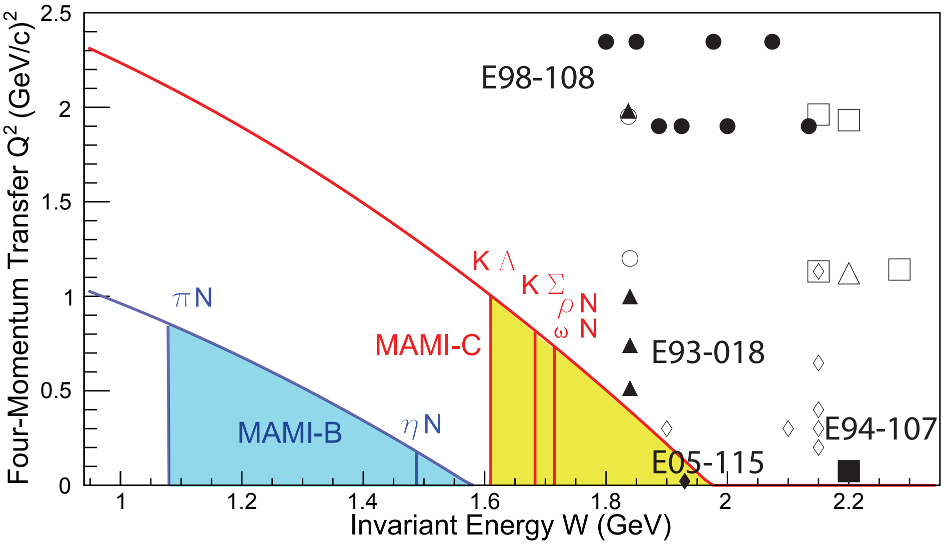

Figure 1.3: The threshold energies for π, η, ρ, ω and ϕ production off the nucleon and for the associated strangeness channels $K\Lambda$ and $K\Sigma$ are indicated. Open symbols show old measured data points and solid symbols correspond to Jefferson Lab experiments: triangles refer to Hall C experiment E93-018, circles refer to Hall A experiment E98-108, square to Hall A experiment E94-107 and diamond to Hall C experiment E05-115 . Blue and yellow triangles are the kinematical regions accessible by MAMI-B and MAMI-C, respectively.

the $Q^2 - W$ plane. There is a lot of empty space, especially at low four-vector momentum transfers and close to threshold. In the low-Q^2 region the cross-sections of $K^+\Lambda$ and $K^+\Sigma^0$ electro-production may be of interest for further study, where additional data would significantly improve the world data-base.

With the upgrade of the electron accelerator at the Institute of nuclear physics, University in Mainz, (MAMI) the investigation of hypernuclei and kaon electro-production cross-section near threshold is possible. The acceleration system has been extended in 2007 by the harmonic double sided microtron- HDMS stage (also known as MAMI-C stage) to the beam energy up to 1.5 GeV and recently upgraded to 1.6 GeV [12]. So far the MAMI-B accelerator stage was able to reach the production threshold for the lightest mesons (π, η). With MAMI-C accelerator stage the production threshold has risen to the kaon level which enables studies on strange hadrons. The kinematic regions accessible in electro-production by the electron accelerator stages MAMI-B (end-point energy of 855 MeV) and MAMI-C (end-point energy of 1508 MeV) are shown in Fig. 1.3. Electro-production experiments at MAMI-B were devoted often to pion production and $N\Delta$ transitions, whereas at MAMI-C the electro-production of open strangeness in the Q^2 region below 1 $(\text{GeV/c})^2$ is possible.

With the new acceleration stage, the three spectrometer facility was not fully prepared for kaon electro-production because the existing spectrometers did not cover the full momentum range for hypernuclei experiments. Furthermore, the kaons produced have a low probability of detection due to the short life-time ($c\tau = 3.7$ m) and the long flight path through the spectrometers (close to 10 m). Therefore, kaons are analyzed at forward scattering angles with the new KAOS spectrometer which was built in 2008 and is now routinely operated by the A1 Collaboration.

With the KAOS spectrometer we can get more kaon electro-production data at very small kaon angles and small momentum transfers. The relatively low end-point energy of the MAMI-C stage in comparison with the beam at Jefferson Lab is of no disadvantage, because such kinematic is well suited for measurements with the KAOS spectrometer.

CHAPTER 2

Strangeness physics

2.1 A brief history of strangeness physics

For a brief period in 1947 it was believed that major problems of elementary particle physics were solved. This state lasted till George D. Rochester and Clifford C. Butler from Manchester University (UK) published an article with a photograph of a particle tracks in a cloud chamber, which shows a presence of a neutral particle by its charged decay products, forming the upside-down "V". This was a completely new phenomenon in the study of cosmic rays. A detailed analysis showed that two decay products of a neutral particle were in fact a π^+ and a π^-. Thus a new neutral particle was discovered with at least twice the mass of the pion. According to the pattern of the tracks of both decay products with opposite charge they called it the V^0 particle [13]. Now we call it the K^0, kaon:

$$K^0 \longrightarrow \pi^+ + \pi^-. \tag{2.1}$$

Two years later Powell published a photograph, showing the decay of a charged kaon [14]:

$$K^+ \longrightarrow \pi^+ + \pi^+ + \pi^-. \tag{2.2}$$

Their identification as neutral and charged version of the same particle was not clear until 1956. Because kaons behave similar to pions the meson family was extended to include them.

Later on, in 1950 another neutral "V" particle was discovered by Carl Anderson and Eugene Cowan's group at Caltech. Simultaneously the Manchester group brought its magnet, weighting 11 tons, and associated equipment up the 2850 m high mountain in the French Pyrenees and found tracks showing the "V"- pattern. The photographs were similar to Rochester's but this time the decay products were a p and a π^-. This particle is obviously heavier than the proton. We call it now the Λ:

$$\Lambda \longrightarrow p + \pi^-. \tag{2.3}$$

It and belongs with the proton and the neutron to the baryon family.

The following terminology was adopted by 1953: "K-meson" meant a particle heavier than pion and lighter than nucleon and "Hyperon" meant any particle heavier than a nucleon. Over the next few years many more heavy baryons/hyperons were discovered: the Σ's, the Ξ's and the Δ's, and so on.

All these new baryons (except Δ) and mesons became collectively known as "strange" particles. Not only these particles were unexpected, but their life-time was much longer than expected. It was known that they are created by the strong nuclear force, so it was expected for these particles to decay by the same force, which means they should decay in about 10^{-23} s. But they decay relatively slowly, typically in about 10^{-10} s.

This suggests that the mechanism involved in their production in entirely different from that which governs their decay. Now we know that these particles decay by the weak force.

In 1953, when four strange particles were known, Murray Gell-Mann in USA and independently Tadao Nakano and Kazuhiko Nishijima in Japan assigned to each particle a new property that (like charge, lepton number, baryon number) is conserved in any strong interaction, but (unlike those others) is not conserved in weak interactions. They have formulated a new quantum number called strangeness. [15]. The strangeness of a particle S is defined as:

$$S = -(n_s - n_{\bar{s}}), \tag{2.4}$$

where n_s represents the number of strange quarks (s) and $n_{\bar{s}}$ represents the number of strange antiquarks ($\bar{s}$).

The list of elementary particles, which seemed so short by 1947 had grown into a mess by 1969. The abundance of strongly interacting particles was divided into two great families: the baryons and the mesons. The members of each family were distinguished by its charge, strangeness and mass. This was similar to the situation in chemistry a century earlier, in the days before the periodic table, when elements had been identified, but there was no order or system. The elementary particles awaited their own "Periodic table".

2.2 Basics of hypernuclear physics

Hypernuclear physics was born in 1952, when the Polish physicists M. Danysz and J. Pniewski observed photographic emulsions, exposed to cosmic rays at around 26 km above the ground flown in a balloon. A high energy proton, colliding with a nucleus of the emulsion (Ag or Br), breaks it into several fragments forming a star. All the nuclear fragments stop in the emulsion after a short path, but one decays, revealing the presence of an unstable particle, the hyperon, stuck inside the nucleus. The analysis revealed that the reaction was

$${}^{7}_{\Lambda}\mathrm{Li} \rightarrow \alpha +^{3}\mathrm{He} + \pi^{-}. \tag{2.5}$$

The ${}^{7}_{\Lambda}$Li nuclear fragment, and the others obtained afterwards in similar conditions, were called hyperfragments or hypernuclei [16].

A hypernucleus is a normal nucleus, with atomic weight, A, and atomic number, Z, with the addition of one or more hyperons, such as Λ, $\Sigma^{\pm,0}$, $\Xi^{-,0}$, Ω^{-}, etc. A hyperon is a baryon composed of at least one strange quark and is usually denoted by Y. Hypernuclei are described by the element symbol, Z, which is measure of charge and not necessarily the number of protons. The symbol is labeled additionally by the number of baryons, A, and the symbol of the bound hyperon. For example, the hypernucleus ${}^{\Lambda}_{12}$C has 12 baryons, with one of these being a Λ hyperon. It has atomic number 6, as noted by the label C (see Fig. 2.1). Neutrons, protons and hyperons are considered distinguishable particles so each is placed in an independent potential well in which the Pauli exclusion principle applies. Hypernuclei are often in their excited states and deexcite or fragment [18].

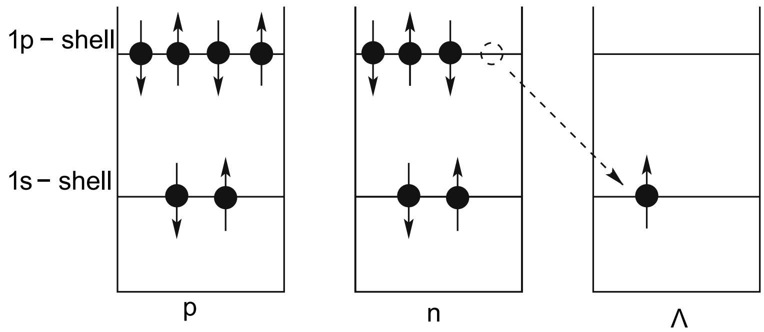

Figure 2.1: A simple model for the ${}^{\Lambda}_{12}$C hypernucleus. A neutron from 1p-shell is changed into a Λ, creating the hypernucleus in its ground state. Figure taken from [18].

Hypernuclei with Λ hyperon bound inside ($S = -1$), being the less unstable hypernuclei, have been extensively studied during the past 60 years [46]. Until now, around 40 different Λ hypernuclear isotopes have been identified. Different hypernuclear states can be identified by a missing-mass analysis, with known energy of the incident particles and other reaction products. For such reactions stable target nuclei are required, so the production and accessibility of hypernuclei by these reactions are limited.

As mentioned before hyperons are baryons with non-zero strangeness ($S \neq 0$) and decay through reactions which do not conserve strangeness, isospin nor parity. According to their masses they belong to several isospin multiplets: Λ is an isospin singlet, Σ^{+}, Σ^{0}, Σ^{-} belong to the isospin triplet, and Ξ^{0}, Ξ^{-} to the isospin doublet. All baryons have baryon number $B = 1$ and their electrical charge q is evaluated from the Gell-Mann-Nishijima formula:

$$q = t_3 + \frac{1}{2}Y, \tag{2.6}$$

where t_3 is the third isospin component and $Y = B + S$ is the hypercharge, which is also not conserved in weak interactions. All baryons and mesons are identified by the baryon number B, the hypercharge Y, and t_3. This was a hint that all hadrons are composed of 3 different constituents, called quarks. They are the elementary building blocks of all hadrons, have baryon number $B = \frac{1}{3}$ and differ in t_3 and hypercharge Y. These elementary blocks correspond to three different quark flavors: u, d and s. Only s quark has non-zero strangeness $S = -1$, so all hyperons contain at least one s quark. In 1964, Gell-Mann and George Zweig described a new classification scheme that has put all particles known at that time into order [19, 20, 21]. In total 10 combinations of 3 quarks are possible with spin $\frac{3}{2}$ and 8 combinations with spin $\frac{1}{2}$ for the lightest (ground-state) baryons. Thus baryons are arranged in SU(3) super-multiplets: a decuplet with 10 members and an octet with 8 members, which are presented Fig. 2.2. Later on three more heavier quarks were discovered, named c, b and t. Based on these concepts the standard model of particle physics emerged during the 1970s and Quantum Chromodynamics (QCD) became the theory about the strong interactions of particles.

The Λ particle is the lightest particle among the hyperons. It has a rest mass of (1115.683 ± 0.006) MeV/c^2, 20 % greater than the mass of the nucleon, zero charge, spin $\frac{1}{2}$ and strangeness $S = -1$. The Λ hyperon is unstable and decays in free space with a life-time of (263 ± 2) ps, via weak interaction that does not conserve strangeness (see Section 2.8).

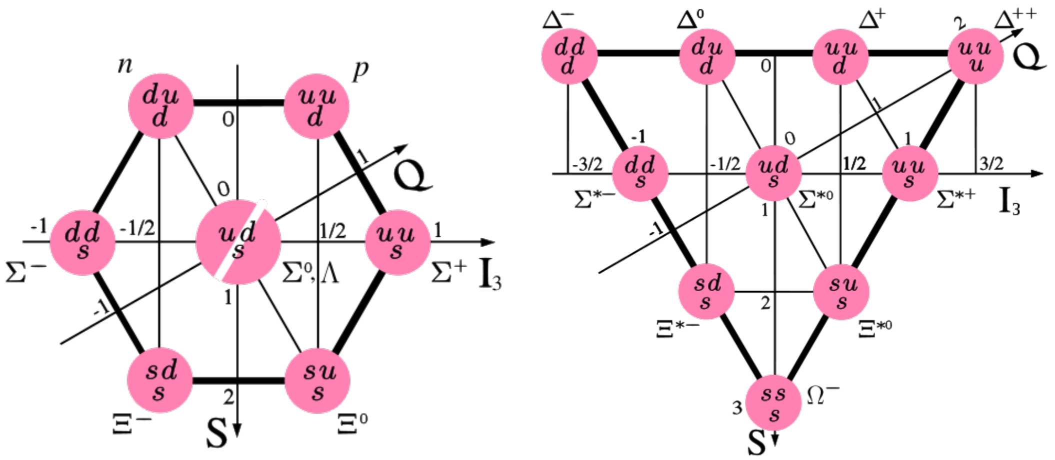

Figure 2.2: Ground state baryons. Left: baryon octet with $\frac{1}{2}$ spin. The only stable particles from this multiplet are nucleons: p and n with $Y = 1$. Isospin singlet corresponds to Λ hyperon. Right: baryon decuplet with $\frac{3}{2}$ spin. Figure is taken from [17].

2.3 Production mechanisms of hypernuclei

The production of hypernuclei at accelerators can be performed with different beams using different experimental techniques. So far the experimental data on hypernuclear binding energies is limited to (s- and p-shell) hypernuclei. As you can see in Fig. 2.1, a hypernucleus is in its ground state when the hyperon and nucleons are in their lowest shell states, and this generally requires rearrangement of the hypernucleus structure after production. In these rearrangements the energy can be released by gamma rays or neutron (or proton) emission. Thus the final hypernucleus is not necessarily the same as the one initially produced.

At the beginning K^- beams were used to study hypernuclei. The typical reaction was the *strangeness exchange reaction*, where a neutron in the nucleus hit by a K^- is changed into a Λ hyperon and a π^- is emitted ($K^-+n \to \Lambda+\pi^+$). Such reaction has been used for production and decay studies of light hypernuclei. Because of the small momentum transfer and the large background coming from in-flight kaon decays, the measurements could not be extended to heavier hypernuclei. Corresponding quark-level process is schematically shown in Fig. 2.3 a). In these experiments the hyperon binding energies are mainly measured and the identification of excited hypernuclear levels. About 40 years ago a series of experiments started at the proton synchrotron at CERN and at the Brookhaven National Laboratory (BNL). The energy resolution of the (K^-, π^-) reaction was relatively poor ($\Delta E \approx 5$ MeV) compared to modern experiments. By measuring the energy spectrum of the emitted pion dN/dE_π and knowing the energy of incoming kaon E_K and rest-mass of the nucleus M_{targ} the spectrum of hypernuclear levels can be directly calculated. For each event the hypernuclear exitation energy is:

$$E_x = E_K + M_{\mathrm{targ}} - E_\pi. \tag{2.7}$$

A decade after, the π^+ beams were used at the Alternating gradient synchrotron (AGS) of BNL [23, 24] and 12 GeV proton synchrotron (PS) of the High Energy Accelerator Organization (KEK) in Japan [25, 26, 27, 28, 29]. With this technique the Λ hyperon is produced inside the nucleus by an *associated production reaction* ($\pi^+ + n \to \Lambda + K^+$), as shown in Fig. 2.3 b) for a quark-level schematic. This reaction has a reduced cross section, compared to the strangeness exchange reaction, however this drawback is over compensated by the greater intensities of the π^+ beams. Because the mass of the final hadron pair is much larger than the mass of the initial particle, the momentum transfer to the hyperon is relatively large: $q_\Lambda \approx 300 - 400$ MeV/c at 0° scattering angle.

Hypernuclei can be also produced by heavy ion collisions, which was first studied by Kerman and Weiss [30]. Such reactions can be explained by participant-spectator model, where two nucleons (participants) collide, while the other nucleons (spectators) pass by each other without experiencing a large disturbance. Because the energy threshold for Λ production in the process $NN \to \Lambda KN$ is $E_{\mathrm{thr}} \approx 1.6$ GeV the produced hypernuclei have a large velocity with $\beta > 0.9$ resulting in a longer life-time in the laboratory frame due to the large Lorentz factor. Such hypernu-

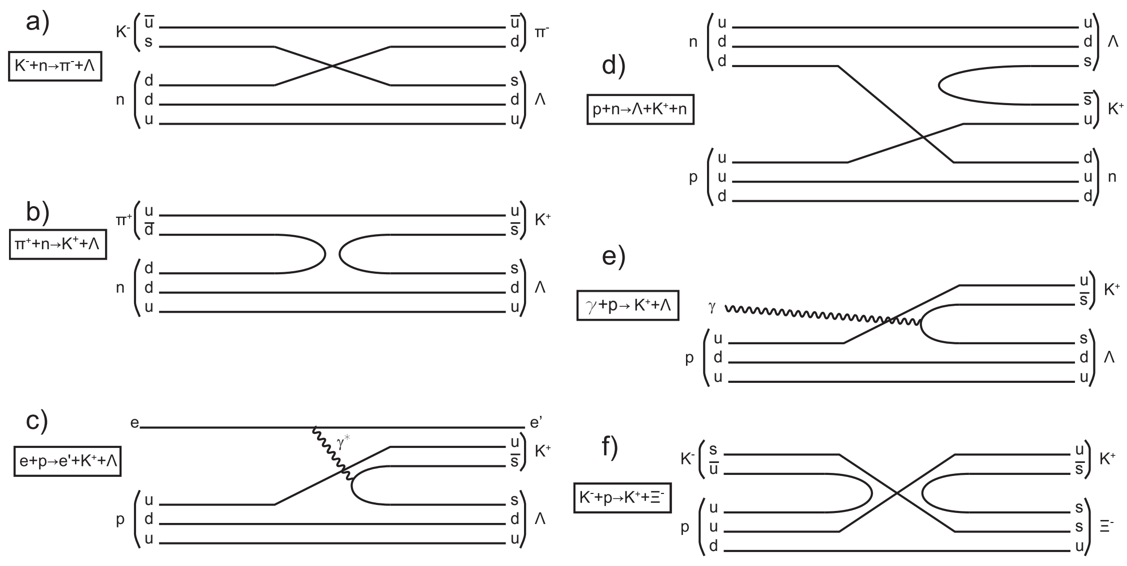

Figure 2.3: Diagrams for several hypernuclei production mechanisms: a) strangeness exchange reaction, b) associated production reaction, c) electro-production, d) possible hadro-production reaction, e) photo-production, f) Ξ-production via charge exchange reaction, leading to double strange hypernuclei. Figure adopted from ref. [22]

clei decay a few tens of centimeters behind the target where they were produced. Such experiments with heavy ion beams are performed at GSI Helmholtz Center for Heavy Ion Research GmbH in Germany. At FAIR, which is the future facility of GSI, the experiments at 20 *A* GeV are planned.

2.4 Kinematics

In order to form a hypernucleus, the hyperon produced in the reaction has to stay bound inside the nuclear potential well. This depends very much on the transferred momentum to the hyperon.

The kinematics of several elementary processes are shown in Fig. 2.4. As you see in the figure, in the $n(K^-,\pi^-)\Lambda$ reaction the momentum transferred to a produced Λ or Σ hyperon can be very low, essentially zero. Thus the probability that this hyperon will be bound and interact with the nucleons is large. On the other hand the reactions such as $n(\pi^+,K^-)\Lambda$ or $p(\gamma,K^+)\Lambda$ have high momentum transfer relative to the maximum momentum of hyperons in their own potential well (Fermi momentum), and produce hyperons that have a high probability of escaping the nucleus. The cross sections are reduced, when the momentum transfer is higher than the Fermi momentum.

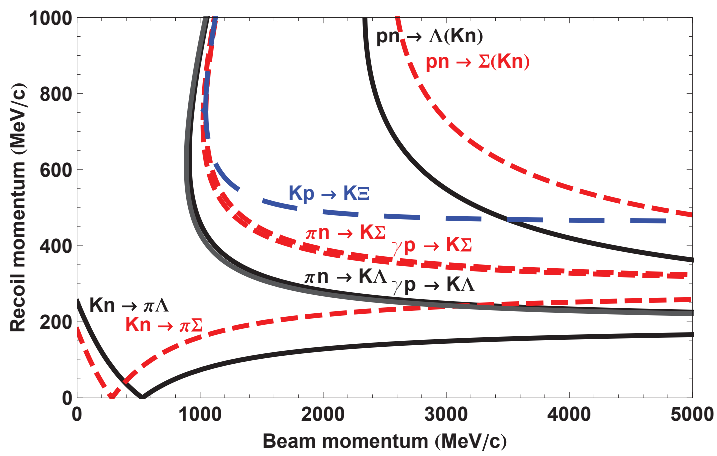

Figure 2.4: The minimum momentum transfer to the hyperon $Y = (\Lambda, \Sigma^0, \Xi)$ as a function of the projectile momentum for different production mechanisms at forward emission angle $(\theta = 0°)$ in the laboratory frame. In all shown processes the hyperon can not be produced at rest, except at $(K, p^{\pm})$ reaction. At higher projectile momenta the hyperon might be produced with momentum above its emission threshold. Figure taken from ref. [31].

A K^- strongly interacts with nucleons and thus the incident kaons in a (K^-, π^-) reaction attenuate rapidly in nucleus. In this case the (K^-, π^-) reaction most likely occurs at the surface with an outer shell neutron with little momentum transfer, simply replacing this neutron with a Λ in the same shell. On the other hand energetic K^+ have longer mean free paths in nucleus, and give larger momentum transfer to the hyperon.

2.5 The $(e, e'K^+)$ reaction

As an example of a production mechanism, let us discuss in more details the $(e, e'K^+)$ reaction. The study of hypernuclei via this process is relatively new.

Figure 2.5 illustrates such a process in the one photon exchange approximation, where incident electron, labeled e, scatters by radiating a virtual photon, γ^*. The scattered electron, labeled e', is emitted at polar angle θ_e with respect to the direction of the incident beam and is detected in a spectrometer. The plane defined by the incident electron and the scattered electron is called the scattering plane. The virtual photon carries momentum and energy from the incident electron and interacts with a proton to form a charged kaon, K^+, and a hyperon, Y, which is either a Λ or Σ^0. The kaon is emitted at a polar angle θ_K with respect to the virtual photon direction and is detected in a second spectrometer. The plane defined by the produced kaon and the produced hyperon is referred to as the reaction plane. The azimuthal angle, ϕ, is the angle between the electron-scattering plane and the reaction plane, which

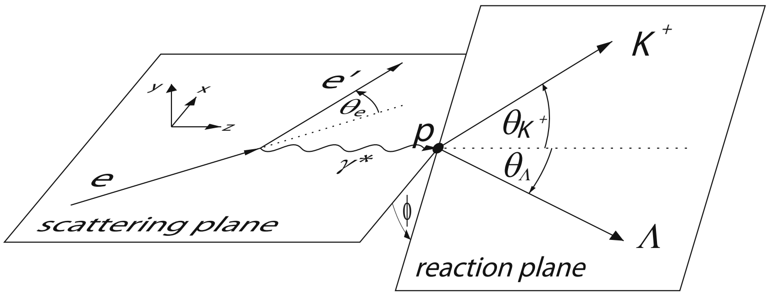

Figure 2.5: The geometry of an $(e, e'K^+)$ reaction, with the definition of the kinematic variables in the one photon exchange approximation. Scattered electron e' and the kaon K^+ are detected by two spectrometers. Scattering and reaction plane are rotated by the angle ϕ. The virtual photon γ^* transfers a four-momentum of Q^2. Fig. from A1 Collaboration.

is determined by the measurement of the scattering angles ϕ_e and ϕ_K [22].

The typical electro-production experiment requires two spectrometers, one to detect the scattered electrons which define the virtual photons, and one to detect the kaons.

2.5.1 Formalism

The kinematics of electro-production of a kaon off a nucleon, can be described as:

$$N(p^\mu_{\mathrm{targ}}) + e(k^\mu_e) \to e'(k^\mu_{e'}) + K(p^\mu_K) + Y(p^\mu_Y), \tag{2.8}$$

with stationary proton as a target and incoming electron with mass m_e in initial state. Their four-vectors are:

$$k^\mu_e = (E_e, \mathbf{k}_e), \quad p^\mu_{\mathrm{targ}} = (M_{\mathrm{targ}}, \mathbf{0}) \tag{2.9}$$

and three particles in the final state (scattered electron, kaon, hyperon Y) are described by:

$$k^\mu_{e'} = (E_{e'}, \mathbf{k}_{e'}), \quad p^\mu_K = (E_K, \mathbf{p}_K), \quad p^\mu_Y = (E_Y, \mathbf{p}_Y). \tag{2.10}$$

Such process can be well described by a first order perturbation calculation as the exchange of one virtual photon, γ^*, between the beam electron and the proton, which is changed into hyperon with the emission of kaon. In electro-production, the energy, ω, and momentum, $\mathbf{q}$, of the virtual photon are defined by the difference of the four-vectors of the incoming and outgoing electron:

$$\omega = E_e - E_{e'}, \quad \mathbf{q} = \mathbf{k}_e - \mathbf{k}'_e, \tag{2.11}$$

with $q_\mu = (\omega, \mathbf{q})$. The four-momentum transfer of the virtual photon is given by

$$Q^2 = -q_\mu q^\mu = |\mathbf{q}|^2 - \omega^2 \approx 4E_e E_{e'} \sin^2 \theta/2, \tag{2.12}$$

and can be deduced in the ultra-relativistic limit for electron scattered into the angle θ.

It is desirable to use variables invariant under Lorentz transformations. We have at our disposal the particle four-momenta, and so possible invariant variables are the scalar products: $q_\mu p^\mu_{\mathrm{targ}}$, $q_\mu p^\mu_K$, $q_\mu p^\mu_Y$. Since $p_i^2 = m_i^2$, and since $q^\mu + p^\mu_{\mathrm{targ}} = p^\mu_K + p^\mu_Y$, only two of the three variables are independent. Rather than these, it is conventional to use three independent combinations of four-vectors, called Mandelstam variables. The invariant energy, W, relates to the invariant (Mandelstam) variable s by:

$$W^2 = s = (q^\mu + p^\mu_{\mathrm{targ}})^2 = (p^\mu_K + p^\mu_Y)^2. \tag{2.13}$$

The second variable t is given by:

$$t = (q^\mu - p^\mu_K)^2 = (\omega - E_K)^2 - |\mathbf{q}|^2 - |\mathbf{p}_K|^2 + 2|\mathbf{q}||\mathbf{p}_K| \cos\theta_K, \tag{2.14}$$

where $|\mathbf{q}| = \sqrt{\omega^2 + Q^2}$ is the magnitude of the virtual photon's three-momentum. And the third variable is given by:

$$u = (q^\mu - p^\mu_Y)^2 = (p^\mu_K - p^\mu_{\mathrm{targ}})^2. \tag{2.15}$$

The cross-section for such process can be written in a standard form:

$$d\sigma = \frac{|\mathscr{M}|^2}{4\sqrt{(k_{e,\mu} p^\mu_{\mathrm{targ}})^2 - (m_e M_{\mathrm{targ}})^2}} \mathrm{dLips}, \tag{2.16}$$

where $\mathscr{M}$ is the invariant amplitude for the process under consideration and dLips is the Lorentz invariant phase space factor:

$$\mathrm{dLips} = (2\pi)^4 \delta^4(k^\mu_{e'} + p^\mu_K + p^\mu_Y - p^\mu_{\mathrm{targ}} - k^\mu_e) \frac{d^3\mathbf{k}_{e'}}{(2\pi)^3 2E_{e'}} \frac{d^3\mathbf{p}_K}{(2\pi)^3 2E_K} \frac{d^3\mathbf{p}_Y}{(2\pi)^3 2E_Y}. \tag{2.17}$$

In the exclusive reaction only scattered electron and the outgoing kaon are detected, while the momentum of the daughter nucleus is not. After the integration of differential cross-section in the laboratory frame (2.16) over $\mathbf{p}_Y$ we get:

$$\frac{d\sigma}{dE_{e'} d\Omega_{e'} d\Omega_K} = \frac{1}{4M^2_{\mathrm{targ}} (2\pi)^5 2^3} \frac{|\mathbf{k}_{e'}||\mathbf{p}_Y|}{\mathbf{k}_e} |\mathscr{M}|^2 f^{-1}_{\mathrm{rec}}, \tag{2.18}$$

with the introduction of the hadronic recoil factor:

$$f_{\mathrm{rec}} = \left| 1 + \frac{\omega |\mathbf{p}_k| - |\mathbf{q}| E_K \cos\theta_K}{M_{\mathrm{targ}} |\mathbf{p}_K|} \right|, \tag{2.19}$$

and where θ_K is the angle between $\mathbf{p}_K$ and $\mathbf{q}$.

The Lorentz invariant amplitude $\mathscr{M}$ is written as a product of electron current, the photon propagator and the hadronic current:

$$-i\mathscr{M} = (ie\bar{u}_{e'}(k^{\mu}_{e'}, s_{e'})\gamma^{\mu}u_e(k^{\mu}_e, s_e))\frac{-ig_{\mu\nu}}{q^2}\left(iJ^{\nu}(q)\right), \tag{2.20}$$

where u_e are standard Dirac's spinors for electrons with four-vector k^{μ}_e and spin s_e and J^{ν} is the four-vector current of the hadronic system. To calculate the unpolarized cross-section we must average over the spins of the incoming particles and sum over the spins of the particles in the final state. It is convenient to separate the sums over the electron and hadronic spins by writing:

$$|\mathscr{M}|^2 = \frac{e^4}{q^4}L^{\mu\nu}W_{\mu\nu}, \tag{2.21}$$

where the electronic tensor is:

$$\begin{aligned} L^{\mu\nu} &= \frac{1}{2}\sum_{\text{spin}}\{\bar{u}_{e'}(k^{\mu}_{e'}, s_{e'})\gamma^{\mu}u_e(k^{\mu}_e, s_e)\}^*\{\bar{u}_{e'}(k^{\mu}_{e'}, s_{e'})\gamma^{\nu}u_e(k^{\mu}_e, s_e)\} = \\ &= 2\left(k^{\mu}_{e'}k^{\nu}_e + k^{\mu}_e k^{\nu}_{e'} + \frac{q^2}{2}g^{\mu\nu}\right), \end{aligned} \tag{2.22}$$

and the hadronic tensor is:

$$W_{\mu\nu} = \sum_{\text{spin}} J_{\mu}(q)^* J_{\nu}(q). \tag{2.23}$$

By replacing the square of invariant amplitude with electronic and hadronic tensor in the cross-section (2.18) we get:

$$\frac{d\sigma}{dE_{e'}d\Omega_{e'}d\Omega_K} = \frac{\alpha^2}{M^2_{\text{targ}}64\pi^3}\frac{|\mathbf{k}_{e'}||\mathbf{p}_K|}{|\mathbf{k}_e|(Q^2)^2}f^{-1}_{\text{rec}}L^{\mu\nu}W_{\mu\nu}(Q), \tag{2.24}$$

where $\alpha = e^2/4\pi$ is the electromagnetic fine-structure constant. Since electron is elementary particle we know the exact form of the electron tensor $L^{\mu\nu}$ only, while hadrons are composed of smaller fragments the exact form of hadronic tensor $W_{\mu\nu}$ is unknown. In the most general case, we can express contraction of electron and hadron tensor in the form:

$$L^{\mu\nu}W_{\mu\nu}(Q) = v_0\sum_K v_K\mathscr{R}_K, \tag{2.25}$$

where the label K takes on the values L, T, TT, TL, TL', etc. Here, the labels L and T refer to the longitudinal and transverse components of the virtual photon polarization, respectively. Other labels correspond to the interference of these components. The various $\mathscr{R}_K$ are hadronic structure response functions. The factor $v_0 = (E_e + E_{e'})^2 - q^2$ and the v_K are electron kinematic and polarization factors [32].

The differential cross-section for the $p(e, e'K^+)\Lambda$ process can be expressed as a product of a virtual photo-production cross-section in the hadronic center-of-mass (labeled by $*$) frame, and a photon flux factor:

$$\frac{d\sigma}{dE_{e'} d\Omega_{e'} d\Omega_K^*} = \Gamma_{\rm v} \frac{d\sigma_{\rm v}}{d\Omega_K^*}. \tag{2.26}$$

The flux of virtual photons per scattered electron into $dE_{e'} d\Omega_e$ is given by:

$$\Gamma_{\rm v} = \frac{\alpha}{2\pi^2} \frac{E_{e'}}{E_e} \frac{k_\gamma}{Q^2} \frac{1}{1-\epsilon}, \tag{2.27}$$

where the photon equivalent energy, $k_\gamma = (W^2 - M_{\rm targ}^2)/2M_{\rm targ} = \omega - Q^2/(2M_{\rm targ})$, is the energy a real photon would have in the laboratory frame to excite a hadronic state of energy W. This factor contains all the information we need from the electromagnetic vertex. The transverse polarization factor of the virtual photon is denoted by ϵ:

$$\epsilon = \left(1 + \frac{2|\mathbf{q}|^2}{Q^2} \tan^2 \frac{\theta_e}{2}\right)^{-1} \tag{2.28}$$

The flux is calculated from the measured electron scattering angle and energy. It is evaluated in the laboratory frame. All physics from the hadronic part is contained in the differential virtual photo-production cross-section. With given polarization of the virtual photon it is expressed as a 2-fold differential cross-section:

$$\begin{aligned} \frac{d\sigma_{\rm v}}{d\Omega_K^*} &= \frac{d\sigma_T}{d\Omega_K^*} + \epsilon \frac{d\sigma_L}{d\Omega_K^*} + \sqrt{2\epsilon\,(1+\epsilon)} \frac{d\sigma_{LT}}{d\Omega_K^*} \cos\phi + \epsilon \frac{d\sigma_{TT}}{d\Omega_K^*} \cos(2\phi) + \\ & h\sqrt{2\epsilon\,(1-\epsilon)} \frac{d\sigma_{LT'}}{d\Omega_K^*} \sin\phi, \end{aligned} \tag{2.29}$$

where the terms indexed by T, L, LT, TT, LT' are transverse, longitudinal and interference cross-sections which are functions of the kinematic variables W, Q^2 and θ_K. The helicity of the incoming electron is denoted by h. For real photons, where the longitudinal polarization and the four-vector momentum transfer vanish, only the transverse term remains.

Since the cross section falls rapidly with increasing Q^2 and the virtual photon flux is maximized for an electron scattering angle near zero degrees, experiments must be done within a small angular range around the direction of the virtual photon. At very forward angles the virtual photons can be considered to be almost real. In this situation electro-production provides a connection to photo-production, with the photon flux factor, $\Gamma_{\rm v}$, multiplying the on-shell photon cross-section.

The experimental geometry requires two spectrometers, one to detect the scattered electrons which defines the virtual photons, and one to detect the kaons. Both of these spectrometers must be placed at extremely forward angles. In reality the limited momentum, solid angle acceptance and the scattering angle restrictions of the magnetic spectrometers must be taken into account. Typical magnetic spectrometers have 15-40% momentum acceptance and 5-30 msr solid angle acceptance. Especially for the electro-production of strange systems with low cross-sections, only forward scattering angles are experimentally appropriate. In parallel kinematics, with kaons emitted close to the direction of the virtual photons, the interference terms σ_{LT} and σ_{TT} vanish due to their $\sin\theta_K^*$ and $\sin^2\theta_K^*$ dependence. However, for experiments at small kaon angles the electron and kaon spectrometers could physically interfere with each other or with the electron beam-line.

2.5.2 Example of energy spectrum measurement

Let's discuss an example of the $^{12}\mathrm{C}(e, e'K^+)^{12}_{\Lambda}\mathrm{B}$ reaction measured at Jefferson Lab [33]. The measured excitation energy spectrum of $^{12}_{\Lambda}\mathrm{B}$ with differential cross sections is seen in Fig. 2.6. In order to effectively do such high-resolution spectroscopy experiments with the electrons we need the high-current electron beam, two high resolution spectrometer arms and excellent particle identification. By measuring the type of the outgoing particles and their energies ($E_{e'}$, E_{K^+}) and knowing the energy of incoming electrons (E_e) it is possible to calculate the energy which was left inside the nucleus in each event:

$$E_x = E_e - (E_{e'} + E_{K^+}), \tag{2.30}$$

where E_x is the energy left inside the nucleus and related to the excitation energy. With such analysis we can see the energy spectrum of the produced hypernuclei. In this plot a best fit (solid line) and an unnormalized theoretical computation result (dashed line) are also shown. The two prominent peaks represent the nuclei in the ground state with the Λ particle in the s- and p- shell, respectively. This occurs after replacing a s- or p-shell proton by a Λ residing in s- or p- shell (see Fig. 2.1). The other peaks between them are the core excitations with nucleons in p-shells. The widths of the peaks are due to the effects of the spin-orbit couplings of the hyperon. Due to this effect the energy levels of the pure nucleus are split, when one hyperon is added, which are separated for a few 100 keV or even less.

In a same way the mass of the produced Λ hyperon or so-called missing-mass can be measured. It is derived from the known electron energy, proton mass and measured scattered electron and hadron momenta:

$$M_x^2 = (E_e + M_p - E_K - E_{e'})^2 - (\mathbf{p}_e - \mathbf{p}_K - \mathbf{p}_{e'})^2, \tag{2.31}$$

with kaon energy, E_K, calculated from hadron momentum and assumed kaon mass. For the $p(\vec{e}, e'K^+)\Lambda$ reaction the missing-mass spectrum should reveal a peak at $M_x \approx 1115$ MeV/c^2, corresponding to Λ hyperon rest-mass.

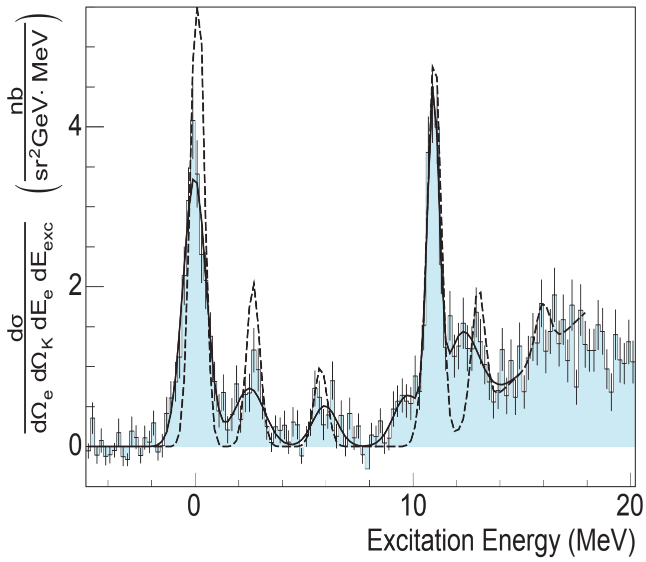

Figure 2.6: The $^{12}_{\Lambda}$B excitation energy spectrum. The best fit (solid curve) and an unnormalized theoretical computation result (dashed curve) are plotted on the data [33].

2.6 Theoretical background

The electromagnetic production of kaons off the nucleon provides an important tool for understanding the dynamics of hyperon-nucleon systems. There are many models which try to describe the electromagnetic strangeness production, that have been developed over the past few decades. First model of kaon photo- and electro-production was proposed by Kawaguchi and Moravcsik more than 50 years ago [34]. In general the theoretical models are divided into two categories: *parton-based models* and *hadron-dynamic approaches*. The first category describes kaon production with elementary constituents of interacting hadrons, such as quarks and gluons, while the second one describes the reaction dynamics with hadrons as elementary particles. Models from latter category use an effective Lagrangians for describing the strong inter-particle interactions. The form of these Lagrangians is based on the symmetries in physics and the exact mathematical structure is found by applying the fits to the experimental data.

2.6.1 Isobar approaches

The isobar approach is a common name for a particular type of effective Lagrangian model, which is very successful in describing the pion photo-production in the Δ-resonance region and η photo-production in the second resonance region.

As mentioned before in this approach hadrons are treated as elementary objects that interact with one another. The reaction amplitudes are derived from lowest-order (or so-called tree level) Born terms with intermediate particles and with the addition of extended terms. In these lowest-order terms interactions occur via N, Δ, etc. resonances in the so-called s- channel or by exchange of intermediate particles, such as K, Y, etc. in the t- and u-channels, as shown in Fig. 2.7. Masses of the exchanged particles are related to the three Mandelstam variables defined in Eq. (2.13), (2.14) and (2.15). Each intermediate state enters into the model through its strong and electromagnetic coupling constant. Processes that are described by transfers via nucleon resonances in the s-channel produce large peaks in the cross-section diagrams at corresponding hadronic energies W, or equivalently $\sqrt{s}$, that match the masses of intermediate resonances. Processes described by t- and u-channels with exchange of kaons and hyperons do not produce such peaking behavior, and are often referred to as background contributions.

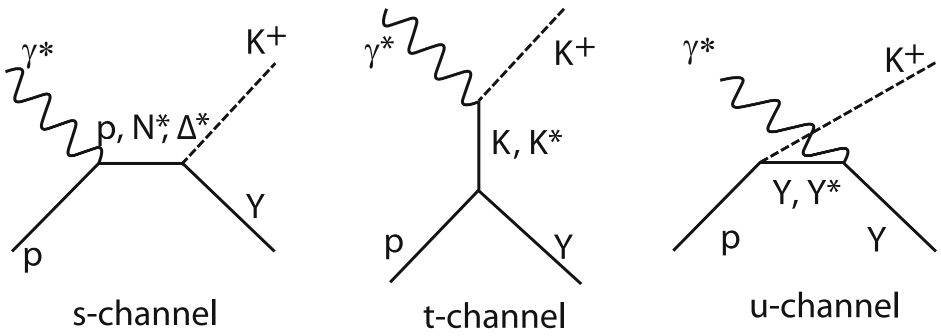

Figure 2.7: The lowest-order Feynman diagrams of s-, t- and u-channel for the $p(e, e'K^+)Y$ reaction. The intermediate states are defined by their masses and effective couplings constants. Different models use different sets of exchange particles and resonances.

For a complete description of the reaction process all possible channels are needed. Many models neglect higher orders, like final-state interactions. Most of the calculations for kaon photo- and electro-production have been done in the framework of tree-level isobar models [35, 36], but only a few with additional higher-order terms exist [37]. Even in a three-level calculation the main trends can be identified. But there are still several dozen parameters that need to be found, due to large and unknown number of exchanged hadrons and intermediate resonances of the reaction. Models differ in the use of nucleon, hyperon and kaon resonances with their effective coupling constants. Strength of the contributing diagrams strongly depends on set of resonances included. The nomenclature for characterizing nucleon resonances is $L_{2I;2J}(M)$, where L is the orbital angular momentum of the partial wave, I is the isospin, J is the spin and M is the mass of the resonance. Some of the models from this category are:

- **variants of the K-Maid model**
  In Kaon-Maid model four nucleon resonances, the $S_{11}(1650)$, $P_{11}(1710)$, $P_{13}(1720)$,

kaon resonances $K^*(890)$ and $K_1(1270)$ and the "missing resonance" $D_{13}(1900)$ are included. This D_{13} resonance has never been observed, but the existence was predicted by the constituent quark model calculations [38]. The interactive version of this model is available through the internet and is referred to in this thesis as the original variant [39]. In another variant of this model the strong longitudinal couplings to the nucleon resonance are removed. This variant of the K-Maid model is referred to in this thesis as the reduced variant.

- **Saclay-Lyon model**
  The Saclay-Lyon model shares with K-Maid the same kaon resonances, but differs in the set of nucleon resonances with spins up to $\frac{5}{2}$ and uses the spin $\frac{1}{2}$ hyperon resonances $S_{01}(1405)$, $P_{11}(1660)$, $S_{01}(1670)$ and $P_{01}(1810)$ etc. No longitudinal couplings are included in this model and it is very successful in predicting correct cross-sections for electro-production of hypernuclei at low Q^2 [40].

2.6.2 Regge model

At energies more than 1 GeV above the strangeness threshold the isobar approach becomes inefficient as the quark-gluon structure of the interacting particles starts to manifest itself. At this energies the so-called Regge model provides a useful method for describing reaction processes [41, 42]. It has only a few free parameters and can be treated as a modified version of isobar approach. In Regge model each intermediate state is considered as a set of many hadrons instead of a single particle, and the amplitude of the reaction process is described by the so-called Regge propagator.

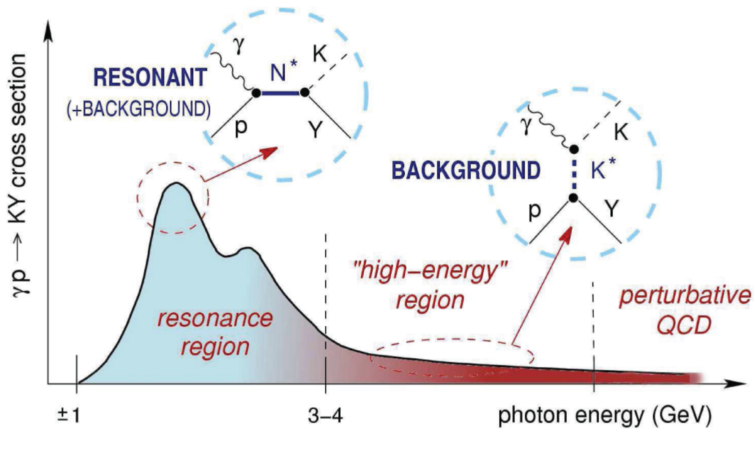

Figure 2.8: Schematic representation of the total KY photo-production cross-section as a function of photon energy in the laboratory frame. In the resonance region, the cross-section is described by the isobar approach with resonant and background diagrams, while at higher energies it is described by a Regge model assuming background diagrams only. Figure is taken from [43].

Fig. 2.8 illustrates schematically the KY photo-production cross-section. At higher photon energies where the resonant peaks vanish the cross-section can be described by a background diagrams only (t-channel predominantly from Fig. 2.7). The Regge model is thus simpler than the isobar approach because it does not contain any intermediate resonance states. The background part of the cross-section in the resonance region can be described by the Regge model, because it has been observed that the model can reproduce experimental data down to photon energies of a few GeV. By adding the Feynman diagrams, which contain intermediate nucleon resonances, to the Regge model in the low-energy domain, the total cross-section with resonant peaks can be described. Such resonant contributions to the background vanish at higher energies.

In the Regge-plus-resonance variant the resonance part of the amplitude includes contribution from exchanges of the nucleon resonances $S_{11}(1535)$, $S_{11}(1650)$, $F_{15}(1680)$, $P_{13}(1720)$, $D_{13}(1900)$, $P_{13}(1900)$, $P_{11}(1900)$ and $F_{15}(2000)$ [44, 45].

2.7 The effective Λ-nucleus potential

At short distance (less than 1.7 fm) baryons interact with the nuclear force, which is a residual effect of the even more powerful strong force. The interaction between two baryons is expressed with the corresponding potential (e.g. Yukawa potential for long-range interaction). But when the nucleon or hyperon is bound inside the nucleus it interacts via effective potential generated by the other nucleons. In the most simplistic form a hypernucleus can be considered as an ordinary nuclear core with a hyperon in the hyperon-nucleus effective potential. Within a nucleus the general hyperon-nucleus potential can be expressed in the form:

$$V^{\mathrm{eff}}(r,\vec{\sigma}_A,\vec{\sigma}_Y) = V_0(r)+V_\sigma(r)(\vec{\sigma}_A\cdot\vec{\sigma}_Y)+V_T(r)S_{12}+V_{\mathrm{ls}}(\vec{L}\cdot\vec{\sigma}^+)+V_{\mathrm{als}}(r)(\vec{L}\cdot\vec{\sigma}^-), \quad (2.32)$$

where r is a distance between the hyperon and the center of the nucleus and the $\vec{\sigma}_A$, $\vec{\sigma}_Y$ are the spin operators of the nucleus and the hyperon. In the above equation, $S_{12} = 3(\vec{\sigma}_A\cdot\hat{r})(\vec{\sigma}_Y\cdot\hat{r}) - \vec{\sigma}_A\cdot\vec{\sigma}_Y$ is the spin-tensor operator, L is the angular momentum of the hyperon relative to the nucleus and $\vec{\sigma}^{\pm} = 1/2(\sigma_A \pm \sigma_Y)$ are the symmetric and anti-symmetric combinations of nucleus and hyperon spin operators. V_0 is the spin-averaged central interaction (e.g. Woods-Saxon potential). The potential contains both symmetric and anti-symmetric spin orbit terms. Both of the spin-orbit terms are very small in the Λ-nucleus interaction. Each term of the effective interaction depends on the distance between the hyperon and the nucleus: $V_k(r); k \in \{0,\sigma,T,ls,als\}$. Those therms usually have a Gaussian shape ($V_k(r) = \sum_i v_i e^{-r^2/\beta_i^2}$), and depend on the theoretical model.

The produced hypernuclei can be in an excited state if the proton in p- or higher shell is replaced by a hyperon. Hypernuclear states are labeled with their total angular momentum J and parity P as J^P. The energy of the excited state can be released by emitting the neutrons or protons. But sometimes the energy is released

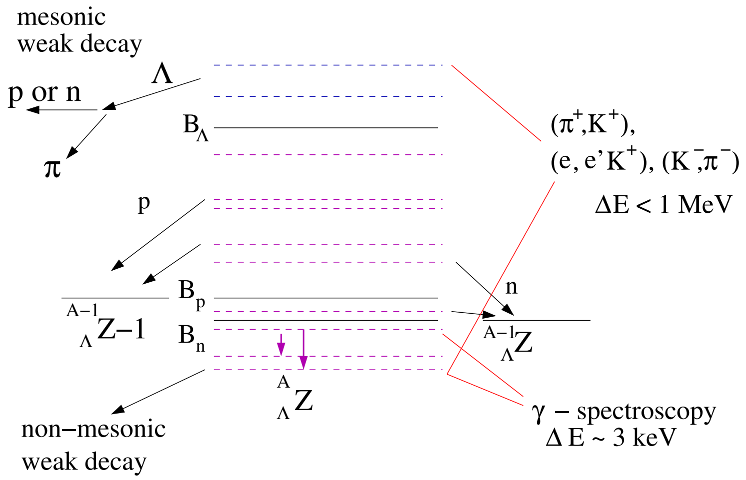

Figure 2.9: Potential well in which the hyperon is placed when bound inside the nucleus. Figure adopted from [46].

by γ-rays, when the hyperon moves to the lower states. The depth of the potential well of a Λ in a nucleus is around 30 MeV. So many energy levels of a single-particle orbits are above the nucleon (proton and neutron) emission thresholds (Fig. 2.9). Thus, the observation of γ-rays is limited to the low excitation region, somehow up to the Λ in p-orbit. Another weak point is the fact that the γ-ray transition only measures the energy difference between two states and not the absolute energy of the system.

Measurements of γ-ray transitions in Λ hypernuclei enables the analysis of various excited levels with an excellent energy resolution ($\approx$ 3 keV) with Ge detectors. Energy spectrum can be measured by various methods [46].

2.8 Weak decays of hypernuclei

Quantitative information on the interactions mentioned before can be also achieved through the study of the decay of hypernuclei. In free space hyperons decay by the weak interaction. Since strangeness is conserved by the strong and electromagnetic interactions, the lightest hyperons can not decay strongly nor electromagnetically. A typical lifetime is of the order of 10^{-10} s, except the Σ^0 which decays much faster electromagnetically, $\Sigma^0 \rightarrow \Lambda + \gamma$. The Λ particle decays into protons, $\Lambda \rightarrow p\pi^-$ (64%), or into neutrons, $\Lambda \rightarrow n\pi^0$(36%). These mesonic decay modes are strongly suppressed when the hyperon is bound in the nucleus, due to the low momentum of the outgoing nucleon (around 100 MeV/c) compared to the typical Fermi momentum in nuclei ($\approx$ 270 MeV/c). This is represented in Fig. 2.10.

While the mesonic decay mode of the Λ hyperon gets Pauli blocked by the presence of the nucleons in the medium, the non-mesonic mode $\Lambda N \rightarrow NN$, becomes dominant in heavy hypernuclei, which is still a weak decay. In these non-mesonic decays more energy is released (e.g. $\Lambda + n \rightarrow n + n + 176$ MeV, $\Lambda + p \rightarrow n + p + 176$ MeV) than in the mesonic decays in hypernuclei (≈ 40 MeV). Heavier hyperons in nuclei are also able to decay via hadronic interaction, like for example: $\Sigma^+ n \rightarrow \Lambda p$, $\Sigma^- p \rightarrow \Lambda n$.

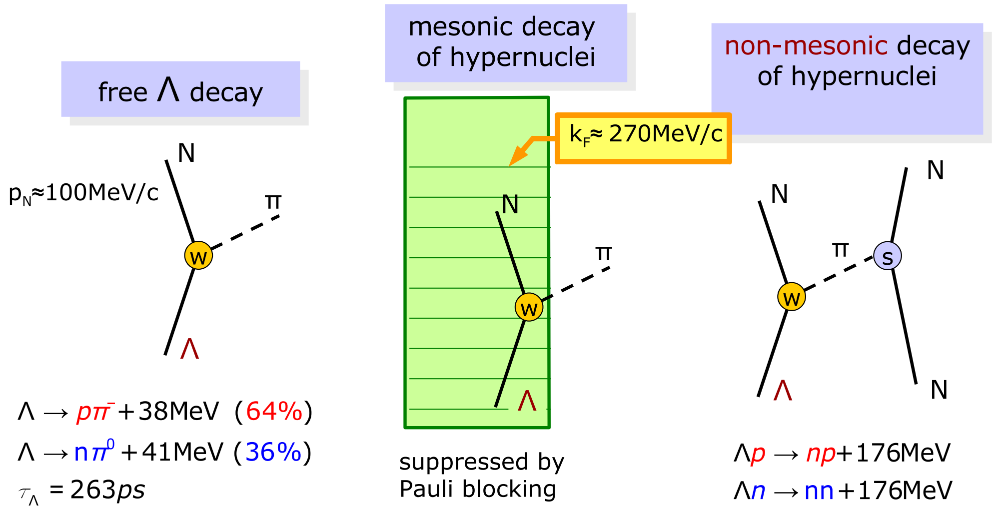

Figure 2.10: The decays of the Λ hypernuclei in free space and inside the nucleus. Mesonic decays are suppressed inside the nucleus due to the Pauli blocking and only hadronic decays are allowed. Figure made by prof. J. Pochodzalla.

CHAPTER 3

Accelerator and experimental hall

3.1 Accelerator

Since 1979 the Mainz Institute for Nuclear Physics operates a continuous wave electron accelerator (MAMI: MAinz MIcrotron) for experiments in nuclear and hadronic physics [47]. The accelerator consists of a cascade of three Race Track Microtrons (RTM) and a fourth stage, a harmonic double sided microtron (HDSM).

The microtrons are built with normal conducting accelerating cavities placed between two high precision and homogeneous magnets allowing for multiple recirculation of the beam. Inside the dipole field B the change of trajectory radius for relativistic electrons is caused by the increase of energy:

$$\Delta R = \frac{\Delta E}{ecB}. \tag{3.1}$$

To satisfy the dynamic coherence condition $L_{i+1} - L_i = n\lambda = 2\pi\Delta R$, the increase of energy by n turns is:

$$\Delta E = \frac{ecB}{2\pi} n\lambda, \tag{3.2}$$

where L_i is the length of the ith loop in the accelerator and $\lambda = c/\nu$, with ν being the frequency of the RF cavity. In this case the energy gain in RTM 3 after total of 90 turns is 675 MeV at the frequency of $\nu = 2.45$ Gz.

Electrons are produced by a thermionic source with an energy of 100 keV. It is also possible to produce polarized electrons by photoelectric effect using polarized laser light on GaAs crystal with polarizations up to 80%. MAMI can provide polarized electrons of more than 20 μA beam-current and unpolarized electron beams of up to 100 μA.

After the source, a linac injects a beam with the energy of 3.5 MeV into the first microtron which is then raised to 14.9 MeV. The second and the third microtrons (called MAMI-A and MAMI-B) rise the energy to 180 MeV and 855 MeV, respectively (see Fig. 3.1) with the energy spread of 30 keV (FWHM).

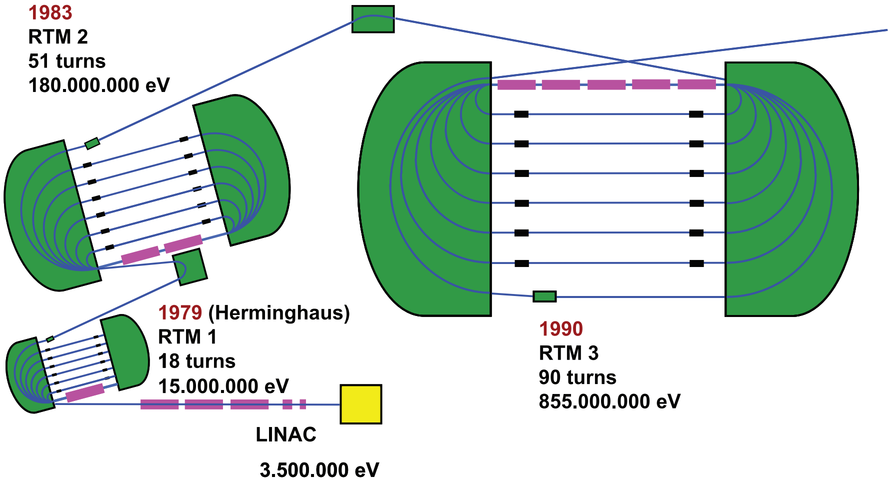

Figure 3.1: The MAMI accelerator complex. The fourth stage (MAMI C) is not shown. Figure by A. Jankowiak.

A fourth stage, called MAMI-C, was completed in 2007 which increases the beam-energy up to 1.6 GeV. Recirculation is realized by four magnets with 45° bending, because of limited space in the hall and the electrons are accelerated by normal conducting cavities, arranged in two antiparallel linacs (see Fig. 3.2). The magnets used for the accelerator stage MAMI C are approximately 5 m wide and weigh 250 t, leaving MAMI to be the biggest microtron in the world.

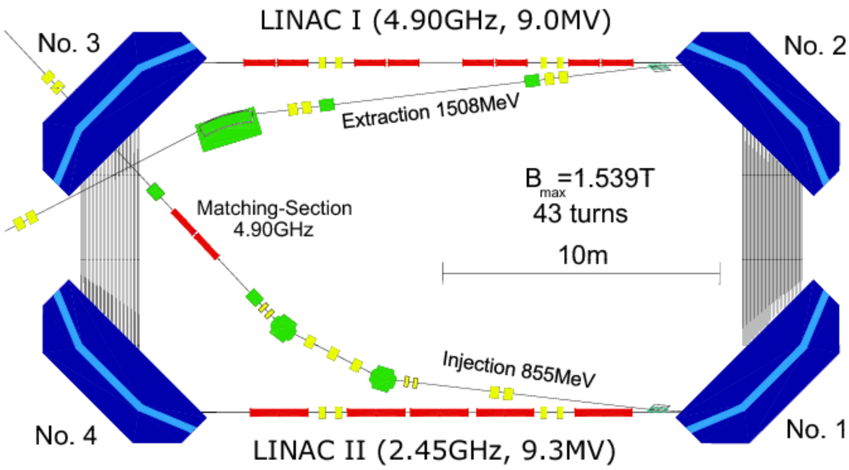

Figure 3.2: Detailed scheme of the Harmonic Double Sided Microtron (HDSM) for MAMI-C [48].

MAMI is a so-called continuous wave accelerator. The electron beam is clustered into bunches, but the time structure of the beam is too small to be registered by the experiment's detectors so that the beam seems like a continuous current. To accelerator needs 163 kW of power for 67.5 kW of beam power (100 μA) which gives the efficiency of 41.4%.

In Fig. 3.3, the floor plan of the experimental halls and accelerator areas is shown. A beam transport system delivers the beam to four experimental halls: A1 (electron scattering, i.e. experiments with virtual photons), A2 (experiments with real photons), A4 (parity violating electron scattering), X1 (experiments with X-rays).

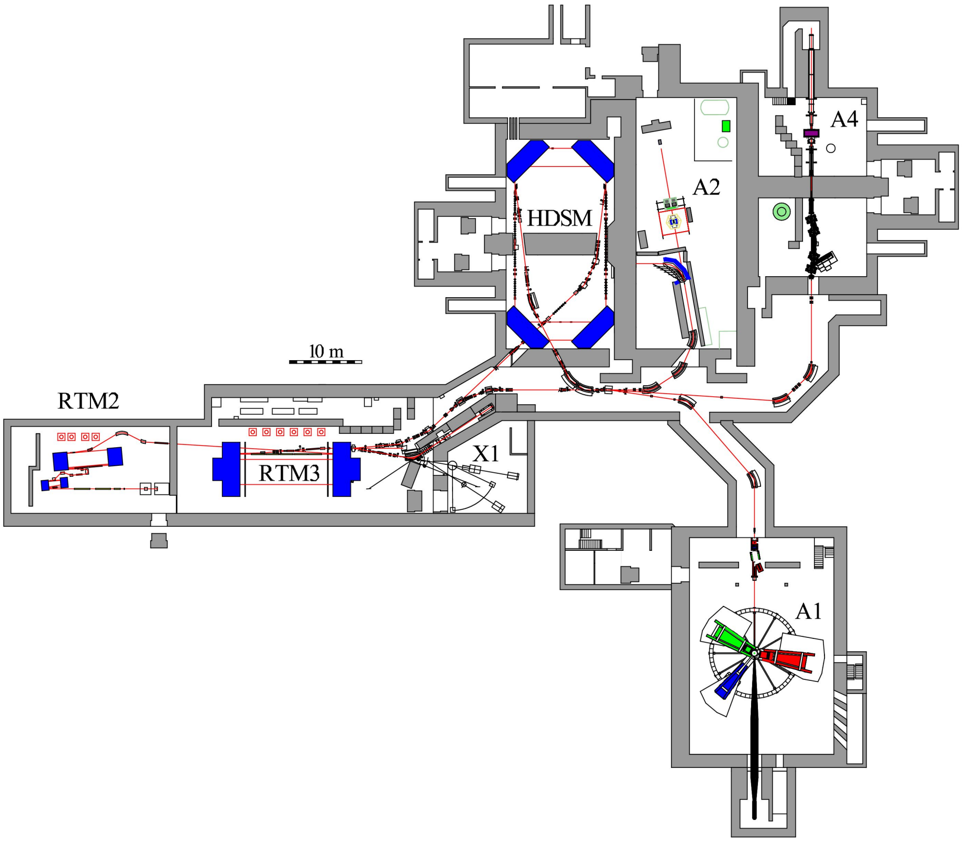

Figure 3.3: MAMI floor plan with the accelerator stages and experimental areas of the A1, A2, A4 and X1 Collaborations.

3.2 A1 experimental hall

The A1 Collaboration at the Institute for Nuclear Physics operates a three spectrometer facility for electron scattering experiments in nuclear and hadronic physics. An overview of the experimental setup with its main components is given in next subsections. The Kaos spectrometer is left out, as it is described separately in chapter 4. The A1 experimental hall together with the spectrometers is shown in Fig. 3.4.

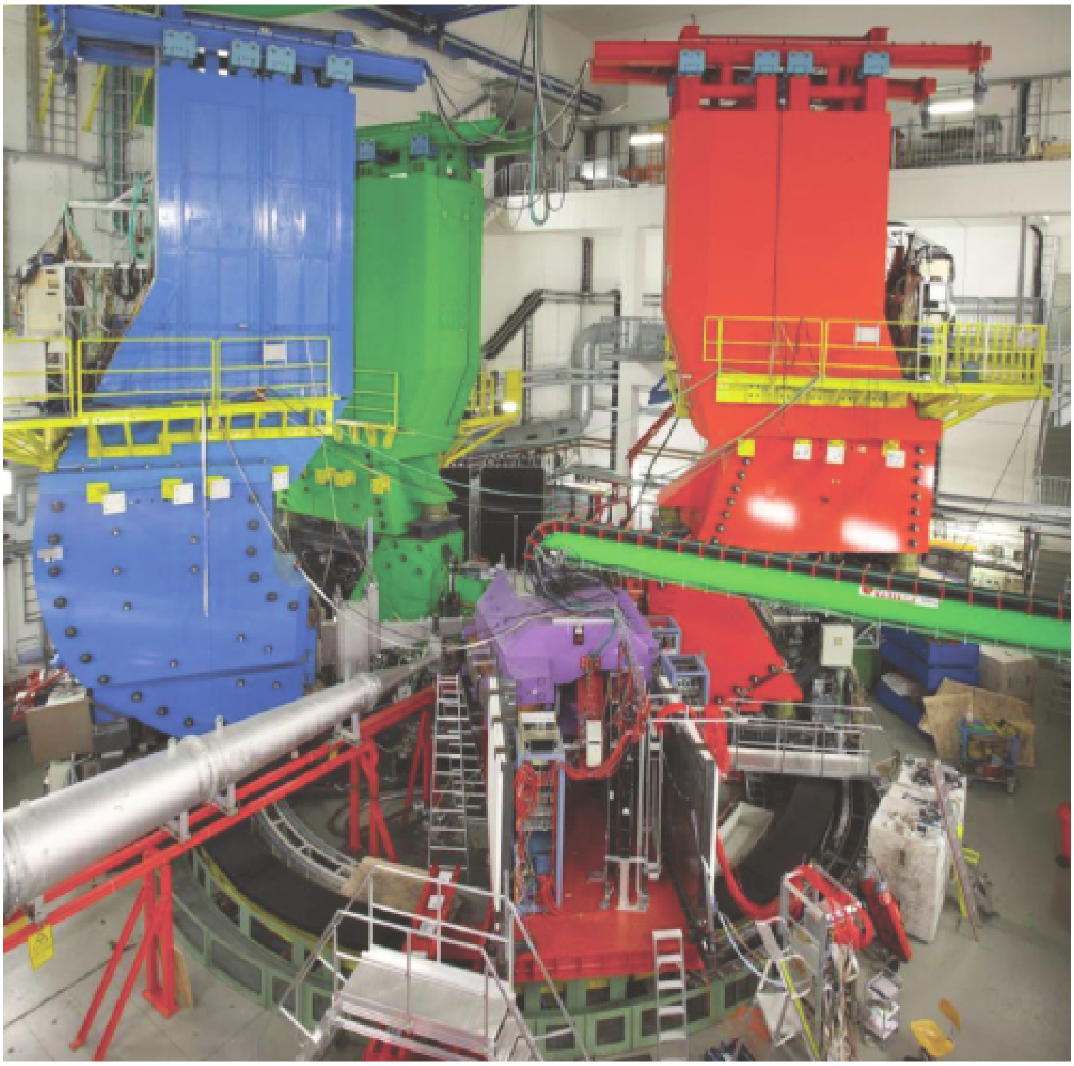

Figure 3.4: The A1 three spectrometer facility at MAMI. The spectrometers are labeled as A (red), B (blue) and C (green) with KAOS spectrometer in the middle (violet).

3.2.1 Magnetic spectrometers

In the A1 experimental hall, three high resolution spectrometers (called A, B, and C) are arranged around a target. They can operate in single, double or triple coincidence mode. The charged reaction products that are scattered within the spectrometer acceptance are guided by the magnetic fields to the detector system of the spectrometers.

Spectrometers A and C have a quadrupole-sextupole-dipole-dipole (QSDD) magnetic configuration, which enables measurement of high particle momenta and a relatively large acceptance (28 msr). Spectrometer B uses a single dipole magnet (so-called slam-shell), which enables higher spatial resolution, but smaller accep-

Table 3.1: Main parameters of the three magnetic spectrometers and layout of spectrometers A and B. Figure from A1 Collaboration.

Spectrometer	A	B	C
Configuration	QSDD	D	QSDD
Max. momentum (MeV/c)	735	870	551
Max. momentum (centr. traj.) (MeV/c)	665	810	490
Max. induction (T)	1.51	1.5	1.4
Momentum acceptance (%)	20	15	25
Solid angle (msr)	28	5.6	28
Scattering angle range (°)	18-160	7-62	18-160
Length of central trajectory (m)	10.76	12.03	8.53
Momentum resolution	$\leq 10^{-4}$	$\leq 10^{-4}$	$\leq 10^{-4}$
Angular resolution at target (mrad)	≤ 3	≤ 3	≤ 3
Position resolution at target (mm)	3-5	1	3-5

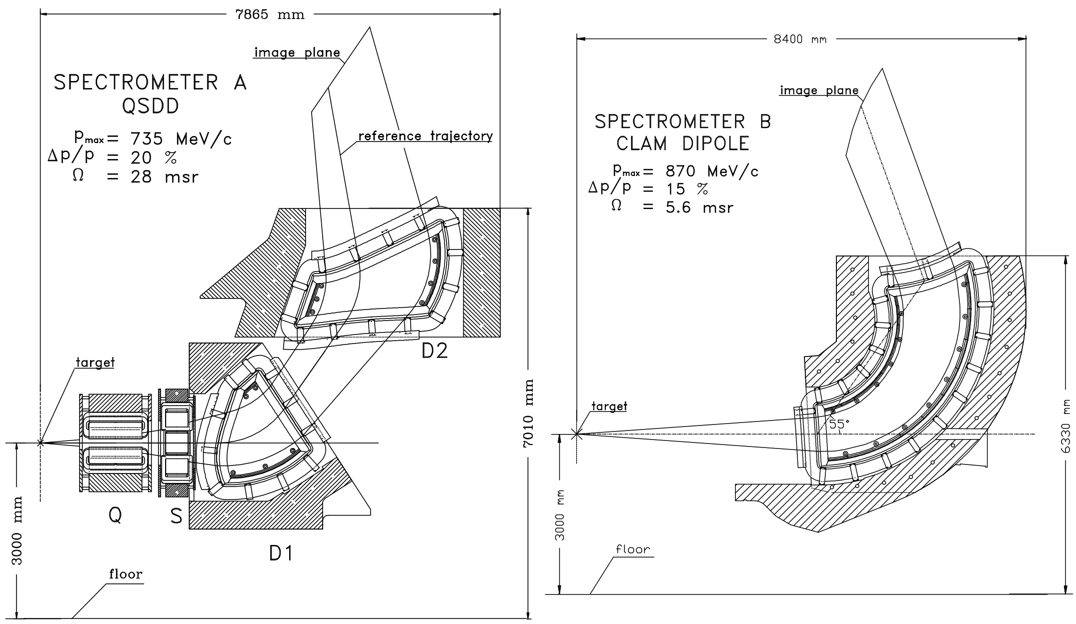

tance (5.6 msr), and point-to-point focusing in dispersive and non-dispersive plane. The optics of spectrometers A and C has point-to-point focusing in the dispersive plane which ensures that the coordinate at focal plane x_{fp} is independent from the initial angle at target θ_0, resulting in high momentum resolution. In the non-dispersive direction the optics is parallel-to-point, meaning that the y_{fp} coordinate at focal plane is insensitive to the initial y_0 position. The last property ensures good angular resolution, but reduces the position resolution. This construction permits a narrower spectrometer which can reach small scattering angles (down to 7°). This spectrometer can also be tilted for reaching out of plane angles up to 10°. Spectrometer C is a down-scaled version of spectrometer A with the scaling factor of $\frac{11}{14}$. The main spectrometer parameters are summarized in Table 3.1. The central magnetic field in the spectrometers, and thus the central momentum, are determined by means of Hall and NMR probes [49].

All three spectrometers have similar detector packages consisting of four vertical drift-chambers (VDCs), scintillators and a gas Čerenkov detector. The drift-chambers are used for particle trajectory reconstruction and the scintillators for triggering and particle identification. As electrons (positrons) and pions cannot be distinguished by the scintillators, the gas Čerenkov detector is used to discriminate among them. Moreover, in spectrometer A the Čerenkov detector can be substituted by a recoil proton polarimeter.

Drift chambers

Each spectrometer consist of two pairs of vertical drift chambers (VDC) which are placed in the focal plane. The VDCs consist of equally spaced signal wires between cathode foils with 5 mm spacing between a pair of wires. One chamber in each pair has wires in the non-dispersive direction, labeled as x wires, to determine the momentum and the out-of-plane angle of the reconstructed particle, while the other set of wires, labeled as s, is in an another plane and in a diagonal direction with 40° in respect to x wires (see Fig. 3.5). The volume is filled with a gas mixture of argon and isobuthan and 15% admixture of pure ethanol to minimize aging. The wires are grounded, while the foils are set at negative potential between 5.6 and 6.5 kV.

The particles traverse the chambers with an average 45° angle to the normal of the plane and produce ionization from where the electrons drift towards the wires with a known velocity. The signal is generated typically in at least three and up to seven wires. The signals from the wires stop the time measurement started by the scintillators and the time information from each wire is translated into the distance between the particle trajectory to the wire. The distance information from one wire-plane gives one coordinate. With two wire-planes in both chambers particle coordinates x_{fp}, y_{fp} and angles θ_{fp}, ϕ can be determined. Here x_{fp} and θ_{fp} are measured in dispersive direction and y_{fp} and ϕ in non-dispersive direction. The final spatial resolution in the drift chambers in the dispersive direction is ≤ 200 μm and ≤ 400 μm in the non-dispersive direction. The single plane efficiency is better than 99%, leading to an overall efficiency of better than 99.9%. More information about the drift chambers can be found at [50, 51].

The VDCs measure the particles coordinates in the focal-plane which are then used for determining the target coordinates and the particle momentum. The particle coordinates at the target (δ, θ_0, y_0, ϕ_0) are reconstructed from the measured focal-plane coordinates (x_{fp}, θ_{fp}, y_{fp}, ϕ) with the aid of transfer coefficients:

$$G = \sum_{i,j,k,l} \langle G | X^i \theta^j Y^k \phi^l \rangle X^i \theta^j Y^k \phi^l, \tag{3.3}$$

where $G \in (\delta,\ \theta_0,\ y_0,\ \phi_0)$, $\delta = (p - p_c)/p_c$ and p_c is the central momentum of the spectrometer, defined by the trajectory of a particle that emerges from the center of the target along the z-axis. The coefficients of the expansion are obtained with a measurement done with a special sieve-slit collimator placed at the spectrometer entrance window.

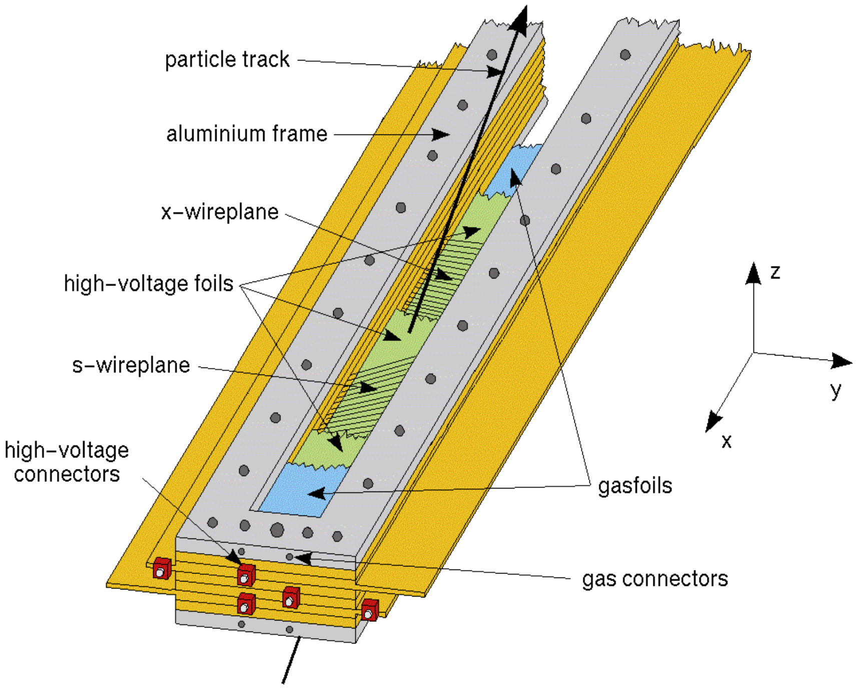

Figure 3.5: Schematic drawing of a vertical drift chamber. The s wires are at an angle of 40° relative to the x wires. Figure from [49].

Scintillators

Two layers of plastic scintillators are used for energy deposition measurement. They also serve as a trigger for the data acquisition system, for the drift chambers time determination and for the time information for coincidence timing. Each scintillator plane has 15 paddles (spectrometers A and C) or 14 (spectrometer B) with dimensions of 15×16 cm^2 and 14×16 cm^2, respectively.

The first plane (called dE) in the particle's path is 3 mm thick and is used for the energy loss determination, while the second plane with 10 mm thickness (called ToF) is used for the time-of-flight measurement. The time resolution of the ToF scintillator plane is better than $\sigma = 255$ ps for all spectrometers. The segmentation enhances the time resolution and gives a rough position of the particle track. The segments are coupled at each of the two sides via plastic light guides to photomultipliers which are read out in coincidence. The scintillators of spectrometer B are short enough to be read out from one side only. The average efficiency across any scintillator plane in spectrometers A, B and C is above 99.5% [52, 53].

Using the correlation of the energy losses in the two planes, particle identification can be done and minimum ionizing particles can be distinguished from protons. But in the momentum range of interest, which is a few 100 MeV/c, pions and electrons are not distinguishable by the scintillation detectors, since they are both minimum ionizing particles, therefore the Čerenkov detector has to be used.

Gas Čerenkov detectors

The discrimination between pions and electrons/positrons in done with a gas Čerenkov detector. They are placed after the VDCs and the scintillator planes (see Fig. 3.6).

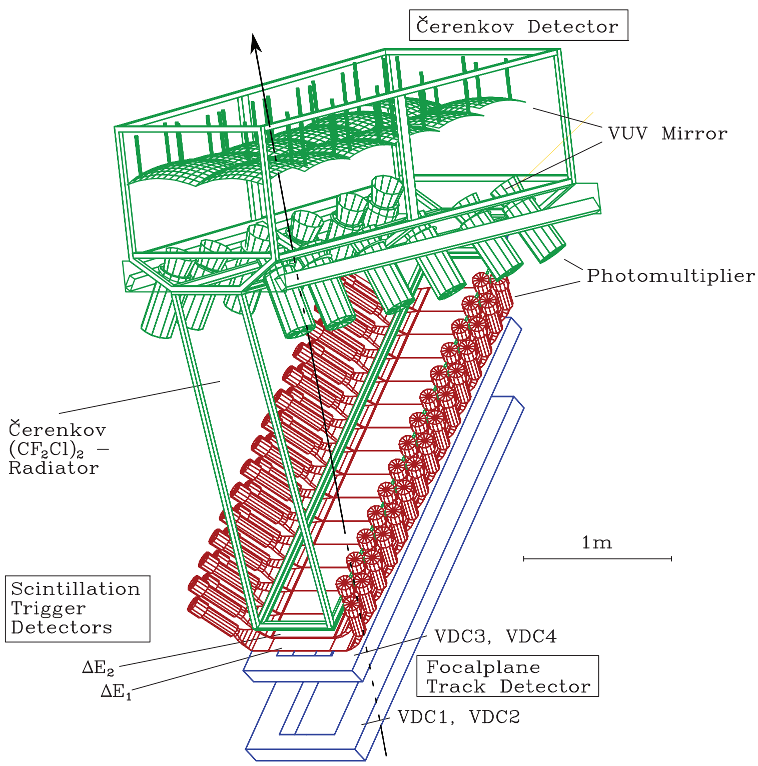

Figure 3.6: Schematic drawing of the detector system of spectrometer A with four VDCs, two layers of scintillators and a Čerenkov detector. Note: freon gas has been used until 2002, while now decafluorobutane, C_4F_{10}, is in use. Figure from [49].

Čerenkov light is generated in the gas at atmospheric pressure and with the index of refraction $n = 1.0013$ at 400 nm by electrons or positrons with energies larger than 10 MeV. The threshold for pions lies at 2.7 GeV, so they never produce

Čerenkov photons by the 1.6 GeV beam. Consequently, in the typical energy ranges of the experiments, only electrons entering the volume of the detector give rise to a signal. The Čerenkov photons are transmitted through the gas, reflected by 2×6 special mirrors (5 in spectrometer B) and then collected by photomultipliers. The efficiency of the Čerenkov detectors for electrons (or positrons) is 99.98%.

3.2.2 Target

The target is located inside the vacuum scattering chamber, which lies between the spectrometers. Various solid state targets can be mounted on the target ladder which holds several interchangeable solid state materials of varying thicknesses. For example, a luminescent screen (an Al_2O_3 plate with a cross hair printed on) is mounted for beam position calibration. Target vertical position is remotely controlled and the desired material can be selected during the beam-time. Also a high-pressure gas target or a cryogenic target can be used for materials like hydrogen or deuterium (H,D) or helium (^{4}He,^{3}He).

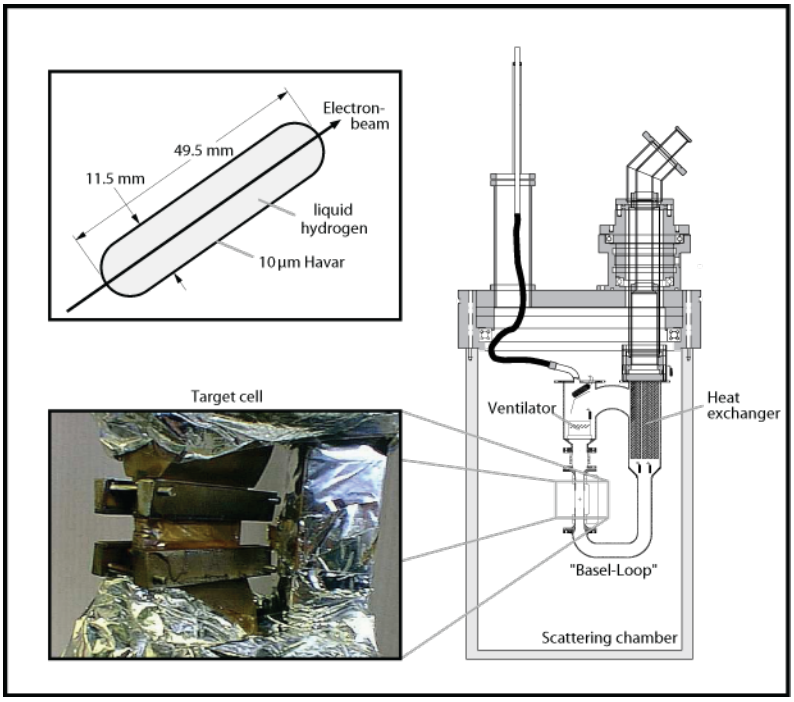

Figure 3.7: Schematic drawing of the scattering chamber. The liquid hydrogen from the first loop comes from the top and cools down the target material which circulates in the second loop. Figure from [54].

The technique for cooling and liquefying them is based on two cooling loops. The liquid hydrogen from the first loop is transported to the target vessel by a transfer pipe and cools down via heat exchanger the second loop (called Basel-loop) which contains the scattering material. The second loop has a fan, which provides The first loop is based on a Phillips compressor for liquefying hydrogen which continuous recirculation (see Fig. 3.7).

By this the heat of the energy deposition by the electron beam (up to 40 μA) is continuously moved to the heat exchanger. The Basel-loop is filled with the scattering material before the experiment and the liquid phase is maintained by the first cooling loop. In the Basel-Loop the target cell is placed which is 49.5 mm long and 11.5 mm wide. The geometry is chosen to maximize the luminosity by a long target cell and to minimize the uncertainty by energy loss. During the experiment the temperature and pressure of the liquid target are measured. To avoid local boilings of the liquid the temperature oscillations must be kept as small as possible by moving the beam in the transverse directions. This is done at an frequency of several kHz with an amplitude of ± 3 mm. The stability of the liquid phase is important for a precise determination of the luminosity. The target can be rotated around its own axis when necessary.

3.2.3 Møller polarimeter

A Møller polarimeter is placed in the A1 experimental hall in order to have an absolute measurement of the beam polarization. The polarization is measured just before the scattering and after transport of electrons through the accelerator and beam systems, where the polarization can change. A Møller polarimeter exploits the process of Møller scattering of polarized electrons off polarized atomic electrons in a magnetized foil: $\vec{e}^{\,-}\vec{e}^{\,-} \to e^-e^-$ with cross-section:

$$\frac{d\sigma}{d\Omega} = \frac{d\sigma_0}{d\Omega}\left(1 + \alpha_{zz}(\theta_{\mathrm{cm}}) P_b^z P_t^z\right), \tag{3.4}$$

where $\frac{d\sigma_0}{d\Omega}$ is the polarization independent part, P_b^z the beam polarization and P_t^z the target polarization. We speak of polarization with respect to the z-axis which is in beam direction. The analyzing power α_{zz} depends on the scattering angle in the CM frame, θ_{CM}, where the labels indicate the projections of the beam and target polarizations.

The incoming polarized electrons scatter on the polarized ($P_{Fe} \approx 8\%$) electrons of in a 6 μm iron foil placed in a 4 T magnetic field generated by a superconducting coil. The scattered and the recoil electrons are focused by a quadrupole magnet and deflected by a dipole magnet towards two Pb-Glass counters placed on one side of the beam-line (Fig. 3.8).

The target polarization is fixed, while the beam polarization is changing with 1 Hz frequency. By changing the spin direction of the beam, the cross-sections are measured where the electron spins are parallel and antiparallel, labeled: $\sigma^{\uparrow\uparrow}$ and $\sigma^{\uparrow\downarrow}$. By comparing the count rate in the two counters for events that are in time coincidence the following asymmetry is measured:

$$A = \frac{\sigma^{\uparrow\uparrow} - \sigma^{\uparrow\downarrow}}{\sigma^{\uparrow\uparrow} + \sigma^{\uparrow\downarrow}} = \alpha_{zz}(\theta_{\mathrm{cm}}) P_b^z P_t^z. \tag{3.5}$$

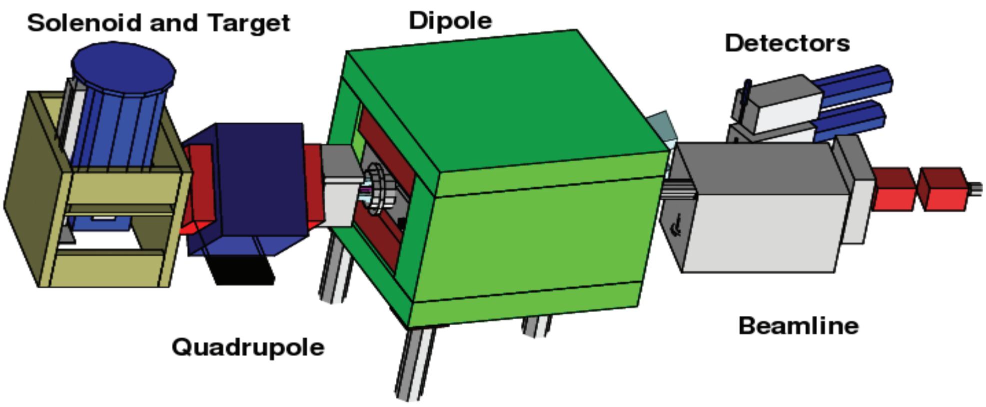

Figure 3.8: Schematic drawing of the Møller polarimeter for measurement of the incident electron polarization. Figure taken from [55].

By measuring the asymmetry (3.5), knowing the analyzing power α_{zz} and the iron polarization degree, the polarization of the beam can be extracted:

$$P_b^z = \frac{A}{\alpha_{zz}(\theta_{\rm cm}) P_t^z}. \tag{3.6}$$

The contributions to the systematical errors come from the knowledge of the beam and detector positions, from the target polarization P_t^z which depends mainly on the temperature and the applied magnetic field, and most of all from the analyzing power which is calculated theoretically. The final systematical error is $\approx \pm 1.2\%$.

3.2.4 Trigger and data acquisition

Each of the three spectrometers has independent electronics which is responsible for signal amplification and analog-to-digital conversion, as well as for trigger generation. The minimum trigger condition requires one hit in one of the scintillator segments in one of the layers in such a way that the photomultipliers on both ends produce signals larger than set thresholds. This condition can be extended by demanding coincidence of both scintillator layers (dE and ToF). The trigger condition can also be put in coincidence or anti-coincidence with the information from the gas Čerenkov detector.

The signals from the paddles are delivered to a PLU (Programmable Logic Unit) which enables selection between these conditions during the beam-time. The output of the PLU is sent to the FPGA (Field Programmable Gate Array). This module receives information from all three spectrometers, with a possibility to change the width and the position of the incoming signals depending on the kinematical configuration and the measured physical reaction. It is possible to scale down each of the incoming signal rates via prescalers if the suppression of any of them is needed.

Finally, when the FPGA accepts an event the gate signals are distributed to start analog-to-digital conversion. Simultaneously the so-called interrupt signal is sent to front-end computers to read-out all data. While the digital conversion and read-out is in progress the electronics can not accept further events. For this reason the so-called busy signal is generated by the micro busy module to prevent any interactions. During the experiment the total "busy time" is measured by scalers and the information is used later for the dead time calculation. In the final subsection of my thesis (7.5.3) the dead time information was used to get the corrected luminosity of data taken into analysis. More information about trigger system can be found at [56].

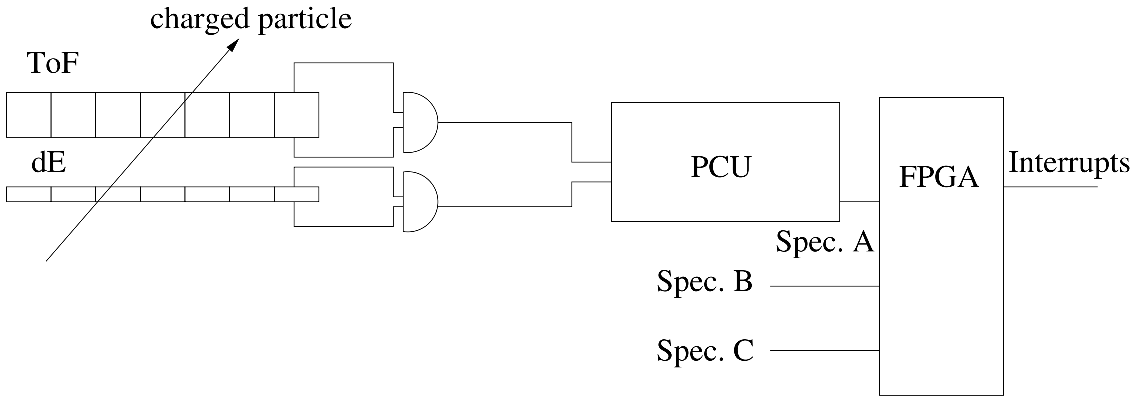

Figure 3.9: Scheme of the trigger system for the spectrometers. Because the FPGA has only three inputs, the signal from Kaos is replaced by one of the spectrometers. Figure adopted from [55].

CHAPTER 4

The KAOS spectrometer

KAOS is a magnetic spectrometer developed and operated at SIS facility at GSI, and manufactured by Danfysik in Denmark in 1991. In 2003 the original KAOS spectrometer was dismantled and brought to Mainz. The installation was completed in 2007 and is operational since 2008 at the A1 spectrometer facility: [31, 57, 58, 59, 60, 61] etc.

Table 4.1: Main parameters of the KAOS spectrometer.

Spectrometer	KAOS
Configuration	D
Max. momentum (MeV/c)	2100
Max. momentum (centr. tra.) (MeV/c)	1400
Momentum acceptance (%)	50
Solid angle acceptance (msr)	10.4
Length of central trajectory (m)	5.3
Momentum resolution	10^{-3}
Angular resolution at target (mrad)	< 3

KAOS is designed for strangeness electro-production reactions analysis and is meant to identify kaons with proton/pion/kaon ratio of $2 \times 10^6/2 \times 10^4/1$. With the new accelerator stage, the spectrometers A, B and C do not cover the full momentum range of MAMI C. The main difference between the existing spectrometers and KAOS are its short distance from the target to the focal plane which reduces the number of kaon decays in flight and its maximum momentum. This means that for experiments involving production of strange particles, the kaons produced have a low probability being detected in spectrometers A, B and C due to their short life time ($c\tau_K = 3.7$m) and the long flight path through the spectrometers (see Table 4.1). Figure 4.1 shows the survival probability for kaons to be detected in all spectrometers at the A1 experimental hall. It is clearly seen that the detection of kaons is not effective in spectrometers A, B and C. KAOS has a large momentum and solid angle acceptance, as shown in Table 4.1. All these properties give spectrometer KAOS the central importance for strangeness electro-production reactions on protons or light nuclei at MAMI [62].

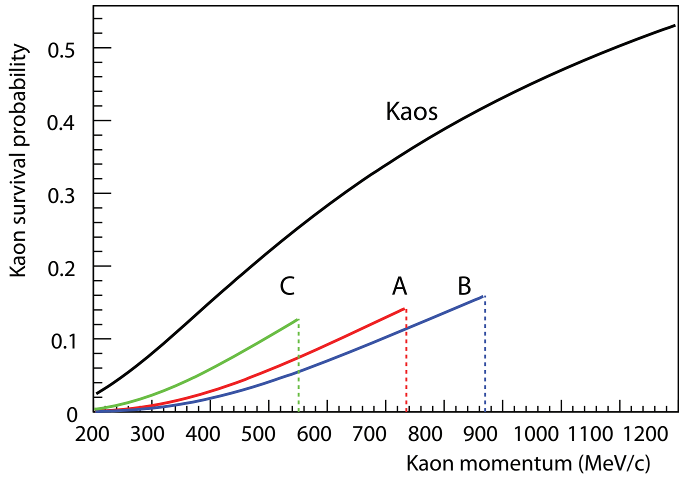

Figure 4.1: Kaon survival probability as function of its momentum. It shows the range of detection of the spectrometers A, B, C and KAOS. Clearly, spectrometers A,B, and C have low probability of kaon detection due to the long flight path. Figure from [31].

The magnetic field is provided by the electric current that flows through 72 turns per coil with an average length of 7.7 m per turn. The maximum current is 2500 A, that is provided at $U \approx 180$ V, corresponding to 450 kW of power. The ohmic losses are cooled by water at a flow rate of 200 l/min.

The platform with the KAOS spectrometer can be moved from a parking to measurement position on segmented tracks by hydraulic pressure cylinders. With this concept spectrometers A, B and C can cover the forward region when KAOS is returned to its parking position. The different kinematics require a flexible position of the spectrometer with respect to the target. For this purpose three hydraulic positioning feet are used. They lift the platform from its support and allow precise vertical alignment of the spectrometer on the beam-line level or up to 100 mm away from it.

The hypernuclear experiments at MAMI require the detection of both the scattered electron and associated kaon at very forward laboratory angles. Therefore KAOS is designed as a double arm spectrometer to detect simultaneously both particles, to either side of the magnetic dipole. So far the electron arm is still under construction with the first beam-test performed in 2009. Vertical coordinate in the focal plane of negatively charged particles will be measured by two planes of vertically positioned scintillating fibers. For more details see [63, 64]. For detection of positively charged particles a set of detectors is used: multi-wire proportional chambers (MWPC) for trajectory and momentum measurements, time-of-flight walls (ToF) for triggering and energy-loss measurements and aerogel Čerenkov counter for π/K discrimination. The scheme of the KAOS spectrometer with all detectors is shown in Fig. 4.2 which are explained in more details in the following.

The vacuum chamber of the dipole is extended to the electron arm focal plane region with pressure of $p \approx 9 \cdot 10^{-6}$ mbar. Because the KAOS spectrometer is placed at small forward angles the background is very high. For this reason the detector platform is protected by the shielding house. More information about KAOS can be found in [22, 65].

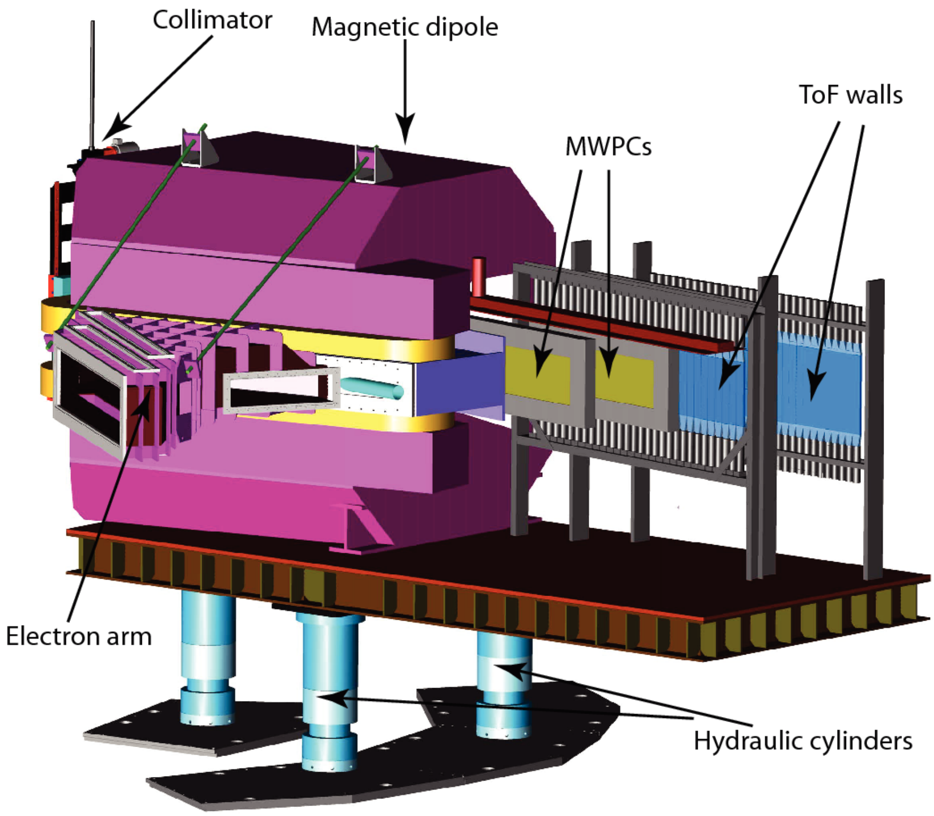

Figure 4.2: Schematic representation of the KAOS spectrometer. Aerogel Čerenkov counter is located between the ToF walls and thus not seen from this point of view.

The dipole field of spectrometer KAOS deflects the unscattered electrons from the primary beam away from its original axis when operating close to 0°. These electrons miss the beam-dump and produce large radiation level. To solve this problem two additional magnetic dipoles are installed upstream of the target to compensate the deflection. A schematics of the experimental hall with pre-target beam chicane and the KAOS spectrometer used for the beam return is shown in Fig. 4.3.

The angle of deflection in KAOS dipole depends on the field strength. For instance, with a field of 1 T the first magnet of the chicane has to deflect the beam by 13.5°

and the second one by approximately twice the angle in the opposite direction. Thus the electron beam enters into the KAOS dipole with an angle of 16° relative to the preliminary direction and is deflected inside KAOS straight into the beam-dump with the final inclination of only 1.47° relative to the preliminary beam direction.

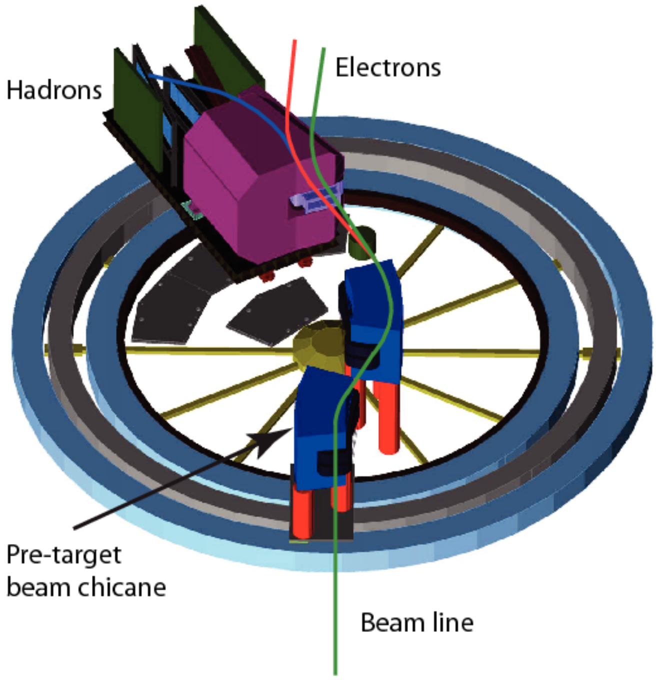

Figure 4.3: Schematic representation of the experimental hall with the pre-target beam chicane. Positively charged hadrons and electrons are deflected to opposite directions inside KAOS magnetic field. Unscattered electrons are deflected directly towards the beam-dump by the magnetic dipole of the KAOS spectrometer.

The Magnetic dipole of KAOS bends the trajectories of positively and negatively charged particles to opposite sides by $\approx 45°$. The focal plane on the electron side is almost straight, while on the hadron side it has paraboloidal shape.

The particle coordinate along the focal plane is directly related to its momentum. Figure 4.4 shows the simulated coordinates in the dispersive (horizontal) direction of particles with momenta from 350 MeV/c to 600 MeV/c in steps of 25 MeV/c. The plot also shows the coordinates of particles emitted from target towards the spectrometer (i.e. $\theta_0 = 0$, $\Phi_0 = 0$), over the full momentum acceptance.

4.1 Hadron arm

The hadron arm of KAOS has several detectors for particle identification and tracking (see Fig. 4.5). Right behind the vacuum chamber two multi-wire proportional chambers (MWPCs) are situated, labeled as M and L, followed by two segmented

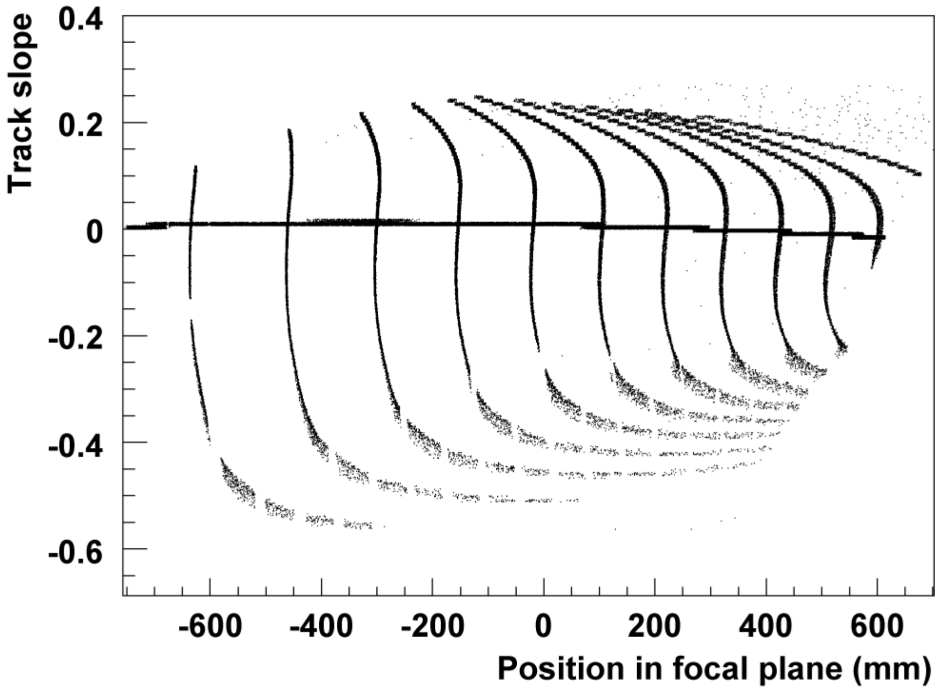

Figure 4.4: Simulated particle position along focal-plane in the dispersive direction versus track slope. Events with momenta from 350 MeV up to 600 MeV in steps of 25 MeV/c are shown together with the events emitted from target at angle of $\theta_0 = 0$ and $\phi_0 = 0$ towards the spectrometer, over the full momentum acceptance. Difference of the track slope and position with respect to the reference trajectory are used as coordinates. A related discussion on the momentum reconstruction can be found in [57].

scintillator walls, labeled as G and H. Between scintillator walls an aerogel Čerenkov counter is located.

4.1.1 Multi-wire proportional chambers

Trajectories of positively charged particles in the Kaos spectrometer are measured by two MWPCs with an active area of 1190×340 mm^2 each. The chambers are filled with argon, together with a mixture of 9% CO_2 and 7% C_4H_{10} acting as quenchers. To determine the particle track the charge distributions generated on the cathode wires are analyzed.

The chamber have two planes of orthogonal cathode wires in horizontal and vertical direction (1 mm spacing). Between them a plane of anodes (2 mm spacing) is located with wires aligned in diagonal direction with an angle of 45° to either cathode wire. Above the wires are two electrodes, called the grid (G) and transfer (T) plane. They are made out of woven fabric of plastic coated with nickel layer. Ionizing particles produce primary electrons in the pre-amplification gap, which is

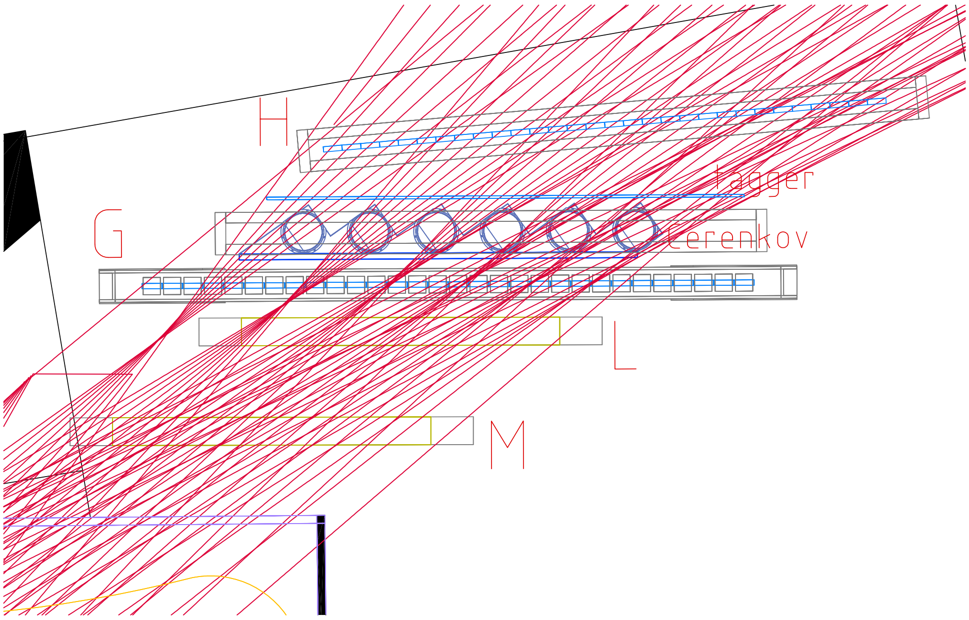

Figure 4.5: The schematic drawing of the hadron arm of KAOS spectrometer with all corresponding detectors. Particle trajectories are shown with red lines. Drawing made my F. Schulz.

between two electrode planes, with an amplification factor of $\approx 10^2$. These electrons drift through the transfer gap, which is between T electrode and first cathode plane and reach the anode plane, where the second amplification occurs, now by a factor of $\approx 10^3$. During this process electric charges are induced on the cathode wires in both planes. This process is schematically shown in Fig. 4.6. The avalanche broadens in the transfer gap due to transverse diffusion. Typical potentials applied to the electrodes are: $U_G = -9.1$ kV, $U_T = -2.0$ kV and $U_A = +4.0$ kV, with the cathodes grounded.

The distribution of the collected charge is measured on the cathode wires. Five wires are connected to the same channel, which gives a total of 240 analogue channels in the x-direction (horizontal)and 70 analogue channels in the y-direction (vertical). The signals, typically ≈ 2 μs wide, are amplified by preamplifier and digitized by an 8-bit ADC card.

Particles from the target cross the MWPC planes at an average angle of about $(50 \pm 20)^\circ$ to the normal. Nevertheless the measured central position of charges is assumed to coincide with the coordinate of the ionizing particle in the grid plane.

With an electron beam-current of several μA the chambers are exposed to multiple tracks in almost every event due to high electromagnetic background radiation. This limits the beam-current for experiments involving KAOS.

More about multi-wire proportional chambers can be found at [66].

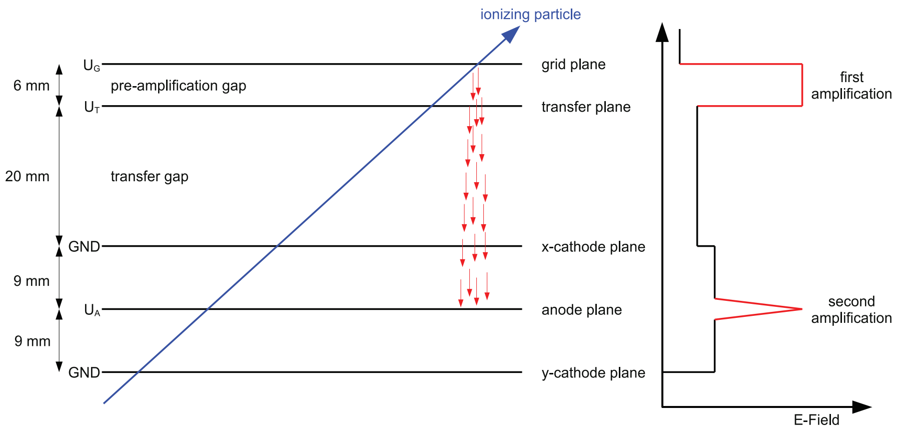

Figure 4.6: The schematic representation of the MWPCs two-stage amplification process. Left: avalanches of electrons drift through transfer gap towards the anode wires and where an electric charge is collected on the cathode wires. Right: a typical distribution of the electric field versus the distance from anode wire is shown. Figure taken from [22].

4.1.2 Scintillator walls

The energy losses of hadrons in Kaos and their time-of-flight are measured by two planes of scintillator walls, labeled G and H. They consist of 30 scintillator paddles made from material Bicron BC-408 and read out at both ends by fast photomultipliers (Hamamatsu R1828). The dimensions of paddles are $470 \times 74 \times 20$ mm^3 in the G wall and $580 \times 70 \times 20$ mm^3 in the H wall, which gives a total length of 2.28 m and 2.13 m, respectively. The G wall is parallel to both wire chambers, while the H wall is tilted by 4.6° relative to the G wall.

ToF walls are also used for generating the trigger of the spectrometer by a coincidence of hits in both scintillator planes. In total there are 60 analogue and 90 timing signals per wall, which are digitized by Fastbus TDC and ADC modules.

The scintillator material has a 2.1 ns decay constant, suitable for time-of-flight measurements. The time spectrum is systematically broadened by the decay constant of the scintillators, propagation time dispersion inside the scintillator, the time differences between the photo-electron arrival from the cathode to the first dynode, by the variation of the time-of-flight, being proportional to the path length through the spectrometer etc. The response time of discriminators may shift with the signal amplitude. This is called time-walk and can be corrected by various methods, either by hardware or software. In Kaos constant-fraction-discriminators are used because they provide the best time resolution with scintillator walls. All mentioned effects together give a time-of-flight resolution of $\Delta t_{\mathrm{FWHM}} < 350$ ns, as shown in Fig. 4.7.

The timing information from scintillator walls is usually converted to the coincidence-time between the spectrometers. By knowing the flight path lengths, momentum and type of particles the raw coincidence-time, can be corrected as:

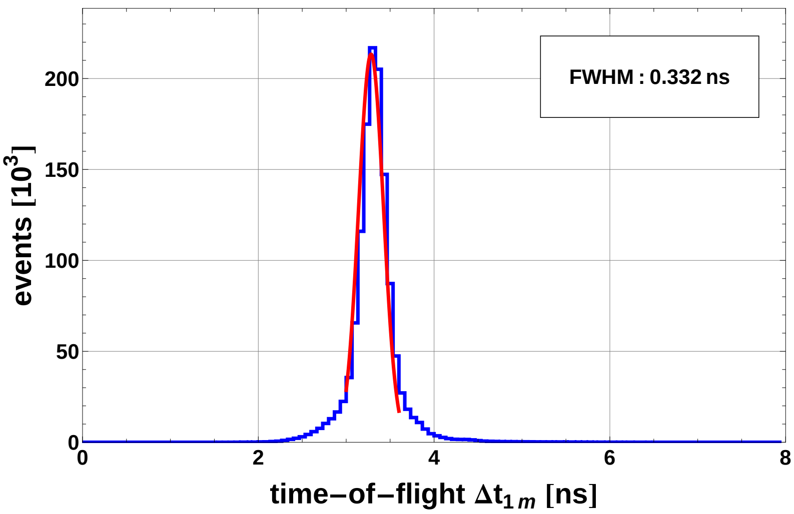

Figure 4.7: Time-of-flight resolution between scintillator walls normalized to 1 m flight path. Because ToF walls are not parallel the raw time-of-flight between the walls is wider and a normalization to 1 m distance is used. This resolution was achieved at low beam-current [67].

$$t^c_{G,H} = t^{\text{raw}}_{\text{coinc}} - t^{\text{offset}}_i - \left| \frac{L_e}{v_e} - \frac{L_{\text{Kaos}}}{v_{\text{Kaos}}} \right|, \tag{4.1}$$

where $t^c_{G,H}$ is the corrected coincidence-time between wall G or wall H and electron arm spectrometer, $t^{\text{raw}}_{\text{coinc}}$ is the raw coincidence-time, t^{offset}_i are the time offsets of the individual scintillator paddle i, L_e and L_{Kaos} are the flight paths in two spectrometers, and v_e, v_{Kaos} are the velocities of the particles in both spectrometer. The last term is theoretical prediction for coincidence-time between the electron detected in the electron arm and associated positively charged hadron in hadron arm. This term is determined from the path length and particle velocity, which is reconstructed from the momentum and assumed particle mass M:

$$v_{Kaos} = |\vec{p}_{\text{Kaos}}|c/\sqrt{|\vec{p}_{\text{Kaos}}|^2 + M^2c^2}. \tag{4.2}$$

For the energy-loss measurements the raw signals are corrected according to reconstructed path length through the scintillators, as the particles cross the paddles at non-zero angles θ and ϕ. This is an important correction for precise energy-loss measurement. The mean deposited energy is described by the Bethe-Bloch equation:

$$-\frac{dE}{dx} = 2\pi N_a r_e^2 m_e c^2 \rho \frac{Z}{A}\frac{z^2}{\beta^2}\left[\log\left(\frac{2m_e\gamma^2 v^2 W_{\max}}{I^2}\right) - 2\beta^2\right], \tag{4.3}$$

where $2\pi N_a r_e^2 m_e c^2 = 0.1535$ MeVcm^2/g, $W_{\max}$ is the maximum energy transfer in a single head-on collision, I is the mean excitation potential, A and Z are atomic mass and number of the absorbing material, ρ is the density of absorber, r_e is the classical electron radius, $r_e = 2.8$ fm, and z is the charge of the incident particle in units of e. The measured values are in good agreement with the Bethe-Bloch formula for a given particle type (see Fig. 4.8).

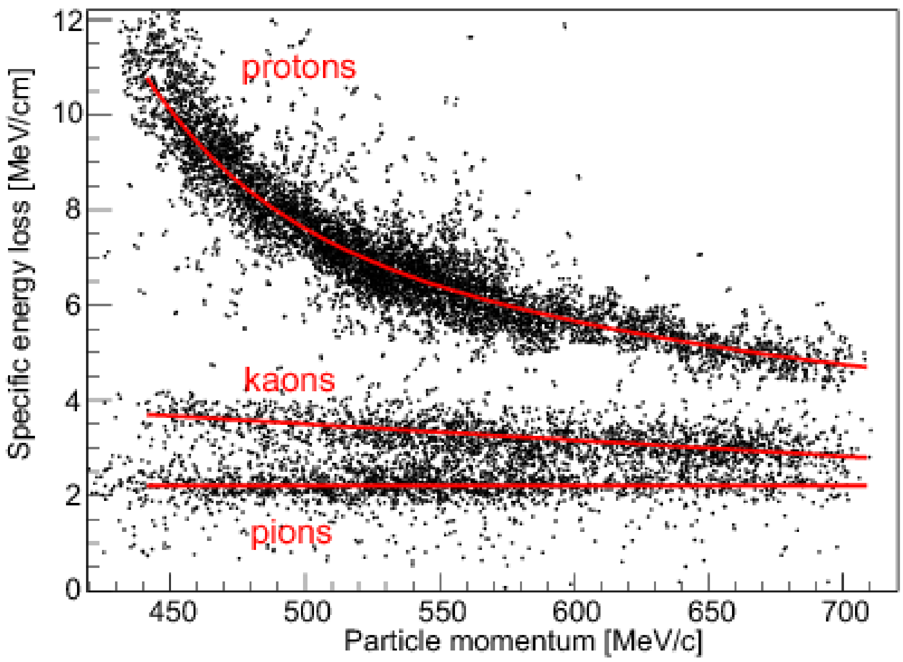

Figure 4.8: Energy-loss in one scintillator wall as a function of momentum after a cut on pions, protons and kaons. For comparison the energy-loss lines calculated from Bethe-Bloch formula for a specific particle type are shown [59].

4.2 Track reconstruction

Tracks in the Kaos spectrometer are reconstructed based on the detected clusters from MWPCs and ToF walls.

Clusters in MWPC are defined as a group of neighboring channels with detected charges and belong to the same event. They are typically 3-5 channels wide. In ToF walls clusters are defined by a group of neighboring paddles with detected signals above the threshold. They are limited by 3 paddles in maximum and by 275 ps time difference between signals in neighboring channels.

With n clusters in each MWPC cathode wire plane n^4 possible tracks through both chambers are generated. Each track goes through the center of one cluster in each plane. All possible tracks are taken into account and classified according to a set of track quality factors. These factors range from 0 (excluded) to 1 (highest quality).

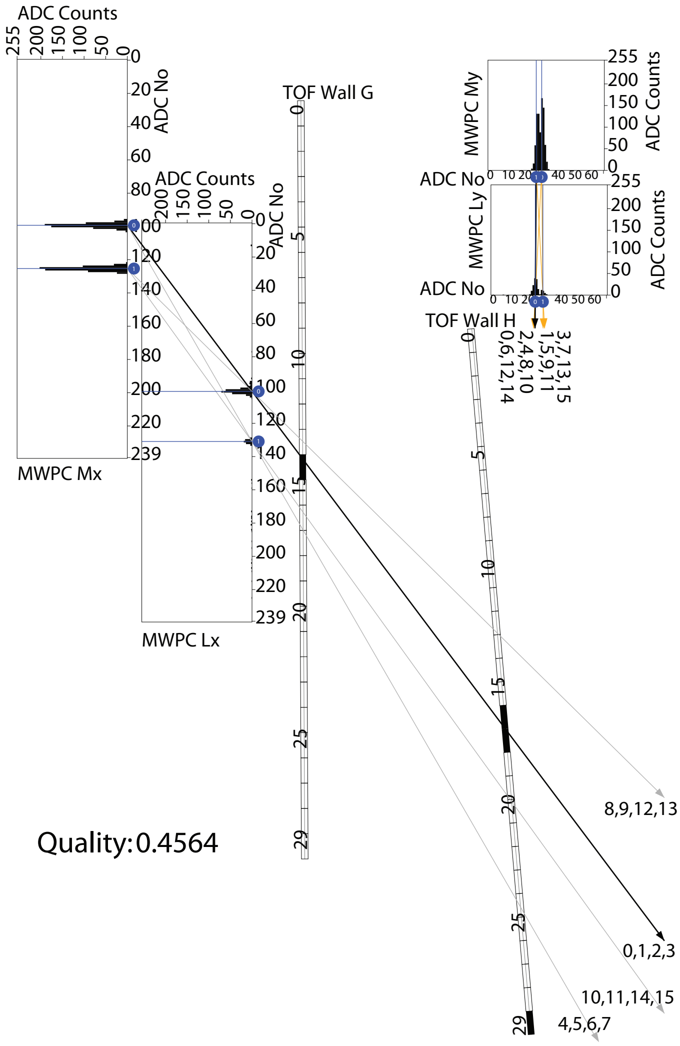

track	Quality total	$\frac{Q_x}{Q_y}\|_M$	$\frac{Q_x}{Q_y}\|_L$	Δx_H	Δx_G	Δt_H	Δt_G
0	0.4564	0.4574	1	1	1	1	0.9978
1	0.4335	1	0.5311	1	1	0.8162	1
2	0.0414	1	1	1	1	0.0883	0.8392
3	0.0002	0.4574	0.5311	1	1	0.0047	1

Figure 4.9: Event with multiple hits in each detection plane. The track-finding algorithm has found 16 possible tracks. Only 4 of them are physically possible traces (black and orange colored arrows). All other hit combinations are excluded by at least one of the quality criteria. The track with the highest quality factor (black arrow) has been chosen to be the correct one. The quality factors for tracks 0-3 are also listed.

To find a proper pair of x and y coordinates the correlation between the collected charge in both cathode planes is analyzed. The correlation between collected charge in both directions is described by the phenomenological curve, which is parametrized by a third order polynomial function. Deviation of measured charge in the x- and y-direction from this phenomenological curve determines the quality factor in both chambers. The quality factor $Q_x/Q_y|_{M,L}$ relates to the charges in both cathode planes for chamber M and L, respectively. There is also a strong correlation between the vertical hit position and vertical angle, ϕ, which provides another powerful criterion for the track finding. Another criterion is a small correlation between horizontal hit position and horizontal angle θ.

Another set of quality factors is determined from the ToF walls. Because both MWPCs are situated outside of the magnetic field, the particle trajectories are extrapolated linearly to the scintillator walls. The spatial difference in horizontal direction between observed hits and extrapolated coordinates are used to determine the quality factors. They are labeled as Δx_G and Δx_H. Even thought scintillators are segmented in x-direction, the vertical position can be measured from the time difference in the top and bottom photomultiplier in individual paddle. The spatial difference between measured and extrapolated hit position is also used to determine the quality factors, labeled as Δt_G and Δt_H. The accuracy of the time difference measurement becomes worse when particles deposit a small amount of energy in a scintillator bar [68].

Fig. 4.9 shows a typical event. It can be seen that with two clusters in each chamber, there are 16 possible track combinations. The track-finding algorithm has returned four possible sets of clusters in the MWPCs. These clusters are combined with hits in the ToF walls to form the track. Other track combinations are excluded by the quality criteria and assigned to background.
More about tracking algorithm in Kaos can be found at [69].

4.3 Trigger and experiment control system

Figure. 4.10 shows the simplified scheme for the signals coming from the two TOF walls. Each analog signal is split by a sum and split card (GSI SU 1601). The signals for energy-loss measurement are delayed by 250 ns (GSI DP1620) and brought to an ADC module (LeCroy 1885F). The timing signals are digitized by a constant-fraction discriminator (GSI CF8105), delayed by 500 ns (GSI DL 1610) and fed into a TDC module (LeCroy 1875) in a Fastbus crate. The sum of top and bottom PMT from each paddle is digitized by the CFD and brought to the VUPROM logic modules where trigger is generated. The signals from the MWPC (620 channels in total) are converted by ADC and read out by a transputer network.

The trigger is generated by VME Universal Processing Module (VUPROM). This logic system is programmable and can handle high complexity of valid trajectory patterns in the hadron arm to reduce high background. When the valid trigger signal is generated it is used as a common stop signal for the TDC, the gate signal for the ADC and the interrupt signal for the front-end CPU.

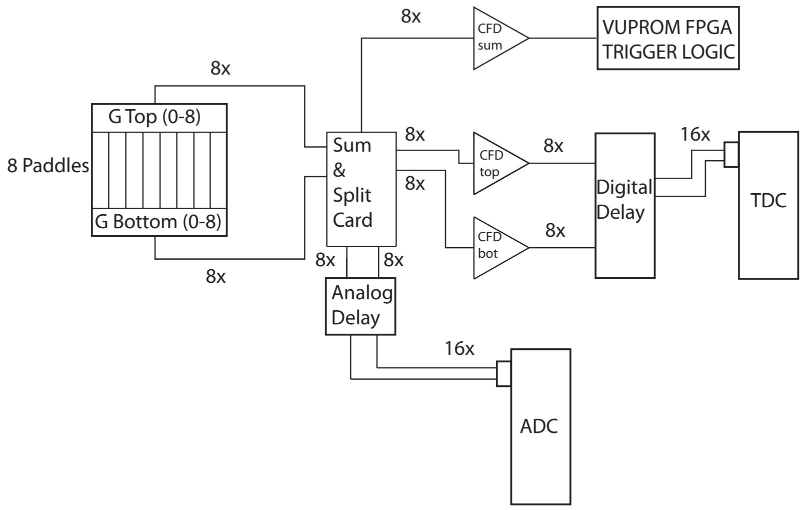

Figure 4.10: A drawing of data acquisition system of the KAOS spectrometer's hadron arm for eight paddles in the G wall. Figure taken from [22].

CHAPTER 5

Aerogel Čerenkov counter

Since the upgrade of MAMI to 1.6 GeV end-point energy it is very important to have an efficient kaon identification system within the KAOS spectrometer. One of the major challenges of strangeness electro-production experiments is to reduce the background level by discrimination of rare kaons from the abundant pions. This can be performed by their time-of-flight, but the method becomes difficult at higher momenta. Even with perfectly tuned scintillator arrays and calibrated detectors, the separation power for pions and kaons deteriorates with $\Delta t \propto 1/p^2$ because of relativistic effects at higher velocities [70]. At higher momenta, $p \geq 800$ MeV/c, a Čerenkov detector is the best solution for π/K separation.

A typical Čerenkov counter contains three main elements: (i) a radiator through which the charged particle passes, (ii) a diffusive box where Čerenkov photons scatter diffusively and (iii) a photodetector. As Čerenkov radiation is a weak source of photons, light collection and detection must be as efficient as possible. The refractive index n and the path length of the particle in the radiator allows tuning these quantities for a particular experimental application. There are different schemes for collecting Čerenkov light. The produced light scatters randomly in the diffusive box until it hits the attached photomultiplier tube (PMT). The greatest challenge for all Čerenkov detectors is an efficient collection of the Čerenkov radiation. Some of the strategies for an efficient light collection use mirrors inside the diffusive box, that focus the light onto the PMTs and some use wavelength shifters, which convert the light to a different wavelength band and transport it to the PMTs. The most important consideration when designing a large, diffusely reflective Čerenkov detector is how many photo-electrons will be detected per event. The greatest challenge for all Čerenkov detectors is the effective collection of the Čerenkov radiation. The photo-electron signal, typically less than ten photo-electrons, determines the detector's efficiency for detecting relativistic particles.

5.1 Principle of operation of Čerenkov counters

The operation of a Čerenkov counter is based on the phenomenon discovered by Pavel Aleksejevič Čerenkov in 1934, while working under S.I. Vavilov. He observed the emission of blue light from a bottle of water exposed to radioactive bombardment. This process was theoretically explained in 1938 by I. Y. Tamm and I. M. Frank. Such radiation arises when an arbitrary charged particle passes through transparent medium (radiator) with a refractive index $n = \sqrt{\epsilon}$ with a velocity v exceeding the phase velocity of light in this medium, c/n:

$$v_{\text{particle}} > c/n. \tag{5.1}$$

In this process, an electromagnetic shock wave is created with the polarized wavefront emitted at a well-defined angle θ_C:

$$\cos\theta_C = \frac{1}{\beta n(\omega)} = \frac{c}{v n(\omega)}, \tag{5.2}$$

with respect to the trajectory of the particle, as seen in Fig. 5.1. The angle of emission increases with the velocity reaching a maximum value of $\theta_C^{\max} = \arccos(1/n)$ at $\beta = 1$.

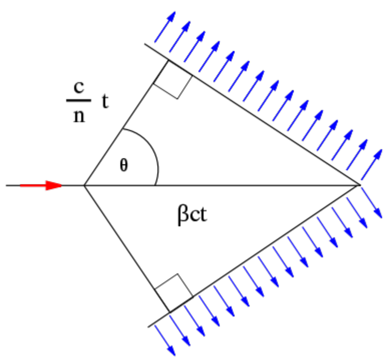

Figure 5.1: Čerenkov radiation: an electromagnetic wave is formed when the particle travels faster than the speed of light in the same medium [71].

For a particle of charge ze the number of emitted photons N per unit of energy, $E_\gamma = \hbar\omega$, at distance L traveled by that particle is

$$\frac{dN}{dE_\gamma} = z^2 \frac{\alpha}{\hbar c}\left(1 - \frac{1}{\beta^2 n^2}\right) L = z^2 370(\text{cm})^{-1}(\text{eV})^{-1}\sin^2(\theta)L. \tag{5.3}$$

Here one can see that the number of Čerenkov photons per unit energy is constant over the energy range for which the condition $\beta > 1/n(\omega)$ is satisfied (up to ≈ 10 eV). Dividing by L and integrating over frequencies then yields:

$$-\frac{dE}{dx} = \frac{1}{L}\int \hbar\omega \frac{dN}{dE\gamma}\mathrm{d}E_\gamma = z^2\frac{\alpha\hbar}{c}\int\left(1-\frac{1}{\beta^2 n(\omega)^2}\right)\omega\mathrm{d}\omega. \tag{5.4}$$

The energy-loss thus increases with β. Typically in condensed materials the energy loss is only on the order of $\approx 10^{-3}$ MeV cm^2/g, which is negligible with respect to the collision loss. For gases such as H_2 or He, this is somewhat higher ranging from $\approx 0.01 - 0.2$ MeV cm^2/g, but is still quite small. Of interest is also the number of photons emitted per unit wavelength per unit length as a particle passes through the radiating medium. This can be found from (5.3):

$$\frac{d^2N}{d\lambda dx} = \frac{2\pi z^2\alpha}{\lambda^2}\left(1-\frac{1}{\beta^2 n^2(\lambda)}\right). \tag{5.5}$$

Due to the $1/\lambda^2$ dependence, most of the photons are produced in the UV range. In most Čerenkov detectors, the Čerenkov radiation is generally detected by photomultipliers which have a typical range of sensitivity between 350 nm and 550 nm. Integrating (5.5) over λ and evaluating at these limits then yields:

$$\frac{dN}{dx} = 2\pi z^2\alpha\sin^2\theta_C\int_{\lambda_1}^{\lambda^2}\frac{d\lambda}{\lambda^2} = 475z^2\sin^2\theta_C \text{ photons/cm}, \tag{5.6}$$

which is not an enormous amount as one can see [72]. Therefore, it is an important requirement of every Čerenkov detector to have a high detection efficiency in this wavelength band. For a Čerenkov counter with inner walls having reflectivity η and photodetectors which cover an areal fraction κ of the surface, the average number of photons being detected by the PMTs, for particles with $z = 1$, can be parametrized by:

$$N = F_0 L\left(1-\frac{1}{\beta^2 n^2}\right)\frac{\kappa}{1-\eta(1-\kappa)}, \tag{5.7}$$

where F_0 is the figure of merit, and includes all parameters which cannot be determined prior to construction, such as photon detection efficiency and transmission of the radiator and windows [73]. This value is typically $F_0 = 50 - 100$/cm.

The basic properties, such as relative number of Čerenkov photons and relative Čerenkov angle are functions of $\beta\gamma/\beta_t\gamma_t = p/p_t$, with p_t the threshold momentum, γ_t the threshold Lorentz factor:

$$\gamma_t = (1-1/n^2)^{-1/2} = 1/\sin\theta_C^{\max}, \tag{5.8}$$

and β_t the threshold velocity:

$$\beta_t = 1/n. \tag{5.9}$$

The relative light yield $N/N_{\max}$, with $N_{\max} = F_0 L/\gamma_t^2$, and the relative emission angle $\sin\theta/\sin\theta_C^{\max}$ as a function of particle velocity are:

$$N/N_{\max} = 1 - \left(\frac{\beta_t\gamma_t}{\beta\gamma}\right)^2, \tag{5.10}$$

$$\sin\theta/\sin\theta_C^{\max} = \sqrt{1 - \left(\frac{\beta_t\gamma_t}{\beta\gamma}\right)^2}. \tag{5.11}$$

which is shown in Fig. 5.2.

The properties of Čerenkov effect are exploited in different types of Čerenkov counters, divided into two major types: (i) Threshold counters, which count photons to separate particles below and above threshold and (ii) Ring Imaging Čerenkov detectors (RICH), which measure the Čerenkov angle and count photons.

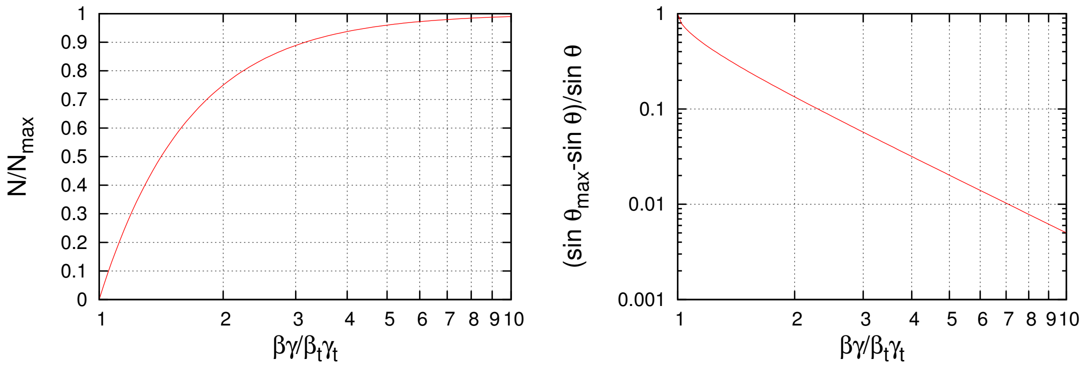

Figure 5.2: The basic relations of the ratio $\beta\gamma/\beta_t\gamma_t$ to the relative number of Čerenkov photons (left) and the relative Čerenkov angle (right).

5.2 Theory of Čerenkov radiation

Let us consider a particle of mass M, velocity $\mathbf{v}$ and momentum $\mathbf{p}$, which interacts with the medium via a virtual photon with energy $\hbar\omega$ and momentum $\hbar\mathbf{k}$, as shown in Fig. 5.3. The medium is characterized by a complex dielectric constant $\varepsilon(\omega) = \varepsilon_1(\omega) + i\varepsilon_2(\omega)$.

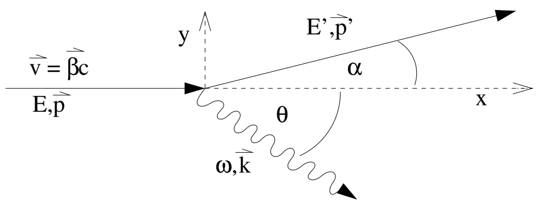

Figure 5.3: Emission of a virtual photon in a medium.

With the restriction to soft collisions, $\hbar|\mathbf{k}| \ll |\mathbf{p}|$ and $\hbar\omega \ll E$, the conservation of energy and momentum gives:

$$\omega = kv\cos\theta, \tag{5.12}$$

where θ is the angle between $\mathbf{v}$ and $\mathbf{k}$. The behavior of a photon in a medium is described by the dispersion relation $\omega^2 = k^2c^2/\varepsilon$, which gives together with the equation above:

$$\sqrt{\varepsilon}\beta\cos\theta = 1. \tag{5.13}$$

The dielectric constant is complex in general where both components strongly depend on the photon frequency ω. It is real only when the energy of the photon is below the ionization threshold of the medium. Fig. 5.4 shows ε as a function of ω for argon gas as an example.

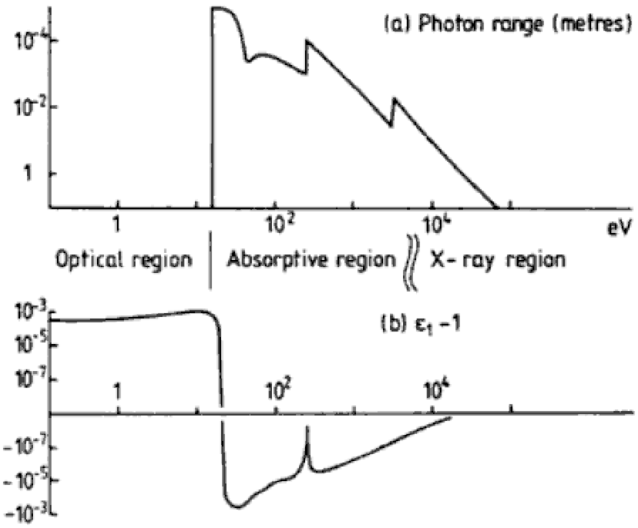

Figure 5.4: The dependence of ε versus photon energy for argon gas at normal density. Top: imaginary part, expressed as a photon range in meters, bottom: real part, expressed as $\varepsilon_1 - 1$. Figure taken from [74].

As we see there are three frequency ranges:

- **The optical region** In this region $\varepsilon(\omega)$ is real because $\varepsilon_2 = 0$ and $\varepsilon_1 > 1$. This means there are no photons absorbed, resulting in transparent material. It is typically at $\hbar\omega < 2$ eV, but depends on the material properties.

  This also means that at higher velocities condition (5.13) can be satisfied where $\sqrt{\varepsilon}v/c > 1$, so the angle θ is real for which free photons can be emitted. This is known as the Čerenkov angle. At lower velocities condition (5.13) is not satisfied because $\cos\theta$ can not be greater than unity. This means that free photons are not emitted in the medium. The velocity at which v is equal to $c/\sqrt{\varepsilon}$ is called the Čerenkov threshold.

- **The absorptive region** Here the dielectric constant is complex and the range of photons is short, because $\varepsilon_2 > 0$. Absorbed virtual photons ionize and excite atoms of the material. The absorptive region is typically in the range 2 eV $< \hbar\omega < 5$ keV.

- **The X-ray region** At $\hbar\omega > 5$ keV the medium may be treated as being nearly transparent, $\varepsilon_2 \ll 1$, with very few ionizations. Because $\varepsilon_1 \lesssim 1$ the Čerenkov threshold is greater than c.

Let the particle move in the x direction with velocity v. From the dispersion relation and Eq. (5.12) we get the y component of the wave vector:

$$k_y = (\omega/v)\sqrt{\beta'^2 - 1}, \tag{5.14}$$

where $\beta' = v\sqrt{\varepsilon}/c$. The x component is as usual: $k_x = \omega/v$. If $\beta' > 1$ then both k_x and k_y are real so the electromagnetic field is a traveling wave at an angle $\arccos\left(c/\left(v\sqrt{\varepsilon}\right)\right)$. This is the case of Čerenkov radiation.

If the velocity v is below the phase velocity of light in the medium k_y becomes imaginary. The electromagnetic field is absorbed in the transverse direction and the wave propagation in two dimensions is described as: $\exp i\omega(\frac{x}{v} - t)\exp(-y/y_0)$, where

$$y_0 = \frac{v}{\omega\sqrt{1-\beta'^2}} \tag{5.15}$$

is the characteristic range of the photons. We see that in the optical region ($\varepsilon > 1$) with increasing values of velocity the range increases until at $\beta' = 1$, the range becomes infinite and we have a Čerenkov radiation. In the X-ray and absorptive region ($\varepsilon < 1$) the range also increases with velocity but reaches an upper limit when $\beta' = \sqrt{\varepsilon}$. The maximum range is given by:

$$y_0^{\max} = \sqrt{\varepsilon}/(k\sqrt{1-\varepsilon}). \tag{5.16}$$

5.3 Threshold Čerenkov counters

Threshold Čerenkov counters, in their simplest form, make a yes/no decision based on whether the particle is above or below the Čerenkov threshold velocity (see Eq. (5.1)). The number of observed photo-electrons (or a calibrated pulse height) from these detectors is used to discriminate between particles by properly choosing refractive index of radiator n for a given kinematic region. Such detectors are in used at Jefferson Laboratory, Hall A, [75, 76, 77, 78] and Hall C [79], J-PARC [80], MIT-Bates Linear Accelerator Center [81], KEK-B factory [82], VEPP-2000 e^+e^- collider [83, 84, 85] etc. The minimum momentum at which a particle of mass m will exceed the phase velocity of light in the medium is given by:

$$p_t c = \frac{mc^2}{\sqrt{n^2 - 1}}. \tag{5.17}$$

For the Čerenkov detectors one of the first criteria that one would take into account in order to choose the refractive index n of the radiator is the momentum threshold. For MAMI beam energies of 1508 MeV, the maximum momentum of the K^+ is about 1200 MeV/c. One should therefore choose a radiator with an index where the minimum momentum for Čerenkov emission of kaons is equal or larger than the maximum momentum of kaons in the extreme MAMI kinematics. In such a case kaons will not be able to produce Čerenkov radiation, but only pions will. From Eq. (5.17), we get $n \approx 1.08$. But we have chosen a radiator with smaller refractive index to increase the momentum threshold for kaons, so we can be sure that no kaons will be able to produce Čerenkov photons:

$$n = 1.055. \tag{5.18}$$

On the other hand the momentum threshold for pions remains approximately the same in this area of n, so no pions will be lost at this value of refractive index (see Fig. 5.5 left).

This gives us the momentum threshold for pions $p_t^{\pi^+} \approx 415$ MeV/c, and for kaons $p_t^{K^+} \approx 1.47$ GeV/c which means that the momentum range is approximately 1200 MeV/c - 415 MeV/c $\approx$ 800 MeV/c. In this range all the pions emit Čerenkov photons, while the kaons do not.

The relative number of detected photons, generated inside the radiator medium with refractive index n, as a function of particle momentum is:

$$N/N_{\max} = 1 - \frac{m^2}{p^2(n^2 - 1)}. \tag{5.19}$$

The relative number of detected photons for pions and kaons vs. momentum is shown in Fig. 5.5 right.

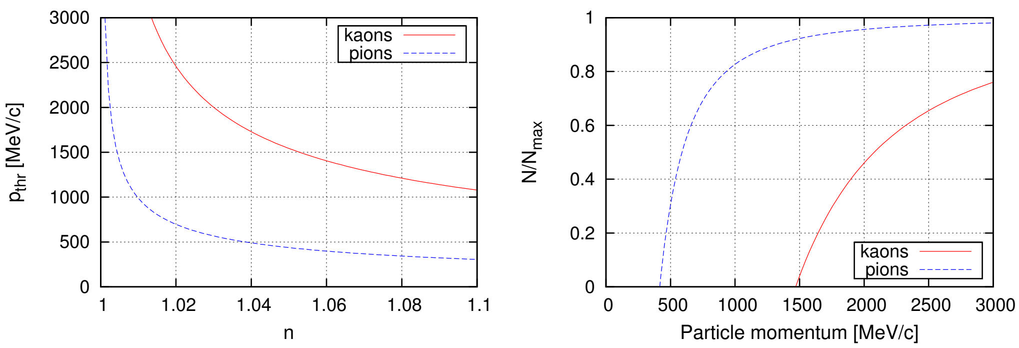

Figure 5.5: Left: the momentum threshold $p_t^{\pi^+}$ and $p_t^{K^+}$ as a function of the radiator refractive index n. Right: relative number of detected photons as a function of a momentum for $n = 1.055$.

As the rejection of the particle that is below the threshold depends on *not* seeing a signal, electronic and other background noise can be important. Physics sources of light production for the below threshold particle, such as the decay of the above threshold particle ot the production of delta rays in the radiator, often limit the separation attainable, and need to be carefully considered.

The requirements for the Čerenkov detector are: (i) large sensitive area to match the acceptance of KAOS, (ii) it has to be slim enough to fit in the available space, (iii) it has to have good time resolution and high rate capability. Because aerogel is the best candidate for this purpose it has been chosen to be used as a radiator.

5.4 Silica aerogel

Silica aerogel is widely used as a radiator for Čerenkov detectors [86]. It is a highly porous solid (more than 95% of its volume is air), low-density, transparent and fragile substance with refractive index n ranging between the values of $n \approx 1.007$ to $n \approx 1.25$.

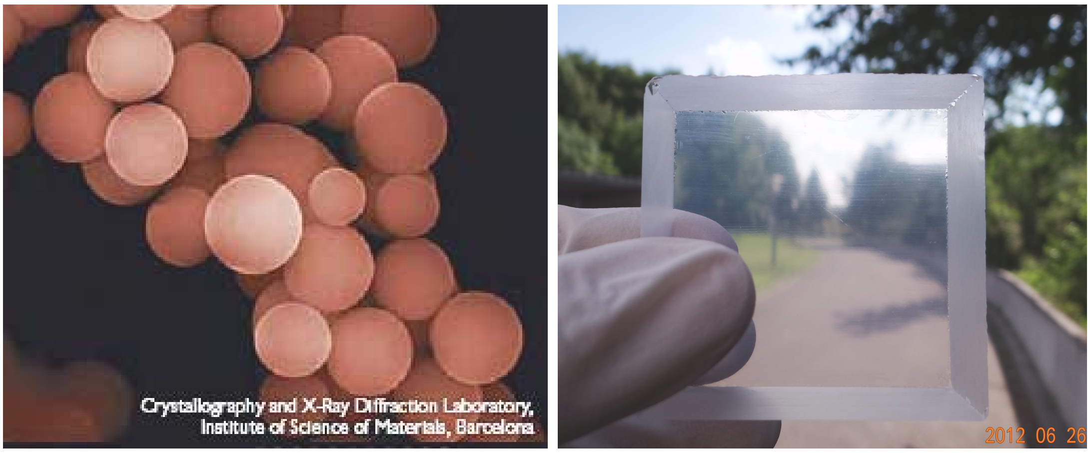

Figure 5.6: Aerogel structure (left) and an aerogel sample 50 mm ×50 mm ×20 mm in size and with $n = 1.055$ (right). The sample to the right is the one used at the experiments at MAMI. This photograph was made in the park in front of the A1 experimental hall.

It was manufactured for the first time in 1974 by Cantin *et al.* [87] who have demonstrated its applicability as a Čerenkov radiator. The first large-scale employment was in the TASSO detector at PETRA [88]. The silica aerogel is formed of silica oxide, Si_xO_y, small spherical clusters up to 10 nm in size connected in chains forming a 3D net with pores which are filled with air (see Fig. 5.6). The pore sizes can achieve from several tens to hundreds of nm. The aerogel density can be thus from 0.03 to 0.55 g/cm^3 which corresponds to a large range of n, which is roughly given by $n - 1 = (0.210 \pm 0.001)\rho$. It is derived from a gel in which the liquid component of the gel is replaced with a gas. The advantage of aerogel is the adjustable refractive index, which is tuned during the manufacturing procedure as it is proportional to its density. By introduction of new fabrication technique, called "pinehole drying method", hydrophobic aerogel with ultra-high refractive index up to $n \approx 1.26$ and excellent transparency can be produced [89, 90]. Thus, the aerogel firmly took the intermediate place between such radiators as compressed gases and liquids, having in additional advantage over them because there is no necessity of high pressure. They are compact and simple to use, which is very important in modern complicated spectrometers.

Such aerogels are available from Airglass Co. (Sweden), Jet Propulsion Lab (USA), Boreskov Institute of Catalysis (Russia), KEK-Matsushita Electronic Work and Chiba U. (Japan). In the past few years considerable improvement in aerogel production methods has been achieved: (i) better transmittance length (> 4 cm for hydrophobic and ≈ 8 cm for hydrophilic tiles), (ii) larger tiles (LHCb: 20 cm $\times 20$ cm $\times 5$ cm) and (iii) tiles with multiple reflective indices.

In our Čerenkov counter we are using aerogel from two different manufacturers: Matsushita Electric Works Ltd. and aerogel produced jointly by Boreskov Institute of Catalysis and Budker Institute of Nuclear physics (BIC/BINP) in Novosibirsk. The aerogel from Novosibirsk is hydrophilic with dimensions $5 \times 5 \times 2$ cm^3, while the aerogel from Matsushita is hydrophobic with dimensions $11.5 \times 11.5 \times 1$ cm^3.

5.4.1 Aerogel optical properties

The crucial optical properties of aerogel are its refractive index n, scattering length, Λ_{sc}, absorption length, Λ_{abs}, and reflection. Refractive index is measured by the deflection of laser beam at aerogel block surface or by measuring the emission angle of Čerenkov photons radiated by fast particles [91]. The combined process of absorption, scattering, and reflectance influence the transmittance $T(\lambda)$, which accounts for the light from the aerogel in the forward direction. In order to separate reflection, absorption and scattering it is necessary to measure also the transflectance, $TF(\lambda)$, and reflectance, $R(\lambda)$. Transflectance is the fraction of light emerging in all directions from the sample and is linked to the absorption. Reflectance is the fraction of light emerging in the backward direction.

Transflectance and reflectance could be measured by an integrating reflecting sphere. The inner walls of the sphere are covered with a material which has high and near Lambertian reflectivity. The transflectance is determined as the ratio between the measurements of light collected by the sphere with and without the sample. The sphere is has two small holes, one for the entrance of the light and one for the PMT (see Fig. 5.7). In this case only the absorbed light is not detected, so the transflectance is directly linked to the absorption length:

$$TF = \exp(-d/\Lambda_{\mathrm{abs}}), \tag{5.20}$$

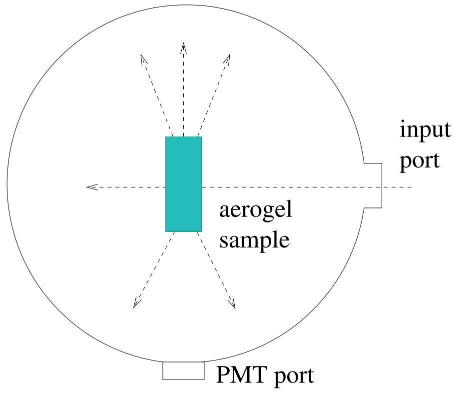

Figure 5.7: Scheme of the integrating sphere for transflectance measurement.

where d is the sample thickness. The transmittance is measured by spectrophotometer and is linked to the absorption length and scattering length:

$$T = \exp(-d/\Lambda_{\text{abs}} - d/\Lambda_{\text{sc}}). \tag{5.21}$$

By using these equations first the Λ_{abs} is extracted from TF and then the Λ_{sc} from T. Fig. 5.8 shows the transflectance and transmittance together with deduced absorption length, and scattering length, as functions of the wavelength λ, obtained at HERMES [92]. It can be seen that the scattering dominates ($\Lambda_{\text{sc}} < \Lambda_{\text{abs}}$) up to $\approx$ 600 nm and the absorption dominates ($\Lambda_{\text{abs}} < \Lambda_{\text{sc}}$) at $\lambda >$ 600 nm. The absorption length remains constant above $\approx$ 300 nm. The absorption length in the region of λ of about 250 nm is well described by the λ^8 dependence and the scattering at $\lambda >$ 350 nm is described by the λ^4 dependence, which corresponds to Rayleigh scattering. The light specularly reflected from aerogel is negligible over the entire wavelength-range. Also the diffusive reflection is negligible since the measured reflectance is totally described by bask-scattering from inside the aerogel [92].

By taking these aerogel optical properties into account the transmittance (5.21) above 350 nm can be described by the Hunt formula [93]:

$$T(\lambda) = A\exp(-Cd/\lambda^4), \tag{5.22}$$

where A and C are the so-called Hunt parameters describing the absorption and scattering. The parameter C, also called clarity factor is proportional to the radiation which is scattered per unit of sample length, while the value $1 - A$ describes the light absorption in the aerogel. For high-quality aerogel samples, the values of A and C are close to 1 and 0, respectively.

Aerogels by themselves are hydrophilic, but chemical treatment can make them hydrophobic. If they absorb moisture they usually suffer a structural change, and deteriorate, but degradation can be prevented by making them hydrophobic. Available aerogel materials from the Boreskov Institute are hydrophilic, so they need baking and storage in dry nitrogen atmosphere to maintain the initial good transmittance.

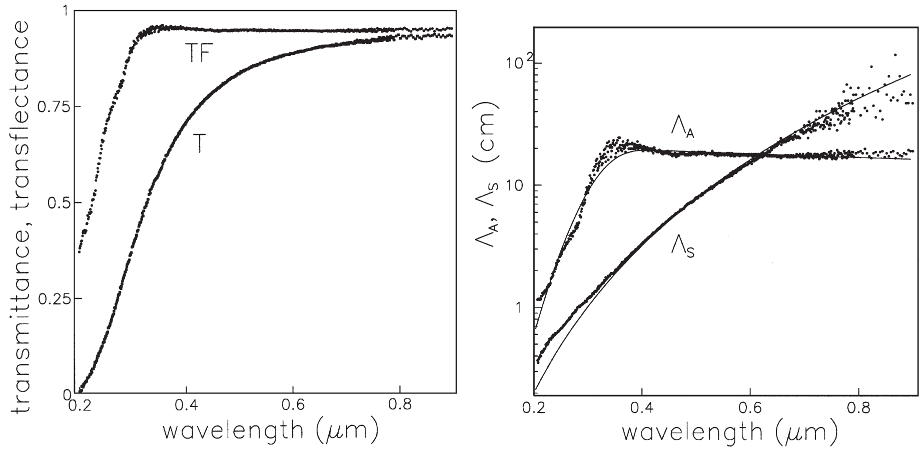

Figure 5.8: Typical measured transflectance (TF) and transmittance (T)(left) and deduced absorption and scattering length (right) as a function of the wavelength λ, measured by [92].

The technology which makes the aerogel hydrophobic results in $\approx$ 30% decrease in light scattering and absorption length. More results about optical properties of aerogel produced by BIC/BINP can be found in [94, 95].

Influence of moisture and ageing

Because the aerogel produced by BIC/BINP is hygroscopic the adsorbed water influences its optical properties. The absorbed water changes the aerogel refractive index.

Under normal atmospheric conditions (room temperature and 15-35% humidity) the aerogel can absorb water from 1 to 5% of its mass. The clarity factor can increase for up to $\approx$ 50% during one year [97]. Usually a 30% drop in the amplitude in the Čerenkov counter is seen after several months and after this the signal is stable. This is the effect of absorption length degradation.

It was found that Λ_{abs} in aerogel also degrades after exposure of aerogel to atmospheric conditions with. The reason for the degradation of Λ_{abs} due to water absorption could be the presence of impurities in the aerogel such as Fe, Co, Cu, Mn, etc. These metals appear in the aerogel during the production from the raw materials. They are able to attract water molecules and create complex conjunctions which absorb light in the visible region [98].

This process of degradation of optical properties can be slowed down by a constant gas flow (CO_2 or N_2) through the diffusive box or by sealing the detector frame.

No detectable degradation of the optical parameters has been observed for γ and proton irradiation. However, a small worsening of the clarity due to neutron irradiation has been observed, which is not a concern for the particle identification performance [97].

5.4.2 Measuring the transmittance of the aerogel

The transmittance was measured by the spectrophotometer from 200 to 800 nm in steps of 1 nm. The scheme of this device is shown in Fig. 5.9. The lamp is the source of the light, which enters into the device through the collimator. The beam is not continuous but divided into pulses, with each pulse having different wavelength. The monochromator extracts only one wavelength from the whole spectrum of the light and reflects the beam onto the 50/50 mirror splitter. At this point the beam is split into two arms, where one part goes through the sample under investigation. Both arms enter the same tube with white inner walls where the light is diffusely reflected. At the bottom of the tube there is a PMT which measures the intensity of the light. The light from two arms enters the tube alternately, so the intensity of light from only one arm is measured by the PMT at the time. The transmittance is the ratio of the intensities from both beam arms. The whole device is placed inside the black box to shield out external light.

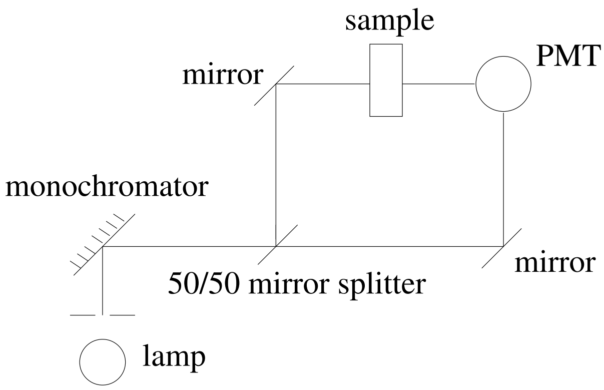

Figure 5.9: The scheme of the spectrophotometer.

With this spectrophotometer I was able to measure the transmittance only, because we did not have the integrating sphere to measure the transflectance. By using Eq. (5.22) I was able to calculate the absorption and scattering length of the aerogel tiles used for the Čerenkov counter in Kaos.

The transmittance was measured at different orientations of the aerogel tiles, so the optical path of the beam through the sample was different. It was also measured at different distances of the sample from the tube to assess the scattering effect. The transmittance may vary from one surface position to another as well as from one aerogel tile to another. To investigate the possible inhomogeneity in each sample, the transmittance was measured at five different surface positions on each aerogel tile (four corners and in the center). From all measurements at each wavelength I have calculated the average transmittance and its RMS to get the spread of transmittance at each wavelength. The spread of the transmittance is shown in Fig. 5.10.

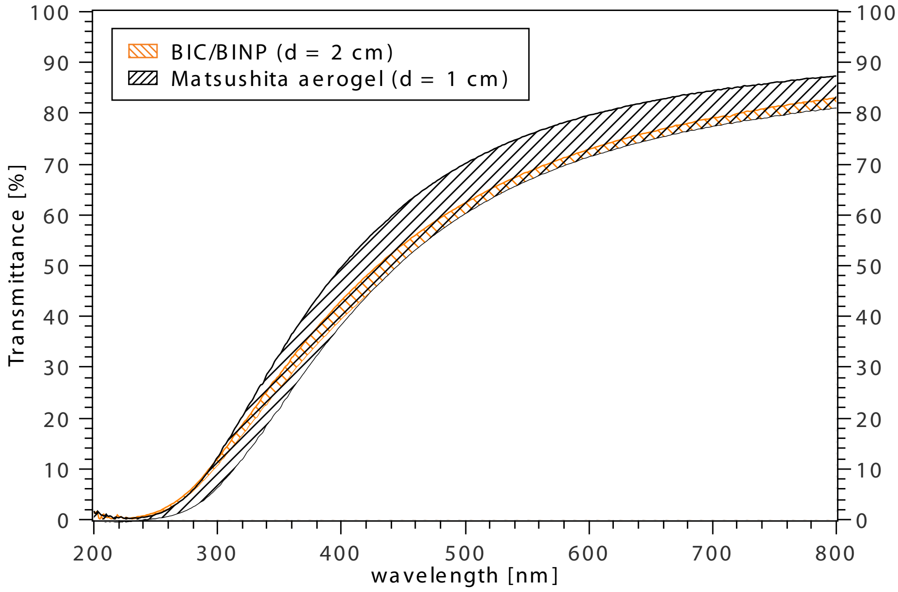

Figure 5.10: Spread of the transmittance of the aerogel. Difference between the BIC/BINP and the Matsushita aerogel occurs due to different thicknesses and manufacturing procedures.

Determining $\Lambda_{\mathbf{abs}}$ and $\Lambda_{\mathbf{sc}}$

By fitting the transmittance with the Hunt formula (Eq. 5.22) the parameters A and C are obtained which determine the absorption and scattering lengths. The fit is evaluated at $\lambda > 350$ nm, because below this wavelength the Hunt formula does not describe $T(\lambda)$ well, as shown in Fig. 5.8. Their mean values and standard errors are given in Table 5.1. The errors on the deduced A and C parameter values are the uncertainties resulting from the fit procedures.

Table 5.1: The mean values of Hunt parameters and their uncertainties for aerogel tiles from two manufacturers.

Hunt parameters	BIC/BINP aerogel	Matsushita aerogel
A	0.828 ± 0.001	0.8710 ± 0.0003
C	$(905 \pm 4) \times 10^{-5}$ μm^4/cm	$(1783 \pm 4) \times 10^{-5}$ μm^4/cm

From these parameters the $\Lambda_{\text{abs}}(\lambda)$ and $\Lambda_{\text{sc}}(\lambda)$ are obtained as:

$$\begin{aligned} \Lambda_{\text{abs}} &= -d/\ln A, \\ \Lambda_{\text{sc}} &= \lambda^4/C. \end{aligned} \tag{5.23}$$

For the wavelength region 200 nm$-$350 nm I kept the λ^4 dependence for scattering length and assumed a λ^8 dependence for absorption length, as described in Subsection 5.4.1. The corresponding absorption and scattering lengths for aerogel tiles used in the Čerenkov counter in KAOS are shown in Fig. 5.11. In the wavelength region of $\lambda > 350$ nm the aerogel from Novosibirsk has a constant absorption length of $\Lambda_{abs} \approx 10.6$ cm, while the aerogel from Matsushita has an absorption length of $\Lambda_{abs} \approx 7.2$ cm. The scattering length of the Russian aerogel at $\lambda = 400$ nm is $\Lambda_{sc} \approx 2.8$ cm, while for the Japanese aerogel it is $\Lambda_{sc} \approx 1.4$ cm.

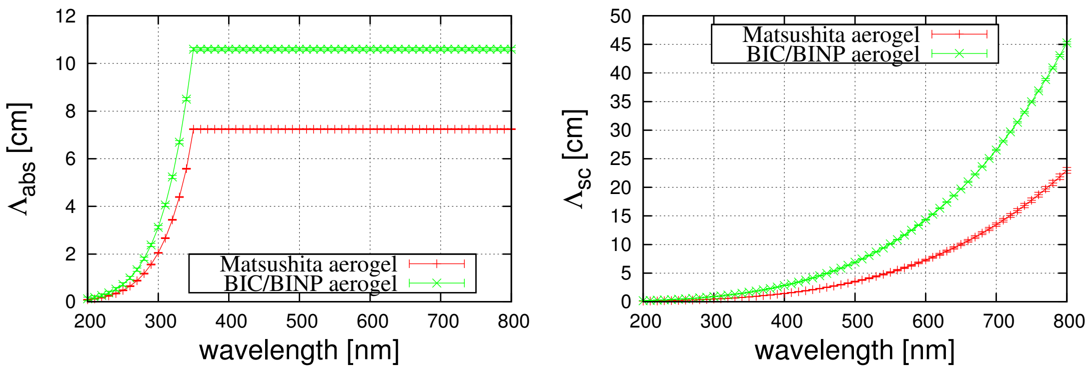

Figure 5.11: Scattering and absorptions lengths obtained from the measured transmittance. The aerogel from BIC/BINP has better optical properties than the aerogel manufactured by Matsushita.

5.4.3 Recovery procedures of silica aerogel

The efficiency of the Čerenkov counter depends on the light absorption length, so the degradation and recovery of the BIC/BINP aerogel optical parameters was studied. The clarity of the aerogel can be completely restored by baking the tiles at high temperature [96, 97, 98].

Usually the aerogel tiles are baked just before assembling. The baking procedure is the following: 6 h to ramp the oven temperature from room temperature to 500 °C, stay for 5 h at 500 °C, and temperature decrease down to room temperature in 6 h. Then the aerogel is taken from the oven and put into the counter or sealed into the envelope or temporary box. It is suggested to use a clean oven, i.e. not an oven where metals or some aggressive chemicals were manipulated.

The effect of the baking on the aerogel optical properties is shown in Fig. 5.12, where the transmittance (T) of light in the 200-800 nm wavelength-range through BIC/BINP aerogel is plotted. It was measured before and right after the baking of several samples. As shown, the transmittance has improved, moreover the largest improvement is in the wavelength region where our PMTs are sensitive the most, e.g. the improvement is $\approx 5\%$ at $\lambda = 400$ nm.

The transmittances of Fig. 5.12 are well fitted by the Hunt formula, Eq. (5.22).

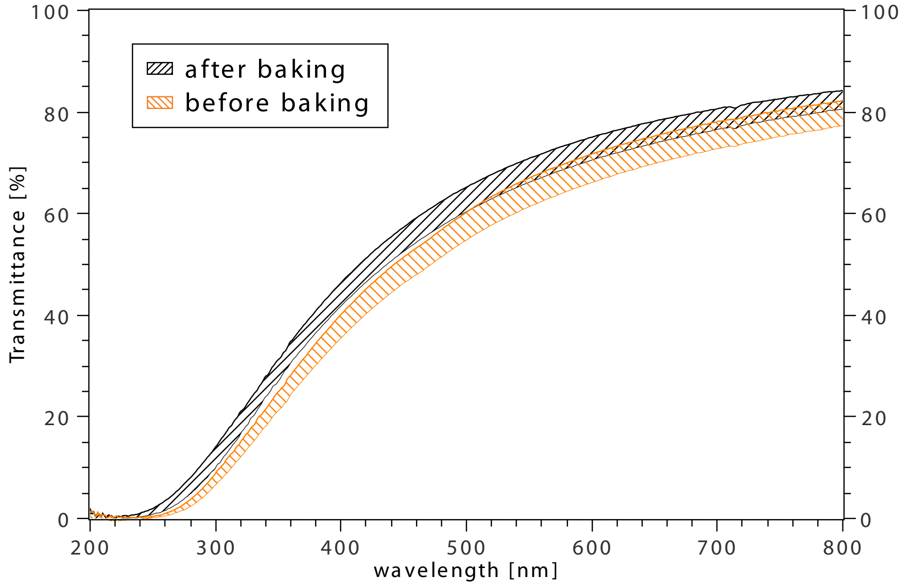

Figure 5.12: The improvement of aerogel transmittance before (black lines) and after (orange lines) 17 hours of baking. The spread of the transmittance is shown by the shaded bands.

Their mean values and standard errors are given in Table 5.2. The obtained values indicate the validity of the baking procedure, both in improving the aerogel transparency and in reducing its absorption. We see that the Hunt parameters have improved.

Table 5.2: The Mean values of the Hunt parameters and their uncertainties for aerogel before and after baking.

Hunt parameters	before baking	after baking
A	0.815 ± 0.001	0.8393 ± 0.0008
C	$(1006 \pm 4) \times 10^{-5}$ μm^4/cm	$(842 \pm 4) \times 10^{-5}$ μm^4/cm

The corresponding absorption and scattering lengths for aerogel tiles have been recalculated to see the improvement due to baking. The result of the recovery in the wavelength region 200-800 nm is shown in Fig. 5.13.

The absorption length has changed from $\Lambda_{\text{abs}} \approx 9.8$ cm to ≈ 11.4 cm and the scattering length at $\lambda = 400$ nm from $\Lambda_{\text{sc}} \approx 2.5$ cm to ≈ 3.0 cm.

Transmittance before and after baking was measured a year after the aerogel has been delivered to Mainz and first optical properties have been measured and described in Subsection 5.4.2. By comparing Λ_{abs} and Λ_{sc} measured before baking

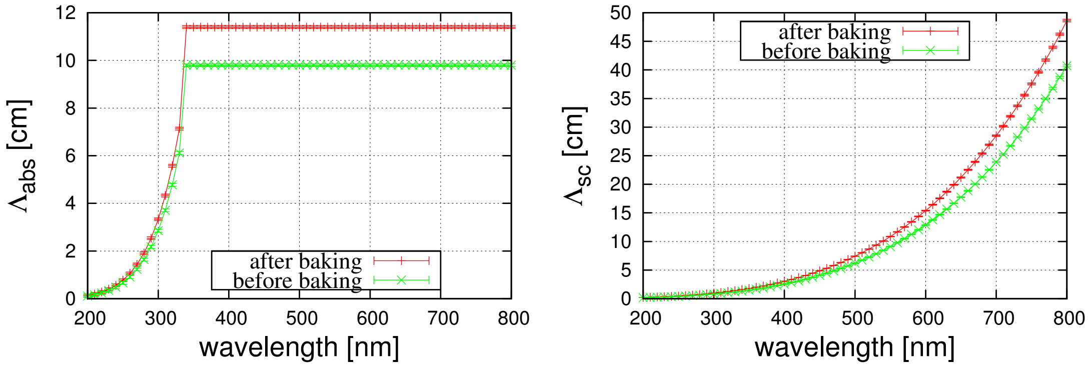

Figure 5.13: Scattering and absorptions lengths obtained from the measured transmittance before and after baking. The optical properties have improved after the baking procedure.

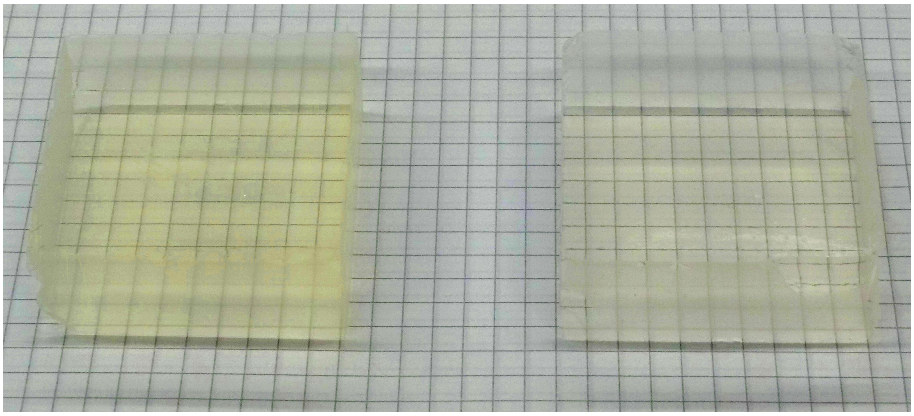

Figure 5.14: Comparison between two aerogel tiles, where right tile has been and the left one has been not exposed to high temperature in the oven.

with the ones measured right after delivery (i.e. a year ago) we can see the deterioration of the optical properties. In one year the absorption length has shortened for $\approx 7.5\%$ and scattering length for $\approx 11\%$ at 400 nm. We can also see that new Λ_{abs} and Λ_{sc} are even better than a year ago. Most probably because the transmittance has been measured right after the baking procedure while the new aerogel must have had already absorbed some moisture from the air when delivered to Mainz.

The improvement of transmittance is also visible by human eye. By comparing two tiles in Fig. 5.14, where right aerogel tile has been exposed to high temperature in the oven, we can see the yellowish color has gone. Before baking both tiles had the same yellowish color.

5.5 The detector design

The simplest geometry for a Čerenkov detector is a cubic box. One part of the detector is filled with the radiator (aerogel in our case), with thickness d and the other part of the detector - called the diffusive box - is filled with air. On top and at the bottom several PMTs are attached to detect the generated photons. The inner walls are covered with a highly reflective coating to prevent the absorption of the generated photons.

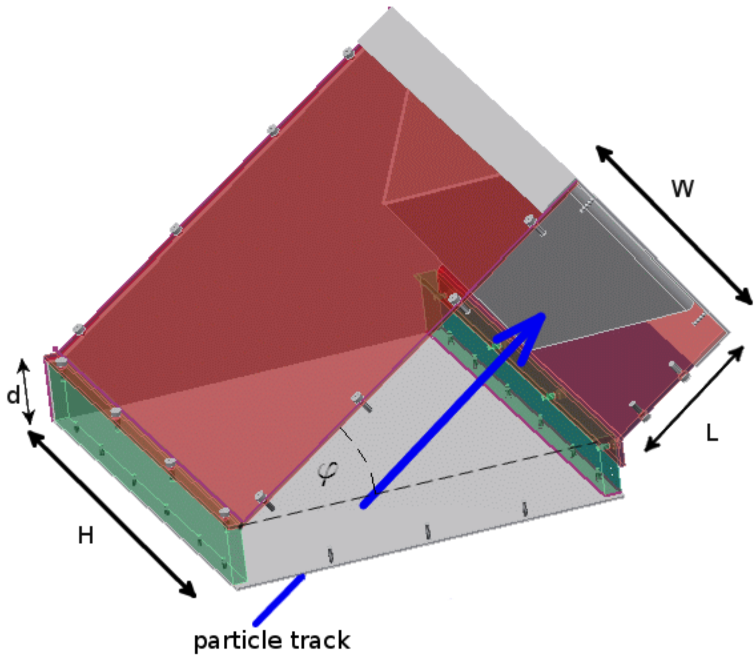

Figure 5.15: The geometry of the detector prototype, which is almost identical to one segment of the final detector. The trajectory of the incoming particle is indicated by the blue arrow.

Because of the available space in Kaos hadron arm and direction of the trajectories relative to the aerogel plane, the geometry of Čerenkov detector in our case is more complex than a simple cubic box. The Čerenkov detector in Kaos has some additional characteristics: (i) additional reflective foils are used, which reflect the light onto the PMTs, (ii) the diffusive box is tilted relative to the aerogel plane so the cone of Čerenkov photons is reflected towards the PMTs more efficiently, and (iii) the diffusive box is separated horizontally with additional inner walls, dividing the full detector volume into six smaller segments. Segmentation of diffusive box prevents Čerenkov light to spread over entire detector. In this case more photons are detected per one PMT which generates larger electrical signal. The detection of signals per segment gives rough vertical position of particle trajectory, so it also influences the determination of track quality factors in hadron arm.

The prototype of the detector was basically one segment of the final detector. In Fig. 5.15 the drawing of a prototype/single segment is shown, where two plates are removed, so that one can see inside. Aerogel is placed at the bottom flat portion (gray floor and dark green side bars), and the diffusive box above (dark red sides) is tilted by $\varphi = 35°$ relative to the aerogel plane. The angle is the same as the average angle of the incoming particles (blue arrow). The mirrors are also visible (in gray). The final detector has six copies of such segments placed next to each other. The main geometry parameters that define the dimension of the detector are height, H, width, W, length of diffusive box, L, and aerogel thickness, d. The size of the prototype is $H \times W \times L = 35$ cm $\times 15$ cm $\times 10$ cm.

Aerogel tiles are placed in the so-called aerogel basket as shown in Fig. 5.16. The surface area of the basket is 450 mm in height (this is vertical in the experimental hall), and 1500 mm in length (this is horizontal in the experimental hall). The first layer is populated by 270 BIC/BINP aerogel tiles with dimension $5 \times 5 \times 2$ cm^3 (9 tiles vertically and 30 tiles horizontally), while the second layer is populated by 1 cm thich aerogel tiles from Matsushita, which gives the total thickness of $d = 3$ cm. The bottom part of the aerogel basket is the entrance plate where the incoming particles impinge into the Čerenkov detector. It is only 1 mm thick because we do not want the particles to lose much energy when they enter the box.

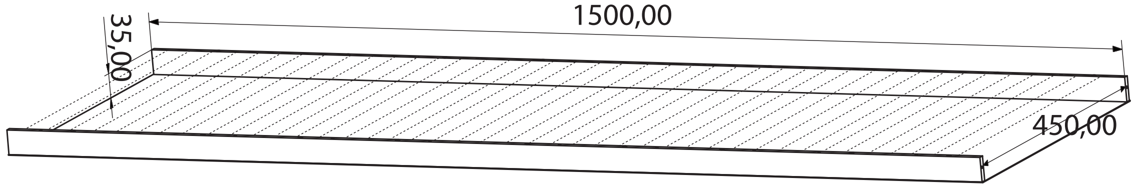

Figure 5.16: The aerogel box where the 270 pieces of 5×5 cm aerogel tiles are placed between the two bars. The side bars are a bit higher than the total thickness of the aerogel, in order to have some space between the aerogel and the inner walls separating the segments. Wires holding the aerogel in place are seen through the holes for the PMTs. All dimensions are in mm.

The whole aerogel basket is covered by multiple plates combined into one piece, comprising the diffusive box as seen in Fig. 5.18. The leftmost and the rightmost plates are bent, because they must act as the remaining two side bars of the basket.

To finally close the detector, two more plates are needed. These plates hold the PMTs and constitute the top and bottom covers of the detector when it is positioned vertically. Each plate is placed right atop of the side bars of the aerogel basket.

All these parts are finally combined to form the complete detector, as seen in Fig. 5.17. Here we can see the Čerenkov detector under construction with aerogel tiles at the bottom barely visible because of high transparency. In the left photograph the orientation of the reflective surface relative to the PMT photocathode is visible. The particle trajectories are shown with yellow arrows together with Čerenkov cone and Čerenkov photons which are reflected towards photocathodes. In the right

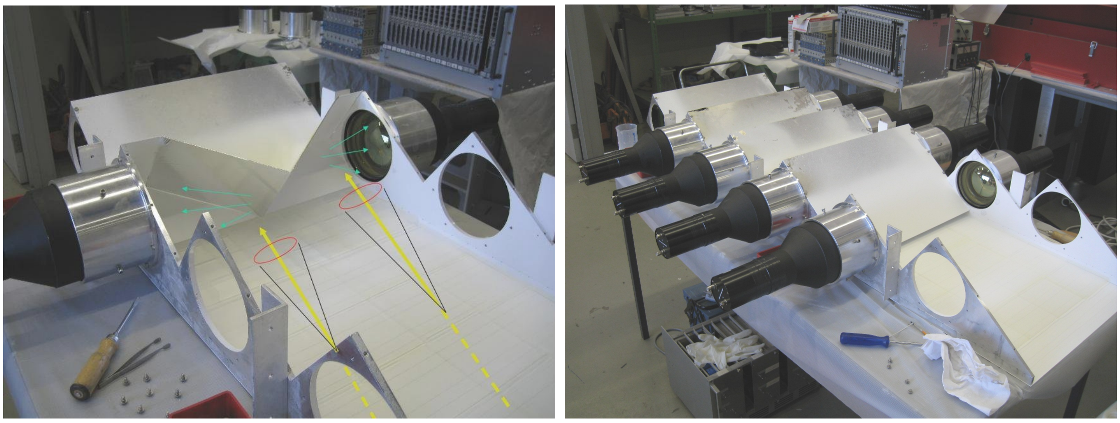

Figure 5.17: The Čerenkov detector under construction. Aerogel tiles are at the bottom and 5” PMTs are attached at both sides.

photograph four segments are already completely closed and we can also see how the inner walls separate neighboring segments.

The whole detector attached to a support frame as shown in Fig. 5.19 and covered with black plastic sheet to prevent any light leakage. In this figure two R877-100 PMTs are attached to segment 0 and R1250 PMTs to segments 1-5. Finally it is mounted inside spectrometer Kaos between the scintillator walls, being parallel to wall G as shown in Fig. 5.20. Each segment has one pair of mirrors, like the prototype. In principle each plate at the back of a segment is covered by an aluminized mylar foil acting as a mirror.

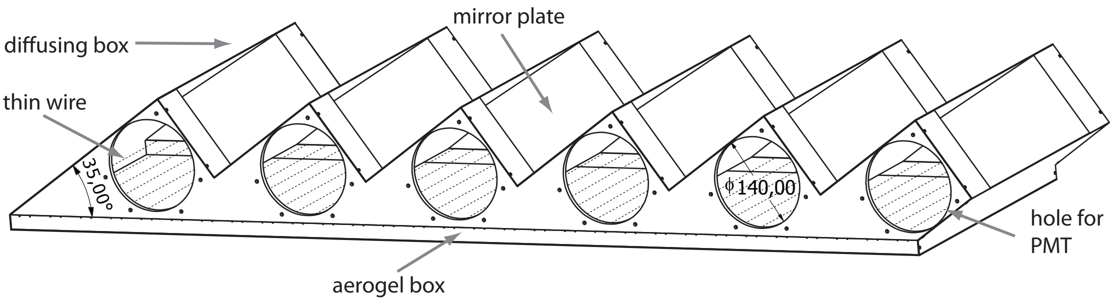

Figure 5.18: The drawing of the detector frame. Particles enter into detector from the bottom side. All dimensions are in mm.

To have the best reflection of photons towards the PMTs the optimal angle between the mirrors was determined by simulating the performance of the whole detector at different angles (see Sec. 6.2). That is why only a fraction of the plate is bent and covered by the mylar foil. The schematic drawing of the mirror assembly within each cell is shown in Fig. 5.21.

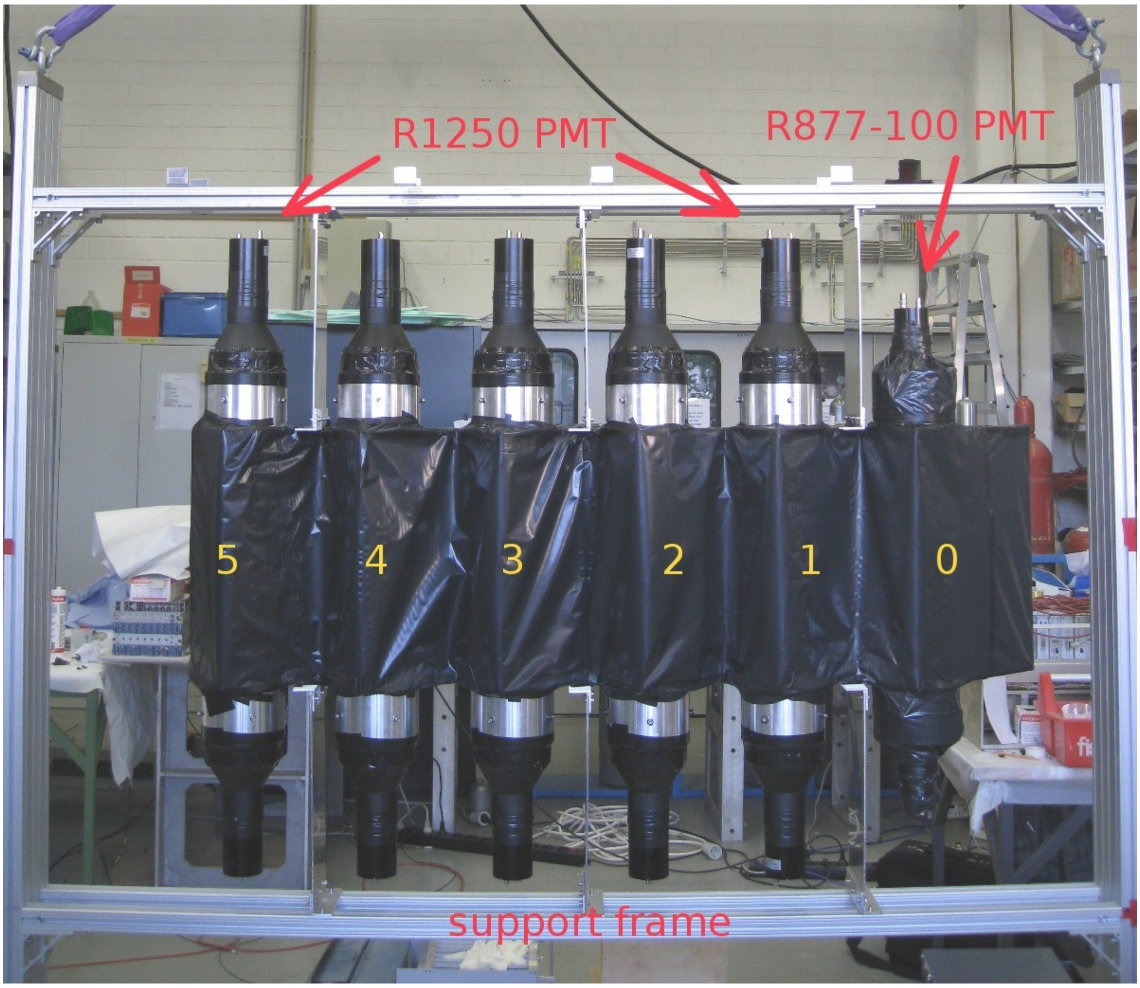

Figure 5.19: The complete Čerenkov detector in its vertical position mounted on support the frame. To prevent the light leakage it is covered with black sheet. Twelve PMTs are attached to top and bottom side. Segment numbers from 0 to 5 are indicated.

Six PMTs are mounted on either of the both "long" sides of the box. With this alignment two PMTs are attached to each segment at the opposite sides; in the experimental hall this is one on the top end the other at the bottom of the detector. The total area covered by the photo-cathode windows of these PMTs amounts to $\approx 5\%$ of the inner surface area of the detector. The PMTs are protected from the magnetic field by the mu-metal magnetic shield cases and are attached to the detector by additional shielding cylinders or so-called PMT rings. Each PMT ring holds a phototube in a fixed position above the large holes for the PMTs. There are two o-rings inside each cylinder that hold the magnetic shield case in a fixed position. Just for the security reasons a few more screws are drilled through the PMT-rings that hold the magnetic cases even stronger. This is schematically depicted in Fig. 5.22.

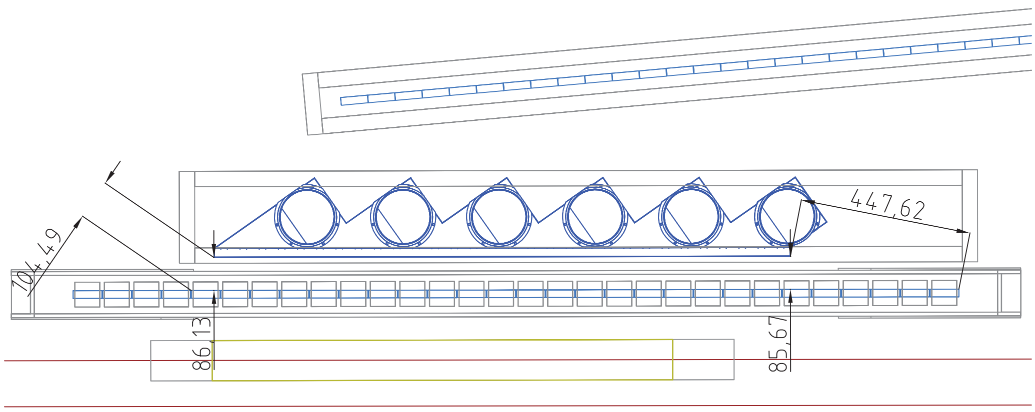

Figure 5.20: Top view of the aerogel Čerenkov counter installed inside the spectrometer Kaos hadron arm. Distances depict the exact location of detector during the experiments described in this thesis. All units are in mm. Figure made by F. Schulz.

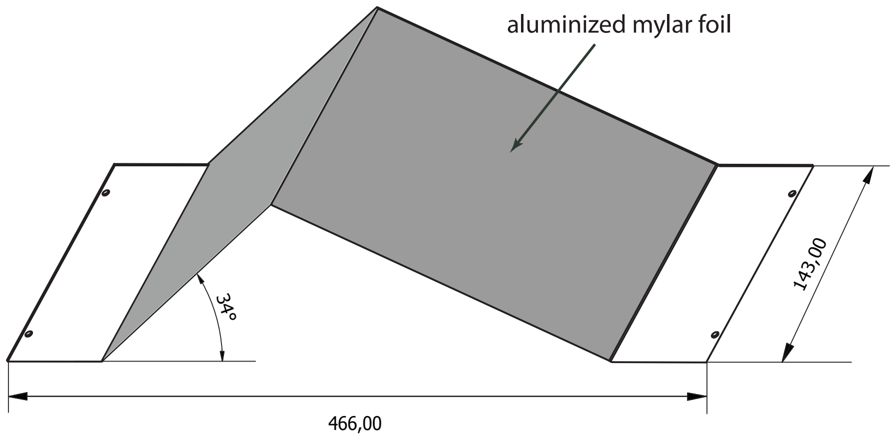

Figure 5.21: The drawing of the plate which is bent and covered by the aluminized mylar foil acting as a mirror. Only the part shaded in gray is covered by the foil, while the white part reflects light diffusively. All units are in mm.

5.6 Photomultiplier tubes

For the experiments described in my thesis two different models of photomultiplier tubes were used. Based on the PID efficiency we have decided which one is more suitable for the final design.

We used 10 R1250 PMTs and 2 R877-100 PMTs, both from Hamamatsu and of 5" diameter. The main difference arises from the photo-cathode material: R1250 pos-

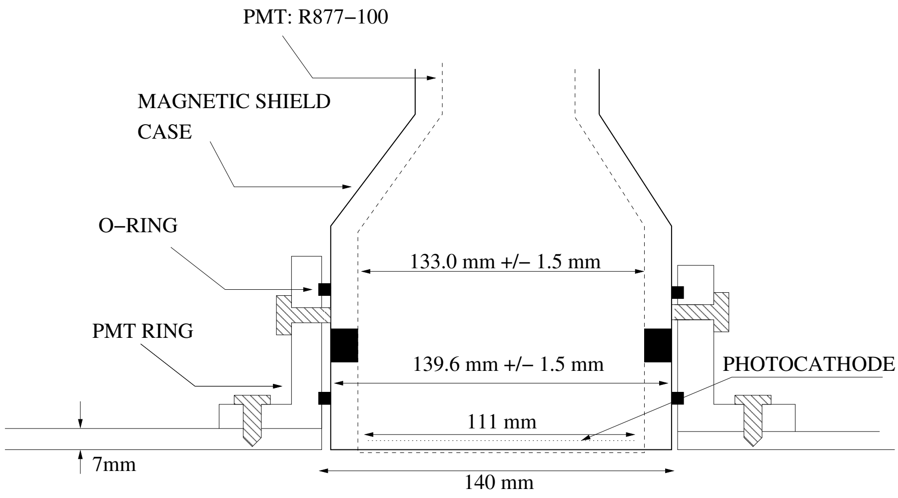

Figure 5.22: The schematic drawing depicting how a phototube, inside the magnetic shield case, is attached to the detector. The dimensions in this figure correspond to the Hamamatsu R877-100 phototube inside the E989-26 magnetic shield case.

sess bialkali photo-cathodes, while R877-100 use the so-called super bialkali (SBA) cathodes, which reach quantum efficiencies (QE) up to 35%. High QE is the main priority of the PMTs, because the number of produced photons is relatively small compared to the scintillating materials, as described in Sec. 5.1. R1250 PMTs have a quantum efficiency of $\approx 23\%$ and R877-100 $\approx 33\%$ in the wavelength range $350 \lesssim \lambda \lesssim 450$ nm, which matches well the transmitted radiation spectrum of aerogel (see Fig. 6.2).

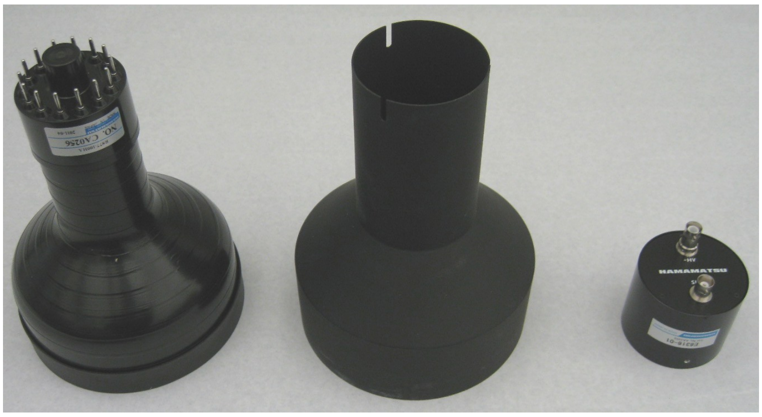

Figure 5.23: Photograph of a R877-100 PMT (left) with E989-26 magnetic shielding (middle) and E616-01 HV base (right).

Another important difference between the two PMT models is the gain. R1250 use a 14-stage dynode structure with a typical gain of $\approx 1.4 \times 10^7$ at nominal voltage, and R877-100 use a 10-stage dynode structure with a lower gain of $\approx 3.1 \times 10^5$.

Even though the gain can be adjusted by high-voltage supply (see Fig.A.5), the compensation for the low gain on the R877-100 PMTs is done by an amplifier which inserted right after the PMT with a signal charge amplification factor of ≈ 200.

R1250 phototubes are much faster with a typical rise time of 2.5 ns at the nominal voltage supply, compared to 20 ns of R877-100 PMT, which makes them more convenient for high-rate experiments.

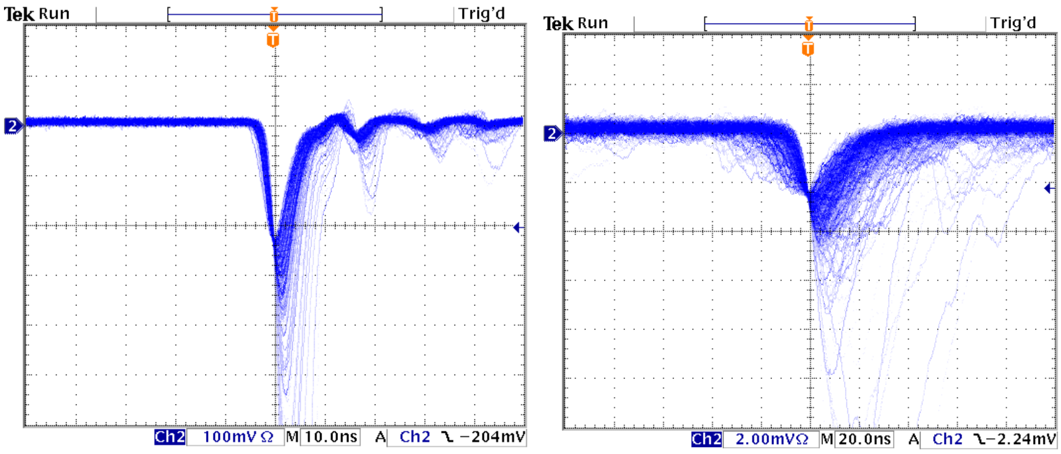

Figure 5.24: Snap-shot of the analog signals from the R1250 PMT (left) and R877-100 PMT (right) at nominal supply voltages.

R1250 PMTs were purchased together with the mu-metal magnetic shield, HV divider circuit and other components, all integrated into a single case, as H6527 photomultiplier tube assembly. For R877-100 PMTs the E989-26 magnetic shielding were purchased separately as well as the E616-01 HV dividers (see Fig. 5.23). All technical details are shown in Appendix A.

In Fig. 5.24 a snap-shot of the analog signals from both PMT models is shown with nominal supplied voltages: 2.0 kV for R1250 and 1.25 kV for R877-100. At this voltages a typical amplitude of a single photo-electron signal is ≈ 5 mV for R877-100, using a 50 Ω LEMO cable. These snap-shots were taken with PMTs placed inside a black box, so only the dark counts are seen. The typical dark current is comparable in both PMT models: 50 nA in R1250 and 20 nA in R877-100, respectively.

The collected charge on the PMT anode is proportional to the integral of the analog signal pulse. The largest contribution to the dark current is thermal emission of the electrons from the cathode and dynodes, described by Richardson's law [99]. The distribution of the signal amplitudes originating from single photons is the consequence of: (i) statistical variation of secondary emission, (ii) variation of secondary emission over dynode surface, (iii) variation of photo-electron energies, (iv) different emission angles from the photo-cathode, and (v) gain variations. The distribution of the integrated dark counts from R877-100 PMT is shown in Fig. 5.25 together with the one photo-electron pulse signal.

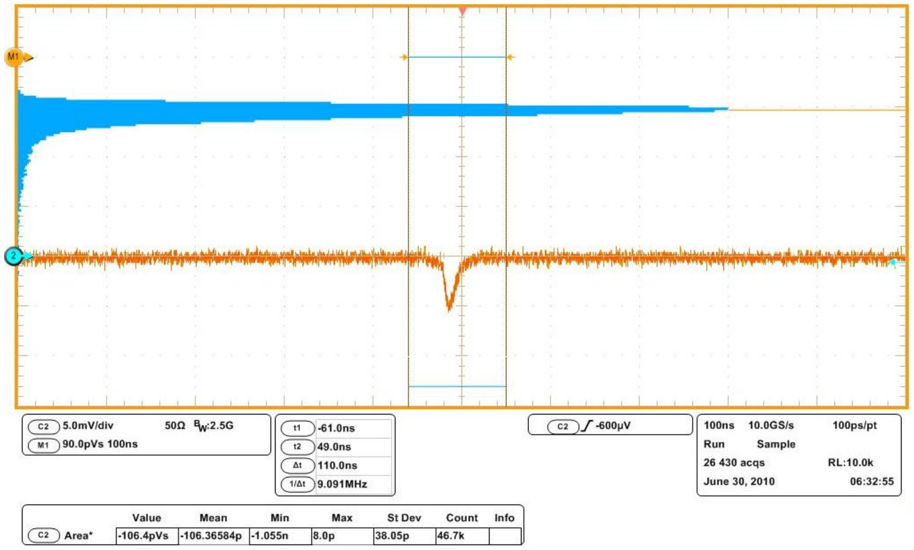

Figure 5.25: Spectrum of the integrated dark counts from R877-100 PMT (in blue and horizontally) with a typical single dark count signal (in orange) at HV = 1300 V supply voltage. The peak position of the distribution is at ≈ 90 pVs. The signal is integrated within the interval limited by two black vertical lines.

5.6.1 Calibration of the photo-multiplier tubes

The calibration of a PMT of the aerogel detector consists of the localization of the single photo-electron peak in the ADC pulse height spectrum which is used to normalize the PMT raw signal. The calibration is necessary when summing the PMT signals in photo-electron units in the data analysis. This is accomplished by matching single photo-electron pulse heights by means of high voltage adjustments or so-called gain matching.

The preliminary calibration of each PMT was performed by measuring the PMT response to a pulsed light source. I have prepared the set-up which imitates the set-up and environment in the spectrometer during real experiments, as shown schematically in Fig. 5.26. The light intensity from the pulsed laser was adjusted by controlling the height of the PMT analog signal. The wavelength was fixed to 370 nm and the pulse rate was set to 1 kHz. The analog signals were driven, through the same cable length as in the Čerenkov detector, to the oscilloscope which was triggered by the internal laser trigger. R877-100 PMTs used an additional amplifier to imitate the set-up of the Čerenkov detector (to compensate their low gain). The laser and the PMTs were placed inside the black box. During the preliminary calibration procedure, the height of the signal for each PMT was found versus the applied high voltage. For the reference signal I used one R877-100 PMT, with the laser intensity set very low where the amplitude of the raw signals is (17 ± 7) mV which corresponds to $3 - 4$ photons per laser pulse. By keeping the laser intensity constant the response function for each PMT was roughly equalized by fine-tuning its HV supply. This high-voltages were later applied to the PMTs during the experiments when mounted inside KAOS. The exact HV value for each PMT is shown in Fig. A.4.

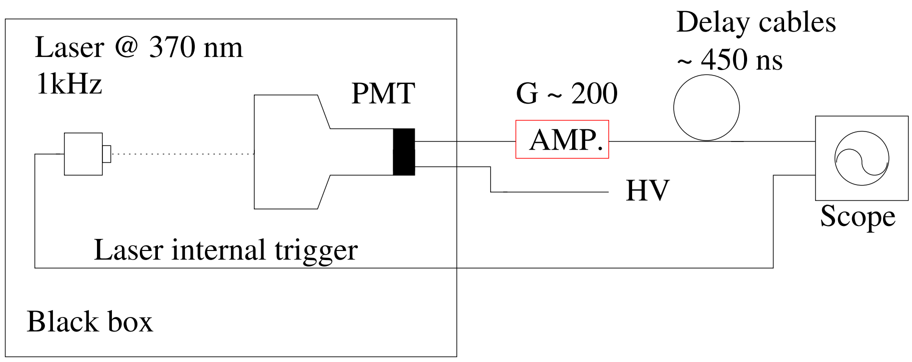

Figure 5.26: The scheme for the preliminary calibration set-up. Each PMT is illuminated by direct hit from the pulsed laser with 3-4 photons per pulse which allowed me to roughly equalize each PMT response by fine-tuning the HV supply. R877-100 PMTs used an additional amplifier with the gain factor ≈ 200.

More accurate calibration was done during preliminary test experiments, where for each PMT the pedestal and single photo-electron (shorter p.e.) peak position was found in the ADC spectrum. The HVs determined in the preliminary calibration were applied to the PMTs, so the position of one p.e. peaks in the ADC spectra were roughly the same but did not match perfectly. One-photo-electron peak is found by fitting the raw ADC spectra with a Gaussian plus a polynomial of third degree: $p_0 \exp\left(-\frac{(x-p_1)^2}{2p_2^2}\right) + p_3x^3 + p_4x^2 + p_5x + p_6$. Hence, the mean value of the Gaussian fit, p_1, tells us the exact position of 1 p.e. peak. The gain and offset factors in the analysis code were adjusted so that the pedestal in the ADC spectrum is at channel #0 and the 1 p.e. peak is located at ADC channel #200 for each PMT,

$$\mathrm{ADC}_i = (\mathrm{ADC}_i^{\mathrm{raw}} - \mathrm{pedestal}_i) * \mathrm{gain}_i. \tag{5.24}$$

The arbitrary ADC units are thus calibrated, where #200 corresponds to one-photo-electron, #400 to two photo-electrons, etc. In Fig. 5.27 an example of a calibration of top PMTs is shown. Blue curve is the fit to the raw ADC with the polynomial function of third degree only, while the yellow curve is the fit which includes also the Gaussian function.

In Fig. 5.27 the R877-100 PMTs were attached to the 5^{th} segment (top and bottom side), while the R1250 PMTs were attached to all other segments. From Fig. 5.27 one can see that no 1 p.e. peak is found in the 5^{th} segment due to the high noise of the R877-100 photo-tubes. For calibration of these PMTs a different approach is needed.

When plotting the distribution of the sum of the ADC values from the top and bottom PMTs for each segment the main peak is seen which is produced by the

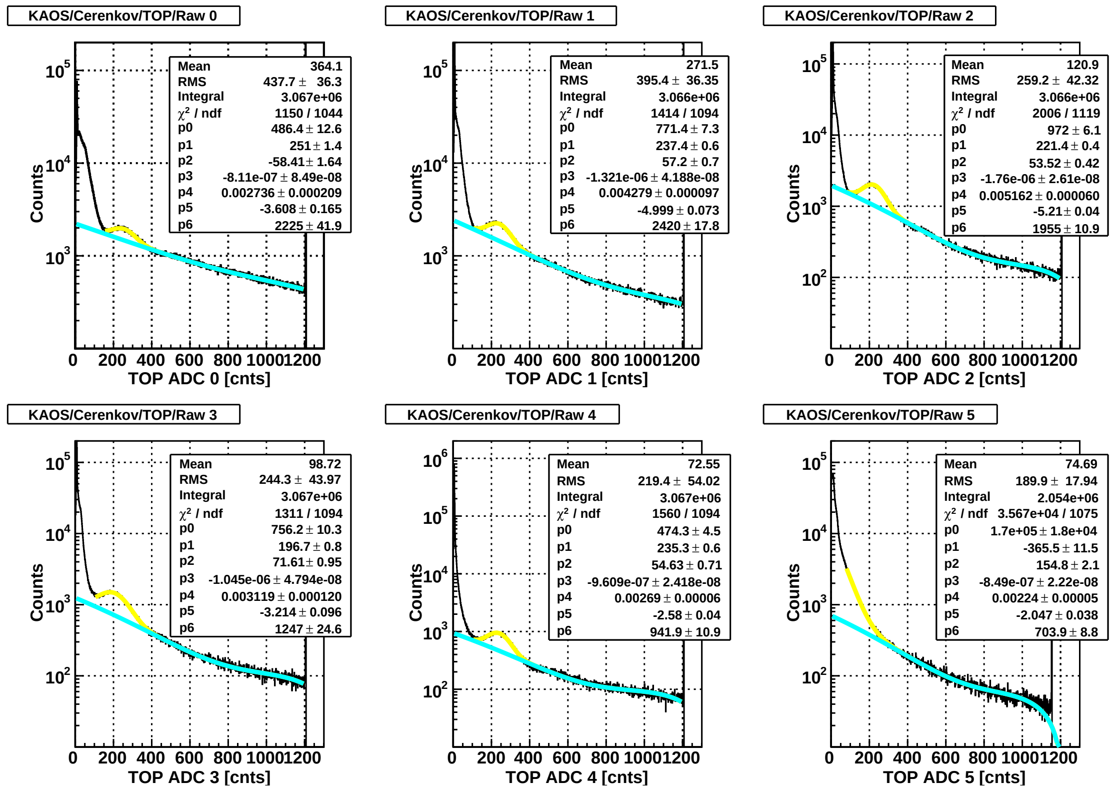

Figure 5.27: An example of the calibration of raw ADC spectra of the six top PMTs. The 1 p.e. peak is found by using a Gaussian fit plus the polynomial function of the third degree (yellow curve). The p_1 fit parameter is the mean value of the Gaussian.

particles above the Čerenkov threshold. In Fig. 5.28 an example of such distribution is shown for all six segments which are already calibrated, except for the 5^{th} cell, where only the pedestal is set to the ADC channel #0. The gain factor for both PMTs in segment 5 is set such that the main peak has the same position in the ADC sum spectra as the average position of the main peaks in all other cells. The exact position or ADC value of the main peak in each segment is found by applying the Gaussian fit to the ADC spectra. The gain factor is found by using the mean values of the fit as:

$$\text{gain}_5 = \sum_{i=0}^{4} \frac{\text{mean}_i}{5}. \tag{5.25}$$

In Fig. 5.28 the 1 p.e. peaks are still visible in all segments, except in the last cell, because different PMT models were used. But on the other hand the valley between the pedestal and the main peak is larger which makes it easier to set the cut condition that separates between the particles above and below the Čerenkov emission threshold.

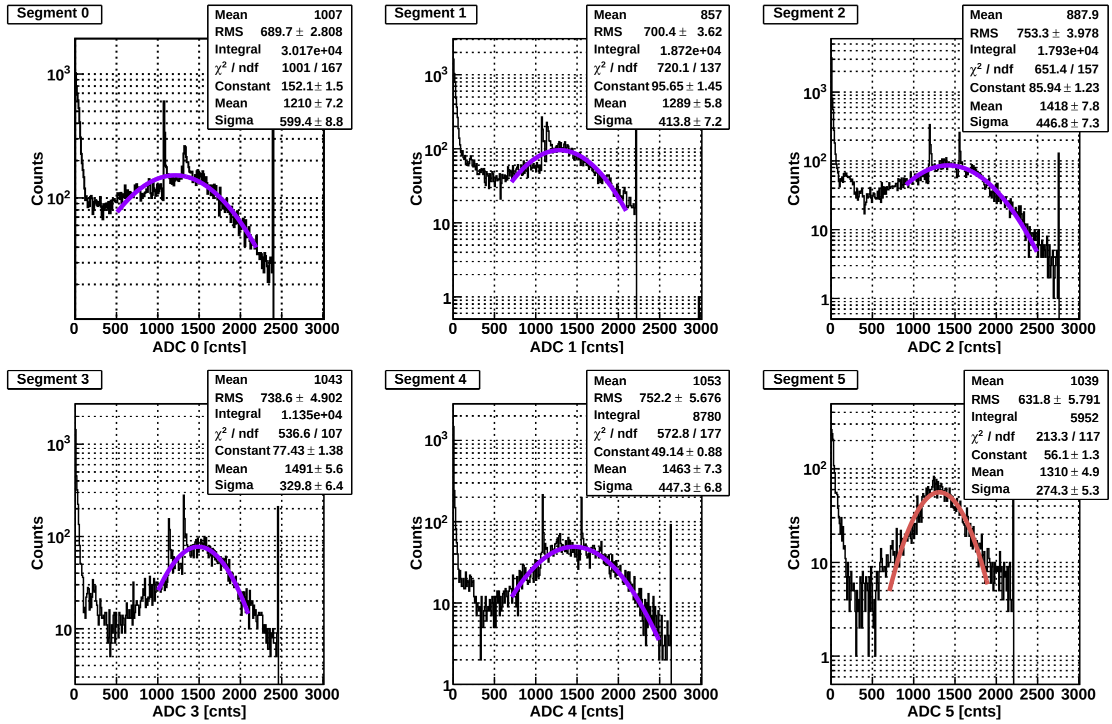

Figure 5.28: An example of the calibration of the 5^{th} segment. A Gaussian fit is applied to the ADC top plus ADC bottom histograms for each segment. By fine-tuning the gain factor the mean value of the main peak in the last segment is the same as the average mean value in other segments.

5.7 Other equipment

5.7.1 Reflective coating

All the interior surfaces of the diffusive box are coated with highly reflective coating to prevent the absorption of the generated photons. This configuration has been found to be superior to millipore paper which is commonly used in Čerenkov counters. We have chosen to use 6080 White Reflectance Coating, manufactured by Labsphere, North Sutton, USA [100]. The same white reflective paint has been used for the BLAST Čerenkov detectors at the MIT-Bates Linear Accelerator center [81]. It is a diffuse white paint for reflectance applications covering the UV-VIS-NIR wavelength region. The surface of the paint follows the Lambert's law, so the light is reflected isotropically. This coating has reflectance values from 95% to 98% over the wavelength region from 300 to 1200 nm, as shown in Fig. 5.29. The optimum coating thickness is between 0.5 and 0.6 mm.

The 6080 coating is a barium-sulfate-based formulation that is easily applied by means of an airless spray gun or, for small-scale use, an airbrush. The coating can be applied to most metal, plastic, and glass surfaces that have been properly cleaned and roughened by mechanical means.

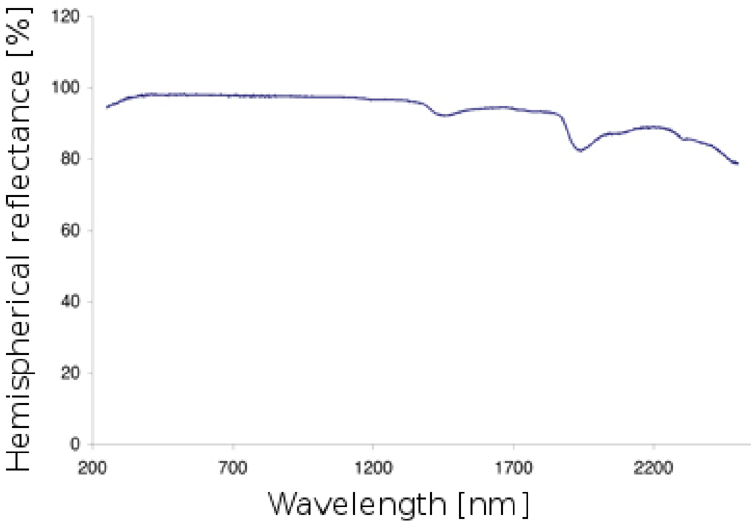

Figure 5.29: Typical hemispherical reflectance of the 6080 white reflectance coating [101].

5.7.2 Mylar foils

The reflective surfaces that imitate the mirrors and specularly reflect light directly towards photocathodes are covered by reflective foil. The reflectivity of several foils has been measured in the wavelength region of our interest using a spectrophotometer. Reflected light is composed of diffuse and specular reflection. Spectrophotometer offers the possibility to measure both reflections individually. The monochromatic light is divided by 50/50 mirror into two arms: reference and measurement light (see Fig. 5.9). Light from both arms is collected by the so-called integrating sphere, with inner walls covered by white diffuse paint and a PMT at the bottom for light detection. By comparing the relative difference of intensity between measurement and reference light the transmittance and reflectance of a sample is measured.

The integrating sphere has four openings: for reference light, for measurement light, one for diffusive reflection and one for diffusive and specular reflection. The latter two can be covered by white board to close them completely, e.g.for transmittance measurement. Diffuse reflection is measured by placing the sample perpendicular to measurement light, as shown in Fig. 5.30 left. In this case bottom opening is closed by standard white board and specular reflected light is not detected because it is reflected out out the integrating sphere. The total reflection (specular and

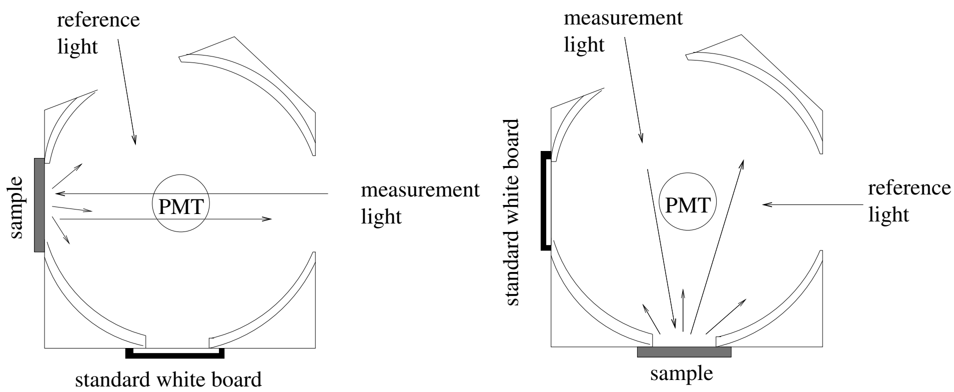

Figure 5.30: The set-up of the integrating sphere from the spectrophotometer to measure the diffusive reflection only (left) and diffusive with specular reflection (right).

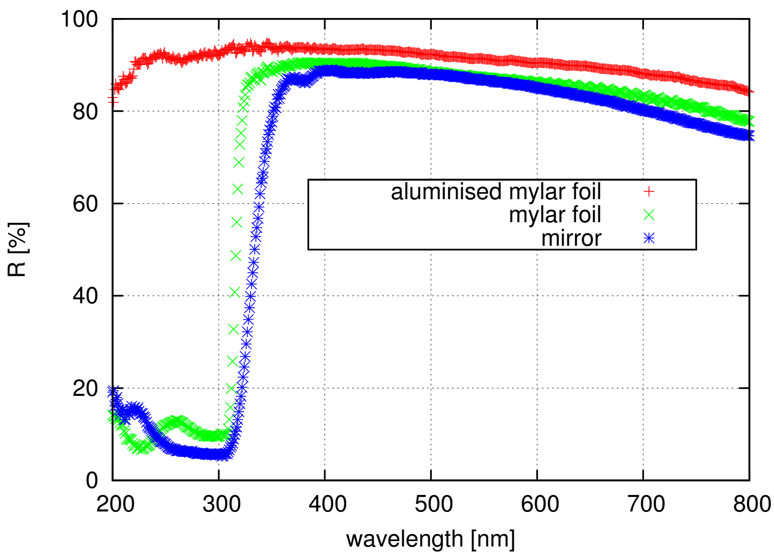

Figure 5.31: The reflectivity of different surfaces. Only the aluminized mylar foil reflects the UV light and has the highest reflectivity in the whole wavelength region.

diffuse) is measured by placing the sample non-perpendicular to the measurement light as shown in Fig. 5.30 right. In this case the sample is exposed to the other arm, which is now called measurement light. This can be done because two arms do not enter the integrating sphere perpendicularly so the set-up is not symmetric and not the same as before. As depicted in the figure left opening is closed by white board and total reflection is measured.

The diffusive reflection of the (aluminized) mylar foil has been measured to be well below 10%. Total reflection is shown in Fig. 5.31. As we can see the aluminized mylar foil has the highest reflectivity in the whole wavelength range (between 80%

and 90%), moreover the reflectivity of the ordinary mylar foil and ordinary mirror deteriorates in the UV region. The problem with an ordinary mirror is the thin layer of glass (borosilicate) over the reflecting aluminum which absorbs light below 350 nm. Thus the use of aluminized mylar foil was the best choice. The thickness of the foil is 4 μm, with an aluminum layer with a thickness of 400 Å.

5.7.3 ADC module

The analog signals are driven through RG-58 cables and digitized by a LeCroy 2249A Analog-to-Digital Converter (ADC). It has 12 input channels, which is exactly the same as the number of the PMTs in the Čerenkov counter, with Lemo-type connectors and 50Ω input impedance. This module is charge sensitive with full-scale range of $256(1 \pm 0.05)$ pC and a 10 bit resolution [102].

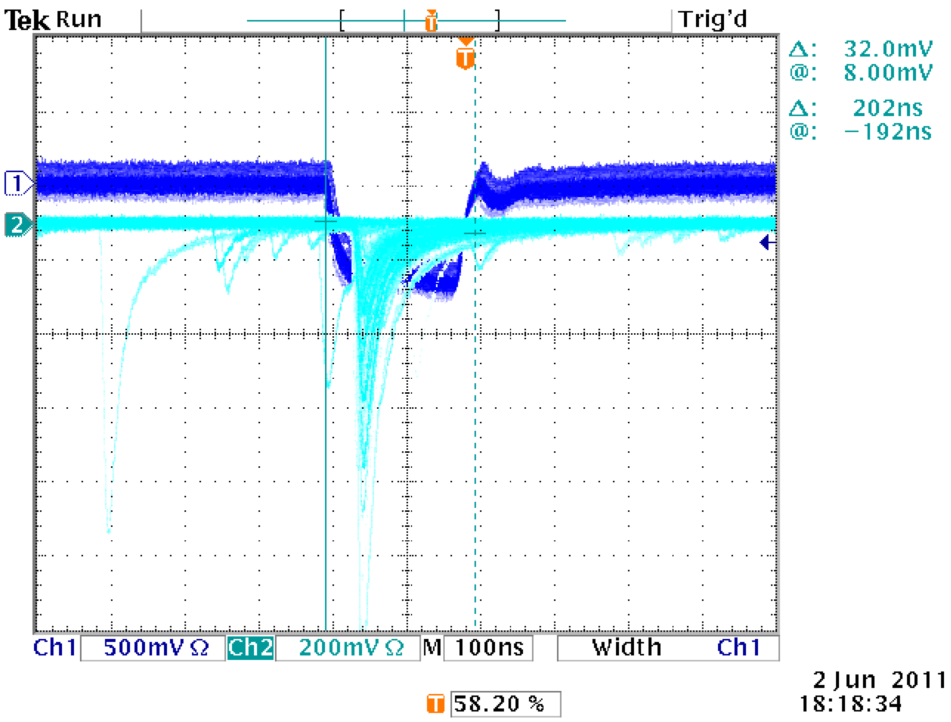

Figure 5.32: A screen-shot of typically analog signals (light blue) from the R877-100 PMT in coincidence with the gate signals (dark blue) taken during the experiment. The gate width was set to 200 ns.

All ADC channels have one common gate. During the experiments described in this thesis the gate width was optimized to the typical analog signal width, thus it was set to ≈ 200 ns as shown in Fig. 5.32. The gate signal comes from the signal that triggers the complete detector system from the hadron arm in Kaos.

To improve the data quality of the Čerenkov detector new ADC-TDC system has been set-up after the experiments described described in this thesis: CAEN V792 for analog-to-digital conversion and CAEN V775 for time-to-digital conversion.

5.7.4 Mesh of wires

To prevent aerogel tiles from falling out of their position when the detector is aligned vertically, the whole aerogel box is covered by a mesh of thin wires. We have used a 10 μm diameter gold-plated tungsten wire. In fact these are the same wires which are used for the VDC's in the magnetic spectrometers because any wire would do the job. The two side bars of the aerogel box have small holes with 1 mm diameter, through which the wires are pulled and their loose ends secured at the exterior by a knot on one side and by a small screw on the other, as shown in Fig. 5.33. Each wire is entangled around the top side of the screw which at attached to the side bar and thus pressing the wire firmly towards the bar. Two wires are placed over each aerogel column at the distance of 17 mm.

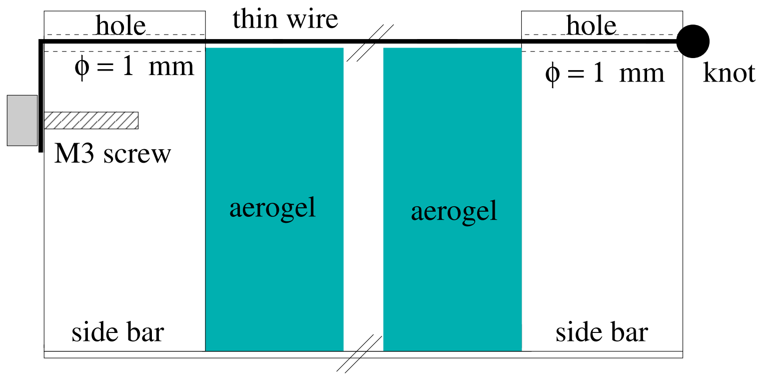

Figure 5.33: Wires are attached by a knot on one side of the so-called side bar and a M3 screw on the other side. Dimensions are not proportional.

CHAPTER 6

Simulations in SLitrani

6.1 Basic geometry simulations

To fully understand the performance of the Čerenkov counter simulations have been done in SLitrani (LIght TRansmission in ANIsotropic media) to reproduce and compare the efficiency results with the real data [103]. SLitrani is a C++/ROOT based program which allows to generate and propagate photons from their emission point to a detecting device through optical materials as complex as anisotropic media. The aim in this program is to follow each photon until it is absorbed or detected. Sources of photons are: spontaneous photons, photons generated by the crossing of particle, photons generated by high energy electromagnetic shower etc. As detectors phototubes, avalanche photo-diodes, or any general type of surface or volume detectors can be used [104]. All the physics behind SLitrani can be found at [105].

SLitrani was used to simulate by Monte-Carlo method the behavior of a single segment as well as the complete Čerenkov counter placed in the experimental hall. By changing the geometry, mechanical and optical properties of the materials, the optimal solution was found to make the final design.

The absorption and scattering length of the aerogel from Boreskov Institute of Catalysis and Budker Institute of Nuclear physics (BIC/BINP) used for the simulations are shown in Fig. 6.1. Due to the deterioration of Λ_{abs} and Λ_{sc}, which become stable after several months, I have used data measured five months after the delivery of aerogel. This gave me more comparable results with data taken half a year after the delivery of aerogel. The fact that I was using deteriorated Λ_{abs} and Λ_{sc} in the simulation explains the difference between optical properties shown in this and in the previous Chapter, were absorption and scattering length were measured on completely new aerogel tiles (see Fig. 5.11). Because the aerogel from Matsushita is hydrophobic the absorption and scattering length do not change much over time so the same data has been used as in Fig. 5.11.

The diffusive box is covered on the inside by diffusively reflective material with the reflectivity of 96%. The quantum efficiency of the photo-cathode versus pho-

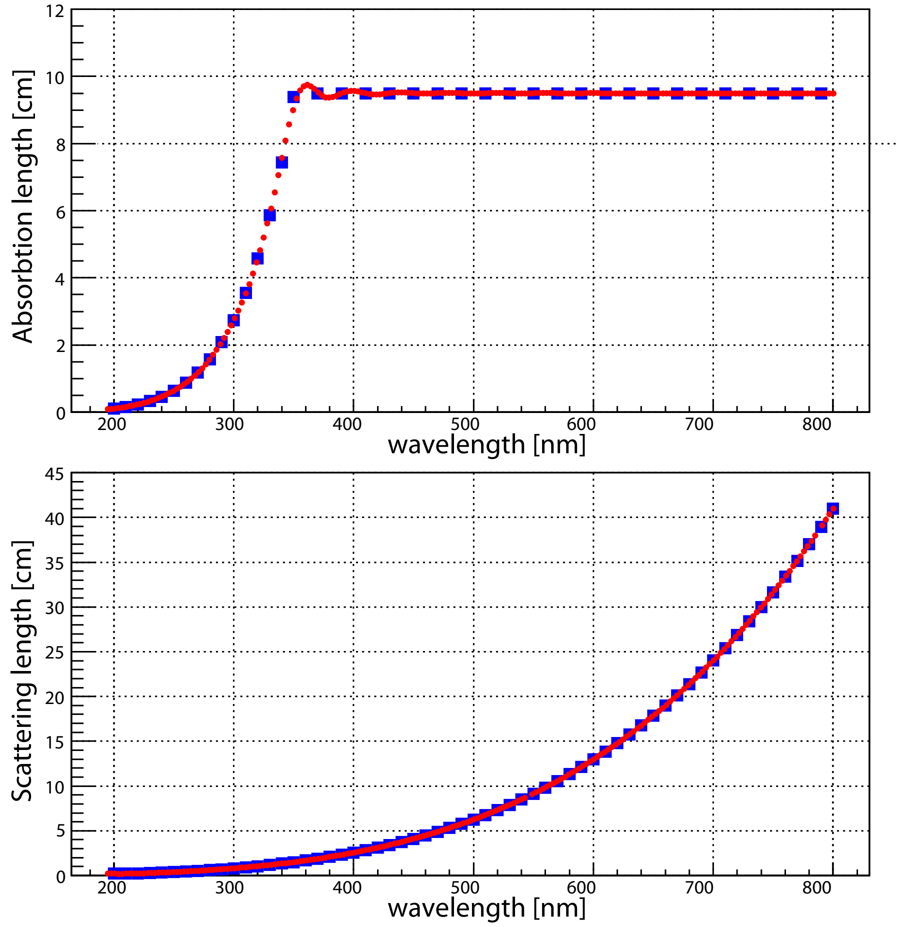

Figure 6.1: Absorption (top) and scattering length (bottom) of the BIC/BINP aerogel versus wavelength used in the simulations. Measured data is shown with solid blue squares and the best fit is shown with red dots.

ton wavelength used in the simulations matches the quantum efficiency values from R1250 and R877-100 (see A.1). The absorption length of the PMT window glass is taken from the measurements done by the Particle Physics Group at Chiba University [106], as shown in Fig. C.1.

The wavelength distribution of generated Čerenkov photons is consistent with the $1/\lambda^2$ dependence (see Eq. (5.5)), as shown in Fig. 6.2. Because of the wavelength dependence of absorption in aerogel and PMT glass window the wavelength distribution at the photocathode surface is different with a maximum at 350 nm - 400 nm (see Fig. 6.2). Based on this simulation results the phototubes with the maximum quantum efficiency in this region have been chosen.

The index of refraction of the PMT window glass used in the simulations is shown in Fig. C.4. The reflectivity of the mylar foil was set to 90%, according to our measurement results (see Fig. 5.31). In the simulation the aerogel is bombarded by a beam of positrons with a fixed momentum of $p = 1$ GeV. Besides momentum

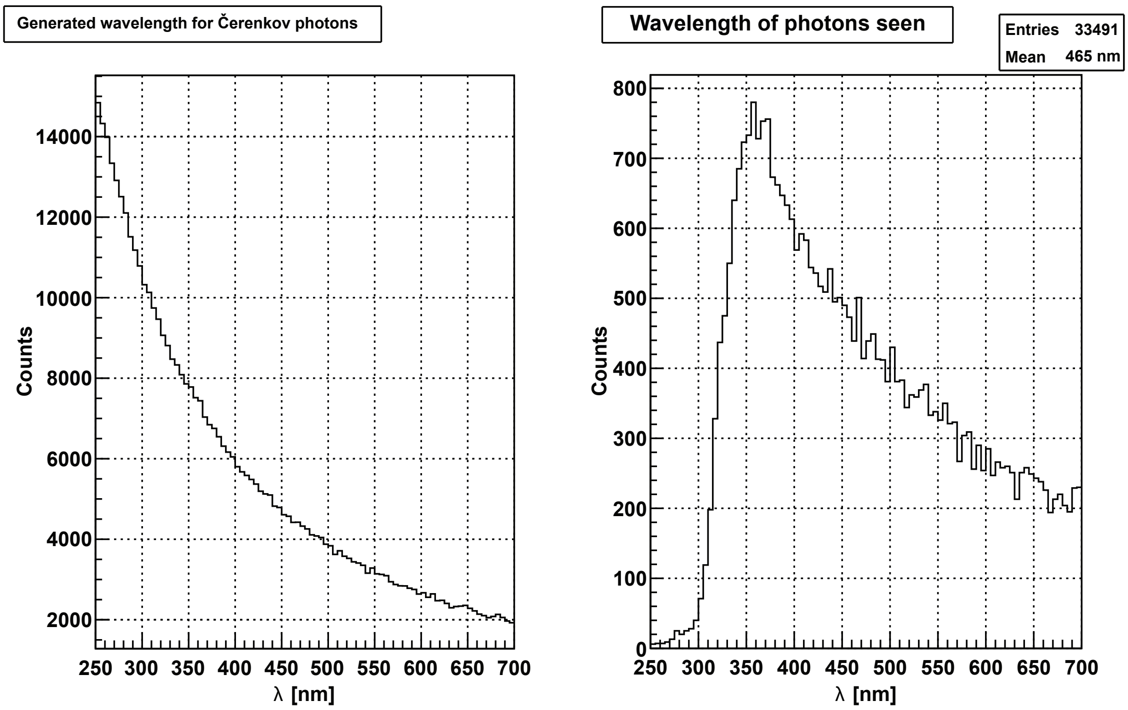

Figure 6.2: The wavelength distribution of Čerenkov photons. Left: the emission spectrum. The number of produced photons per wavelength is proportional to $1/\lambda^2$. Right: the spectrum of photons reaching the photocathode surface.

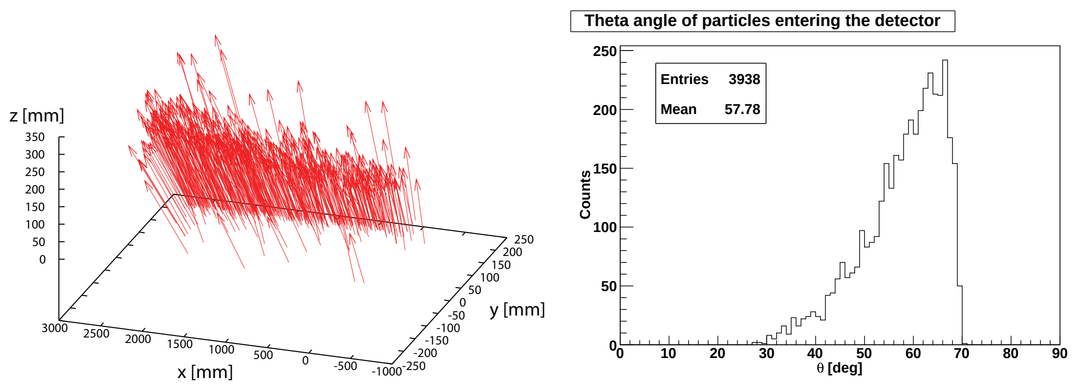

Figure 6.3: Simulated particle distribution over Čerenkov detector. Left: particle momentum vectors on the aerogel plane. Axis x and y go along the plane and z goes into the detector. Right: the angle distribution in dispersive direction along z axis. The average angle, which is $\bar{\theta} = 57.8°$, is similar to the angle of the diffusive box, which is 55°.

the following parameters were kept constant: refraction index of aerogel: 1.055; quantum efficiency; reflectivity of reflective coating; proportion of photons which are reflected diffusively instead of specularly: 100%; height and width of diffusive box: 45 cm × 150 cm, and the active area of the PMTs. Other parameters that were changing in the simulations to see the behavior of detector are: aerogel thickness, d and the angle of the reflective surfaces inside.

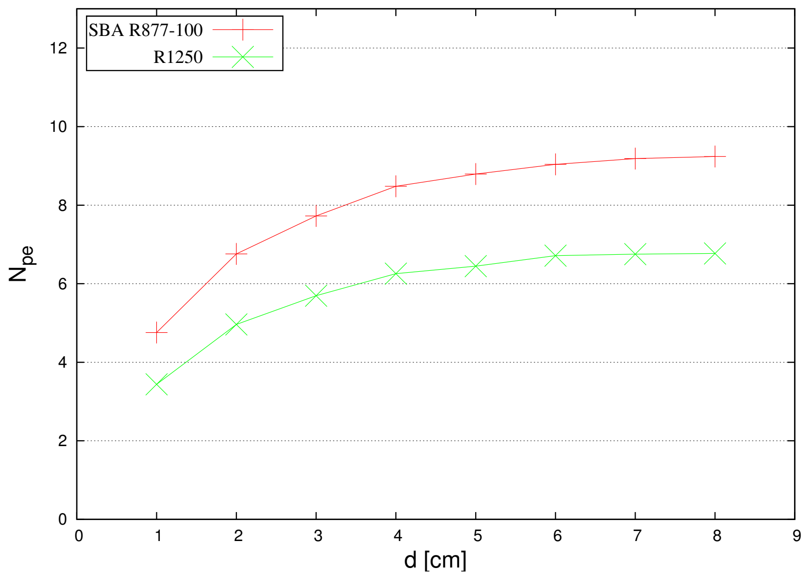

Figure 6.4: Simulated number of photo-electrons in all 12 PMTs as a function of aerogel thickness d with two different PMT models attached to the detector.

To properly simulate the behavior of the Čerenkov detector in the experiment, the angles and coordinates of the incoming particles on the aerogel plane must be known. They are retrieved from the kaon electro-production simulation software used by the A1 Collaboration. In Fig. 6.3 samples of particle vectors are shown at the entrance of the Čerenkov counter. Coordinates x and y are along the aerogel plane, and coordinate z goes into into detector. Coordinate $y = 0$ mm corresponds to the mid-plane and $x = 0$ mm to the low momentum edge of the aerogel box. In the same figure the distribution of the angle in the dispersive direction along z is shown (0 degrees means perpendicular hit). Based on the average angle from this simulation, $\overline{\theta} \approx 55°$, the angle of the diffusive box with respect to the z axis was chosen (see Fig. 5.15 and 5.18). In this case the optimal reflection on the mirror surface is achieved. In this geometry the effective path length of particles through the aerogel layer is larger than its thickness by $d/\sin\theta$, which results in a better light yield and thus higher efficiency.

The main result of our interest is the number of detected photons per incoming particle. Fig. 6.4 shows the total number of photo-electrons at different aerogel thicknesses. For comparison two different 5” PMT models, R1250 and super-bialkali R877-100 PMTs, have been used. We see that the number of the detected photons approaches an asymptotic value, which corresponds to the theoretical Eq.(5.7), where we have to bear in mind that the number of detected photons is proportional to the number of the photons that enter the diffusive box. In case where R877-100 photo-tubes are used more photons are detected due to the higher quantum-efficiency of the super-bialkali photocathode, which results in a higher efficiency of the complete Čerenkov counter.

Another important characteristic of the Čerenkov counter is the time distribution of photons detected and its width, which is equivalent to the distance traveled by Čerenkov photons upon detection. In Fig. 6.5 we see that the simulated average time is $\approx$ 2.1 ns and slightly increases with the aerogel thickness. This gives a $\approx$ 0.5 m distance traveled by detected photons. The time of arrival does not depend on the PMT quantum-efficiency, but on the photocathode diameter. In the case of the PMTs with bigger diameters the average time and the width get smaller as larger detection area results in fewer reflections and faster detection. If there were no other parameters to change, the optimal aerogel thickness would be at the point where the width of the time spectrum is as narrow as possible and where we detect as many photons as possible. Although timing is not of prime importance in foreseen KAOS applications, we still wish to optimize the timing behavior or at least keep in it reasonable limits.

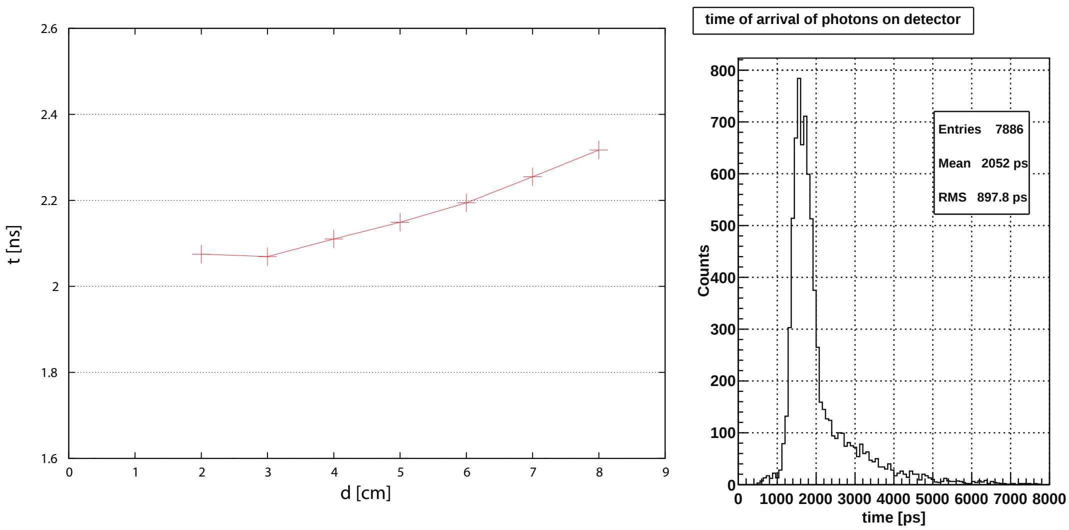

Figure 6.5: Left: simulated time of arrival of photons seen by detector as a function of aerogel thickness d. Right: Typical time spectrum at $d = 3$ cm.

The number of diffusive reflections of each photon depends mostly on the scattering length of aerogel. In Fig. 6.6 a difference of diffusive reflections between two aerogel types is shown. The difference is not so large, but there are more reflections per photon on average in the Matsushita aerogel due to the shorter scattering length. In both cases the complete aerogel box is filled with one aerogel type with thickness of $d = 3$ cm.

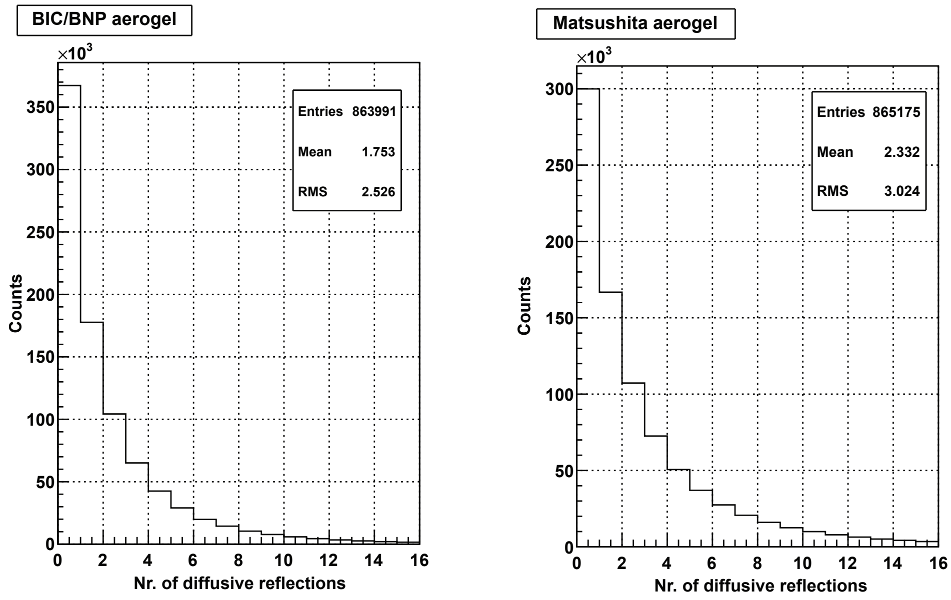

Figure 6.6: Number of diffusive reflections per photon within aerogel from two different manufacturers. Left: BIC/BINP aerogel, right: Matsushita aerogel.

6.2 Comparing different types of diffusive boxes

In order to see the improvement of the light collection efficiency of the detector due to the reflective foil inside the box, the simulations have been done with and without the so-called mirror plates at constant aerogel thickness, $d = 3$ cm. To imitate the aluminized mylar foil 90% reflectivity was assumed, as well as 0% probability for diffusive reflectivity (all light is reflected by the reflection law). Both types of the single cell box are shown in Fig. 6.7. For comparison the simulations have been also done with the mirror plate covered completely with diffusely reflective coating to imitate the coating which is applied onto the walls.

The simulations have been performed with different angles, α, between the reflective plates as well. For easier interpretation, the angle between the plates, 2α, is defined by the distance from the center of the mirror plate to the end of the plate covered with reflective foil, and schematically shown in Fig. 6.7. The relation is: $\tan\alpha = x/L$. The simulations were done at distances $x = 0.25 \cdot a$, $0.5a$, $0.75a$ and $1a$, where $2a$ is the total height of the mirror plate, with $2a = 450$ cm, which is the same as the height of the aerogel box. The simulation with no mirror plate inside corresponds to $x = 0$.

We want to keep the length of the diffusive box, L, as short as possible, since the relative area covered by the PMTs gets bigger and the probability for the photon detection increases (see Eq. 5.7). Another reason to keep short diffusive box length is that the space in in the Kaos spectrometer, where the Čerenkov detector is positioned, is limited.

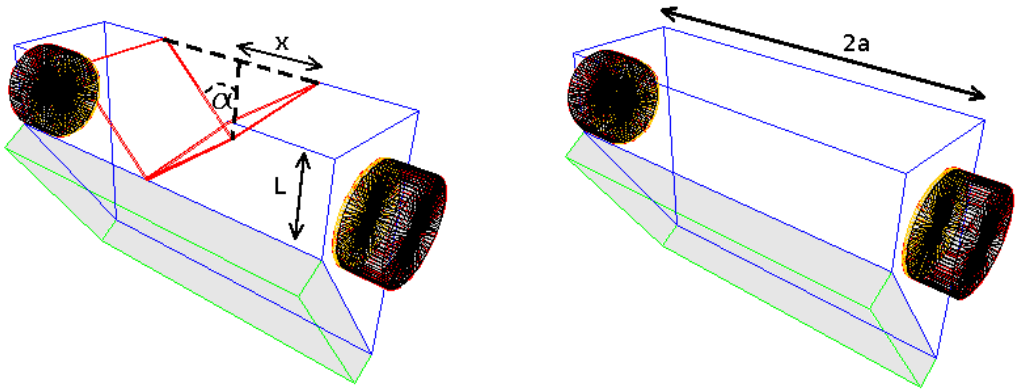

Figure 6.7: Two different types of the diffusive box in a single detector segment: with the mirrors cutting the rear part of the diffusive box into two symmetric halves (left) and without the mirrors (left). Different types of mirror plates have different angles between the plates covered with reflective foil (shown in red). The distance x determines the angle α between the mirrors.

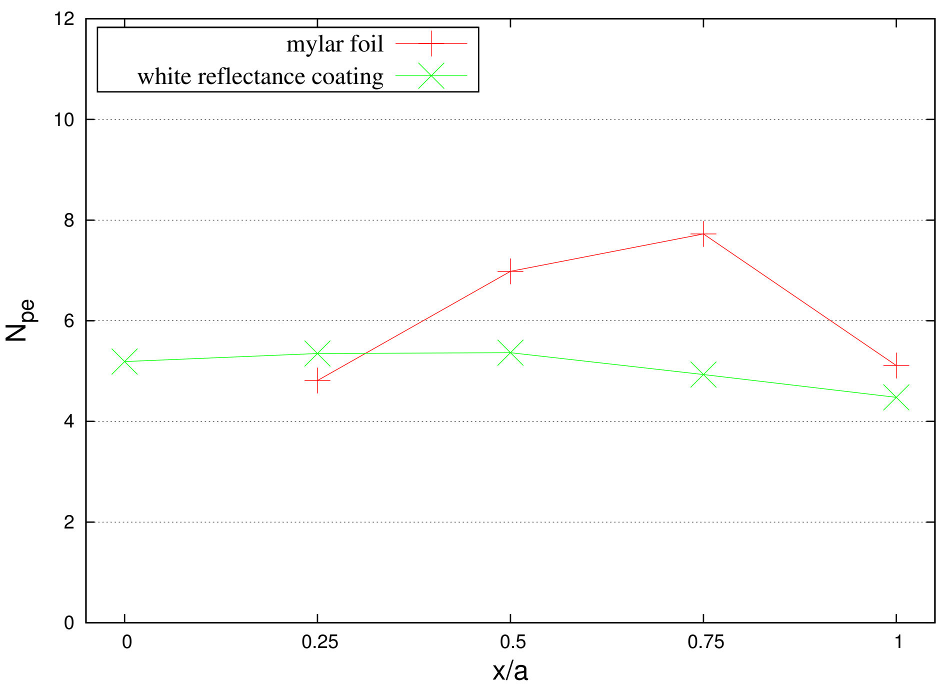

Figure 6.8: Simulated number of photo-electrons at different angles between the mirrors. The simulations also show the difference between the mirror plate covered with aluminized mylar foil or diffusely reflective coating. The set-up with $x = 0$ corresponds to the special case with no mirrors inside diffusive box.

The results are shown in Fig. 6.8 where we can see that the mirror plate with $x = 3a/4$ and covered with aluminized mylar foil gives the best photo-electron yield. Based on this results the angle of the mirror plate has been chosen.

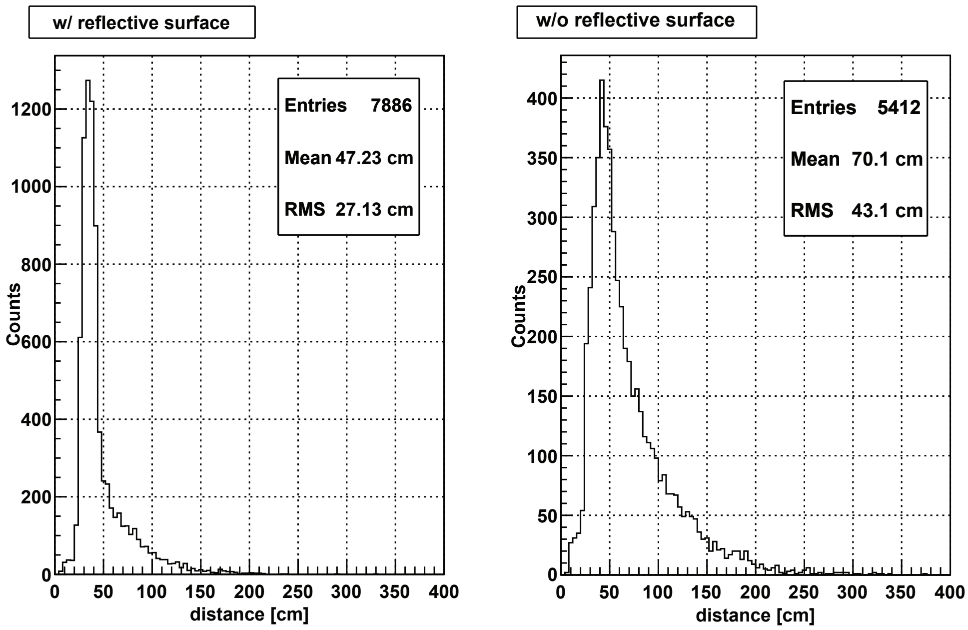

Figure 6.9: The simulated distance traveled by the photons seen in both types of the detector: with reflective surfaces inside (left) and without the reflective surfaces (right).

In case with no reflective surface 5.2 photons per particle are seen on average, but when the mirror plates were placed inside the box with $x = 3a/4$, 7.7 photons per particle are seen, which is an increase of about 48%. There are still other options of shapes and placements of the mirror plates, which depends mainly on the geometry of Čerenkov counter box. The G0 group found out that the best option for their set-up (with different geometry) is to have the mirror plates only in the lower half of the box, which corresponds to the half of our basic cell [107, 108]. The optimum placement of reflective surfaces Because we want to have PMTs on both sides, the mirrors should be placed symmetrically in the middle half of the diffusive box.

Another reason for choosing the diffusive box with the reflective surface is the distribution of the distance traveled by the photons detected, which is related to the time distribution of the photons. In Fig. 6.9 we see that in the case of no mirrors the photons travel longer distances before detection, whereas in the case with the mirrors, photons travel smaller distances on average, because they are reflected directly upwards or downwards into the PMTs. The distance distribution in this case is much narrower.

`SLitrani` also offers the capability to display the number of photons crossing forward from one material of the detector into the next one. The comparison of

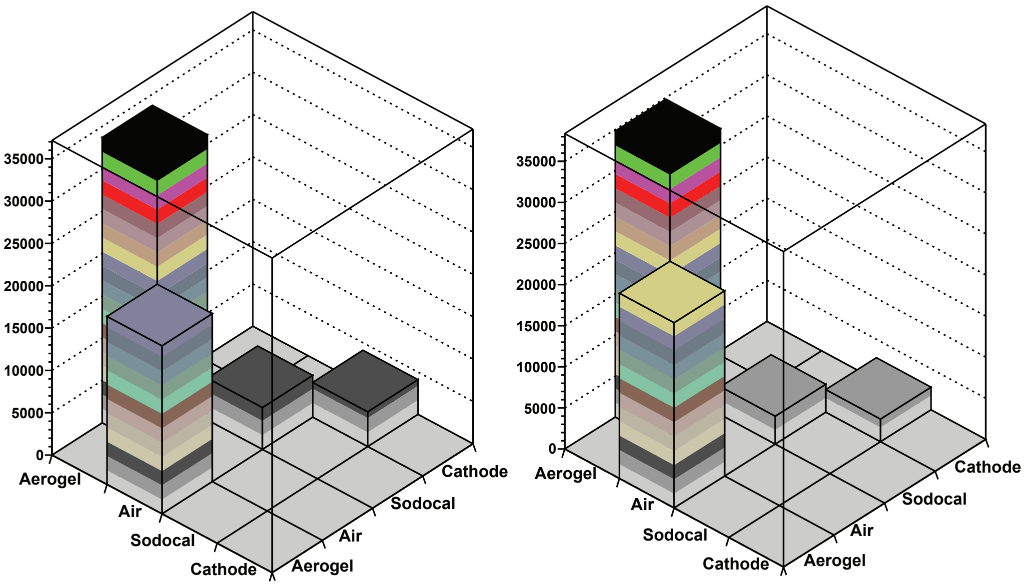

Figure 6.10: Simulated number of photons crossings forward from one material of the detector into the next one within one segment. Histograms correspond to two different types of the diffusive box: with reflective surface (left) and without the reflective surface (right).

the number of crossings has been made in a single segment for both types of the diffusive box (with and without the reflective surface). The results are shown in Fig. 6.10. In this picture the left plot corresponds to the box with reflective surfaces, and the right one to the box without the reflective surface. The photons have crossed from the material, labeled on the left bottom side of the plot, into the material, labeled on the right bottom side of the plot. The highest column in this picture corresponds to the number of crossings from the aerogel to the diffusive box, the column with the middle height corresponds to the number of crossings from the box back into the aerogel and other two smallest columns mean the number of crossings from the box into the particular photocathode through the PMT window, labeled as "sodocal". There is no crossing from the photocathode back into the box. The situation is approximately the same in both cases. The only difference is that there are more crossings from the diffusive box back to the aerogel in the case with no reflective surfaces, while the PMTs detect slightly more photons in the case with the reflective surfaces. The number of crossing in this figure is much larger than the number of the photons generated in the aerogel, because each photon can travel from one element to the next one several times.

6.3 Čerenkov counter for the experiment

The set-up of the Čerenkov detector in the experiments, described in my thesis, was slightly different from the set-up in previous chapter. In order to simulate the existing Čerenkov counter we need: (i) total thickness of aerogel $d = 3$ cm with 2 cm of BIC/BINP aerogel and 1 cm of Matsushita aerogel and (ii) R1250 PMTs attached to segments from 0 to 4 and SBA (super bialkali) R877-100 PMTs to segment 5, respectively. Since the main geometry is the same as in the previous chapters the simulation results can be downscaled properly and used for this set-up. The simulations have been performed with electron (positron) and pion beams within momentum range up to 1.5 GeV/c. These are the particle types and momenta the Čerenkov counter was exposed to in the experiments described in this thesis. The relative number of photo-electrons as a function of particle momentum is shown in Fig. 6.11.

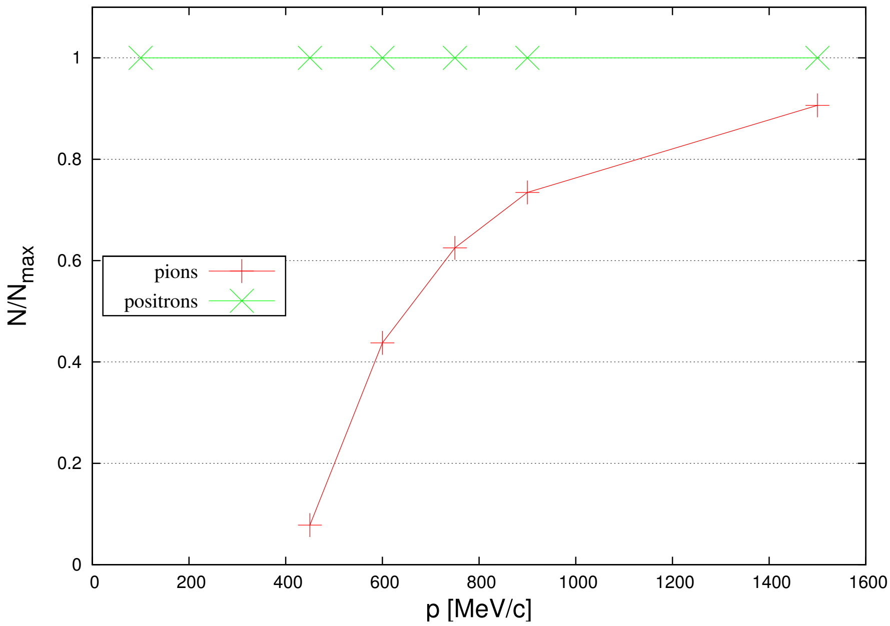

Figure 6.11: Simulated relative number of photo-electrons as a function of momentum for pions and positrons in the Čerenkov counter. Results follow the Eq. (5.19).

The simulated distribution of photo-electrons at fixed momentum at 720 MeV/c is shown in Fig. 6.12 for both particle types. In this figure we can see the deterioration of the light yield with pions compared to the positrons due to their non-zero mass which results in lower number of photo-electrons and thus lower efficiency of the counter. For this detector set-up the expected number of photo-electrons is $N_{\rm pe} \approx 4.3$ for pions and $N_{\rm pe} \approx 6.8$ for positrons, respectively. According to Fig. 5.2 the relative light yield for pions is $\approx 70\%$ while for positrons it is $\approx 100\%$, at this kinematics.

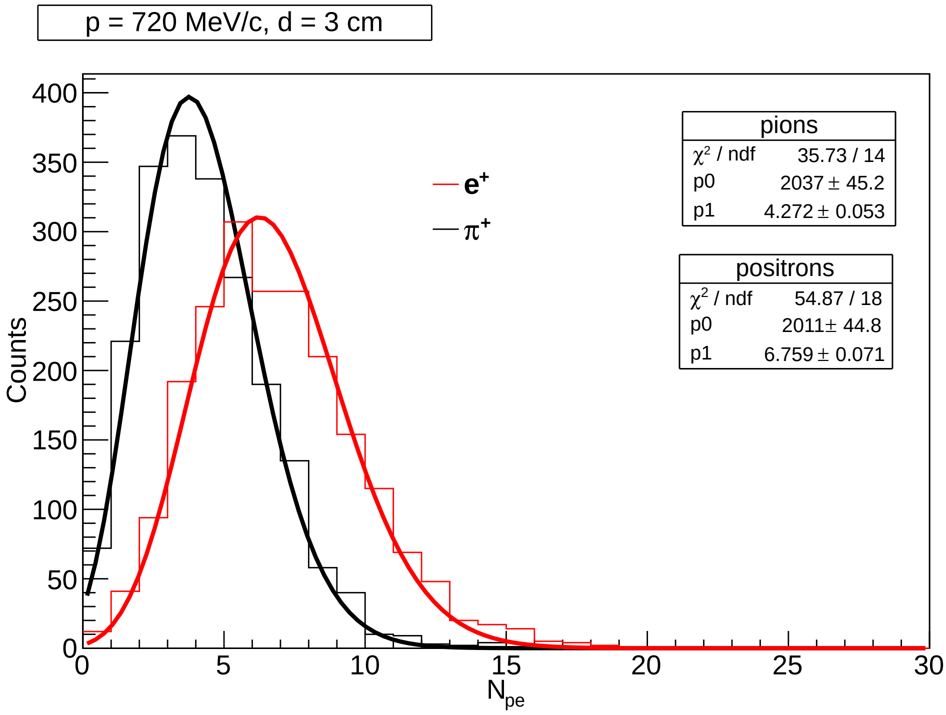

Figure 6.12: Simulated distribution of the total number of photo-electrons from all 12 PMTs for positrons and pions at 720 MeV/c momentum. Histograms are fitted with Poisson function with fit parameters indicated in the tables with p_1 being the mean value and p_0 the normalization factor.

This histogram can be compared to the ADC SUM spectra measured in the experiment (see Sec. 7.4 and 7.5). If the threshold is set to 1.5 photo-electrons, meaning that one-photo-electron events and below are treated as noise or no signal, the simulated efficiency for the Čerenkov counter is 97% for positrons and 86% for pions.

With this set-up we can check the number of photons crossing forward from one material of the detector into the next one. In Fig. 6.13 (top left) we see the number of transitions between the Matsushita aerogel in the bottom layer and BIC/BINP aerogel in the top layer. The largest column corresponds to the transitions from BIC/BINP aerogel to the diffusive box. There are also some transitions from the top layer of aerogel to the bottom layer. These are the photons scattered in the diffusive box back into the aerogel box and photons backscattered in the BIC/BINP aerogel. In the same figure the top right plot shows the number of reflections inside the material on its surface in contact with another material. We see that most of the photons are reflected inside the aerogel on the surface facing the diffusive box due to the total reflection. `SLitrani` also gives the possibility to monitor the number of absorptions and reflections on the wrappings of the materials in the detector, as shown in the bottom plots of Fig. 6.13. We see that most of the photons are

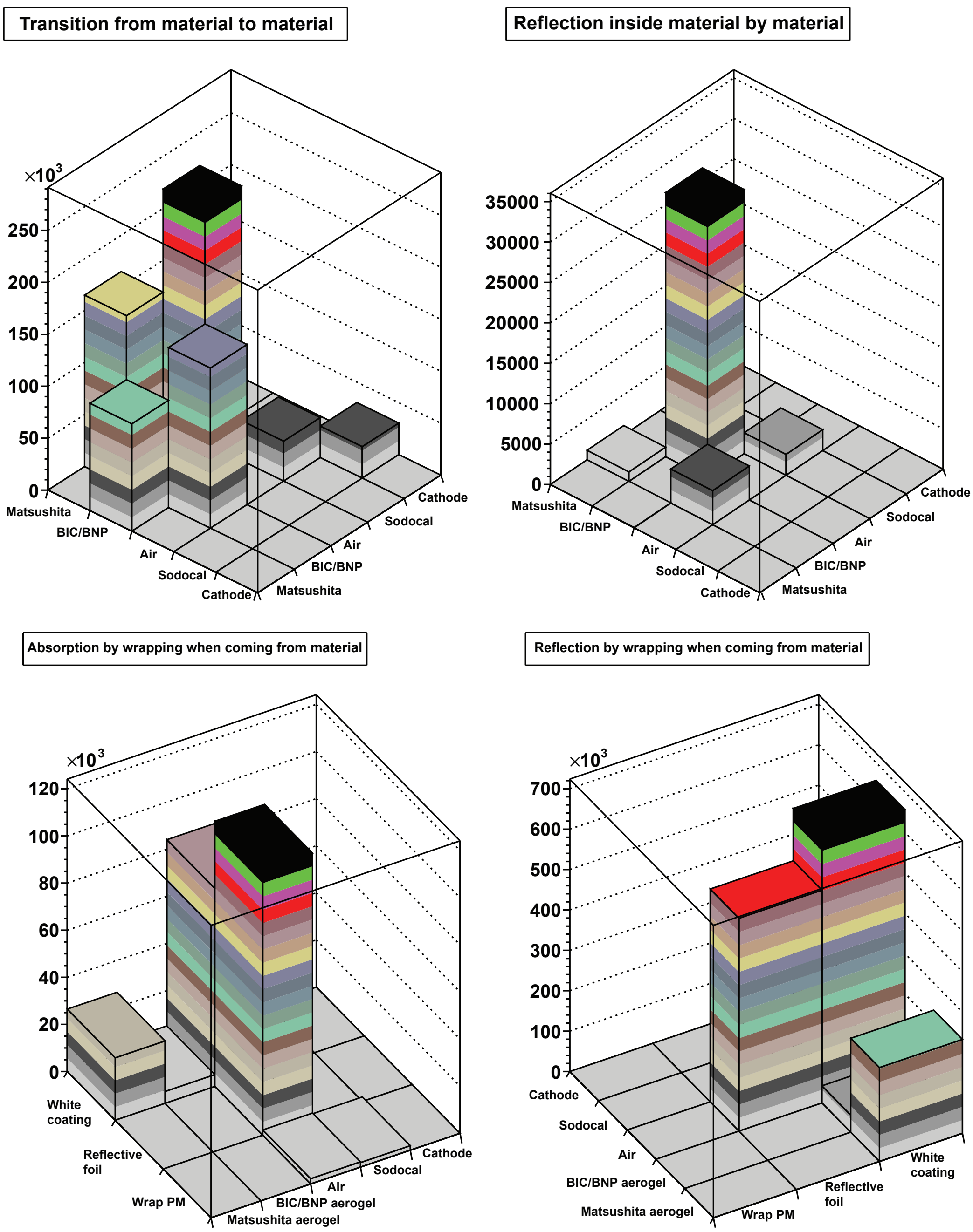

Figure 6.13: Simulated transition, reflection and absorption of photons between/on different detector materials and surfaces.

absorbed in the mylar foil, because it has larger absorption than the white diffusive coating. We can also see that more photons are reflected from the white diffusive paint in the lower part of the aerogel box, filled with Matsushita aerogel, compared

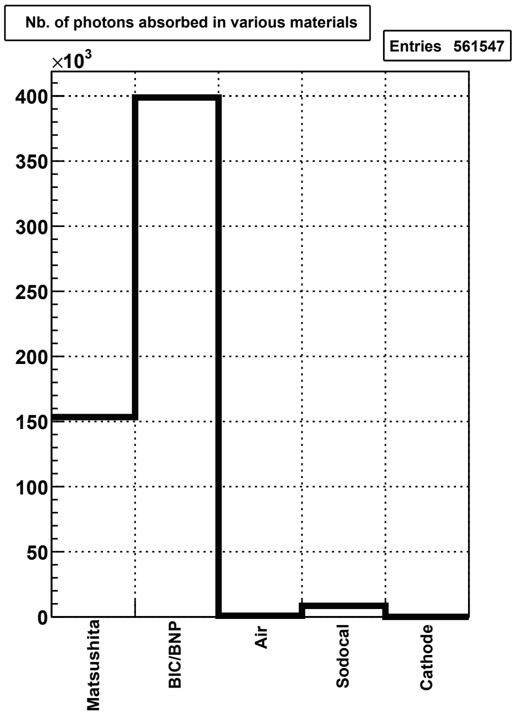

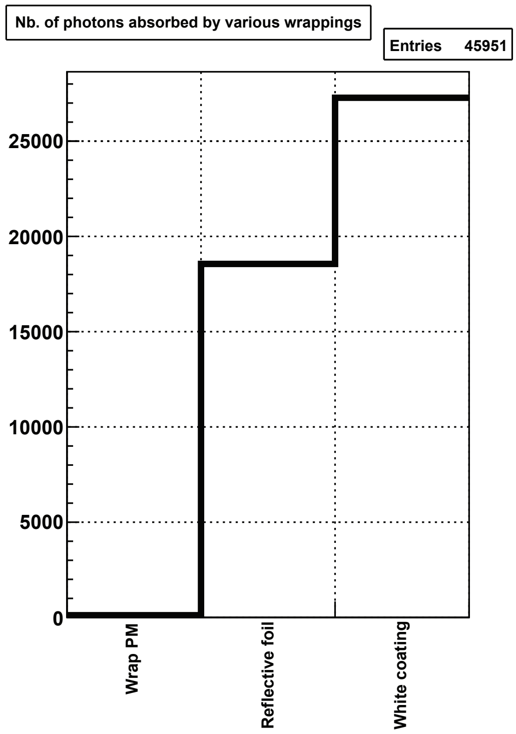

Figure 6.14: Simulated number of absorptions of photons in different detector materials (left) and wrappings (right).

to the number of reflections on the upper part. This is because the BIC/BINP aerogel tiles have a larger scattering length, hence the probability for photons to be scattered out from their original direction is smaller. In this figure "Wrap PM" refers to the wrapping inside the PM tube covering the entrance window glass from the side.

It is interesting to know in which material or wrapping inside the Čerenkov detector most of the generated photons are absorbed. The simulated number of photon absorptions is shown in Fig. 6.14. Here we can see that most of the photons are absorbed inside aerogel because of short absorption length (in comparison with air) and large thickness (in comparison with PMT window). Even though the BIC/BINP aerogel has a larger absorption length than the Matsushita aerogel, there are more photons absorbed due to larger thickness or BIC/BINP aerogel. We can also see that more photons are absorbed in the white diffusive coating than in the reflective foil, which has higher absorption probability. This is because the larger inner surface of the diffusive box is covered by the white coating, resulting in more absorptions in total. A few photons are also absorbed in the wrapping of the PMT window. Photons absorbed by the photocathode are not considered as absorbed but as detected. That is why there are no events in the bin that corresponds to the photocathode, but `SLitrani` keeps considering it as one of the materials.

6.4 Spread of photons

Since the inner walls of the Čerenkov counter separate only individual compartments of the diffusive box, some of the Čerenkov photons might escape to the neighboring segment through the aerogel box, especially if the particle crosses the radiator material near the border of the segment.

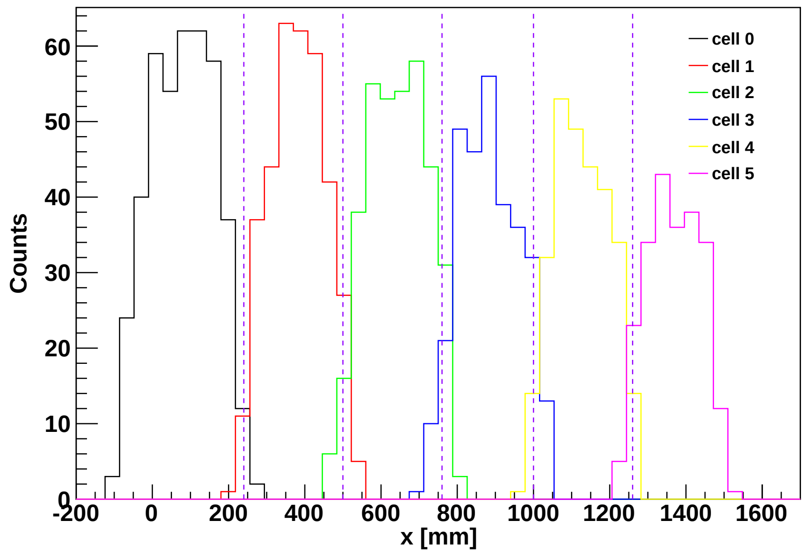

Figure 6.15: Simulated distribution of particle coordinates in aerogel plane that correspond to detection of more than two photo-electrons in the individual segment. In this figure the physical borders between the segments are shown with dashed vertical lines, which is in a good agreement with the real dimensions as the distance between the inner walls is 250 mm.

To see how much the inner walls prevent the photons from passing from one segment into another I have simulated the detector exposed to relativistic particles reaching the detector at given coordinates and at specific angles, and observed the number of detected photons in all twelve photocathodes. The x-coordinate in the aerogel plane of a particle that fired more than two photo-electrons in a particular segment (top plus bottom photocathode) was proclaimed as the coordinate that corresponds to that segment. By comparing the distribution of these x-coordinates for all segments we can see the regions covered by each segment as well as the areas between them where the regions overlap, see Fig. 6.15. If the walls would separate the segments completely there would be no overlap regions. This means that the particles crossing the aerogel near the inner walls generate Čerenkov radiation which is spread into two segments.

I have also add up the number of photo-electrons from top and bottom photocathode and analyzed the total photo-electron distribution in each segment. The

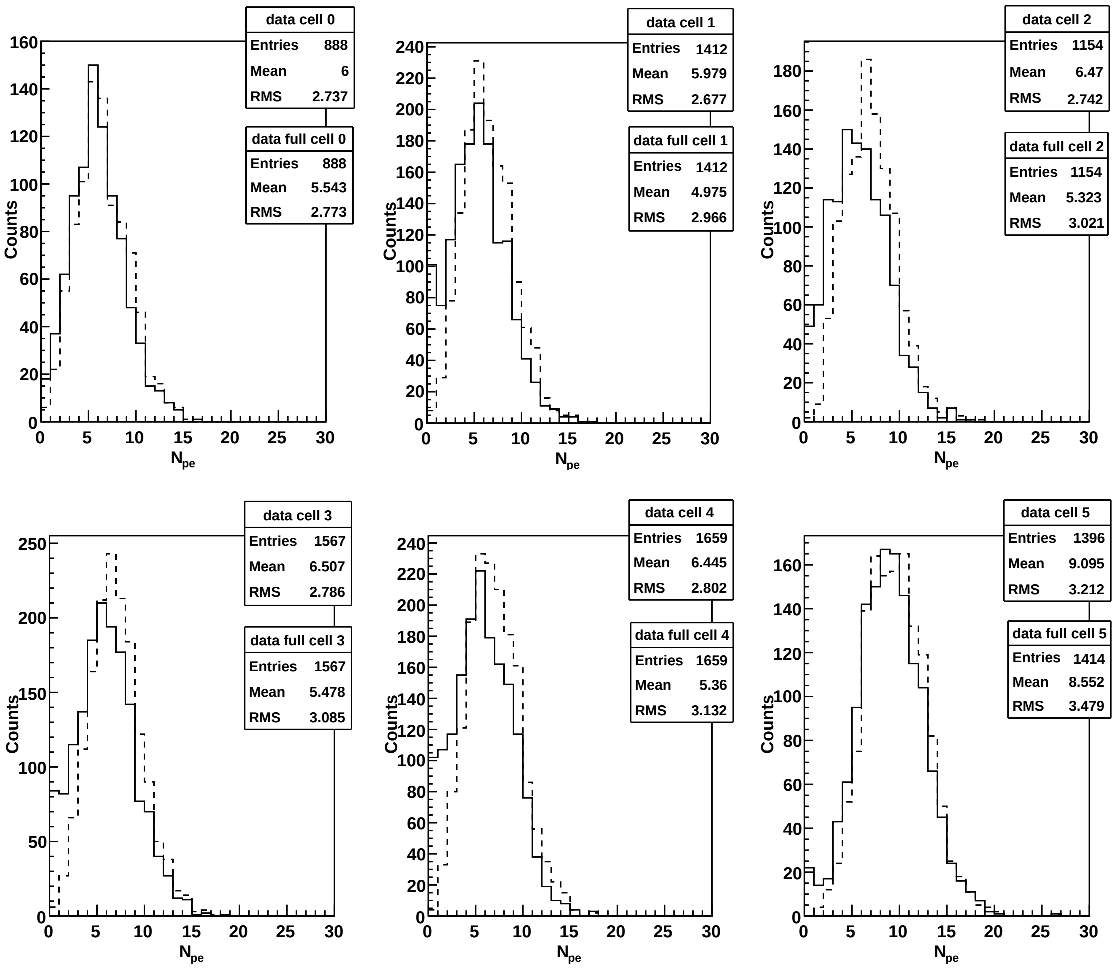

Figure 6.16: Simulated photo-electron distribution in individual segments with a cut on the x-coordinate in the aerogel plane, used to select the complete segment area (solid line) and to select the area deep inside the segment (dashed line). The average number of photo-electrons in segment 5 is larger due to the SBA photocathodes used in the corresponding PMTs.

simulation was performed with two different cuts on the x-coordinate in the aerogel plane: first with the coordinates that correspond to the full width of each segment, $x^i_{\min} < x < x^i_{\max}$, where $x^i_{\min}$ and $x^i_{\max}$ are the coordinates of the inner walls enclosing segment i, as denoted by vertical dashed lines in Fig. 6.15, and then with x coordinates that are deep inside each segment, i.e. 70 mm from the walls, $(x^i_{\min} + 70) < x < (x^i_{\max} - 70)$. In Fig. 6.16 the photo-electron distribution for each segment is shown with both cuts on x-coordinate, where solid lines correspond to the complete area of each segment taken into account, while dashed lines correspond to the inner area of each segment. We see that the histograms with full areas taken into analysis have more events at lower number of photo-electrons, compared to the histograms with events deep inside that area. This means that some of the photons, generated near the borders between the segments, escape through the aerogel box into the neighboring segment, which results in a lower average number of photo-electrons per cell. For this reason I have also chosen the cuts on x-coordinates in the analysis of the experimental data for each segment away from the walls. We can also see that segment 5 has a much higher average number of photo-electrons due to the PMTs with SBA photocathodes possessing higher quantum efficiencies.

`SLitrani` also offers the possibility to see the tracks of generated Čerenkov photons. In Fig. 6.17 tracks of all photons, generated by one relativistic particle inside segment 3 are shown. We can see that some of the photons escape through the aerogel layer into the neighboring segments, especially if the particle is closer to the inner wall.

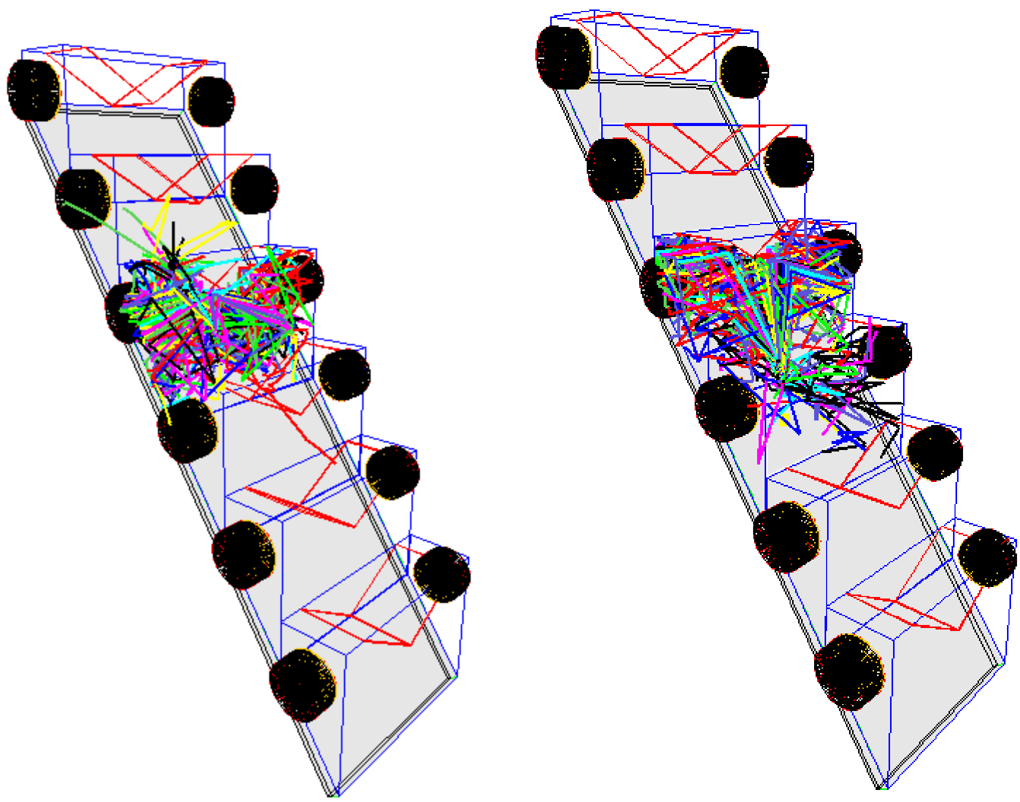

Figure 6.17: Simulated tracks of Čerenkov photons generated by one relativistic particle. Left: particle crossing the aerogel layer near the center of segment 3, right: particle crossing the aerogel layer below segment 3 but much closer to the neighboring segment 2.

CHAPTER 7

Data analysis and results

7.1 Test with cosmic rays

A preliminary efficiency test of the aerogel Čerenkov counter was performed with cosmic rays. Due to geometrical restrictions, The detector was mounted into the KAOS spectrometer in a rather inconvenient orientation for this test, because the aerogel plane is positioned vertically inside the spectrometer. Such orientation of the aerogel gave us a very small cosmic rate; less than 1 Hz.

The detector was sandwiched between two scintillator walls, as shown in Fig. 5.20 in Ch. 5. If the signal is detected in both ToF walls within a certain time window the trajectory of the particle must have passed also the Čerenkov counter. This configuration enabled us to record only those particles that crossed the aerogel. The DAQ system was a simplified version of the standard DAQ system, with the trigger condition set to: hit in any H paddle AND hit in any G paddle.

Cosmic ray at ground level is mainly composed of muons, so the threshold momentum for $n = 1.055$ aerogel is ≈ 315 MeV/c. The time-of-flight data between the scintillator walls was used to select high-energy cosmics. In my analysis I have chosen the events with velocity $\beta = v/c$ between 0.8 and 1.1. For better background subtraction an additional cut on energy-loss has been used with events between 1.5 MeV/cm and 3.0 MeV/cm in wall G and 1.3 MeV/cm and 3.0 MeV/cm in wall H, as shown in Fig. 7.1.

During the test with the cosmics not all aerogel box was filled with the radiator, due to the lack of aerogel tiles. In this set-up the segment 0 was filled only partially, where most of the aerogel plane was uncovered. This inefficient part of detector was disregarded in the analysis by excluding all events that have passed segment 0.

A typical pulse integral spectrum summed over the phototubes from segments 1 to 5 (in calibrated ADC channels) is shown in Fig. 7.2. The mean value of this ADC SUM spectrum (without the pedestal) is 7.6 photo-electrons.

One of the most important properties of each detector is its efficiency. It is defined as the number of events detected by the Čerenkov counter above a certain ADC threshold value or cut condition divided by the number of all detected events.

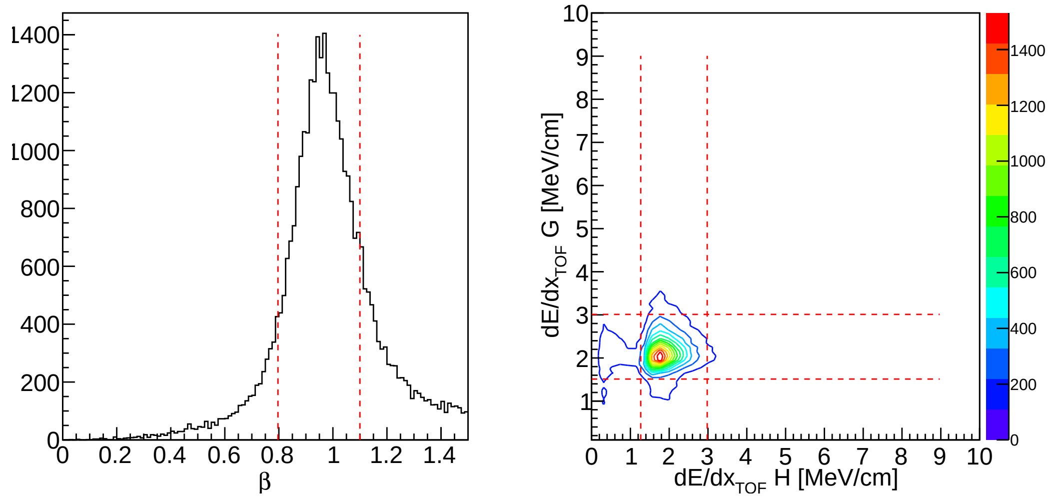

Figure 7.1: Velocity and Energy-losses of cosmics between both scintillator walls. High-energy cosmics were chosen by simple cut on their velocity $0.8 < \beta < 1.1$, with additional cut on energy-losses.

Because no discriminator was included into the electronic chain, the threshold is set manually by software to distinguish between signals produced by Čerenkov photons from noise. The efficiency is calculated from the ADC spectrum as:

$$eff = \frac{\text{Nr. of events above ADC cut}}{\text{Nr. of events w/o ADC cut}}. \tag{7.1}$$

For example if we put the ADC cut condition to 500 which corresponds to 2.5 photo-electrons, as shown in Fig. 7.2 by the red dashed line, the efficiency with cosmics is ≈ 90%.

During the analysis I was choosing different ADC thresholds to see how the efficiency changes as a function of the cut condition. In Fig. 7.3 the efficiency for cosmics is shown at different thresholds. In this figure a clear drop of efficiency is seen if complete detector area is taken into account (black line), due to the lack of aerogel in segment 0. We can also see a small increase of the efficiency if only high-energy cosmics are selected by applying dE/dx cut.

If one photo-electron events are considered as signals generated by cosmic particles (so-called true events), the threshold can be set to 0.5 p.e. By taking all conditions into account (segment 0 excluded and proper dE/dx cut) and considering 1 p.e. signals as true events the efficiency of the Čerenkov counter with cosmics is ≈ 95%.

In this aerogel counter performance test I did not care about the particle identification and their path trajectories. This was just a simple test with relativistic particles, regardless of their hit position in the aerogel plane.

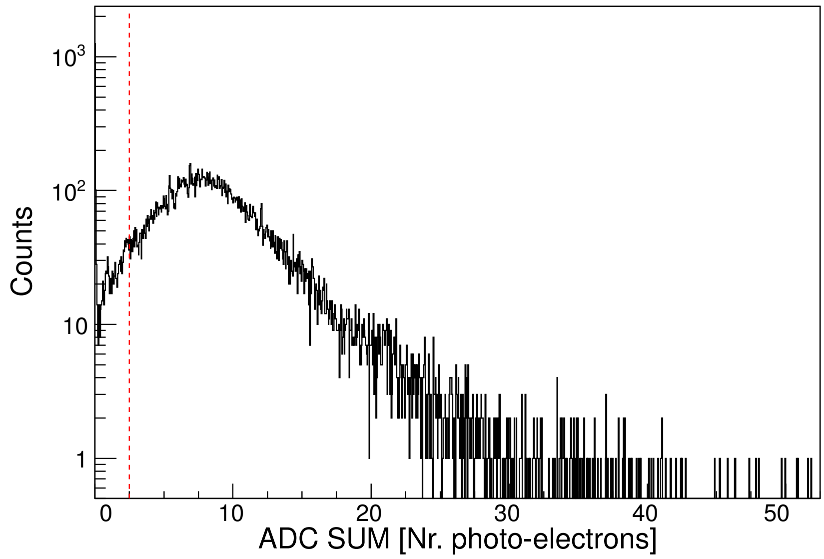

Figure 7.2: Typical ADC SUM spectra of Čerenkov counter. The pulse integral distribution is derived as sum of the PMT signals from segments 1 to 5. The cut condition for efficiency measurement is shown by dashed red line (placed arbitrarily at 2.5 photo-electrons in this plot).

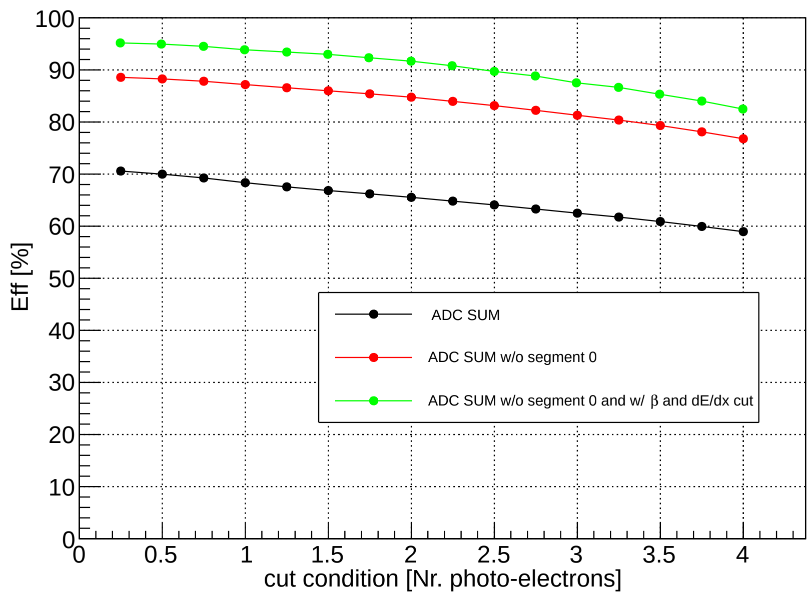

Figure 7.3: The efficiency of the Čerenkov counter with cosmics at different ADC threshold values and other cut conditions.

7.2 Particle tracking

For the analysis with the particles produced by physical reactions in the experimental hall it is very important to have a proper particle tracking information, particularly if one wants to analyze only a section of the Čerenkov detector or just wants to see the particle distribution over the aerogel plane.

Each segment of the Čerenkov counter can be analyzed as one independent individual detector, even though some Čerenkov photons might escape to the neighboring cell. This can be done by knowing the exact hit position for each particle on the aerogel plane. Particle trajectories are measured by two MWPCs, as described in Subsection 4.1.1 or by two ToF walls. The trajectories are determined by the coordinates x and y in dispersive and non-dispersive direction in the MWPC plane, and by the Cartesian angles θ and ϕ relative to the normal to the MWPC plane in dispersive and non-dispersive directions, respectively. From measured particle coordinates (x, y) and angles (θ, ϕ) the particle position (x', y') in any plane at distance D from the chamber (in space without magnetic field) can be calculated by simple linear extrapolation:

$$\begin{aligned} x' &= x_0 + D\tan\theta, \\ y' &= y_0 + D\tan\phi, \end{aligned} \tag{7.2}$$

where x_0 and y_0 are offset coordinates. This is schematically shown in Fig. 7.4. In my analysis I have extrapolated the coordinates from L chamber (the one situated closer to the Čerenkov detector) to the aerogel plane, which was at distance D = 256 mm. The offset coordinates were set so that $y' = 0$ corresponds to the mid-plane position and $x' = 0$ corresponds to the low-momentum corner of the aerogel box.

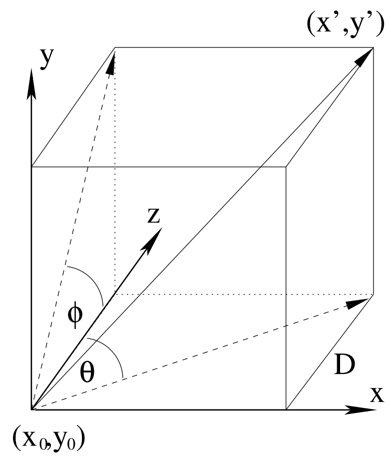

Figure 7.4: Schematic presentation of Cartesian angles θ and ϕ. Solid arrow is particle trajectory and dashed arrows its projections. Distance between start-point plane and end-point plane is D.

By extrapolating the particle coordinates to the aerogel plane only specific Čerenkov counter segment or area can be analyzed by excluding all events with trajectories outside the area covered by that segment. This is done by applying a so-called XY-cut. The cuts in x and y direction corresponds to the physical width and height of the aerogel area in each segment, which is $W \times H = 250 \times 450$ mm^2.

It is mandatory to cross-check if the relativistic particles with coordinates in aerogel plane within the area covered by particular segment have also generated the signal above the pre-defined threshold value in that segment. A cut condition is defined so that the sum of the ADC values from top and bottom PMT from segment nr. i is above the threshold:

$$\mathrm{ADC}_i = \mathrm{ADC}_i^{\mathrm{top}} + \mathrm{ADC}_i^{\mathrm{bot}} > thr, \tag{7.3}$$

where thr is set to 1000 (in ADC channels) or 5 photo-electrons. By applying this cut to the XY plot in aerogel plane for a specific segment in general only the events within the area covered by that cell remain. The events in XY aerogel plane that satisfy the cut condition (7.3) for any of the six segments are shown by different colors in Fig. 7.5. Unfortunately the segment 0 is out of the MWPC acceptance so the evens within that area can not be shown. It is clearly seen that the boundaries between different colors correspond well to the physical boundaries of the segments in x direction as the width of each cell is 250 mm.

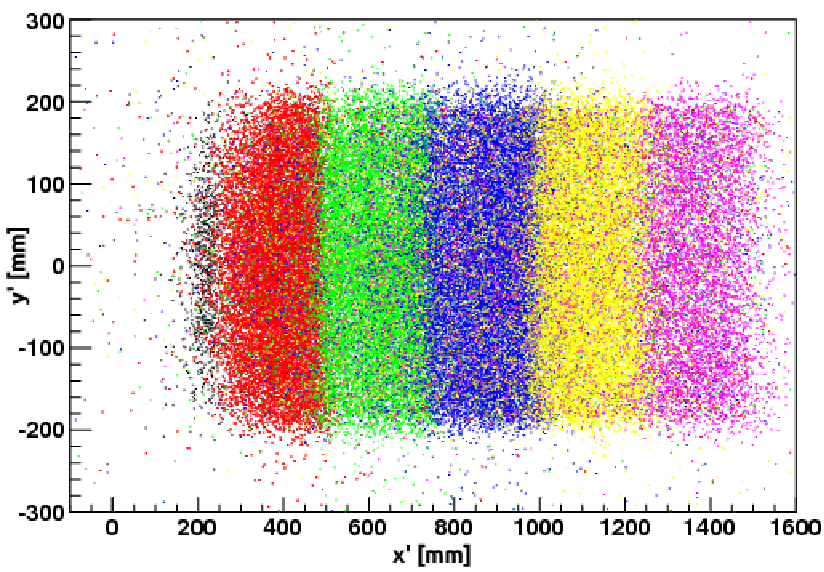

Figure 7.5: The reconstructed $x'y'$-position from the MWPC in the aerogel plane. The events above the threshold value for particular segment are shown by different colors, so the area covered by each cell is clearly seen. The width of the color strip corresponds to the physical width of the segments which is 250 mm. Cell 0 is out of MWPC acceptance.

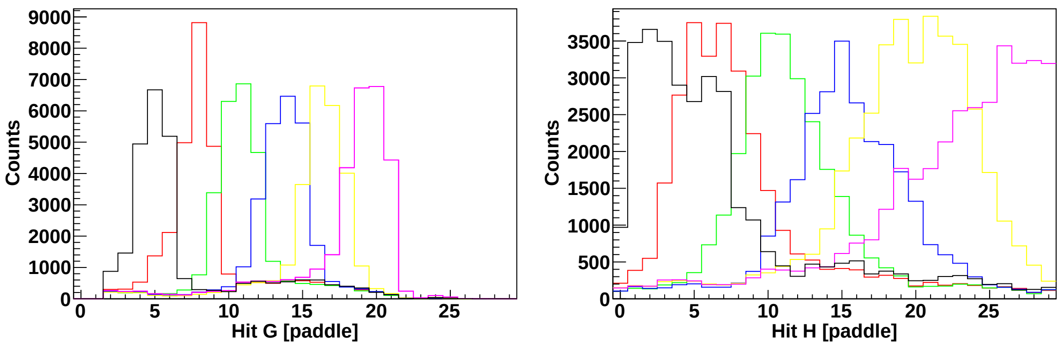

Figure 7.6: The hit distribution in G and H wall for each segment. The events above the threshold value for particular segment are shown by different color, so the set of paddles corresponding to each cell is clearly seen. Because the height of each histogram is not relevant in this figure, the histograms are normalized to approximately the same height for better comparison of hit distributions.

Despite strict threshold condition there is still some background, as seen in Fig. 7.5, due to MWPC small inefficiency. For more reliable particle tracking an additional cut on scintillator paddles is included. This is done in a similar way as with the chambers. By applying the cut condition (7.3) for a specific segment to the hit distribution in the G and H wall in general only those paddles remain that lie in the trajectory path of a particle producing a signal above the threshold in that segment. In Fig. 7.6 the hit distribution in both ToF walls is shown with the threshold condition applied to all six segments. The aerogel plane is located ≈ 85 mm from the G wall, so only 3 or 4 paddles correspond to each segment by applying a threshold cut on G hit distribution. Due to the spread of the particles in the dispersive direction and larger distance between aerogel plane and the second wall, many more paddles from the H wall satisfy the threshold cut condition, as seen in Fig. 7.6 by comparing the width of distributions in both ToF counters. In this figure it is clearly seen which set of paddles corresponds to which Čerenkov segment. All sets of paddles are in fine agreement with the expectation, according to the relative position of detectors and average trajectory angle. By applying a cut on paddles a selection in the horizontal (dispersive) direction only can be done. For the analysis of the individual segment a cut on proper set of paddles is sufficient, because the height of the aerogel plane has been designed to be the same as the height of the ToF walls.

The efficiency of the MWPC deteriorates at higher beam-currents so a different method is needed to get the reconstructed coordinates in the aerogel plane. The second method to get the x, y coordinates and θ, ϕ angles that define the trajectory uses the information from ToF walls only. The so-called x_{TOF} coordinate in both walls is retrieved from the cluster's center of mass, using the signal strength information from each paddle. The resolution is almost comparable to the MWPC resolution, unless only one paddle has fired. The y_{TOF} coordinate is retrieved by the difference between the scintillator photon arrival times in the top and bottom PMTs. For the analysis of data with higher beam-currents x'_{TOF} coordinate is used.

In my analysis I have used a combination of X and paddle cuts to get more reliable tracks, while the cut in vertical direction was not so important for my analysis. To select the events corresponding to cell i only, this cut condition has been used:

$$\mathrm{Cell}_i = [X_i^{\mathrm{min}} < x'_{(\mathrm{TOF})} < X_i^{\mathrm{max}}] \oplus [G_i^{\mathrm{min}} < \mathrm{hitG} < G_i^{\mathrm{max}}] \oplus [H_i^{\mathrm{min}} < \mathrm{hitH} < H_i^{\mathrm{max}}], \tag{7.4}$$

where the symbol $\oplus$ denotes logical AND between the conditions in brackets, hitG and hitH correspond to the paddle hit by the particle in the wall G and H, $G_i^{\mathrm{min/max}}$ and $H_i^{\mathrm{min/max}}$ are the minimum/maximum paddles in the wall G and H that correspond to the segment i, and $X_i^{\mathrm{min/max}}$ are the coordinates of physical boundaries for segment i. The values used in my analysis are shown in Table 7.1.

Table 7.1: The boundary paddles in wall G and H that correspond to each segment and the coordinates of physical boundaries for each segment. This values have been used in my analysis for selection of tracks in the individual segment.

Segment	G^{min}	G^{max}	H^{min}	H^{max}	X^{min} [mm]	X^{max} [mm]
0	4	6	1	7	0	250
1	8	9	4	9	250	500
2	10	12	8	14	500	750
3	13	15	12	19	750	1000
4	15	18	17	23	1000	1250
5	19	21	20	29	1250	1500

This condition (7.4) is schematically shown in Fig. 7.7 with particle trajectories in Kaos hadron arm. In this figure the trajectory nr. 1 is within the limits that correspond to segment nr. 4, so the condition (7.4) for Cell_4 is satisfied. On the other hand the trajectory nr. 2 is only within the limits in the G Wall, and the condition (7.4) is not satisfied completely for any of the segments. Thus the second track is rejected and treated as background or non-physical event.

The condition for the signal to be identified as "above the detection threshold" for the entire Čerenkov detector is defined as: the strength of the signal in the segment, intersected by the particle trajectory, has to be above the given threshold:

$$\begin{aligned} &[\mathrm{Cell}_0 \oplus \{\mathrm{ADC}_0 > \mathrm{ADC}_{\mathrm{thr}}\}] \otimes [\mathrm{Cell}_1 \oplus \{\mathrm{ADC}_1 > \mathrm{ADC}_{\mathrm{thr}}\}] \otimes \\ &[\mathrm{Cell}_2 \oplus \{\mathrm{ADC}_2 > \mathrm{ADC}_{\mathrm{thr}}\}] \otimes [\mathrm{Cell}_3 \oplus \{\mathrm{ADC}_3 > \mathrm{ADC}_{\mathrm{thr}}\}] \otimes \\ &[\mathrm{Cell}_4 \oplus \{\mathrm{ADC}_4 > \mathrm{ADC}_{\mathrm{thr}}\}] \otimes [\mathrm{Cell}_5 \oplus \{\mathrm{ADC}_5 > \mathrm{ADC}_{\mathrm{thr}}\}], \end{aligned} \tag{7.5}$$

where $\mathrm{ADC}_{\mathrm{thr}}$ is the detection threshold value, ADC_i is the sum of ADC value from top and bottom PMT, and symbol $\otimes$ denotes logical OR between the statements. The condition (7.5) states that first we check which segment was intersected by the particle with condition (7.4) and whether the signal in this segment is above the detection threshold. If both logical statements are true for any of the segment the particle, generating the signal, is treated as a particle above the Čerenkov threshold. The signals identified as "below the detection threshold" follow the same definition, where only symbol ">" in Eq. (7.5) is replaced by "<".

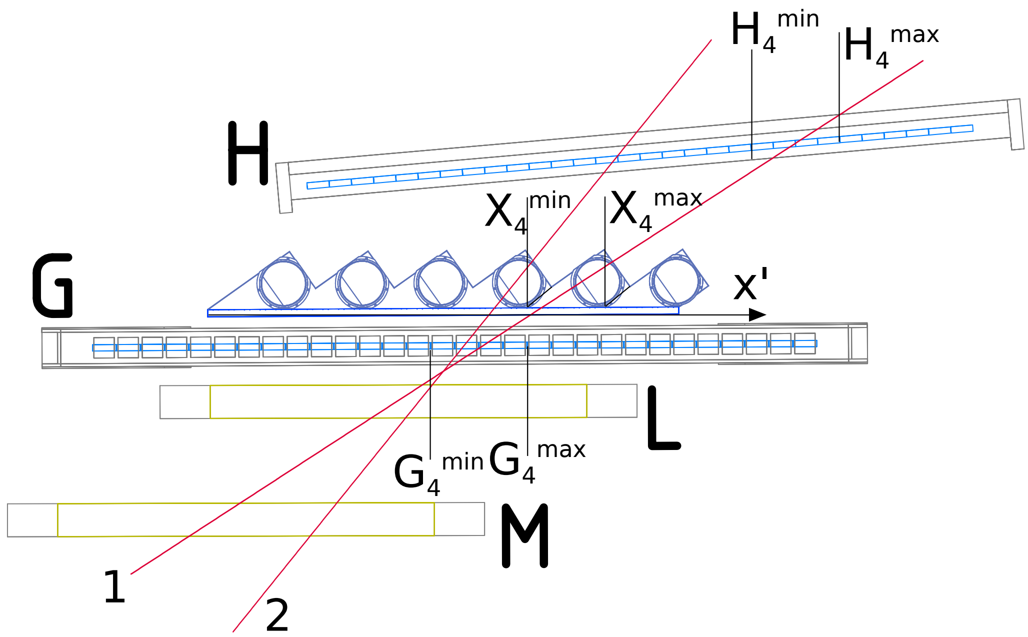

Figure 7.7: The Kaos hadron arm with two particle trajectories. The trajectory that corresponds to specific cell must be within the limits defined by paddles in ToF walls and coordinates in aerogel plane. First trajectory is within the limits that correspond to segment nr. 4, while the second one does not correspond to any segment condition.

There is another and a bit more complicated method for identification of particles that are above or below the detection threshold (not used in my thesis). Additionally to condition (7.4) the y' coordinate in aerogel plane is checked. If the reconstructed y' coordinate is $\gtrsim 100$ mm above (or below) the mid-plane, the ADC value from only top (or bottom) PMT from corresponding segment is used: $\mathrm{ADC}_i = \mathrm{ADC}_i^{\mathrm{top}}(\mathrm{ADC}_i^{\mathrm{bot}})$. Otherwise (for near mid-plane tracks) the sum from both PMTs is taken into analysis: $\mathrm{ADC}_i = \mathrm{ADC}_i^{\mathrm{top}} + \mathrm{ADC}_i^{\mathrm{bot}}$.

Furthermore the detection threshold condition itself is generalized. Instead of a simple "yes-no" cut condition a form of flipped Fermi distribution is used:

$$F(\mathrm{ADC}_i) = \frac{\mathrm{ADC}_{\mathrm{max}}}{\exp(-(\mathrm{ADC}_i - \mathrm{ADC}_{\mathrm{thr}})/\mathrm{ADC}_{\mathrm{wid}}) + 1}, \tag{7.6}$$

where $\mathrm{ADC}_{\mathrm{thr}}$ is now the value where $F(\mathrm{ADC}_i)$ reaches 50% of the pre-defined maximum, $\mathrm{ADC}_{\mathrm{max}}$. So for very low ADC_i values the condition (7.6) is $F(\mathrm{ADC}_i) \approx 0 * \mathrm{ADC}_{\mathrm{max}}$, while for very high values it is $F(\mathrm{ADC}_i) \approx 1 * \mathrm{ADC}_{\mathrm{max}}$. Therefore the $\mathrm{ADC}_{\mathrm{max}}$ gives the total strength of the cut. The $\mathrm{ADC}_{\mathrm{wid}}$ defines how fast shall the function $F(\mathrm{ADC}_i)$ rise. It is defined as the difference of the ADC_i value where the function reaches 95% and 50% of its maximum.

In the end the function $F(\mathrm{ADC}_i)$ enters the final condition for the signal to be identified as "above the detection threshold" for entire Čerenkov detector. The condition (7.5) becomes:

$$\begin{aligned}
&[\mathrm{Cell}_0 \oplus \{F^2(\mathrm{ADC}_0) > 1\}] \otimes [\mathrm{Cell}_1 \oplus \{F^2(\mathrm{ADC}_1) > 1\}] \otimes \\
&[\mathrm{Cell}_2 \oplus \{F^2(\mathrm{ADC}_2) > 1\}] \otimes [\mathrm{Cell}_3 \oplus \{F^2(\mathrm{ADC}_3) > 1\}] \otimes \\
&[\mathrm{Cell}_4 \oplus \{F^2(\mathrm{ADC}_4) > 1\}] \otimes [\mathrm{Cell}_5 \oplus \{F^2(\mathrm{ADC}_5) > 1\}].
\end{aligned} \tag{7.7}$$

Like before, the condition above states that we check which segment was intersected by the particle and whether the square of condition (7.6) is greater than unity. The signals identified as "below the detection threshold" follow the same definition, where only the distribution (7.6) is flipped again or the symbol ">" in Eq. (7.7) is replaced by "<".

7.3 Particle identification

For the tests in the experimental hall a proper particle identification (PID) has been performed to analyze the efficiency of the Čerenkov detector for one particle type only. Particles are identified by their energy losses, dE/dx, and velocity, $\beta = v/c$.

Because the MWPCs become inefficient at higher beam-currents two methods exist for measuring the particle trajectories which are mandatory for dE/dx and β evaluation. The velocity, is calculated from the time difference between the scintillator walls and the path length in between. The path length can be measured either by extrapolating the trajectory from the MWPC plane to the scintillator walls from known coordinates and angles measured by the MWPCs. The other possible method is based on data from ToF walls only: the path length is evaluated from the measured coordinates and angles in ToF walls. The procedure for measuring the energy-losses per unit length also exploits two methods for particle trajectory measurements. The energy-loss is retrieved from the signal strength in the ToF walls while the effective path length through the scintillator material is evaluated either from the trajectory measurement by MWPCs or by ToF walls.

All physical variables that use only the information from the scintillator walls are labeled with "TOF" in contrast to variables that use the combination of data from

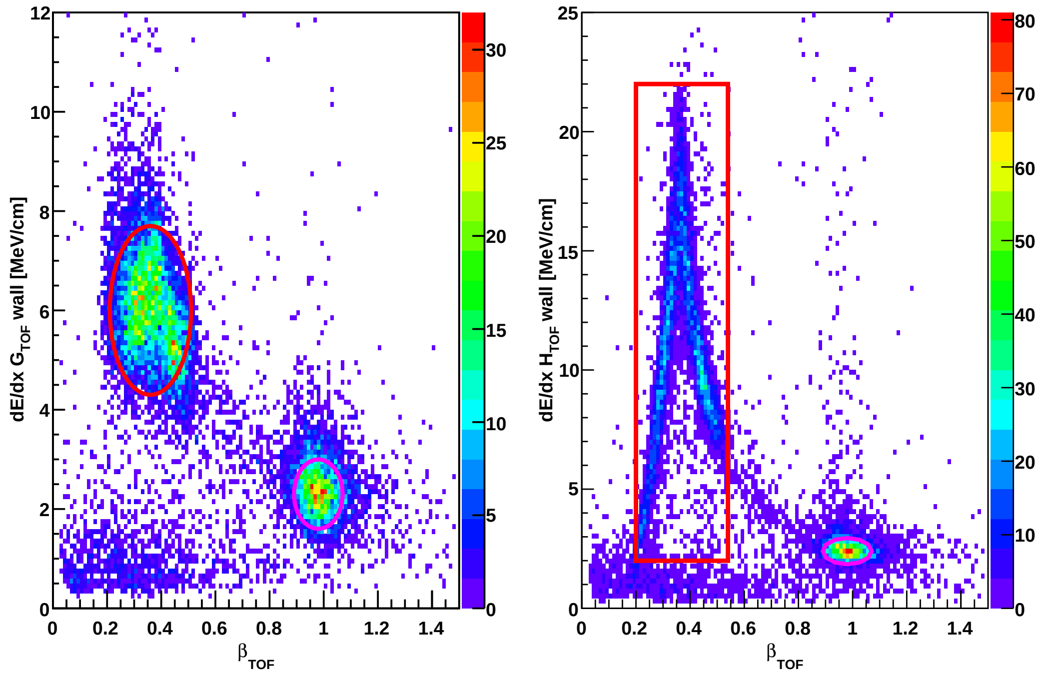

Figure 7.8: Particle identification is done according to energy-losses in both scintillator walls and measured velocity via time-of-flight. In this set-up all events within the pink ellipse are identified as pions and within the red ellipse in G wall and red lines in H wall as protons. Because protons lose some energy in the G wall some of them are absorbed in the second wall as seen by the energy-loss decrease in the H wall at $\beta_{\mathrm{TOF}} \lesssim 0.3$.

MWPCs and ToF walls. In this way two definitions for quantities like energy-loss or velocity exist. They are labeled either by dE/dx and β or by dE/dx_{TOF} and β_{TOF}.

In the 2D plot of dE/dx in wall G and H vs. β a circular or rectangular cut is applied around the events which corresponds to a specific particle type. In Fig. 7.8 an example of PID is shown with a clear separation between protons and pions.

7.4 Test with protons and positrons

The first test with the Čerenkov detector in the A1 spectrometer hall has been performed during the hypernuclear decay-pion study experiment in 2011 with the ^{9}Be target [109]. In this experiment, kaons were tagged by the KAOS spectrometer and pions were detected by the two high-resolution spectrometers Spec. A and Spec. C at backward angles. KAOS was operating at zero-degree relative to the incident beam direction by using pre-target magnetic chicane. The initially produced $^{9}_{\Lambda}\mathrm{Li}^{*}$ hypernucleus is in excited state. Such hypernuclei could be electro-produced in association with a charged kaon emitted predominantly in the forward direction with respect to the beam and and break-up into a lighter hyperfragments. The Λ hyperon bound inside the hyperfragment decays weakly into nucleon and pion. The analysis of the experimental data was focused on the high-resolution spectroscopy of pions produced such two-body decay from a wide range of light hyperfragments. During this experiment the Čerenkov counter was exposed to a large background of positrons ($\approx 99.5\%$) from pair production by high-energy photons produced by bremsstrahlung in the target, that were mainly in the mid-plane of Kaos. The central momentum of Kaos was set to 900 MeV/c so the positrons within the momentum acceptance were high above the threshold and the protons below the threshold for Čerenkov emission [60].

7.4.1 Test at low beam-current

The preliminary test was done with very low beam-current: $I = 300$ nA. Even though the detector was exposed mostly to positrons, for a precise analysis a PID still needs to be done. Because this test lasted for a couple of hours, not enough protons were detected for any reliable analysis. In this test I have concentrated on the efficiency of Čerenkov detector with positrons only.

Segment 0 was excluded from the analysis, because in this preliminary test the R877-100 PMTs, attached to cell 0, were producing a lot of noise, which was eliminated in later test runs, so the R1250 PMTs were used in this test. Thickness of the aerogel layer was $d = 2$ cm.

The ADC SUM over 10 phototubes is shown in Fig. 7.9. In this histogram a specific cut on possible tracks is applied to reduce the background. Despite proper cut and a PID for positrons a pedestal in the ADC SUM histogram is still present.

For the tests with the reaction products in the experimental hall a particle flux is much higher than with the cosmics so a multiplicity more than one, $M > 1$, and thus the overlap of particles per event is possible, especially at higher beam-currents. To avoid such situation only the events with one cluster in wall G and H (commonly referred to as cluster = 1) are included into analysis, so all efficiency results in my thesis include this cut. The ADC SUM histogram includes an additional cut on multiplicity M in the Čerenkov detector, $M \leq 1$. The efficiency of the Čerenkov counter evaluated from the ADC SUM (Fig. 7.9) with cut condition set to 0.5 p.e. is $\approx 98\%$.

After calibration, cuts on X coordinate and G-H paddles and finally positron PID, the efficiency of each segment was calculated at different ADC cut conditions. The efficiency for all segments is shown in Fig. 7.10. If a cut condition is set to 0.5 p.e. the efficiency for all cells is $\approx 92\%$.

Even though only events with one cluster in ToF walls, multiplicity ≤ 1 and possible tracks are included into the ADC SUM histogram, the efficiency of individual segments is smaller than the efficiency for the complete Čerenkov counter. A possible explanation for such discrepancy might come from slightly inefficient track reconstruction. The particle coordinates might be miscalculated where true coor-

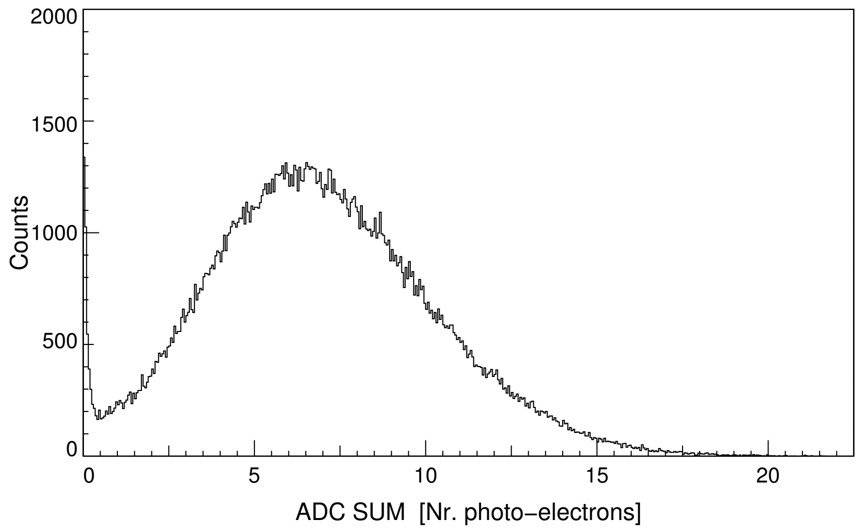

Figure 7.9: The ADC SUM histogram over 10 phototubes at beam-current I = 300 nA. Only positrons are included and a cut on possible tracks is applied together with a cut on multiplicity < 1. The mean value (without pedestal) is ≈ 7 photo-electrons.

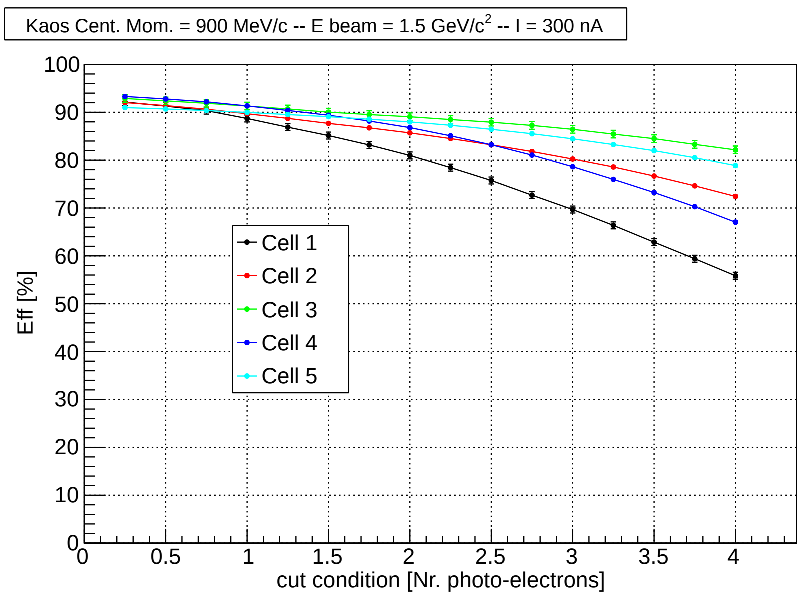

Figure 7.10: The efficiency of each segment of the Čerenkov detector at low beam-current I = 300 nA with relativistic positrons. The average efficiency at 0.5 p.e. is ≈ 92%.

dinates do not lie within the segment of interest but in the neighboring segment, giving rise to the pedestal in the individual ADC spectrum. This obviously does not affect the efficiency measurement evaluated from the ADC SUM spectrum, where all segments are taken into account.

7.4.2 Aerogel in the mid-plane

For the first part of the experiment the aerogel box was covered completely with aerogel with thickness of $d = 2$ cm and with R877-100 PMTs positioned at the lower momentum side of the Čerenkov counter, but were excluded from the analysis due to large noise, like in the previous test. The beam-current was set to 1.5 μA.

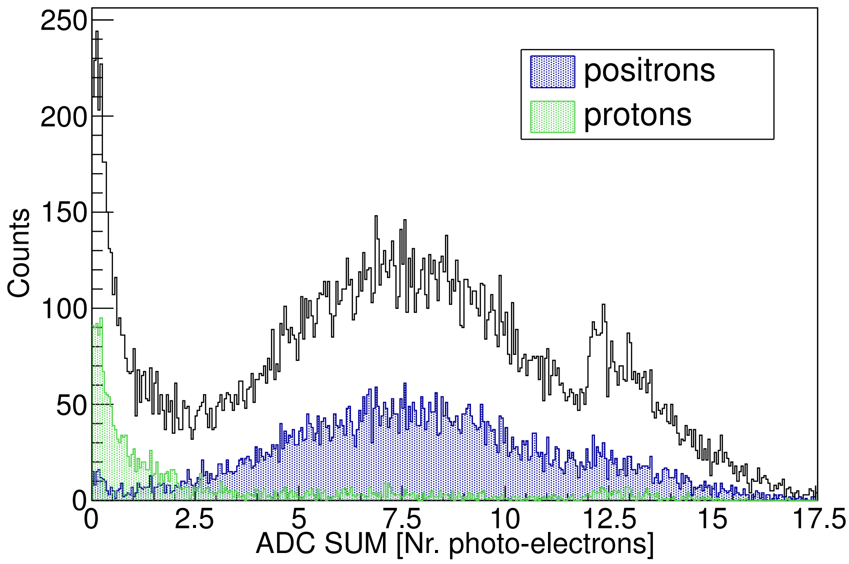

Figure 7.11: Total number of photo-electrons over 10 PMTs (white) with cut on protons (green) and positrons (blue) at $p = 900$ MeV/c. Protons contribute mostly to the pedestal but some of them also beyond zero-photo-electrons.

The distribution of the total number of photo-electrons for 10 phototubes (with cuts on valid tracks, one cluster in ToF walls and Čerenkov multiplicity $M \leq 1$) is shown in Fig. 7.11. The white histogram shows the spectrum without any PID cut, while the blue spectrum corresponds to the same histogram with an additional cut on protons and the green one with the additional cut on positrons. Small bump at ≈ 12.5 photo-electrons in white histogram is the result of summing the ADC value from top and bottom PMT where one ADC value is in the pedestal and the other in the overflow (maximum value of ADC module). This happens when a particle crosses aerogel layer near one on the phototubes where a large signal is produced and none in the opposite phototube in the same segment. In this plot the particles are identified by dE/dx_{TOF} and β_{TOF}. The signals produced by positrons are high above the threshold, while the signals produced by protons at this momentum are still below the detection threshold. Although protons are below the Čerenkov threshold, a small fraction of them produced a Čerenkov signal with a total number of photo-electrons larger than zero. It could be due to proton induced δ-electrons with momentum above the detection threshold, random coincidences of photomultiplier noises with the trigger, or scintillations produced in the coating or the air in the diffusive box. The appearance of signals with particles below the threshold has also been observed in other Čerenkov counters [79, 110]. Search for the reason why some protons produce Čerenkov photons is still in progress.

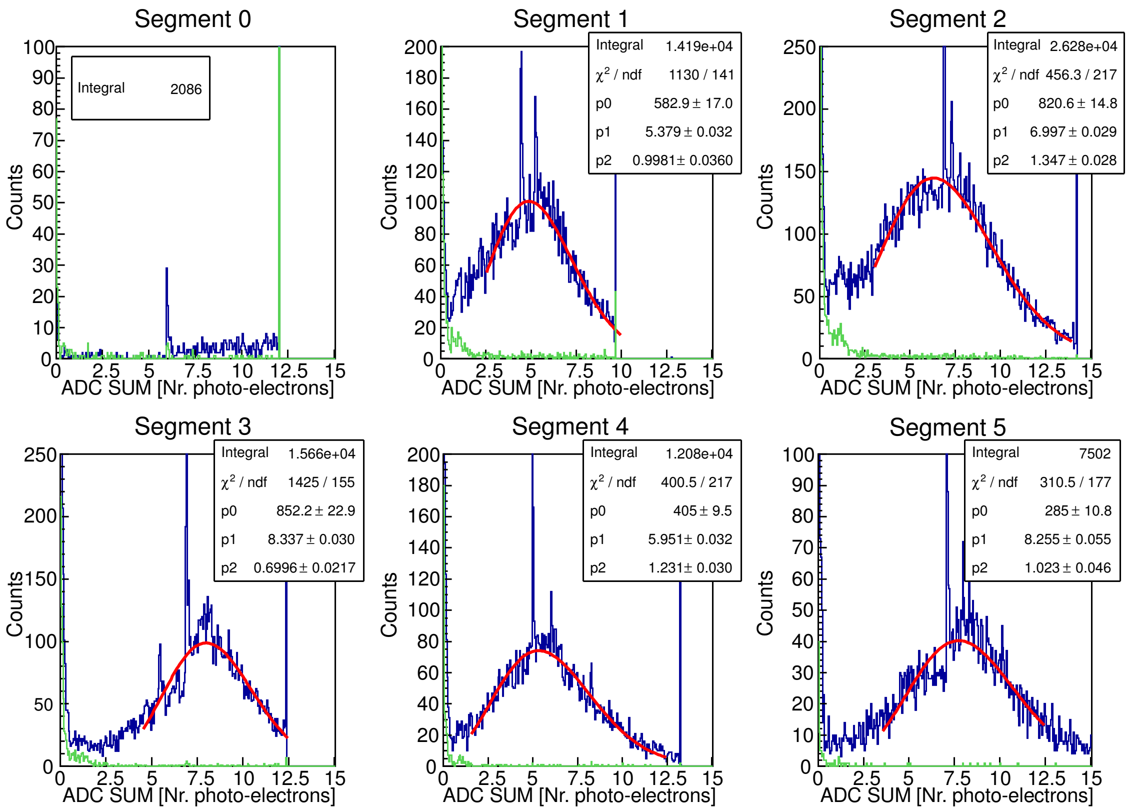

Figure 7.12: ADC spectra from all 6 segments with a cut on protons (green) and positrons (blue). The spectra corresponding to positrons are fitted by a Poisson function, with p_1 being the mean value. The histogram from segment 0 is completely useless, as R877-100 PMTs attached to it were too nosy.

By applying the cut (7.4) to select an individual segment the ADC spectrum from each cell can be selected. All spectra are shown in Fig. 7.12 for protons and pions, respectively. In this figure the spectrum that corresponds to the positrons is fitted by a Poisson function with free parameters p_0, p_1 and p_2:

$$P(x) = p_0 \frac{(p_1/p_2)^{x/p_2} \exp\left(-p_1/p_2\right)}{(x/p_2)!}, \tag{7.8}$$

with p_1 being the mean value, p_0 the normalization factor and p_2 the so-called smearing factor. The ADC spectrum from segment 0 with R877-100 PMTs is also in the figure for reasons of completeness, although the segment was dysfunctional due to excessive noise. The problem was solved in the second part of the experiment (see Subsection 7.4.2).

The efficiency of each segment is evaluated from the individual ADC spectrum, with results shown in Fig. 7.13. The average efficiency for positrons with threshold at 0.5 p.e. is $\approx 90\%$, while the efficiency evaluated from the ADC SUM is $\approx 99\%$. The "efficiency" or the so-called probability for detection of protons is non-zero due to the large tail above the 1 photo-electrons in the ADC spectrum. With threshold set to 1.5 p.e. the average probability is $\approx 12\%$. Particles identified either by dE/dx and β or dE/dx_{TOF} and β_{TOF} give comparable efficiency results.

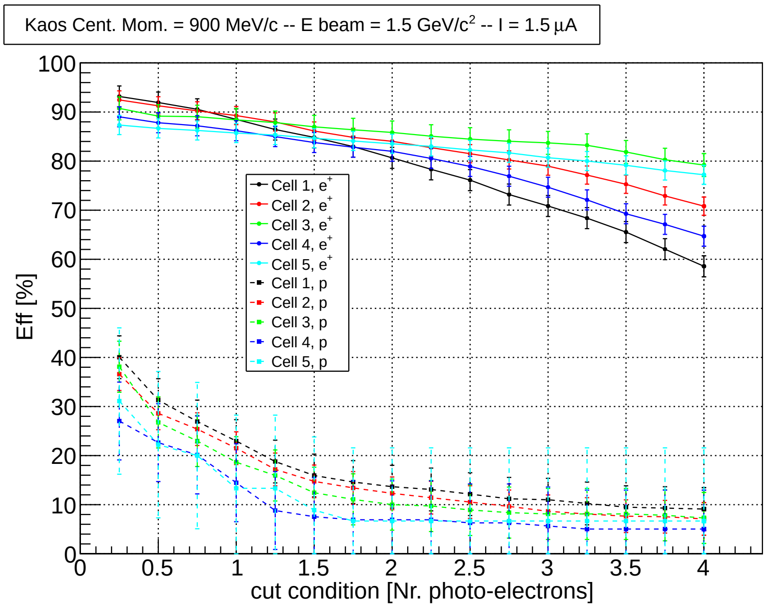

Figure 7.13: The efficiency of each segment of the Čerenkov detector at various threshold conditions for positrons and protons.

By choosing a proper ADC cut condition on the signals from the aerogel Čerenkov detector the background (positrons) can be eliminated. The background in the coincidence-time spectrum between KAOS and Spec. C can be subtracted by setting the proper threshold $\mathrm{ADC_{thr}}$ in cut condition (7.5). Fig. 7.14 shows the coincidence-time spectrum with three clearly separated coincidence peaks corresponding to protons in KAOS and π^- or μ^- or e^- in Spec. C. By applying the cut condition (7.5) for events above or below the detection threshold with $\mathrm{ADC_{thr}}$ set to 1.5 p.e. a clear separation between the coincidental events and background is seen. The time resolution for the (p,π) reaction is $\Delta t_{\mathrm{FWHM}} = 1.47$ ns. In this figure the flight-path correction for Spec. C only applies to pions, leaving the peaks from muons and electrons significantly wider.

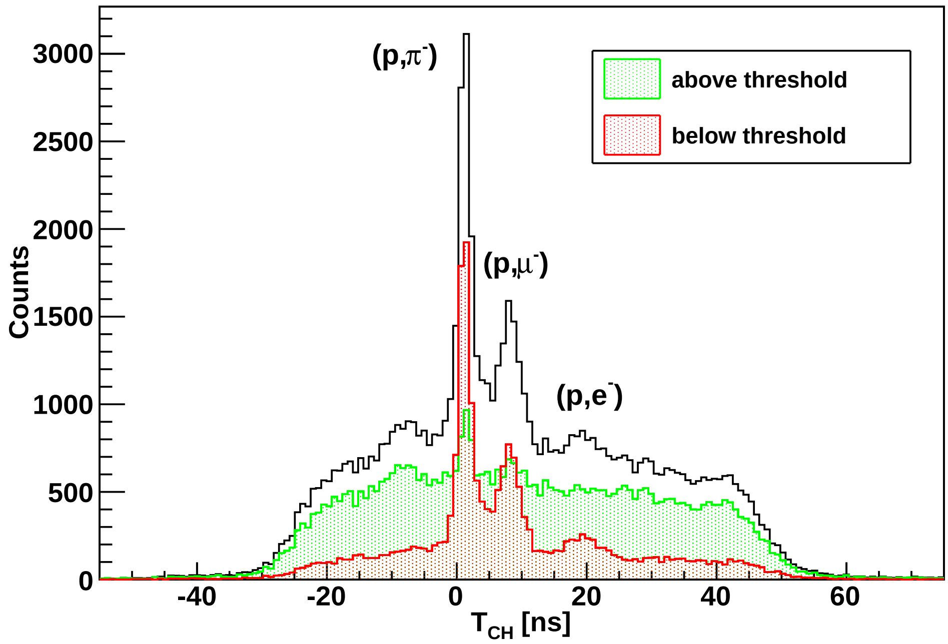

Figure 7.14: The coincidence-time spectrum between spectrometer KAOS and Spec. C with additional cut on events above and below the detection threshold in the Čerenkov detector. The three peaks correspond to protons in KAOS and π^- or μ^- or e^- in Spec. C.

Because some protons produce non-zero signals part of the dominant coincidence peak remains in the time spectrum with "above threshold" cut. On the other hand, some background events (positrons) satisfy the "below threshold" condition due to a small inefficiency of the Čerenkov detector. The detection threshold efficiency depends on the reconstructed coordinates in the aerogel plane, so the decrease of efficiency might be a consequence of inefficient track reconstruction, as mentioned already the previous section. This is also noticeable in the the efficiency of pions evaluated from an individual segment being smaller than the efficiency evaluated from the ADC SUM spectrum (with cluster = 1 and $M \leq 1$ cut), which does not depend on the particle coordinates.

The main peak in the ADC SUM spectrum (Fig. 7.11) is produced by Čerenkov photons generated by relativistic particles as evidently seen in Fig. 7.15. Protons are clearly below the emission threshold, with $\beta_{\mathrm{TOF}} \approx 0.7$ in this kinematical set-up.

R877-100 PMT pedestal shift

During the first part of the experiment the R877-100 PMTs were positioned at segment 0, on low momentum side with the largest rate of positrons. ADC raw spectra at different beam-currents or rates of particles in that segment was measured,

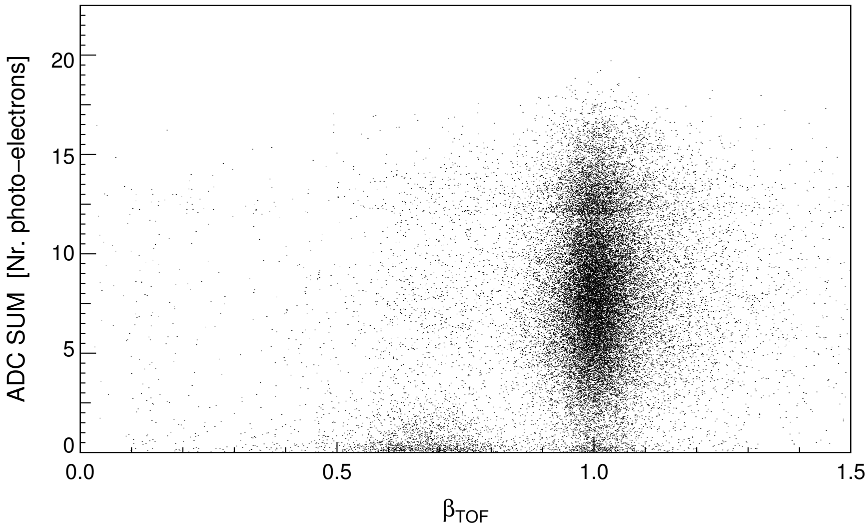

Figure 7.15: Total number of photo-electrons over 10 PMTs versus particle velocity β_{TOF}. A clear separation between particles above and below emission threshold is seen; protons (below the threshold at $\beta_{\mathrm{TOF}} \approx 0.7$) and positrons (above the threshold at $\beta_{\mathrm{TOF}} \approx 1$) in this case.

as shown in Fig. 7.16 with significant pedestal shift at higher beam-currents. As we see the complete spectrum shifts towards the underflow, making the histograms at higher rates useless for analysis. As the beam-current was set to 1.5 μA the rate of particles in that segment was $\approx$ 500 kHz.

Such pedestal shift happens in a AC coupled system. Usually any capacitor in a system prevents the transmission of a DC component. But pulses with random rate and amplitudes lead to fluctuations of the baseline. A sequence of unipolar pulses has a DC component that depends on the event rate. As a result, the baseline shifts to make the overall transmitted charge equal zero. The baseline shift is constant if the signal rate is also constant, which can be significant in AC coupled systems with very high rate.

The cathode current at $\approx$ 500 kHz particle rate is well below the maximum values, so we should not experience pedestal shift at 1.5 μA beam-current. Additional test was done with PMT and laser inside black box, similar to Fig. 5.26 in Ch. 5, only without the amplifier. With laser intensity set to 3-4 photons per pulse at various frequencies up to 10 MHz I did not see any pedestal shift.

One of possible reasons for the pedestal shift could be that the additional external amplifiers are AC coupled and thus inefficient at higher rates.

For the second part of the experiment the problem was solved by replacing the R877-100 PMTs to the higher momentum side with lower particle rate and by adding linear F IN/OUT module in the electronic chain to cancel the potential pedestal shift by setting the base-line.

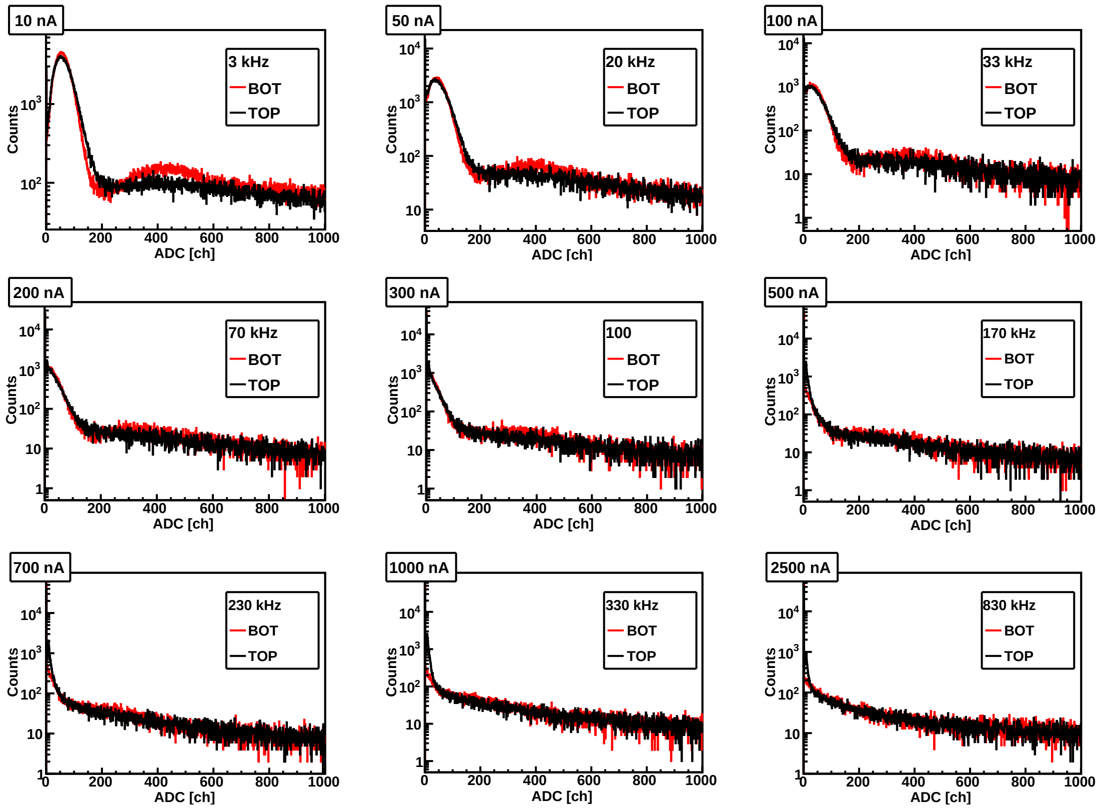

Figure 7.16: The raw ADC spectra from R877-100 PMTs exposed to different particle rates. A clear pedestal shift at higher beam-current is visible.

After the second experiment the external amplifiers were removed and two amplifiers with a total gain of ≈ 100 were integrated into the PMT voltage divider. Furthermore the linear F IN/OUT module was removed and the 2249A ADC module was replaced with an ADC module with adjustable baseline.

7.4.3 Without aerogel in the mid-plane

For the second part of the experiment a few modification to the Čerenkov detector have been made: (i) another layer of 1 cm aerogel was, added giving a total thickness of aerogel d = 3 cm; (ii) to reduce the large background of positrons one row of aerogel in the mid-plane was taken out of the aerogel basket and replaced by a light supporter covered by millipore paper; (iii) R877-100 PMTs from segment 0 were replaced with R1250 PMTs from segment 5, in this set-up the R877-100 phototubes were positioned at higher momentum side with lower rate of particle flux; (iv) linear F IN/OUT was added to set the R877-100 phototubes base-line.

During this experiment the beam-current was set to 2 μA with two additional large horizontal scintillator bars, located 4 cm above and below the spectrometers mid-plane, included into the trigger to reduce the impact of positron rate on the

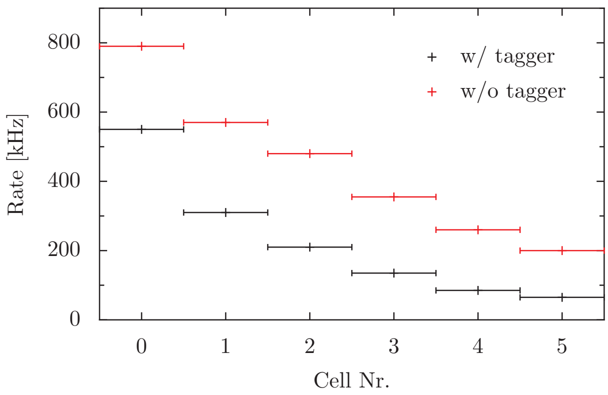

Figure 7.17: The particle rate through the six segments of the Čerenkov detector. If the tagger (see text) is included into the trigger, the rate decreases, due to the 8 cm gap between the paddles in the mid-plane.

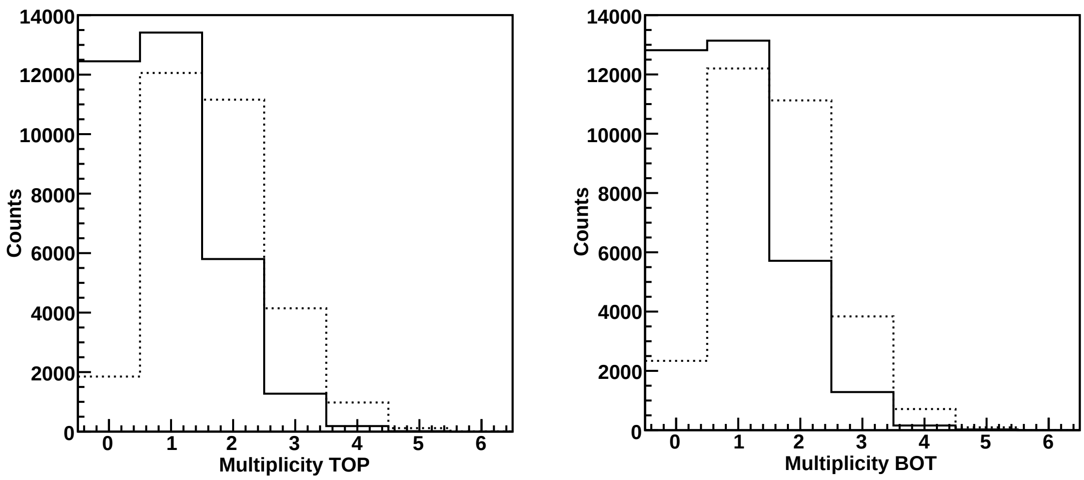

Figure 7.18: The hit multiplicity of the Čerenkov detector for top and bottom phototubes. Despite the higher beam-current ($I = 2\ \mu$A) the multiplicity is smaller with the 5 cm aerogel gap in the mid-plane (solid line), compared to the multiplicity without the gap and $I = 1.5\ \mu$A (dashed line).

dead-time of the data acquisition system. The tagger detector assures that passing particles have an out-of-plane angle of $|\phi_{oop}| > 1°$, therefore discarding many bremsstrahlung induced positrons with momenta distributed over the full range of the momentum acceptance of the spectrometer.

Some 1 cm Matsushita tiles were cut by mechanical saw to dimension of 3×11.5 cm^2 to fit into the aerogel basket, as shown in Fig. D.1, while some of 2 cm thick tiles from Novosibirsk were split by saw to 2×1 cm thick aerogel tiles.

The raw rate of particles at $I = 2\ \mu$A for each segment is shown in Fig. 7.17.

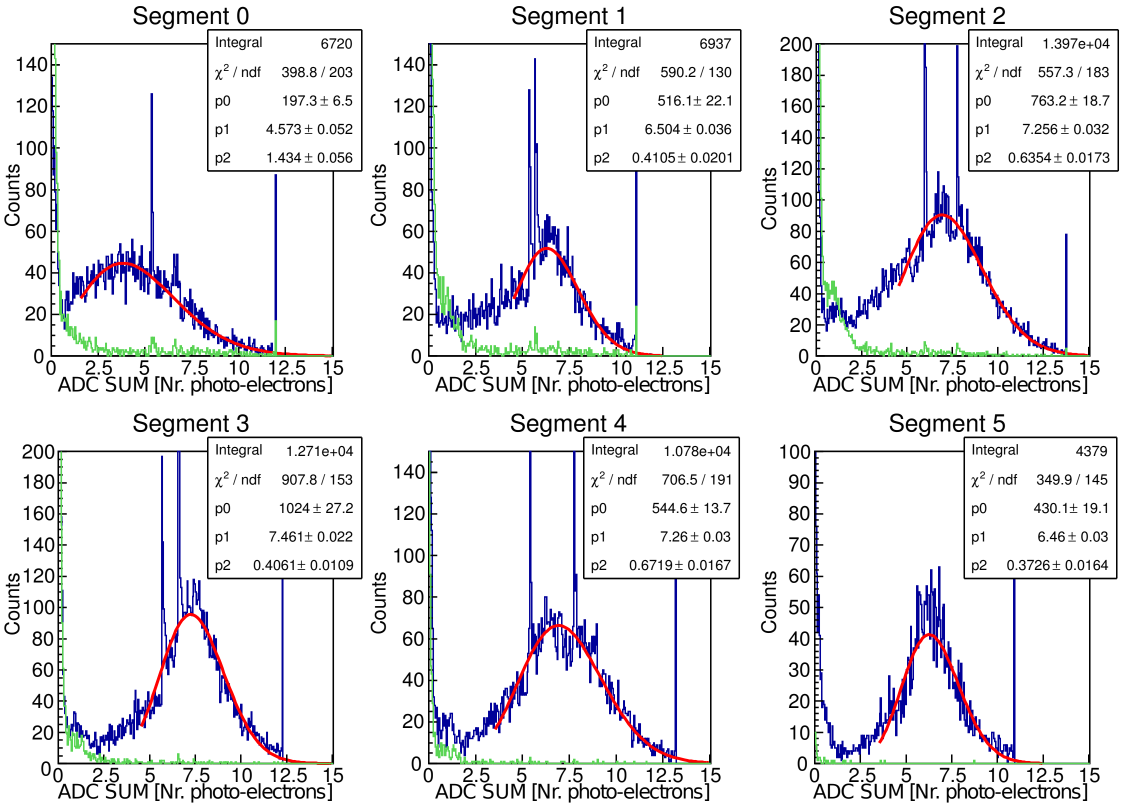

Figure 7.19: ADC spectra from all 6 segments with cut on protons (green) and positrons (blue). Spectra corresponding to positrons are fitted with with Poisson function, with p_0 parameter being the mean value.

Even though the raw particle rate has increased due to higher beam-current the multiplicity in Čerenkov detector has decreased because of the 5 cm gap in the middle of aerogel plane, as shown in Fig. 7.18. The average multiplicity in the first part of experiment was ≈ 1.7, while in the second part it was ≈ 0.9. At such reduced particle rate the R877-100 PMTs worked normally (this is without pedestal shift), so all segments were included into analysis.

Because of the 5 cm gap in the mid of aerogel plane the efficiency analysis has been performed with three different XY cuts on the aerogel plane to see the effect of the gap. The cut was made to include the events: (i) in the mid-plane only with cut on vertical coordinate, -2 cm $< y' < 2$ cm; (ii) outside of the mid-plane, $y' < -4$ cm or $y' > 4$ cm and (iii) without any cuts to cover the complete aerogel surface area. The analysis was done with XY-cut as well as with XY_{TOF}-cut and with particles defined either by dE/dx and β or dE/dx_{TOF} and β_{TOF}. For more reliable efficiency results an additional cut on the quality of the tracks was used, with $Q > 0.001$ (see Sec. 4.2).

The ADC spectra for each segment are shown in Fig. 7.19 with a cut on protons and positrons. Like in the previous part of the experiment the spectra corresponding to the positrons are fitted by a Poisson function. Large spikes in this figure are a consequence of combining top and bottom ADC values with one of them being in overflow and the other in the pedestal. Such events occur when particles cross the aerogel near the PMT windows. In this figure we can also see the improved ADC spectrum produced by R877-100 PMTs attached to segment 5.

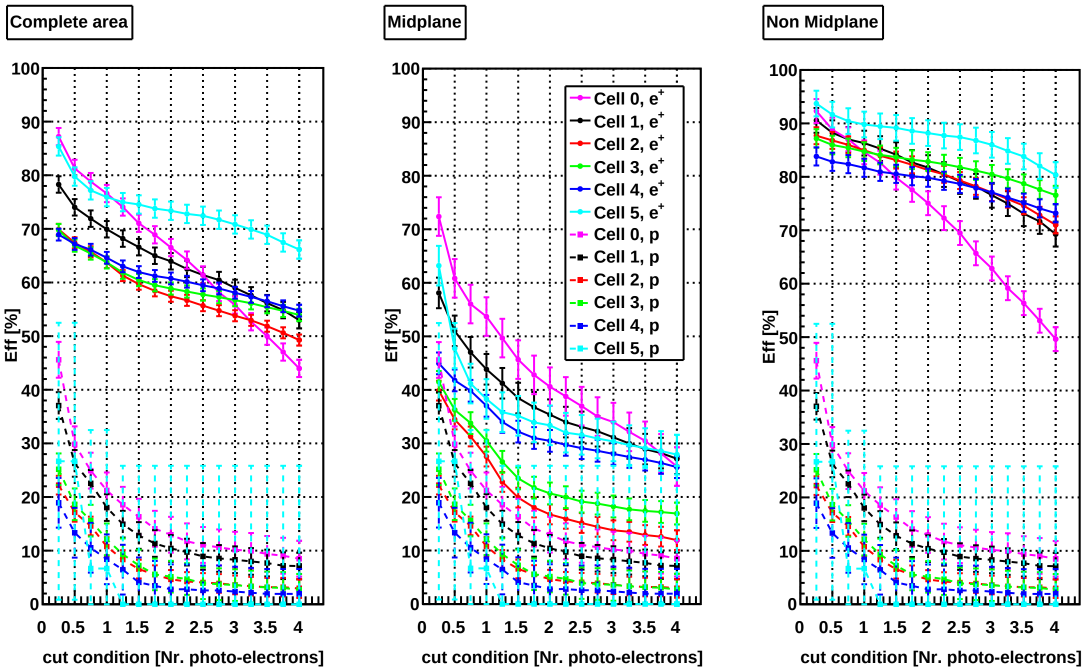

Figure 7.20: The efficiency for all Čerenkov detector segments for positrons and detection probability for protons at various cut conditions on vertical coordinate Y. The KAOS central momentum was set to 900 MeV and the beam enery to $E_e = 1.5$ GeV with $I = 2$ μA. In this set-up the aerogel was taken out from the mid-plane to reduce the high background rate.

The results are shown in Fig. 7.20 for all three cuts on the vertical coordinate. With the cut on the events in the mid-plane, the efficiency is the lowest compared to other two cuts, but is non-zero, which can be explained by scattering of particles inside tagger and ToF walls in vertical direction. In some cases the particles with non-zero ϕ angle hit the G wall near mid-plane, scatter inside tagger detector back towards the mid-plane and hit the H wall at approximately the same vertical position as in the G wall. In this case the tagger detector was hit and the detector system was triggered even though the particle has crosses the ToF walls and Čerenkov counter near the mid-plane. The efficiency for positrons evaluated from the complete aerogel plane is smaller, compared to data taken with $I = 1.5$ μA, due to the gap in the mid-plane. The cut on events outside the mid-plane gives the most reliable results, since this area is completely covered by the aerogel. The average efficiency with this cut for positrons is below 90% at 0.5 p.e. threshold condition. The decrease of efficiency could be explained by the absorption of Čerenkov photons by light supporter in the mid-plane that was covered by only one layer of millipore paper. The probability for proton detection is higher in this set-up, most probably because of higher beam-current and thus higher probability for particles to overlap per event, because the proton detection probability decreases at smaller beam-currents (see Fig. 7.24).

7.5 Test with protons, pions and kaons

The second test with the Čerenkov detector has been performed during the polarized cross-section measurement for the hypernuclei electro-production experiment in 2011. In this experiment, positive kaons were tagged by the KAOS spectrometer and pions were detected by the high-resolution spectrometer Spec. B in out-of-plane position, so that the angle between scattering and production plane was $\phi = 40°$. This set-up enables to measure the polarized structure function $\sigma_{LT'}$ for the reaction $p(\vec{e}, e'K^+)\Lambda$ (see Eq. 2.29). The electron beam was rastered with a few kHz in transverse directions over a liquid hydrogen target cell, in order to avoid local boiling of the liquid, with the density of 0.068 g/cm^3. The central momentum setting for the kaon arm was 460 MeV/c and for the electron arm 365 MeV/c. Spectrometer KAOS was operating at $\theta_K^{\rm lab} = 37.6°$ relative to the incident beam direction with a large angular acceptance. The electron spectrometer was fixed at the minimum forward angle of $\theta_{e'}^{\rm lab} = 14.41°$, thereby maximizing the virtual photon flux. The photon's four-momentum, $Q^2 = 0.05$ (GeV/c)^2, was low, its degree-of-polarization $\epsilon = 0.4$, and its energy was, $\hbar\omega = 1144$ MeV, so the hadronic system was excited to an invariant energy $W = 1726$ MeV.

During this experiment the horizontal gap in the middle of the aerogel plane was filled-up with aerogel tiles (without segment 0). In this beam-time the entrance plane of the Čerenkov detector was not completely covered by aerogel due to the lack of tiles for total thickness of radiator $d = 3$ cm. Almost all aerogel from segment 0 was used to fill the horizontal gap in the mid-plane, so only segments 1-5 were taken into the analysis. The arrangement of aerogel for this experiment is shown in Fig. D.2. Larger Matsushita tiles from segment 0 have been cut to smaller pieces to fit into the gap as well as some 1 cm thick BIC/BINP tiles were used to fill the gap. R877-100 PMTs were located in segment 5, like in the previous experiment.

7.5.1 Test at lower beam-energy

Before the hypernuclear experiment a few days were devoted to the detector test at lower beam energy, $E_e = 852$ MeV, which is below the strangeness production threshold, and lower beam-current. As this was just a detector test the KAOS spectrometer was operating in single arm mode at central central momentum set to 720 MeV/c and 460 MeV/c. In order to tag kaons a large background of protons, pions and some positrons must be subtracted by proper PID. At this KAOS angle ($\theta_K^{\rm lab} = 37.6°$), relative to the incident beam direction, the flux of positrons is much smaller than in the previous experiment, so the main contribution to the background

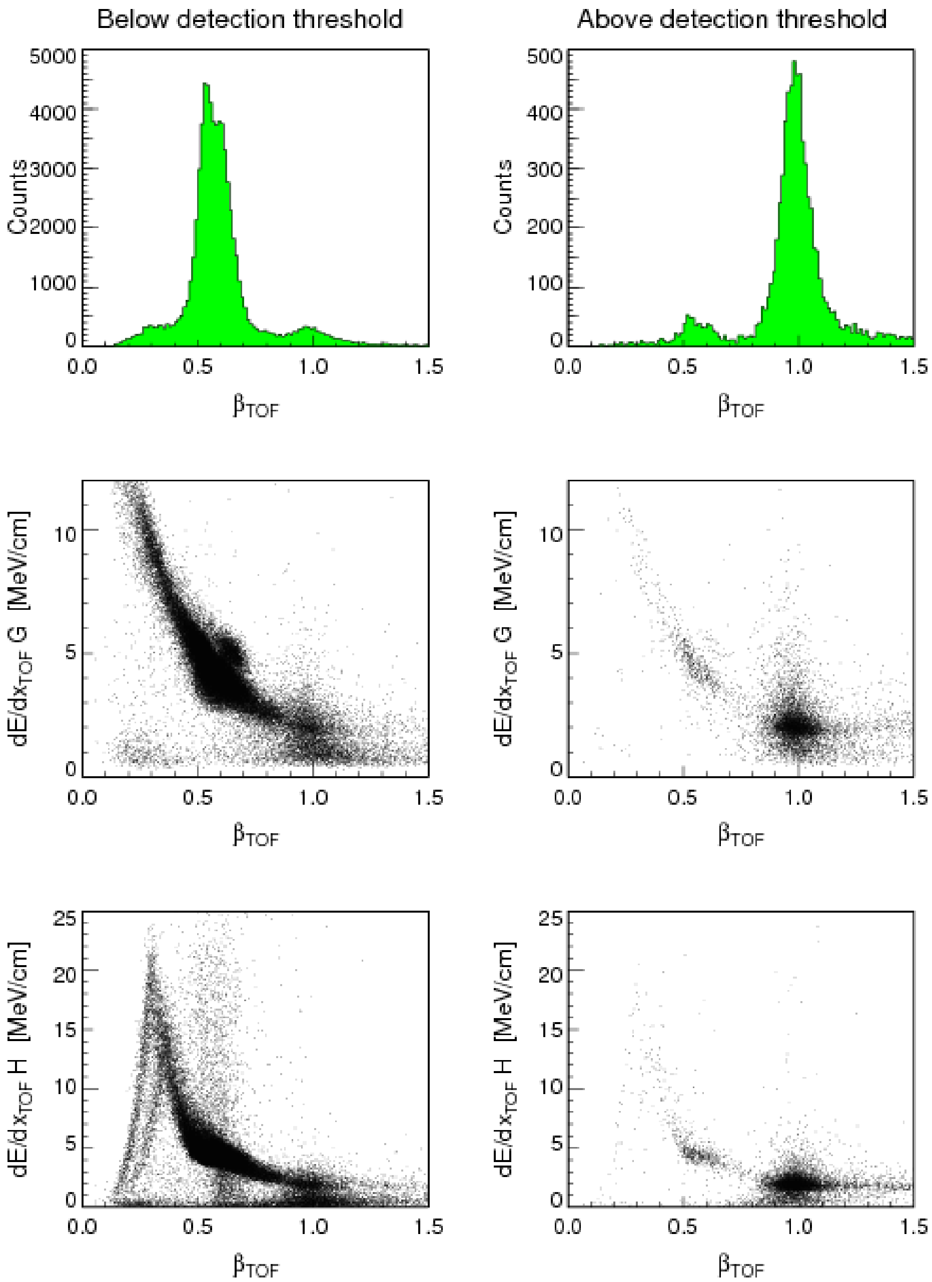

Figure 7.21: Particle velocity and energy-losses measured by ToF walls with Čerenkov counter cut condition. Left column: events below the detection threshold (dominated by protons), right column: events above the detection threshold (dominated by pions). Data was taken at 720 MeV/c central momentum.

are protons. At 720 MeV/c central momentum all protons and kaons are below the Čerenkov emission threshold, while pions and positrons are above it. I will refer to relativistic particles with $\beta \approx 1$ as pions because the contribution of positrons in this set-up is negligible.

By applying a cut condition (7.5) for detection threshold a clear separation between pions and protons is seen in β and dE/dx plots with threshold set to 1.5 p.e. as shown in Fig. 7.21. At 720 MeV/c central momentum the velocity of pions is $\beta \approx 0.99$, while for protons it is $\beta \approx 0.65$, but the measured average velocity for protons is smaller because of inhomogeneous distribution in dispersive direction. Like before, a fraction of relativistic particles (pions in this case) produce signals below the chosen ADC cut condition and some protons above it. In dE/dx vs. β plots in Fig. 7.21 protons have larger energy-losses due to smaller velocity compared to pions. The energy-losses for protons in H wall start to decrease below $\beta \approx 0.3$, because their range in scintillator material is shorter than the effective thickness of the paddles. Hence these events correspond to the protons that are stopped inside the second scintillator wall. In this set-up protons do not stop inside the first scintillator wall, because the momentum is large enough, but they loose energy in and after that wall which results in absorption of protons in wall H. Two branches in dE/dx in H wall vs. β plot (bottom left) are caused most likely because of different amounts of material the particles pass when they fly through the detector system. By applying the Čerenkov cut condition one can easily check whether the β and dE/dx cut conditions used for the PID are consistent.

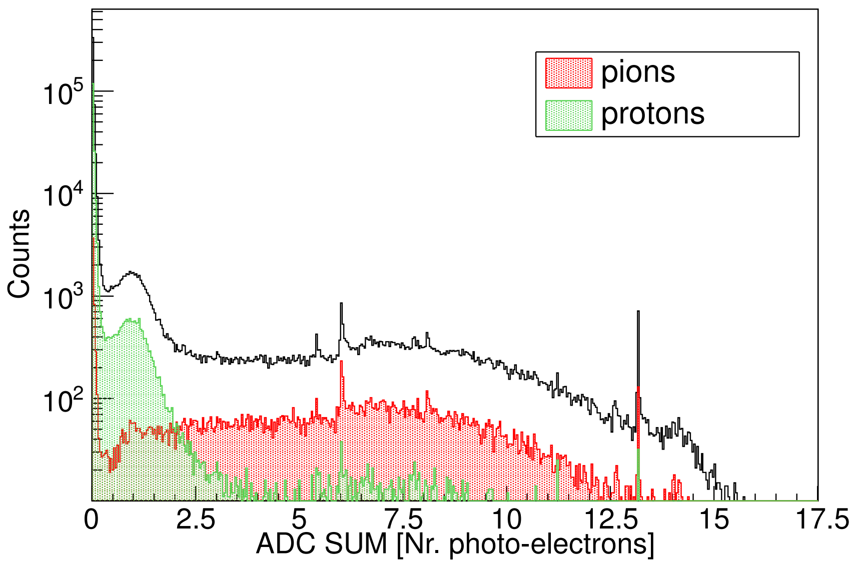

Figure 7.22: Total number of photo-electrons from segments 1-5 (white) with cut on protons (green) and pions (red) at $p = 720$ MeV/c central momentum in Kaos. Protons contribute mostly to the pedestal, but also to the one-photo-electron peak.

The distribution of the total number of photo-electrons from segments 1-5 (with cuts on valid tracks, one cluster in ToF walls and Čerenkov multiplicity $M \leq 1$) is shown in Fig. 7.22. Again the white histogram shows the spectrum without any PID cut, while the blue spectrum corresponds to the same histogram with an additional

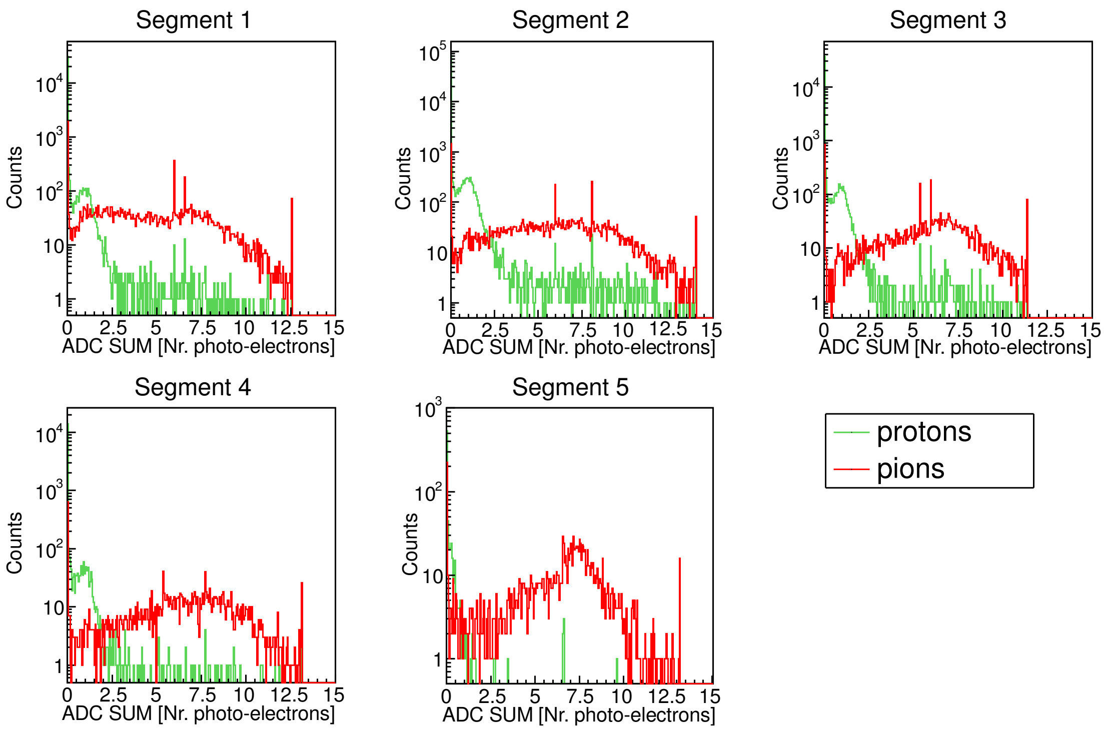

Figure 7.23: The ADC spectrum from each segment for pions (red) and protons (green). Segment 0 was empty and thus excluded from the analysis.

cut on protons and the red one with an additional cut on the pions. In this plot the particles are identified by dE/dx_{TOF} and β_{TOF}. Most of the signals produced by pions are high above the threshold, while the signal produced by protons at this momentum are mostly below the detection threshold. Like in previous experiment a small fraction of protons produce a Čerenkov signal, which is mostly one photo-electron, seen in Fig. 7.22 as a large bump near the pedestal in the histogram that corresponds to the protons. In this figure we can also see that there is an area around 2 photo-electrons, where events identified as protons and pions overlap, which makes it difficult to find a proper detection threshold cut. The average number of photo-electrons produced by pions is $N_{\mathrm{pe}} \approx 5$. This number is comparable with the simulation results, shown in Fig. 6.12.

By applying the cut (7.4) to select individual segment the ADC spectra for each cell is seen. This is shown in Fig. 7.23, with an additional PID cut. In all segments a large one-photo-electron peak is seen, produced by protons, except in segment 5, where R877-100 PMTs have been attached to.

The efficiency is calculated from the histograms in Fig. 7.23 for all 5 segments for pions and protons at 720 MeV/c central momentum in KAOS. The results are shown in Fig. 7.24. The detection probability for protons is well below 10% at 0.5 p.e. threshold cut. We see that the proton detection probability has dropped compared to data taken at higher beam-current (see for instance Fig. 7.13), even though in both cases the protons were well below the Čerenkov emission threshold. At this beam-current ($I = 300nA$), the overlap of particles per event is smaller so the PID is more reliable, giving more accurate efficiency results.

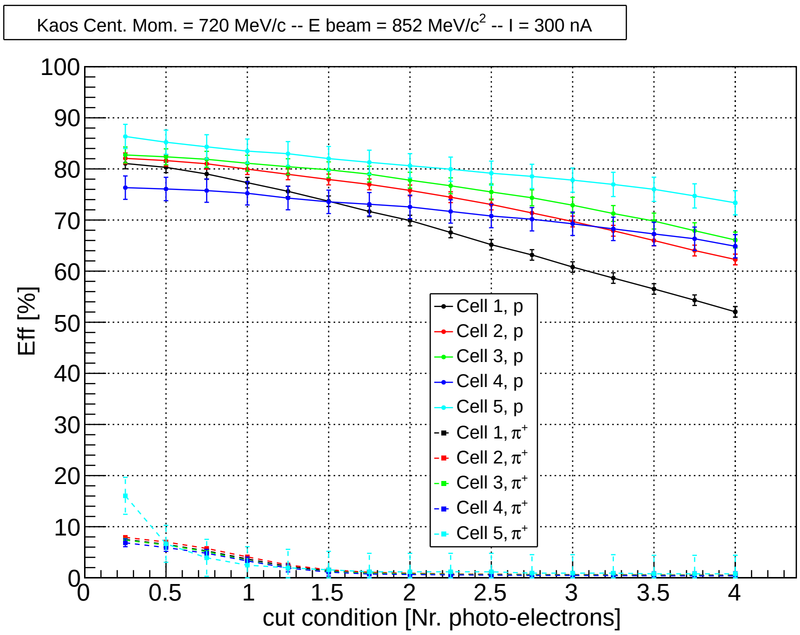

Figure 7.24: The efficiency of each segment of Čerenkov detector at various threshold conditions for pions and protons at 720 MeV/c central momentum in KAOS.

On the other hand, the efficiency of relativistic particles, pions in this case, has decreased to ≈ 82% at 0.5 p.e. threshold cut. Such a drop of efficiency is even larger with data taken at smaller central momentum in KAOS. This inefficiency of pions can be explained by light yield dependence on momentum (see Fig. 6.11).

The second Čerenkov test was done at 460 MeV/c central momentum in KAOS. In this set-up the pions were just slightly above the Čerenkov emission threshold ($p_t^{\pi^+} \approx 415$ MeV/c), moreover segments on the lower momentum side are even below the threshold. The efficiency calculated for all 5 segments for pions and protons at 460 MeV/c central momentum is shown in Fig. 7.25. The detection probability for protons is comparable to data taken at 720 MeV/c central momentum. But we see a drastic drop of efficiency for pions, especially for segments located at the lower momentum side. This is explained by the fact that the light yield and thus the efficiency depends on the particle momentum (see Eq. 5.19 and Fig. 5.5). The dependence is stronger at momenta just above the emission threshold as seen in Fig. 5.5 right. The relative light yield at 720 MeV/c for pions is ≈ 0.65, which explains the small drop of efficiency compared to results with relativistic positrons in pion-decay experiment, while at 460 MeV/c it is only ≈ 0.2. About 90% of relative light yield for pions is achieved at ≈ 1.5 GeV/c.

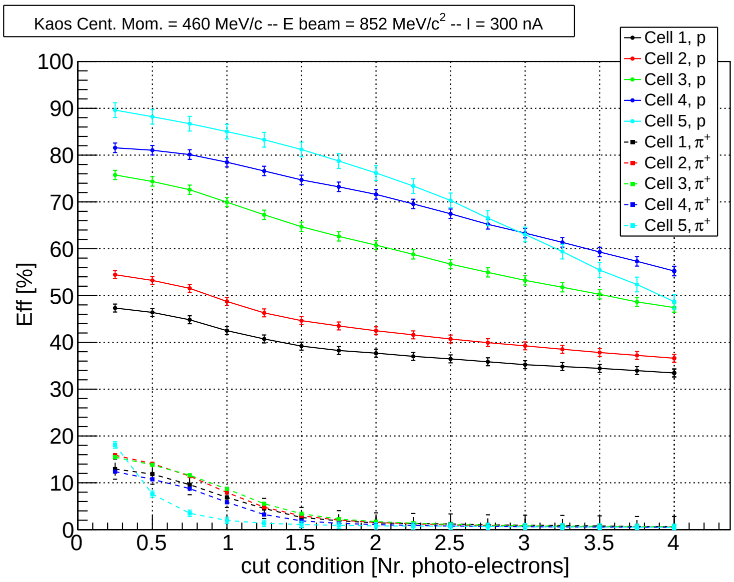

Figure 7.25: The efficiency of each segment of Čerenkov detector at various threshold conditions for pions and protons at 460 MeV/c central momentum in Kaos.

The measured particle momenta versus the reconstructed coordinate x' in aerogel plane are shown in Fig. 7.26 for both central momenta. The threshold momentum is shown by the red dashed line. We see that at 720 MeV/c central momentum all segments are exposed to pions with momenta above the threshold, while at 460 MeV/c segment 2 is exposed to pions with momenta close to $p_t^{\pi^+}$. As the light yield increases with the momentum, so does the efficiency with segment index. This is clearly seen in Fig. 7.25 with segment 5 with the highest efficiency and segment 1 with the lowest. As the coordinates in Fig. 7.26 are reconstructed from the MWPCs, segment 0 is out of acceptance. This is not an issue because this segment is not fully covered with aerogel and thus not taken into the analysis anyway.

Due to low Kaos central momentum and thus small Čerenkov detector efficiency for pions it is very hard to separate pions from kaons/protons at this kinematics. For efficient π^+/K^+ separation a higher central momentum is mandatory and a smaller particle rate.

The efficiency of the Čerenkov detector can also be analyzed without PID. The main criteria for emission of Čerenkov photons is the particle velocity, so the efficiency as a function of β at certain threshold condition can be evaluated. In Fig. 7.27 an example of the efficiency versus β is shown for data taken at 720 MeV/c central momentum with the threshold set to 1.5 p.e. There is a large bump in all segments at $\beta \approx 1$ that corresponds to relativistic particles above the emission threshold, which is comparable to the efficiency for pions as shown in Fig. 7.24 at 1.5 p.e. detection threshold. Particles at $\beta \lesssim 0.8$ have $\approx 10\%$ probability to be above the detection threshold.

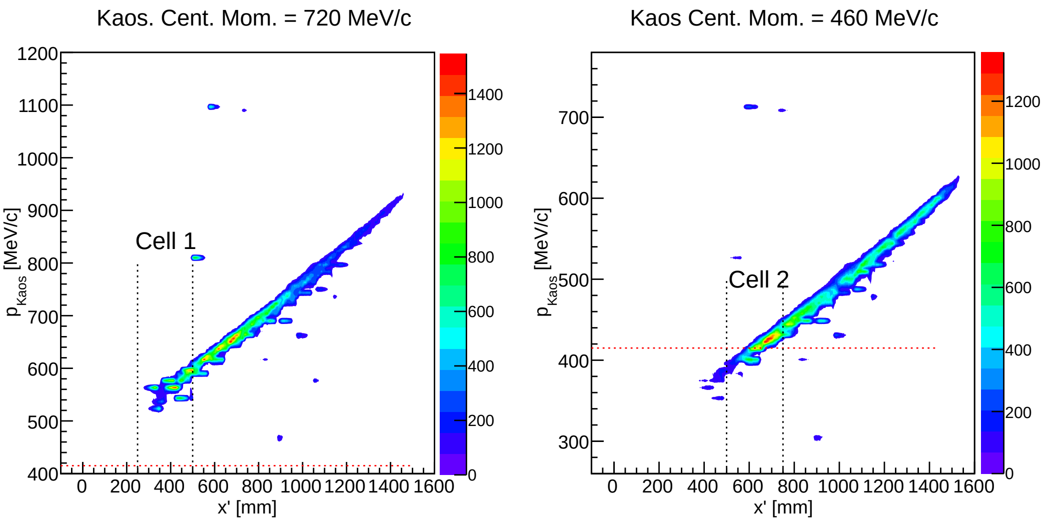

Figure 7.26: Measured particle momenta vs. reconstructed x' coordinate in aerogel plane at two different KAOS central momenta. Pion threshold momentum is shown by the horizontal red doted line. The locations of segments 1 and 2 are shown as a reference.

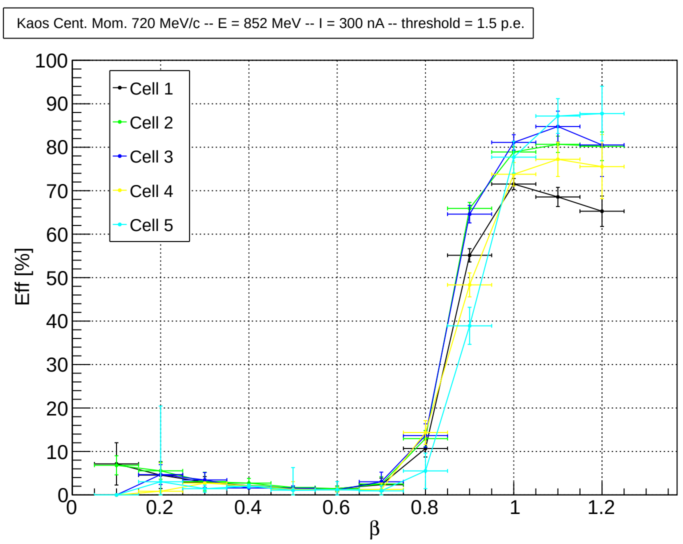

Figure 7.27: The efficiency of each segment of Čerenkov detector vs. particle velocity at threshold condition set to 1.5 p.e.

7.5.2 Test at higher beam-energy

For the strangeness production experiment the beam-energy was $E_e = 1.5$ GeV. As the energy was above the strangeness production threshold, kaons were detected in the hadron arm, along with protons and pions, produced via the hypernuclear reaction $p(\vec{e}, e'K^+)\Lambda$. The KAOS central momentum was kept at 460 MeV/c and the beam-current at $I = 10$ μA.

This was the most inconvenient set-up for efficient π^+/K^+ discrimination, because: (i) pions were just slightly above or even below the Čerenkov emission threshold, and (ii) the probability for high multiplicity and thus the overlap of particles per event was relatively high at this beam-current. The efficiency for pions is the same as in previous detector test at lower beam-current (see Fig. 7.25), while the detection probability for protons has risen up to ≈ 18% at 1.5 p.e. detection threshold.

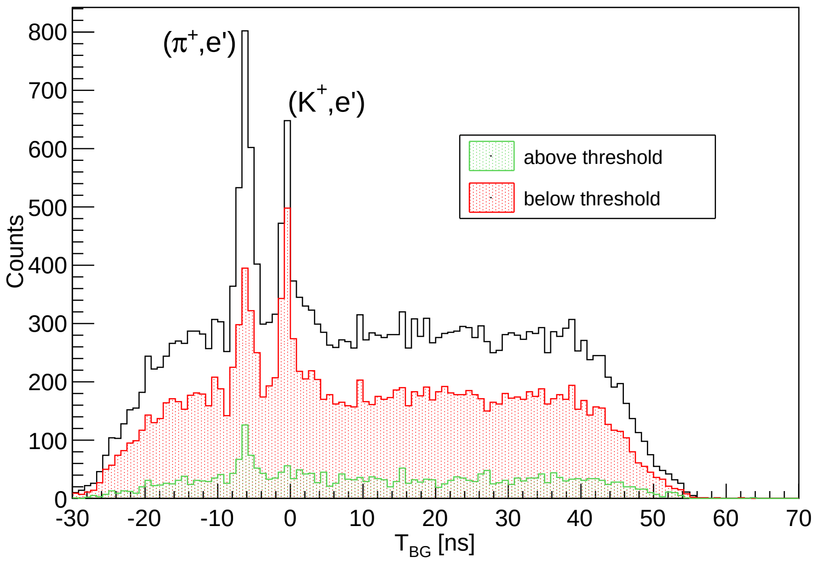

Figure 7.28: The coincidence-time spectrum between spectrometer KAOS and Spec. B with additional cut on events above and below the detection threshold in Čerenkov detector. The two peaks correspond to scattered electrons in Spec. B and kaons or pions in KAOS. In all histograms additional cut on missing-mass and track quality factor are applied that reduce the background in the coincidence-time spectrum with: 1105 MeV/c^2 $< M_x <$ 1125 MeV/c^2.

Like in Sec. 7.4 the performance of the Čerenkov counter can be demonstrated by applying a detection cut condition (7.5) to coincidence-time spectrum between KAOS and Spec. B with threshold $\mathrm{ADC_{thr}}$ set to 1.5 p.e. In order to see the effect of Čerenkov counter cleaner an additional cut on missing-mass and track quality factor has been applied to reduce the background in the coincidence-time spectrum, with: 1105 MeV/c^2 $< M_x <$ 1125 MeV/c^2. In Fig. 7.28 the time spectrum is shown with two clearly separated coincidence peaks corresponding to scattered electrons in Spec. B and K^+ or π^+ in KAOS. By applying the cut condition for events above or below the threshold a separation between the coincidental events and background is seen. Because of low central momentum in KAOS (p = 460 MeV/c) some pions are below the detection threshold and thus can not be separated from kaons by using

Čerenkov counter only. By applying the cut on coincidence-time spectrum for events that are below the threshold the pion peak is reduced compared to kaon peak, but not removed completely as some pions still satisfy the "below threshold" condition. For better background reduction higher momentum is needed.

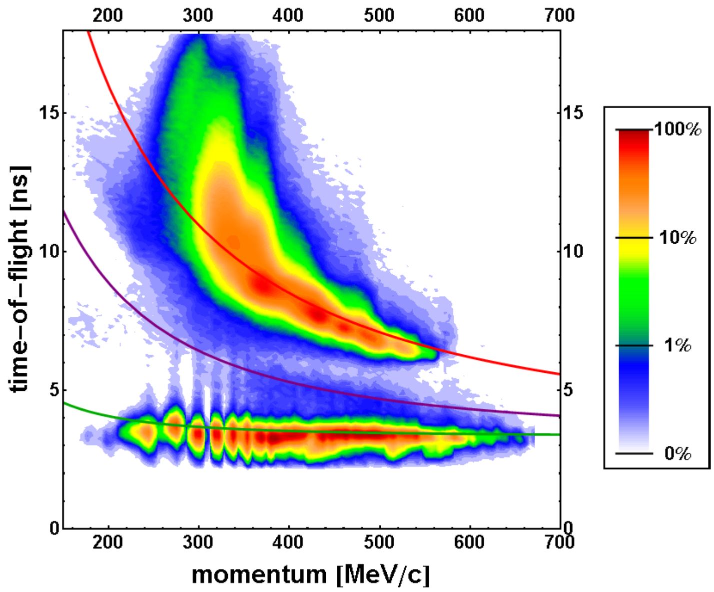

Figure 7.29: Measured time-of-flight normalized to the flight distance of 1 m vs. momentum, compared to the theoretical curves for protons (red), pions (green) and kaons (violet) [111].

Kaon identification is more difficult compared to protons and pions, as the expected yield is $\approx 1500 \pm 40$ $K\Lambda$ pairs per 1800 mC, which is equivalent to 100 hours of 5 μA beam-current. In Fig. 7.29 measured time-of-flight normalized to 1 m versus momentum is shown, with clearly separated bands for pions and protons. As we see the fraction of kaons is very small, making them very hard to identify with such large background. Just like any other particles, kaons are identified by energy-losses in scintillator walls and velocity (see Fig. 7.30). For kaon identification the coincidence-time, T_{BG}, between spectrometer KAOS wall G and Spec. B is used additionally for better background reduction with coincidence peak centered near 0 ns. The corresponding coincidence-time peak for kaons detected in KAOS and scattered electrons in Spec. B is found by comparing missing-mass versus coincidence-time with kaon PID cut (dE/dx and TOF), as shown in Fig. 7.31. For even better kaon identification a cut on aerogel Čerenkov detector is applied with detection threshold set to 1.5 photo-electrons. In Fig. 7.31 an improvement with kaon identification is seen in coincidence-time spectrum with additional cut on aerogel. In both coincidence-time histograms at the top (wall G-Spec. B and wall H-Spec. B) a small peak disappears on the left side from the coincidence peak and the background is slightly reduced. Background reduction is also seen in two-dimensional plots with coincidence-time

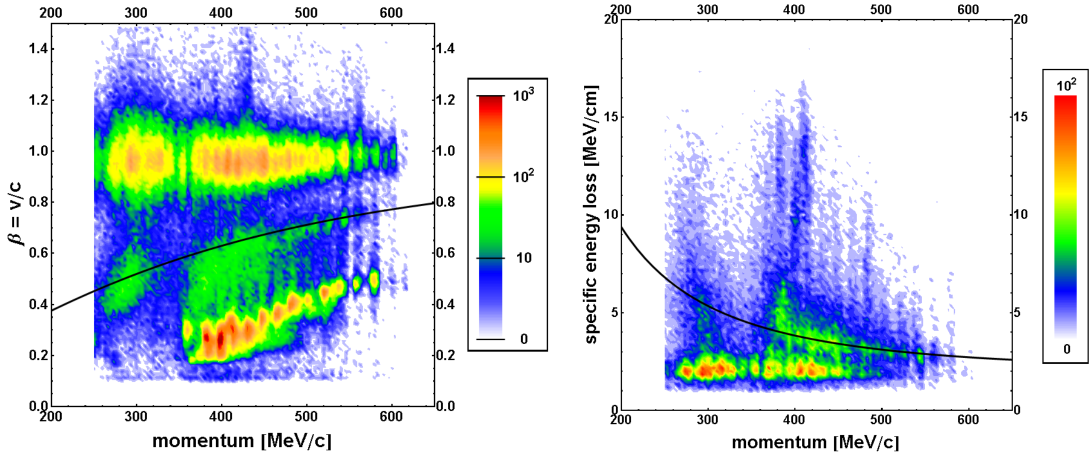

Figure 7.30: Measured velocity (left) and specific energy-losses (right) versus momentum, together with the theoretical Bethe-Bloch function that corresponds to the kaons. Events identified as protons, pions or positrons are reduced so the kaons start to appear more prominently [111].

vs. missing-mass. Middle plots in Fig. 7.31 do not include additional cut on aerogel, while bottom plots include only events below aerogel detection threshold.

The correctness of conditions that identify kaons can be checked by applying the energy-loss, velocity and coincidence-time cuts to the hadron mass spectrum. The mass in the hadron arm is inferred from the measured momentum and time-of-flight as:

$$m = \frac{p}{c}\sqrt{\frac{1}{\beta^2} - 1}. \tag{7.9}$$

The hadron mass spectrum with a cut on kaons is shown in Fig. 7.32, with a clear peak centered at $m \approx 500$ MeV/c^2 that corresponds well to the kaon rest-mass. This confirms that proper cut conditions have been chosen for kaon identification. By applying the same cuts that correspond to the kaons to the ADC spectra from the Čerenkov detector the detection probability for kaons can be evaluated for each segment, like in previous sections. Despite the fact that kaons were well below the Čerenkov emission threshold at this kinematical set-up, the detection probability for kaons is non-zero, as shown in Fig. 7.33. The detection probability for kaons per segment, at 1.5 photo-electrons detection threshold, is $\approx$ 10%. Signals above 1 p.e. produced by kaons can be explained in the same manner as for protons at higher beam-currents: kaon induced δ-electrons with momentum above the detection threshold, random coincidences of PMT noises with the trigger, or scintillations produced in the coating inside the diffusive box.

By applying the kaon cut to the missing-mass spectrum two peaks corresponding to Λ and Σ^0 rest-masses appear. Random background events, identified as accidental coincidence events are subtracted. In Fig. 7.31 we see there are many accidental

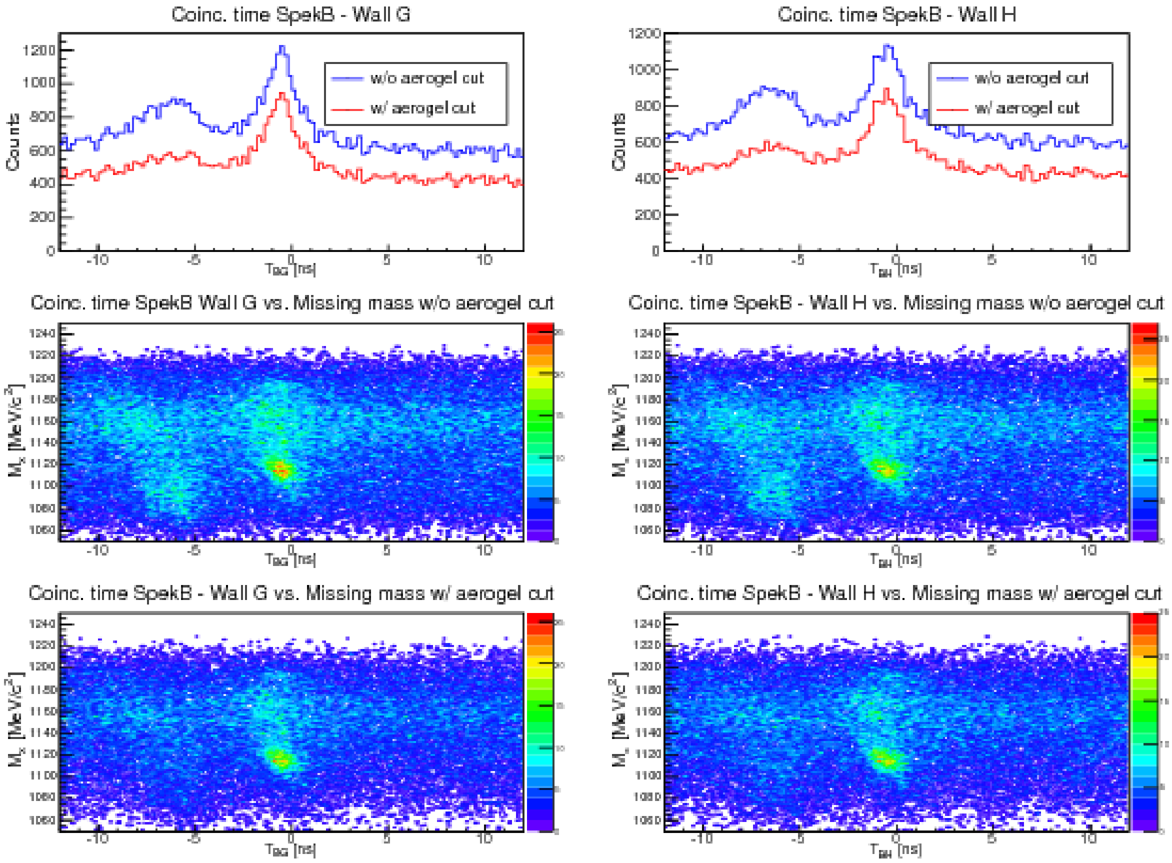

Figure 7.31: Top: coincidence-time between KAOS wall G (left column)/H (right column) and Spec. B with and without aerogel cut. Middle and bottom: measured missing-mass (see Eq. (2.31)) vs. coincidence-time with cut on kaons and with or without additional cut on aerogel. Yellow-red area corresponds to events from the $p(\vec{e}, e'K^+)\Lambda$ reaction. All spectra include kaon dE/dx and β cut.

events in the coincidence-time spectrum between KAOS wall G/H and Spec. B. Even though a correct cut on coincidence-time is chosen, some accidental events are simultaneously selected together with true events and must be subtracted. This is done by applying two cuts on coincidence-time: one around the main peak, which contains true and accidental events and another cut far away from the main peak with the same width, which contains only the accidental events, as shown in Fig. 7.34. To get any histogram with true events only the histogram with the second cut has to be subtracted from the same histogram with the first cut. This can be written as:

$$\text{histo}_T = \text{histo}_{TA} - \text{histo}_A, \tag{7.10}$$

where histo_T is the histogram with the true events only, histo_{TA} is the histogram with the cut around the main coincidence-time peak and therefore contains true

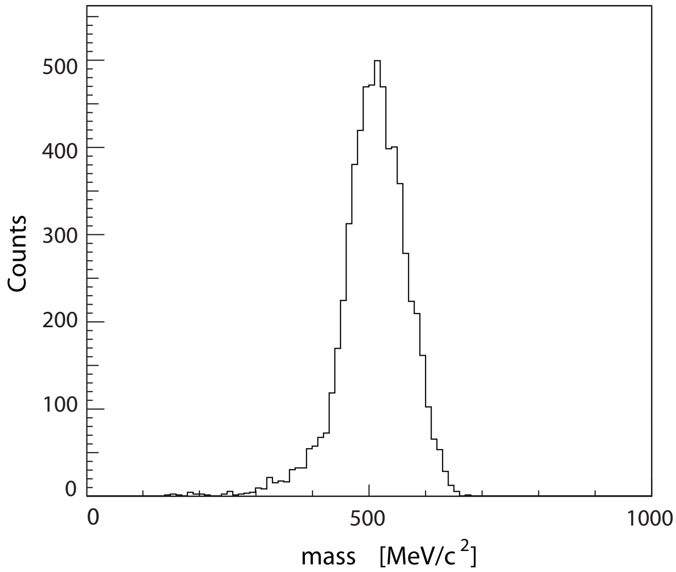

Figure 7.32: The hadron mass spectrum with a cut on kaons. About $\approx$ 6300 kaons have been identified in total with Kaos at $\theta_K = 37.6°$ relative to he incident beam direction, p = 460 Mev/c central momentum and with E_e = 1.5 GeV beam energy.

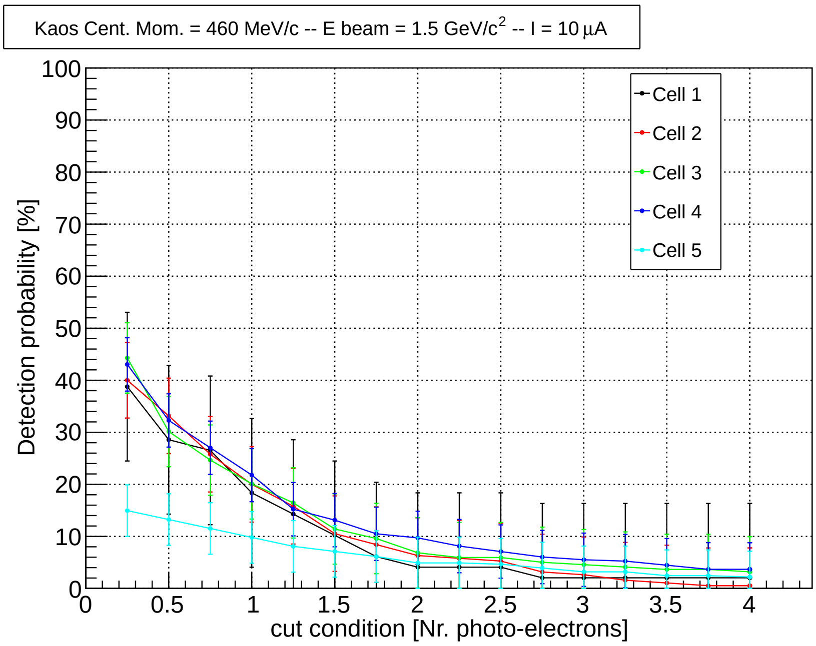

Figure 7.33: The detection probability in each segment of the Čerenkov detector at various threshold conditions for kaons at 460 MeV/c central momentum in Kaos with track quality set to $Q > 0.005$.

and accidental events, and histo$_A$ is the histogram where the cut away from the main peak has been applied and contains background only. Note: histo in (Eq. 7.10) is not the coincidence-time spectrum but any other histogram with a cut on coincidence-time. For example, the Eq. (7.10) for the missing-mass spectrum with true events can be rewritten as:

$$M_x(\text{true}) = M_x(t_{TA-} < t_c < t <_{TA+}) - M_x(t_{A-} < tc < t_{A+}), \tag{7.11}$$

where t_c is coincidence-time, $t_{TA\pm}$ define coincidence-time peak (with true and accidental events) and $t_{A\pm}$ define range of coincidence-time with accidental events only.

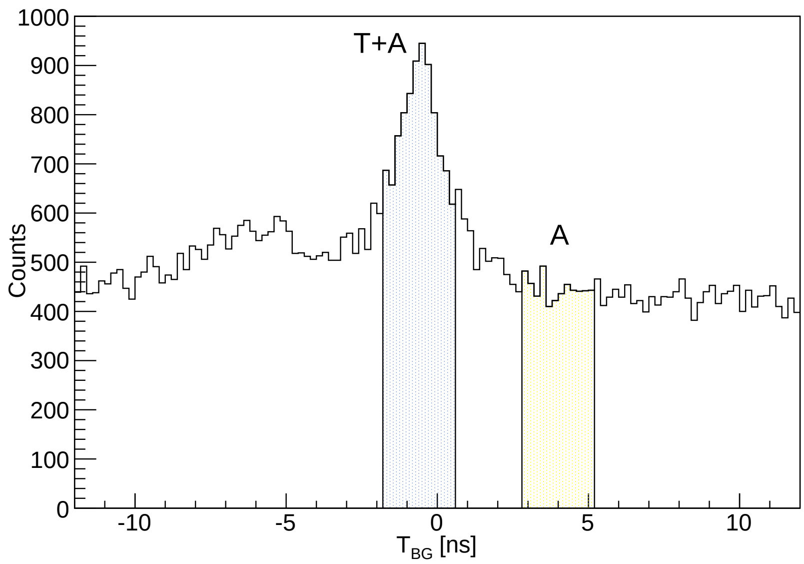

Figure 7.34: Coincidence-time spectrum for the $p(\vec{e}, e'K^+)\Lambda$ reaction. The cut regions for selecting true and accidental events (blue) and for accidental events only (yellow) are shown. The width of each shaded region is 2.4 ns.

The contribution of accidental events to the missing-mass spectrum is shown in Fig. 7.35. If the kaon cut is applied, true and random background events are seen in the spectrum (blue area). A cut on the accidental events does not give any peaks in the missing-mass spectrum and clearly shows the contribution of the background (yellow area). By subtraction of accidentals (blue histogram minus yellow histogram) the missing-mass spectrum with true events only gives a large peak at $M_x \approx 1115$ MeV/c^2, that matches well with the Λ rest-mass. Another small peak is seen at $M_x \approx 1190$ MeV/c^2 that corresponds to the Σ^0 hyperon.

7.5.3 Kaon electro-production cross-section

The purpose of this part of the thesis is to demonstrate that the Čerenkov detector operated in an experiment in which kaons were cleanly identified so that cross-section can be deduced. More accurate analysis of cross-section and interpretation is performed by colleagues in the A1 Collaboration.

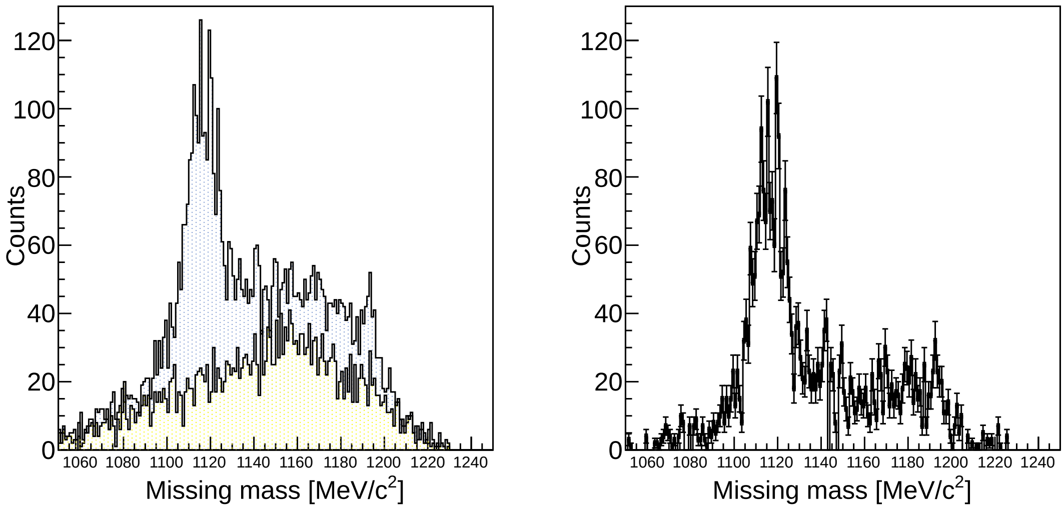

Figure 7.35: Missing-mass spectrum in the $p(\vec{e}, e'K^+)\Lambda$ reaction. The yellow histogram shows the missing-mass distribution of random coincidences (left). With accidental subtraction method the true coincidences events give a missing-mass spectrum with a clear peak at $M_x \approx 1115$ MeV/c^2 (right).

By identifying the Λ peak in the missing-mass spectrum in Fig. 7.35 (right) the cross-section for kaon electro-production can be calculated. The events in missing-mass spectrum within the limits defined by $|M_x - M_\Lambda| < 10$ MeV/c^2, with $M_\Lambda =$ 1116 MeV/c^2, are identified as events corresponding to the kaon electro-production process, $p(e, e'K^+)\Lambda$.

By using this cut on the missing-mass the kaons produced via this process are identified. The distribution of kaons over scattering angle in $K\Lambda$ center-of-mass system within Kaos acceptance is shown in Fig. 7.36.

The differential cross-section in the laboratory frame $d\sigma/d\Omega$ is directly related to the reaction rate $\dot{N}$ seen by the detector, covering a solid angle $\Delta\Omega$:

$$\dot{N}(\Delta\Omega) = \mathcal{L}\frac{d\sigma}{d\Omega}\Delta\Omega, \tag{7.12}$$

with the proportionality factor $\mathcal{L}$, called luminosity. It is defined as:

$$\mathcal{L} = \Phi_a N_b, \tag{7.13}$$

where Φ_a is the flux of the projectiles a and N_b is the number of scattering centers b [112].

The total number of particles detected in the solid angle covered by the spectrometer is:

$$N = \int_t \mathcal{L}dt \int_\Omega \frac{d\sigma}{d\Omega} A(\Omega) d\Omega + N_{\text{BG}}, \tag{7.14}$$

where $A(\Omega)$ is the acceptance function of the spectrometer, t is the collection time and N_{BG} denotes the background. In a (double arm) experiment, where one detector can determine the energy E' of the scattered electron, two particles are detected in coincidence. In our case the kaons were detected by KAOS in coincidence with the scattered electrons detected by Spectrometer B. The cross-section in the $K\Lambda$ center-of-mass system to be measured is five-fold:

$$\frac{d\sigma}{dE_{e'}d\Omega_{e'}d\Omega_K^*} = \Gamma_{\mathrm{v}}\frac{d\sigma_{\mathrm{v}}}{d\Omega_K^*}, \tag{7.15}$$

with the introduction of flux of virtual photons, Γ_{v} (see Eq. (2.27)). The "solid angle" is: $\Delta\Omega^* = \Delta E_{e'}\Delta\Omega_{e'}\Delta\Omega_K^*$ and the Eq. (7.14) becomes:

$$N = \int_t \mathcal{L}dt \int_\Omega \Gamma_{\mathrm{v}}(Q^2, W)\frac{d\sigma_{\mathrm{v}}}{d\Omega_K^*}A(\Omega)d\Omega^* + N_{\mathrm{BG}}, \tag{7.16}$$

With the assumption that $d\sigma_{\mathrm{v}}/d\Omega_K^*$ is constant in a single bin Ω^* the cross-section can be calculated for each bin as:

$$\frac{d\sigma_{\mathrm{v}}}{d\Omega_K^*} = \frac{N - N_{\mathrm{BG}}}{\int_t \mathcal{L}dt \int_\Omega \Gamma_{\mathrm{v}}(Q^2, W)A(\Omega)d\Omega^*}. \tag{7.17}$$

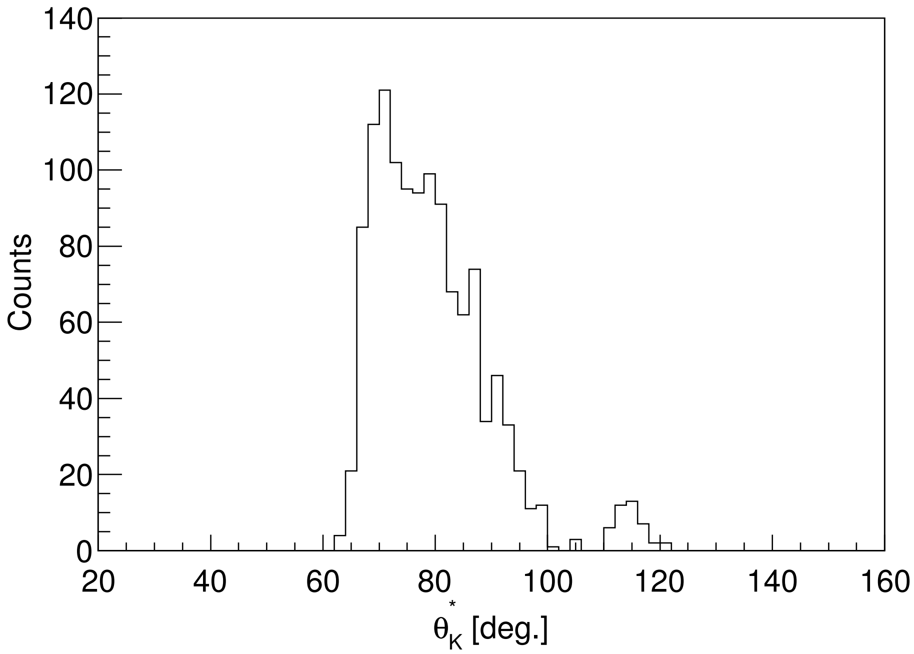

Figure 7.36: Measured kaon scattering angle in the $K\Lambda$ center-of-mass system. Empty bins are out of KAOS acceptance. The gap at $\theta_K^* \approx 110°$ is probably caused by the particle absorption in the MWPC detector frame, but this is currently under investigation.

The quantity $\int_t \mathcal{L}dt$ is called integrated luminosity with units of [(area)$^{-1}$]. In a thin target with thickness l, exposed to the beam with cross-sectional area S, we have $N_b = n_b \cdot l \cdot S$ scattering centers, where n_b is the particle density. The flux is just the number of projectiles a hitting the target per unit area and per unit time: $\Phi_a = \dot{N}_a/S$. By inserting this into Eq. (7.13) the integrated luminosity can be rewritten as:

$$\int_t \mathcal{L}dt = \int_t \dot{N}_a \cdot n_b \cdot l \cdot dt = N_a \frac{N_b}{S} = \frac{Q_a}{e_0}\tilde{\rho}, \tag{7.18}$$

where Q_a is the collected charge in time t and $\tilde{\rho}$ is the target area density.

The total collected charge for the data taken into analysis is $Q_a \approx 5.1$ C, which gives together with known target properties and the dead time correction integrated luminosity of $\int_t \mathcal{L}dt \approx 1930$ fbarn^{-1}.

In order to get the cross-section, the acceptance function of the Kaos spectrometer, $A(\Omega)$, needs to be integrated over the phase-space $\Delta\Omega^*$ with limits that extend beyond the physical acceptance of the spectrometer. The acceptance, with values between 0 and 1, was determined using the simulation package `Geant4` by the A1 Collaboration. The integration of the acceptance over phase-space is performed by the Monte-Carlo simulation of the experiment with reaction products generated isotropically in the solid angle.

With background subtraction, described in subsection 7.5.2, the differential kaon virtual photo-production cross-section can be calculated using Eq. (7.17). To study the dependence of the cross-section on the $K\Lambda$ center-of-mass scattering angle, measured distribution of scattering angle $dN/d\theta_K^*$ (Fig. 7.36) needs to be divided by integrated luminosity and integrated acceptance. The differential cross-section data points for the $p(e, e'K^+)\Lambda$ reaction at $\langle Q^2 \rangle = 0.05$ (GeV/c)^2, $\langle \epsilon \rangle = 0.4$, $\langle W \rangle = 1726$ MeV and $\langle \phi \rangle = 40°$. within experimental acceptance are shown in Fig. 7.37 and compared to variants of K-Maid models, the Saclay-Lyon model and the Regge-plus-resonance model.

The original K-Maid has been calculated through the interactive version available on-line [39], while K-Maid reduced and Saclay-Lyon models have been calculated by the computer code written by Petr Bydžovský, version 30. 11. 2009. The RPR model has been calculated by the computer code from the Theoretical nuclear physics and statistical physics group at the University of Ghent [113].

For more accurate analysis data should be scaled to the center of the electron-arm acceptance through the introduction of a scaling function inside the phase-space integral as well as the correction due to radiative and energy losses should me taken into account.

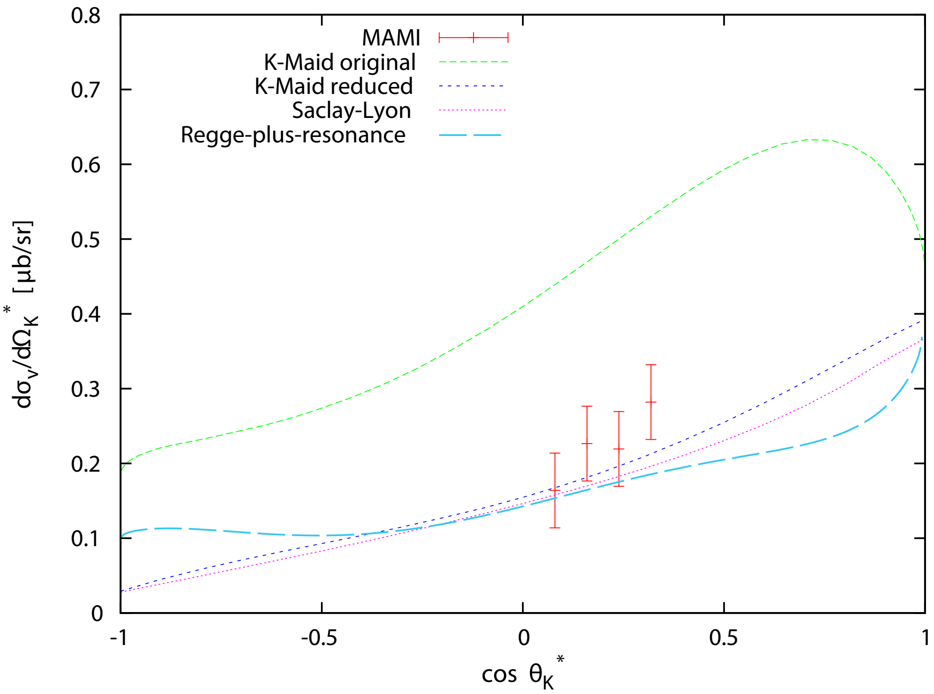

Figure 7.37: Measured differential cross-section for kaon electro-production as a function of $K\Lambda$ center-of-mass scattering angle at $\langle Q^2 \rangle = 0.05$ (GeV/c)^2, $\langle \epsilon \rangle = 0.4$, $\langle W \rangle = 1726$ MeV and $\langle \phi \rangle = 40°$. The measured data (MAMI) is compared to variants of K-Maid model, the Saclay-Lyon model and the Regge-plus-resonance model.

CHAPTER 8

Conclusions

For the effective separation of the rare kaons from the abundant pions in hypernuclear electro-production experiments a threshold aerogel Čerenkov counter has been designed, constructed and mounted onto the KAOS spectrometer in the experimental hall of the A1 Collaboration at the MAMI facility.

For the radiator silica aerogel has been chosen. The refractive index has been chosen to be $n = 1.055$, which gives the effective π/K separation in the momentum range between 600 and 1400 MeV/c. Aerogel from two different manufacturers has been used for the counter: hydrophobic aerogel from Matsushita (Japan) with dimensions of $11.5 \times 11.5 \times 1$ cm^3 and hydrophilic aerogel produced jointly by Boreskov Institute of Catalysis and Budker Institute of Nuclear Physics (Russia) with dimensions of $5 \times 5 \times 2$ cm^3.
Crucial aerogel optical properties have been measured, such as the absorption length, Λ_{abs}, and the scattering length, Λ_{sc}, in the wavelength region from 200 to 800 nm. It has been found that in the wavelength region of $\lambda > 350$ nm the aerogel from BIC/BINP has a constant absorption length of $\Lambda_{\text{abs}} \approx 10.6$ cm, while the aerogel from Matsushita has an absorption length of $\Lambda_{\text{abs}} \approx 7.2$ cm. The scattering length has a λ^4-dependence, which is typical for Rayleigh scattering. In case of the BIC/BINP aerogel it is $\Lambda_{\text{sc}} \approx 2.8$ cm at $\lambda = 400$ nm while for the Japanese aerogel it is $\Lambda \approx 1.4$ cm.
A drop in the transmittance has been observed in hygroscopic aerogel due to absorption of moisture from the air. Optical properties have been recovered by a heating procedure, where the aerogel has been baked in the oven for about 5 hours at 500 °C.

The total thickness of the aerogel layer in the Čerenkov counter is $d = 3$ cm and the surface area is $H \times W = 45$ cm $\times$ 150 cm which coincide with the acceptance area of KAOS. The bottom layer, with 1 cm thickness, is dominated by Matsushita aerogel, while the top layer, with 2 cm thickness, is populated by BIC/BINP aerogel. Aerogel tiles are fixed by a mesh of thin tungsten wires. The diffusive box is segmented into six identical cells, divided by thin inner walls. All segments are tilted by $\varphi = 35°$ relative to the aerogel plane, which is the same as the average angle of incoming particles. Inside each segment additional reflective surfaces are used to reflect the light directly towards phototube entrance windows.

Two different phototube models have been used for light detection: 10 R1250 PMTs and 2 R877-100 PMTs, both from Hamamatsu and of 5" in diameter. The main difference arises from the photo-cathode material: R1250 use bialkali photocathode, while R877-100 use a super bialkali cathode with much higher quantum efficiency that can go up to 35%. These PMTs are sensitive in the wavelength-region that matches well the transmitted radiation spectrum of aerogel and reach the quantum efficiency maximum at $\lambda \approx 350$ nm.
Another important difference between the two PMT models is the gain factor, which is compensated by an amplifier with a signal charge amplification factor of ≈ 200, that is placed right after the R877-100 PMT.
Due to small fluctuations of gain factor all phototubes have been calibrated by means of high voltage adjustments. The preliminary calibration was performed by measuring the PMT response to a pulsed light source and more accurate calibration was done afterwards during preliminary test experiments.

All inner surfaces have been covered by highly reflective coating to prevent the absorption of generated Čerenkov photons or with aluminized reflective mylar foils to reflect specularly Čerenkov light directly towards photocathodes and shorten the mean path length of detected photons.

A detailed simulation of optical processes and performance at various geometries of the detector has been performed using `SLitrani`. The optimal geometry was found by simulating the detector at different PMT effective area and quantum efficiency, aerogel thickness, angle of the reflective surface inside, height, width, angle of the diffusive box. The number of detected photons increases with aerogel thickness until a plateau is reached with a typical time of arrival $t \approx 2$ ns. The angle between the reflective surface has been simulated. The best angle was found to be at $x = 3a/4$ mirror coverage.
The performance of the detector has been simulated for one of the kinematical set-ups in the real experiment. The simulations have been done with electron (positron) and pion beam with fixed momentum of 720 MeV/c. The average number of photo-electrons is $N_{\rm pe} \approx 4.3$ for pions and $N_{\rm pe} \approx 6.8$ for positrons, which is in fair agreement with the experimental data. With threshold set to 1.5 photo-electrons, the expected efficiency of Čerenkov counter at this kinematical set-up is 97% for positrons and 86% for pions.
The number of transitions, reflections and absorptions of photons between and inside different detector materials and surfaces has been simulated as well. There are many photons reflected inside the aerogel due to total reflection and most of the photons are absorbed inside the aerogel because of short absorption length (in comparison with air).
The simulations also show that some of the Čerenkov photons might escape to the

neighboring segment through aerogel, especially if the photons are generated near the inner walls.

A series of in-beam and cosmics tests have been performed with the aerogel Čerenkov counter (Sec. 7.1). The first set of tests were done with cosmic ray with Čerenkov detector sandwiched between two scintillator walls inside spectrometer Kaos. The mean value of ADC SUM spectrum was 7.6 photo-electrons. By considering 1 p.e. signals and above as true events the efficiency of Čerenkov detector with cosmics is $\approx 95\%$.

The preliminary in-beam test with positrons was done at low beam-current $I = 300$ nA, Kaos central momentum 900 MeV/c and aerogel thickness of $d = 2$ cm. The efficiency at this set-up of Čerenkov counter evaluated from ADC SUM with threshold set to 0.5 p.e. is $\approx 98\%$, while the efficiency per segment at the same threshold is $\approx 92\%$.
At higher beam-current, i.e. $I = 1.5$ μA, the detector was exposed to a flux of particles dominated by positrons and a minor fraction of protons. The average efficiency provided by positrons with threshold at 0.5 p.e. in individual segment is $\approx 90\%$, while the efficiency evaluated from ADC SUM is $\approx 99\%$. The decrease of efficiency in individual segment can be explained by slightly inefficient track reconstruction at higher particle rates. The so-called detection probability of protons is non-zero and with threshold set to 1.5 p.e. the average detection probability per segment is $\approx 12\%$. This might arise from proton induced δ-electrons with momentum above detection threshold, random coincidences between PMTs noise and common trigger or scintillation light produced in the coating inside the diffusive box. By setting the detection threshold to 1.5 p.e. a clear separation between protons and background (positrons) is achieved, e.g. in the coincidence-time spectrum.
At $I = 2.0$ μA beam-current one row of aerogel was taken out in the mid-plane to reduce the large background of positrons. Despite larger particle rate the hit multiplicity was reduced to ≈ 0.9 due to lack of radiator material in the mid-plane, which is populated mostly by background. But unfortunately the average efficiency per segment with positrons was reduced below 90% at 0.5 p.e. threshold condition. The decrease of efficiency can be explained by absorption of Čerenkov photons in the light supporter in the mid-plane that substituted the missing aerogel.

Another test with protons, pions and kaons was performed at two different central momenta in Kaos spectrometer: 720 MeV/c and 460 MeV/c, respectively. At 720 MeV/c central momentum the average detection probability for protons is well below 10% at 0.5 p.e. detection threshold, but the efficiency of pions is only $\approx 82\%$ at the same threshold. Such low efficiency of pions is explained by low relative light yield at this momentum, which is ≈ 0.7.
At 460 MeV/c the pions are just slightly above the Čerenkov threshold with relative light yield of ≈ 0.3 only. Drop of efficiency per segment is even larger in this kinematics, especially in the segment positioned at lower momentum side. For efficient

π^+/K^+ separation a higher central momentum is needed.

In the first test experiment (Sec. 7.4) the efficiency with positrons was high, but also the beam-current and thus the occupancy, so that track selection was hard to do (background and proton tracks are likely to be in the same segment as a positron track per event). On the other hand, in the second test experiment (Sec. 7.5) the efficiency with pions was low because of low momentum. To have a Čerenkov detector with good separation power, lower particle rate is needed with one particle type highly above the momentum threshold. As shown in subsection 7.5.1 the relative light yield for pions of $\approx 70\%$ (KAOS central momentum was set to 720 MeV/c) is just enough for sufficient pion/proton separation. To generalize this for efficient separation between other particle species, we need one particle below the threshold and the other with at least $\approx 70\%$ relative light yield, which corresponds to $(\beta\gamma)/(\beta_t\gamma_t) \approx 2$ (see Fig. 5.2). Since the integration time in the ADC module was 200 ns (width of the gate signal) the particle rate shall not exceed ≈ 5 MHz per segment. We saw in subsections 7.4.1 and 7.5.1 that separation was satisfactory at lower beam-currents and thus lower particle flux, while at higher beam-currents (e.g. 2 μA) the separation power has deteriorated. We must also bear in mind that the background rate increases quadratically with the beam-current. To summarize, in order to have an optimal performance of the aerogel Čerenkov counter for the separation of two particle species, the rate shall not exceed ≈ 5 MHz per segment with one particle type highly above the threshold with at least $(\beta\gamma)/(\beta_t\gamma_t) \approx 2$.

At beam-energy $E_e = 1.5$ GeV (and 460 MeV/c KAOS central momentum) the efficiency test with kaons was performed. They are identified by the energy-loss, velocity and coincidence-time between KAOS and spectrometer for detection of scattered electrons. Even though kaons are below the detection probability, signals produced by kaons above 1 p.e. have been detected. The detection probability at 1.5 photo-electron detection threshold with kaons is $\approx 10\%$ per segment. This can be explained by the same manner as for protons at higher beam-currents.

In missing-mass spectrum a clear peak has been found at $M_x \approx 1115$ MeV/c^2, which corresponds to the Λ hyperon rest-mass.

By applying a cut on kaons and cut in missing-mass with $|M_x - M_\Lambda| < 10$ MeV/c^2 the events corresponding to $p(e, e'K^+)\Lambda$ reaction have been identified. From all data taken into account the integrated luminosity with dead-time correction is $\int_t \mathcal{L}dt \approx 1930$ fbarn^{-1}. From the measured kaon scattering angle, integrated luminosity and experimental acceptance function the differential kaon virtual photo-production cross-section has been calculated at $\langle Q^2 \rangle = 0.05$ (GeV/c)^2, $\langle \epsilon \rangle = 0.4$, $\langle W \rangle = 1726$ MeV and $\langle \phi \rangle = 40°$. The average cross-section at $\theta_K^* \approx 80°$ has been found to be $d\sigma_\mathrm{v}/d\Omega_K^* \approx 0.2$ μbarn/srad.

APPENDIX A

PMT technical details

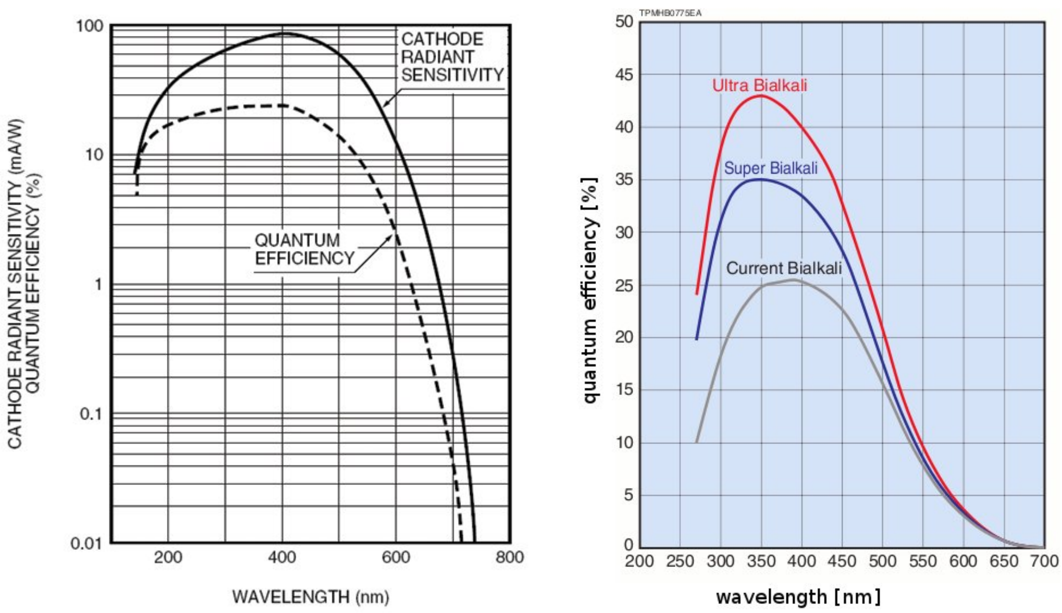

Figure A.1: Quantum efficiency as a function of a wavelenght for Hamamatsu phototubes R1250 (left) and R877-100 with super bialkali photo-cathode (right). Figures adopted from Hamamatsu catalog.

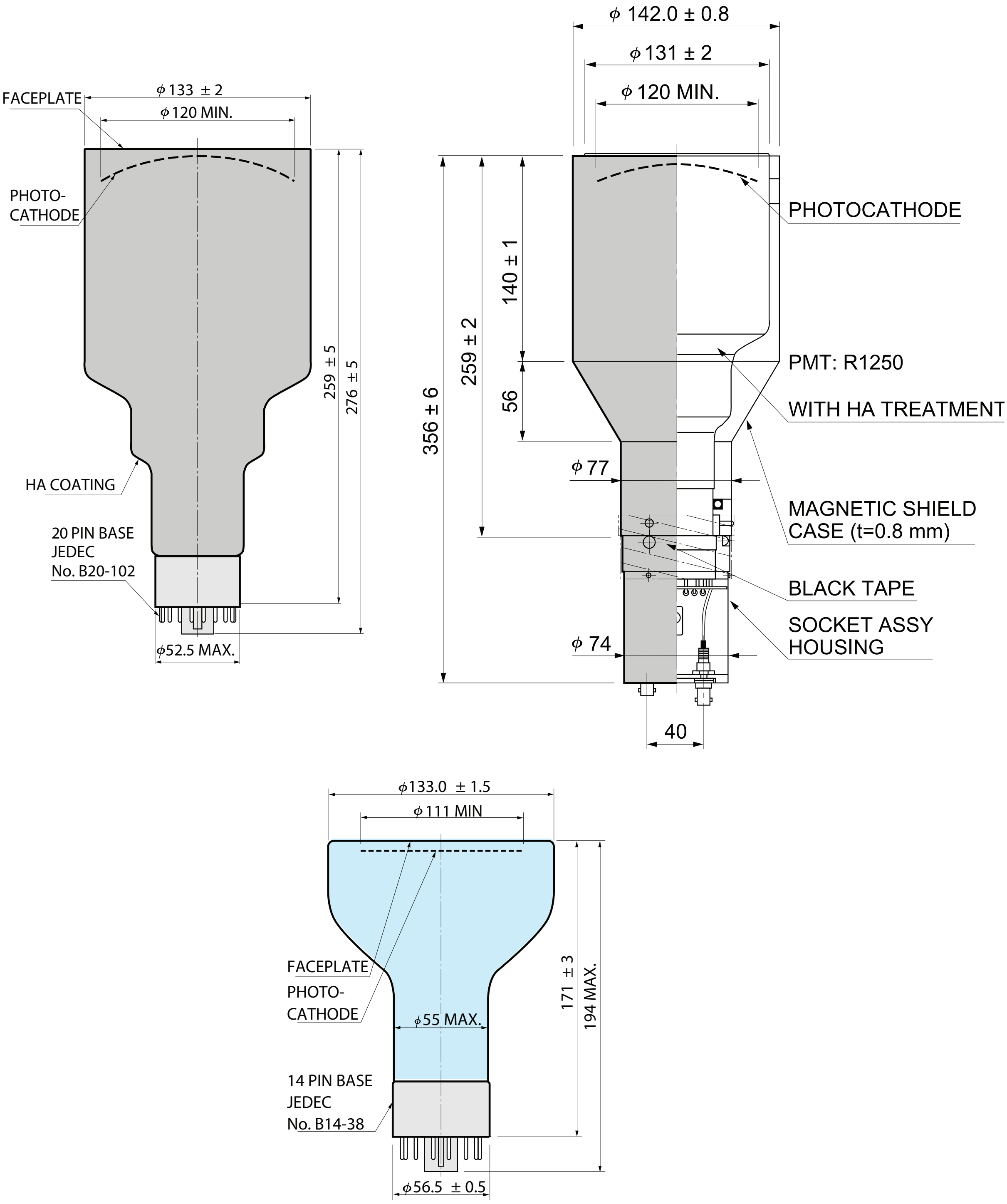

Figure A.2: Dimensional outline for bare Hamamatsu R1250 PMT (top left) and H6527 assembly (top right) and R877-100 PMT (bottom). All units are in mm. Figures adopted from Hamamatsu catalog.

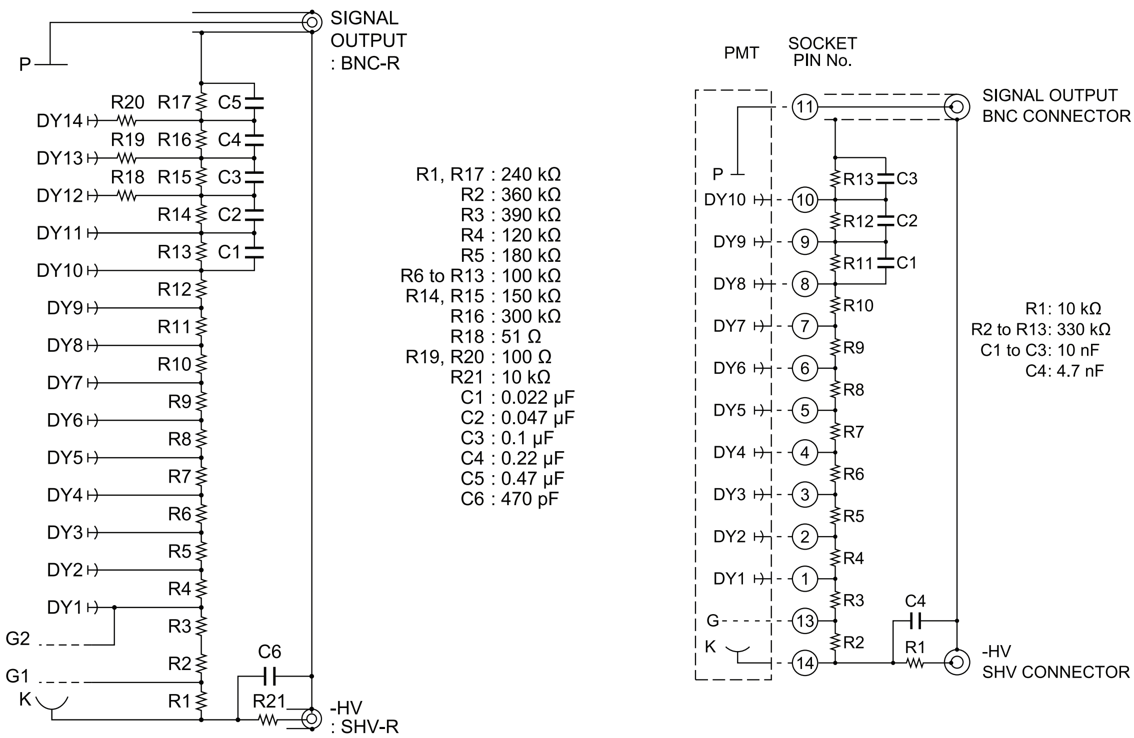

Figure A.3: Diagrams for socket assemblies; for H6527 phototube assembly (left) and E6316-01 for R877-100 PMT (right). Figures adopted from Hamamatsu catalog.

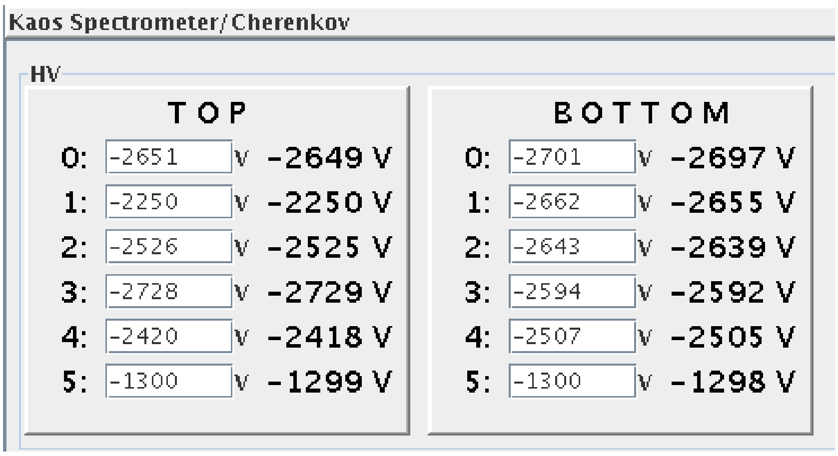

Figure A.4: A screen-shot from mezzo GUI control system of set and read-out HV values for all 12 phototubes used during the experiments described in this thesis.

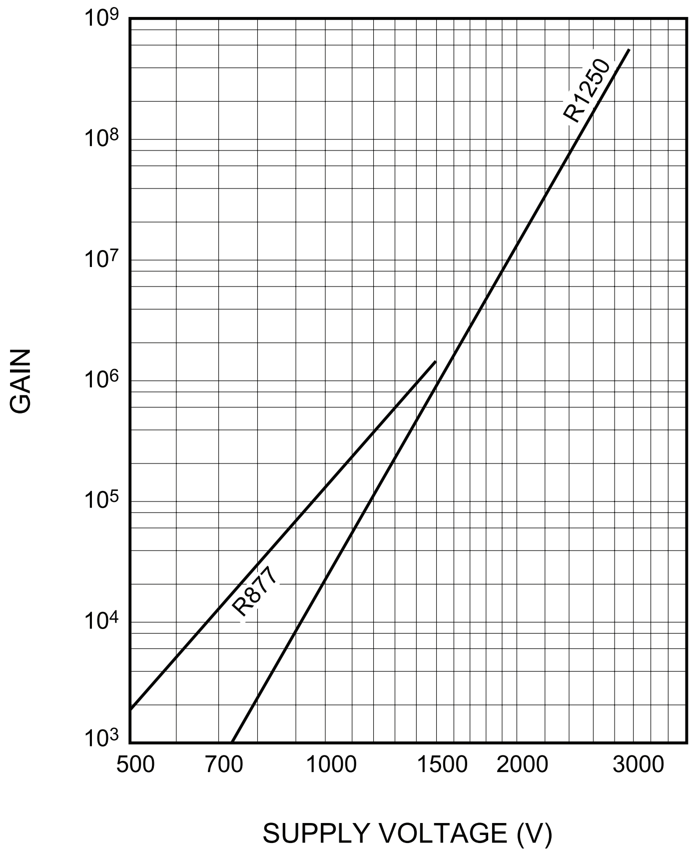

Figure A.5: Gain characteristics as a function of HV supply. Figures adopted from Hamamatsu catalog.

APPENDIX B

Čerenkov counter technical drawings

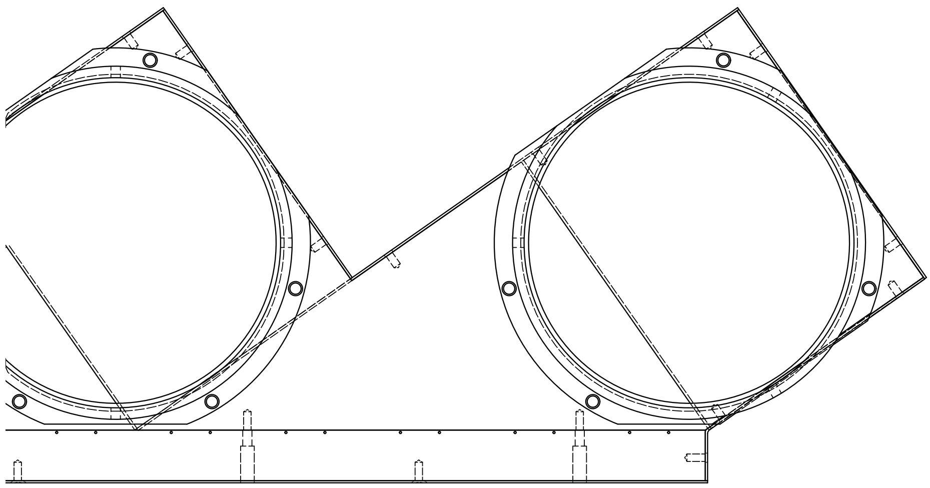

Figure B.1: Transparent drawing of the aerogel box and last segment from Čerenkov detector. The side bar from from aerogel box is attached to the diffusive box by the screws placed inside the holes drilled through the side bar.

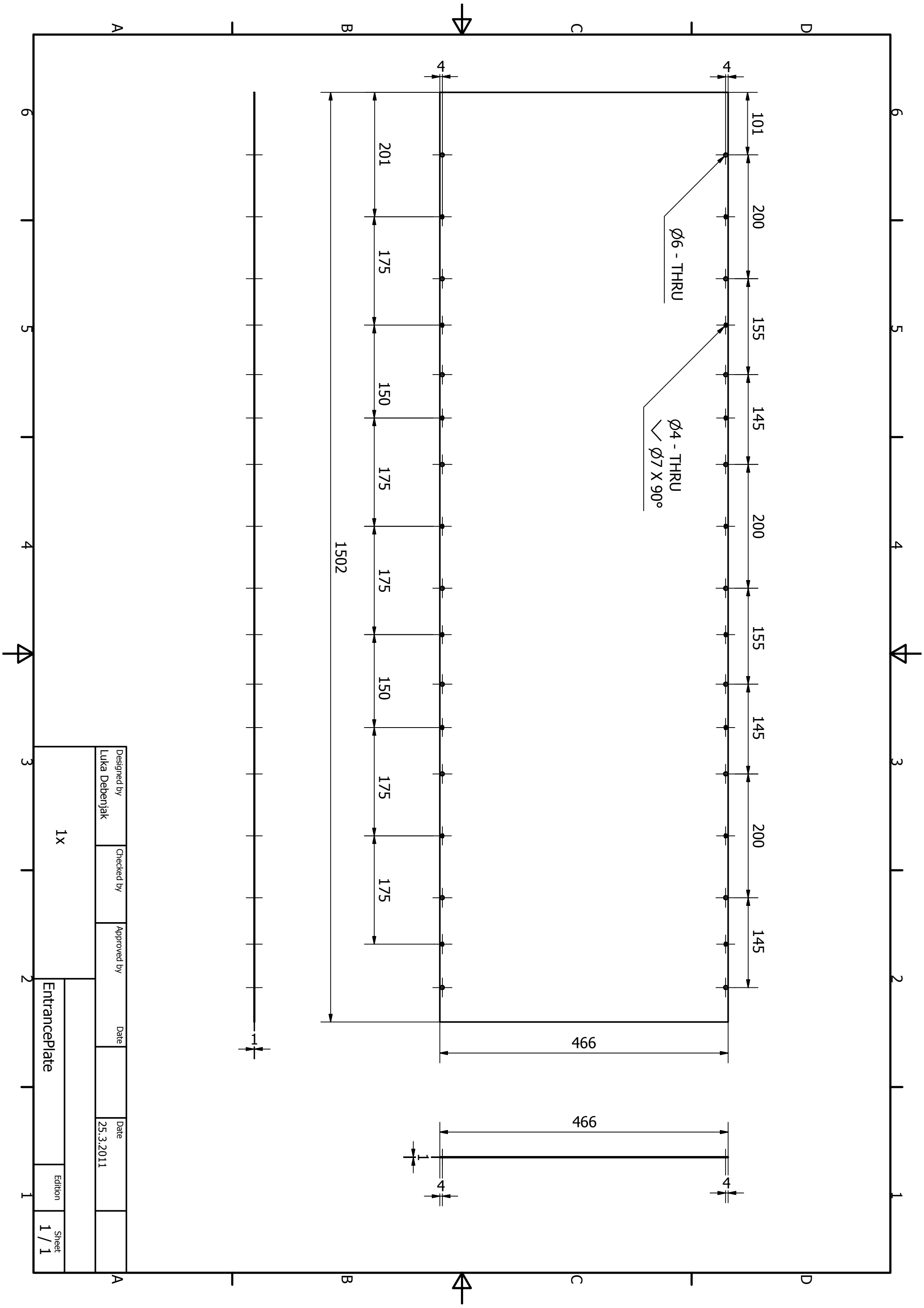

Figure B.2: Drawing of the plate from the aerogel basket. Particles enter into detector through this plate.

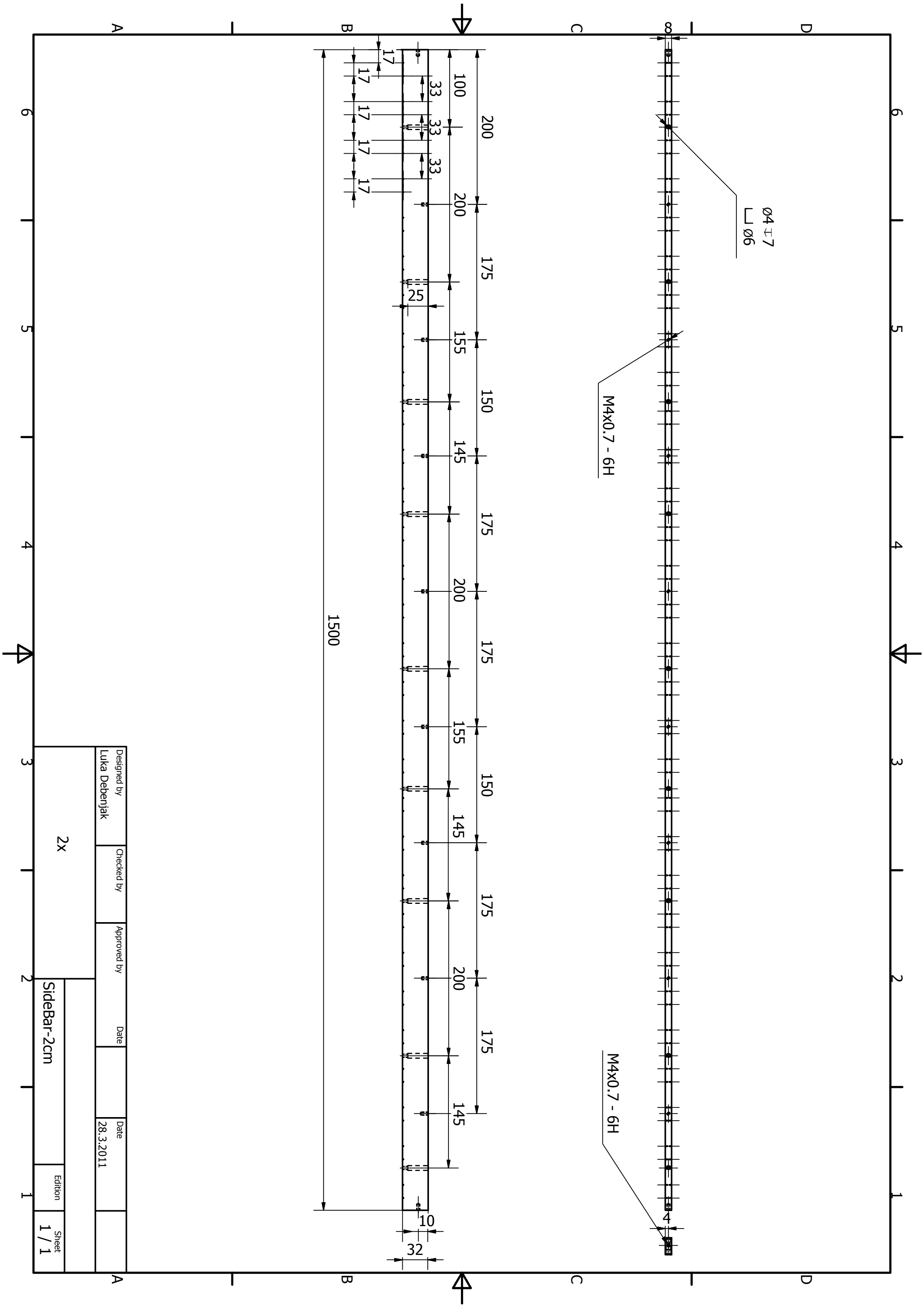

Figure B.3: Drawing of the side bar of the aerogel basket.

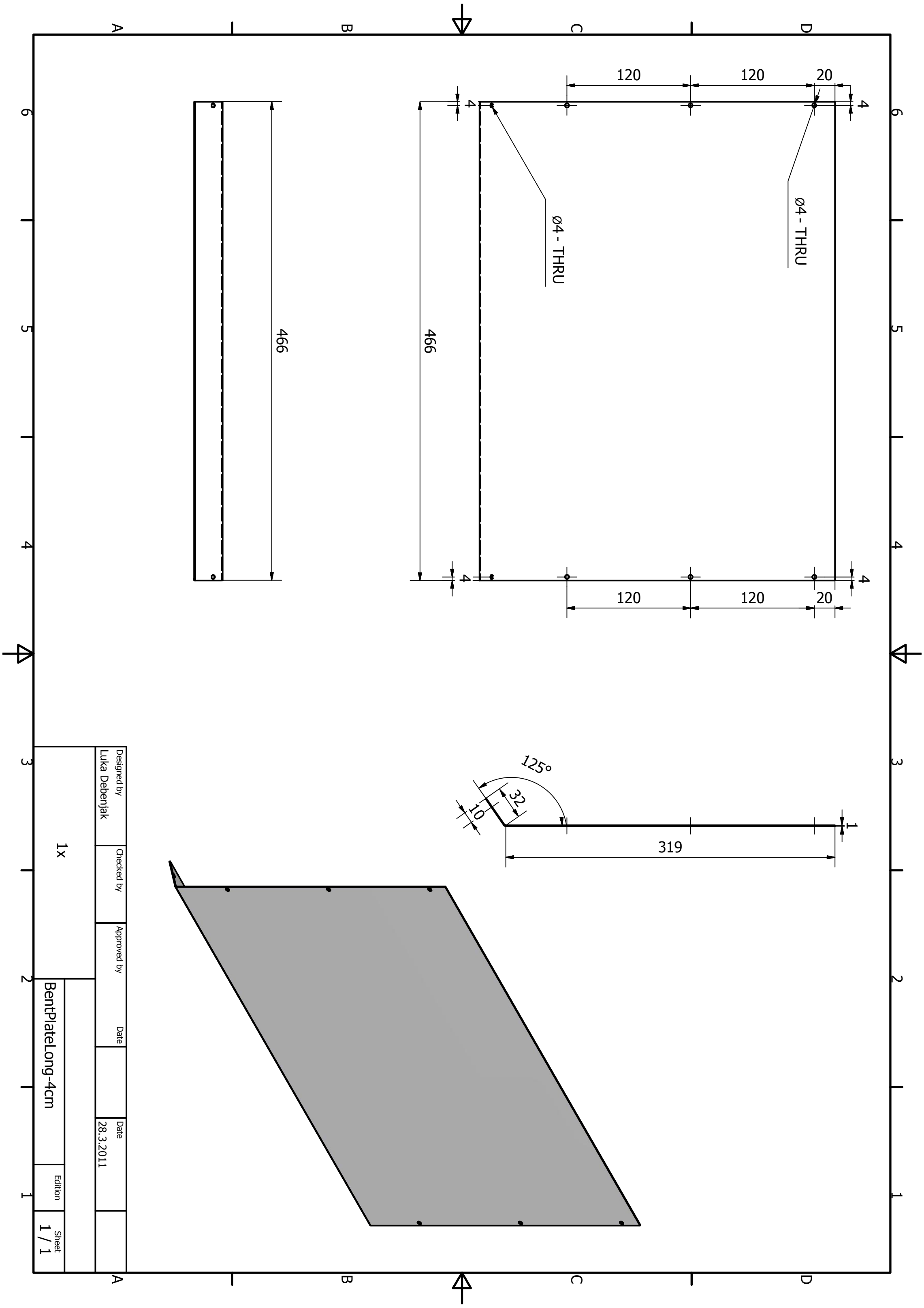

Figure B.4: Drawing of the bent plate that closes the first segment and aerogel basket.

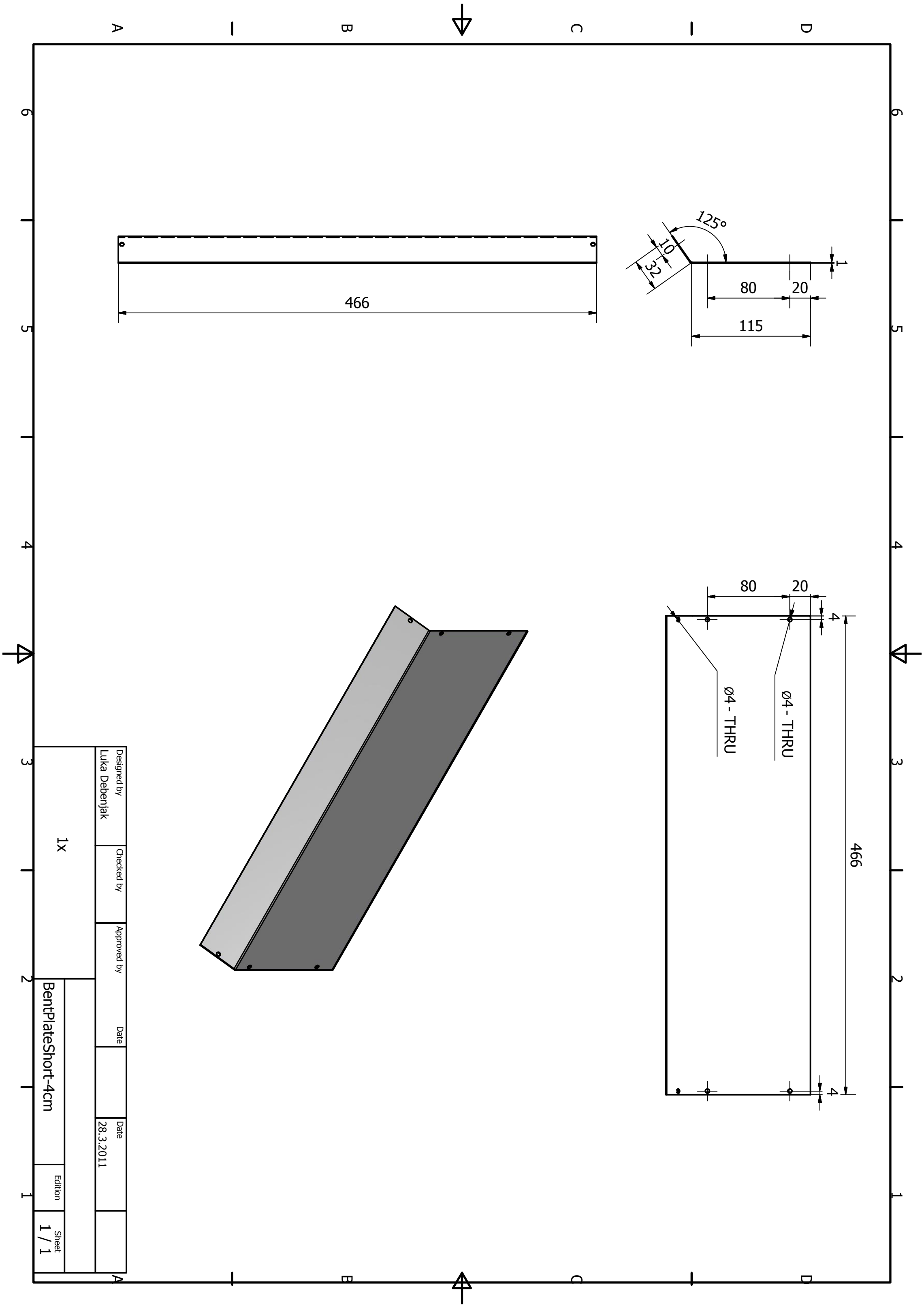

Figure B.5: Drawing of the bent plate that closes the last segment and aerogel basket.

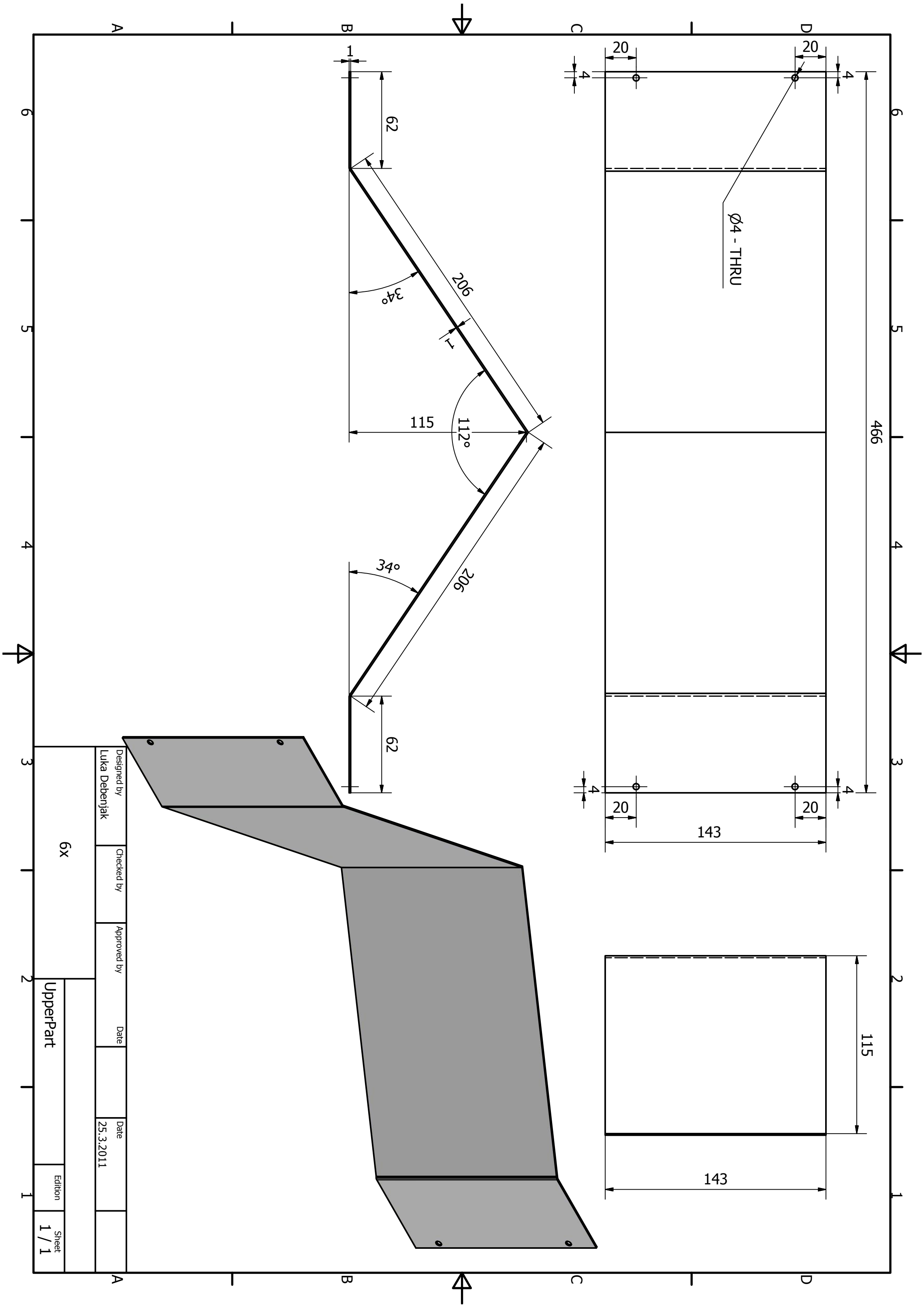

Figure B.6: Drawing of the bent plate that is covered with aluminized mylar to imitate mirrors.

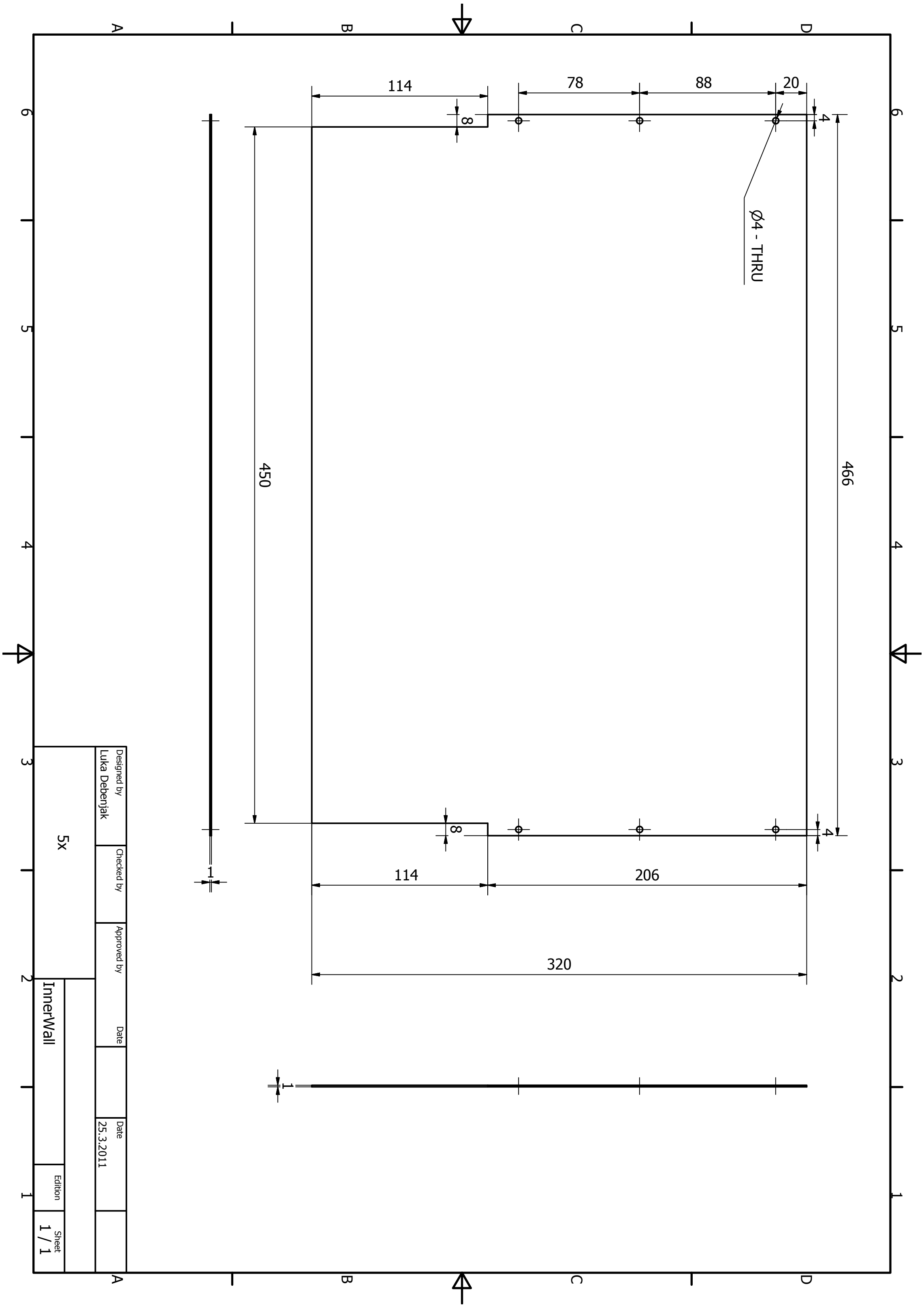

Figure B.7: Drawing of the inner walls to separate neighboring segments.

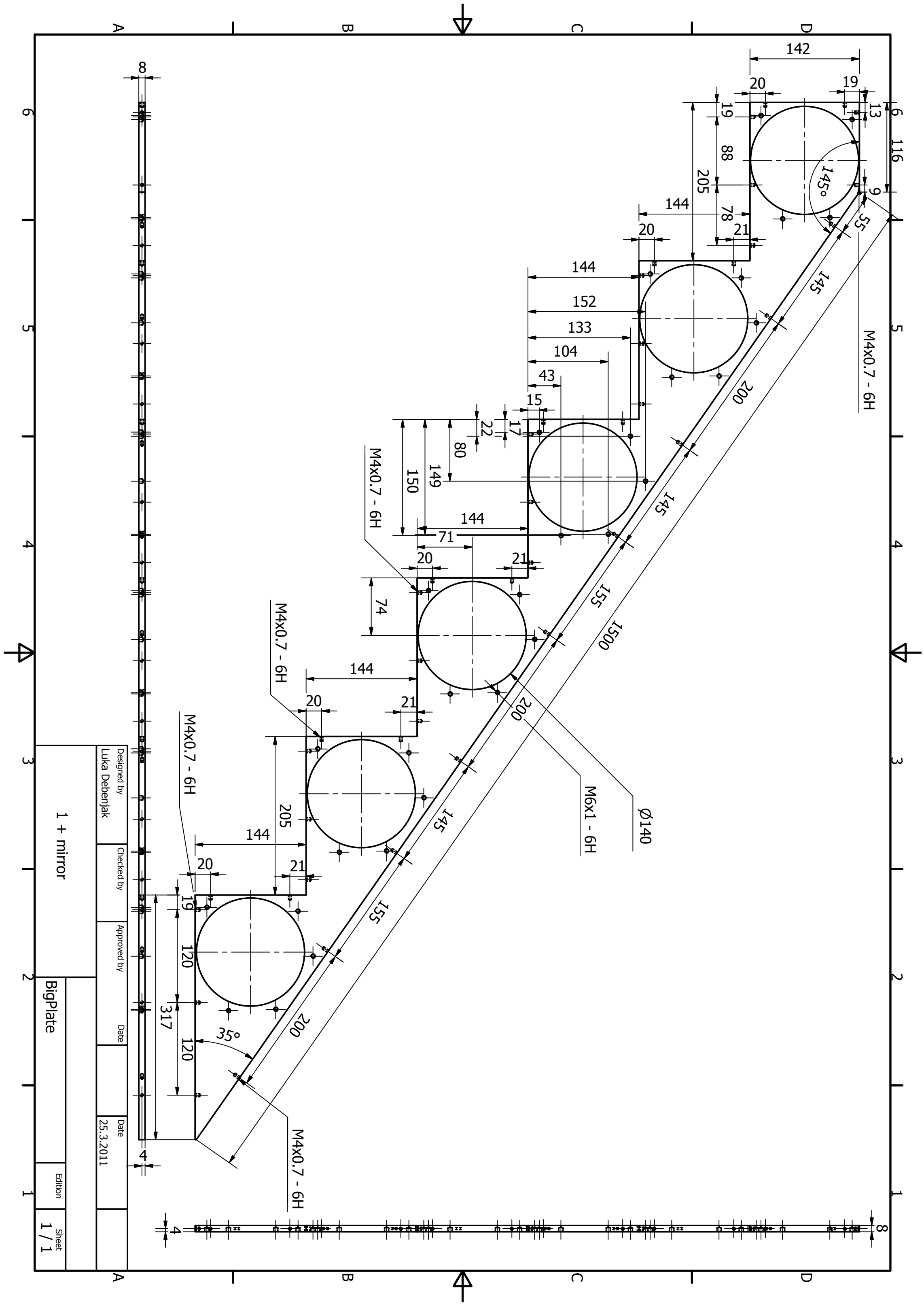

Figure B.8: Drawing of the plate that supports photomultipliers.

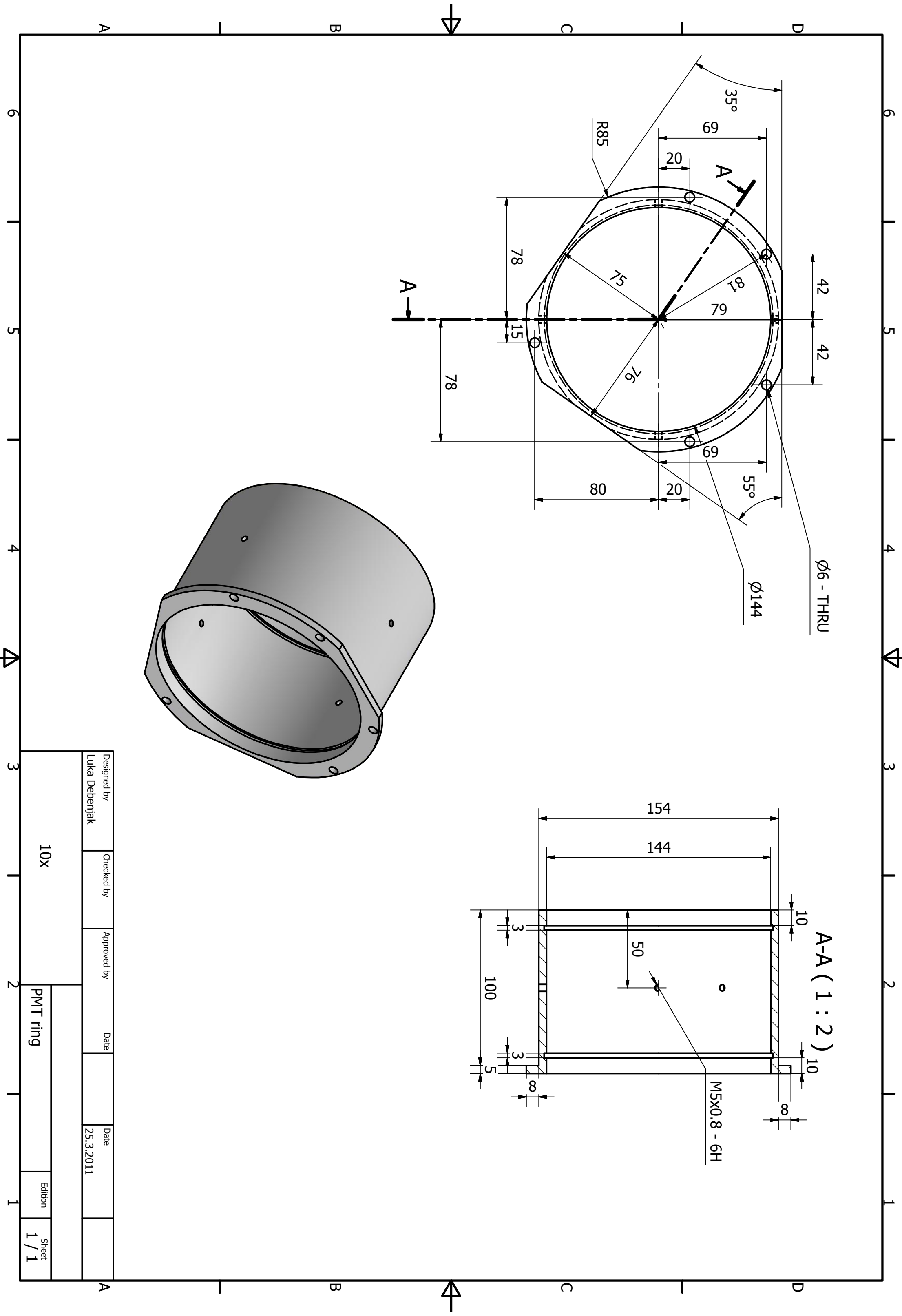

Figure B.9: Drawing of the ring that holds PMT in a fixed position.

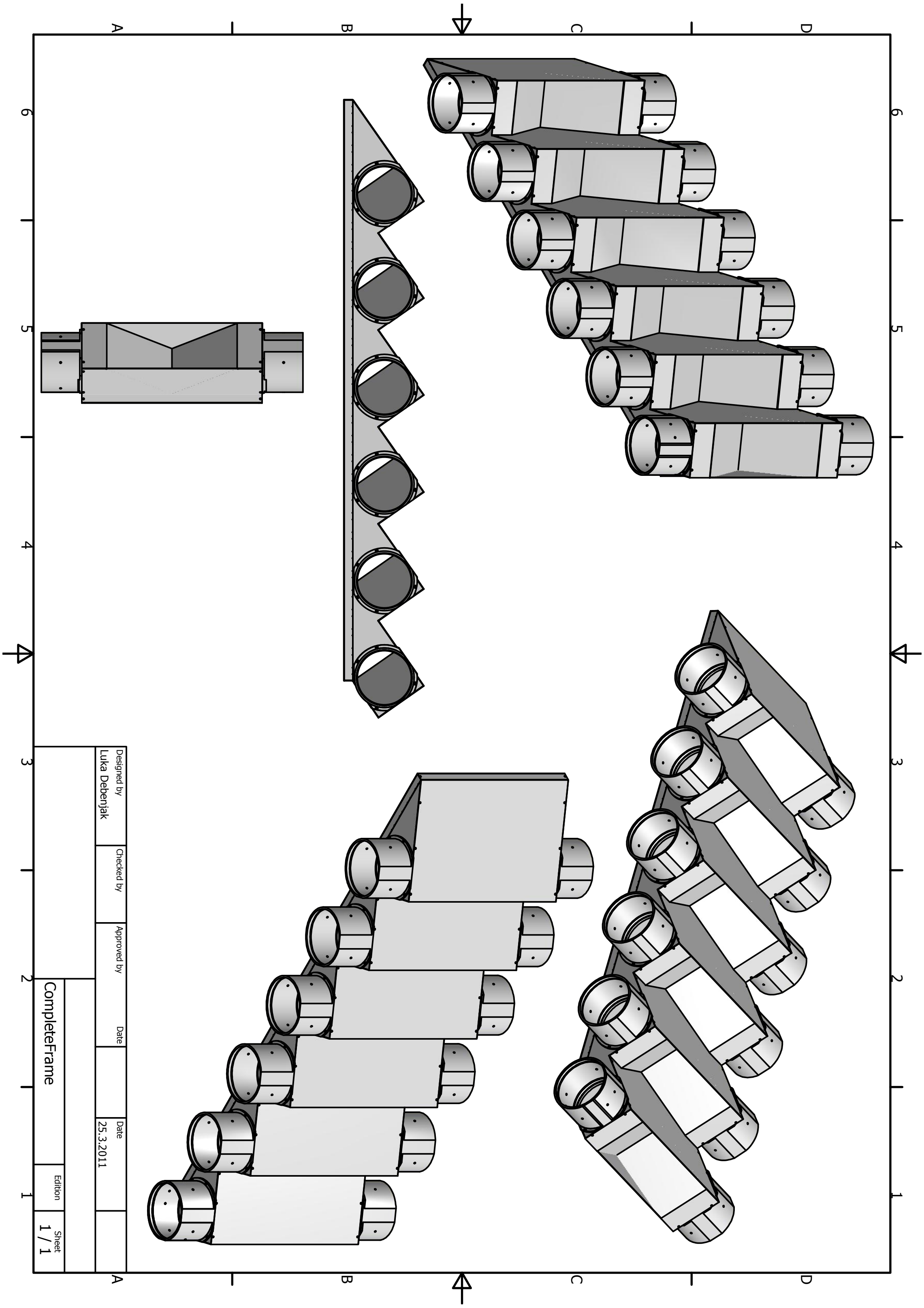

Figure B.10: Drawing of the complete detector frame at various orientations.

APPENDIX C

Simulation input data

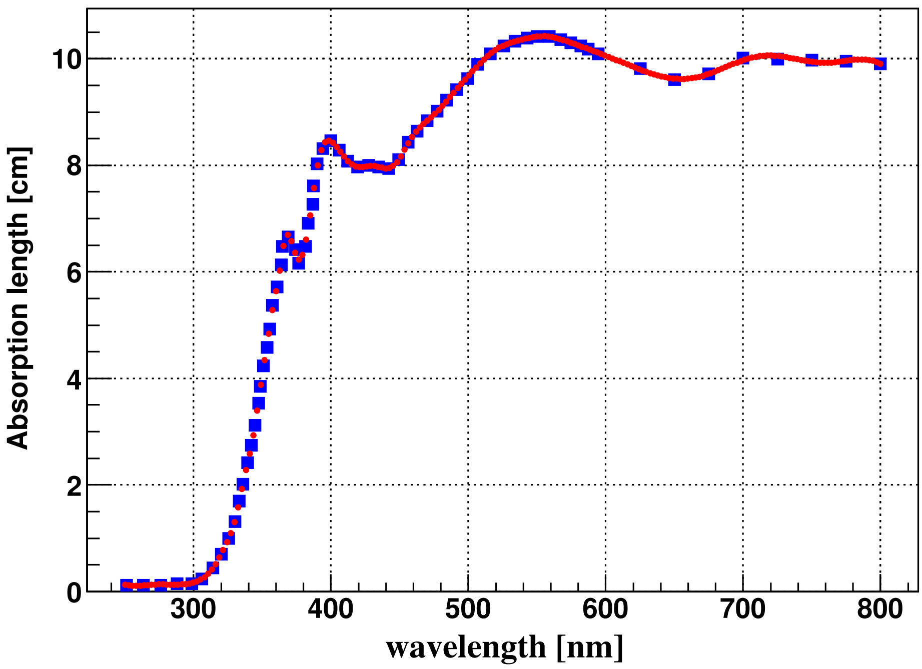

Figure C.1: The absorption length of the PMT window.

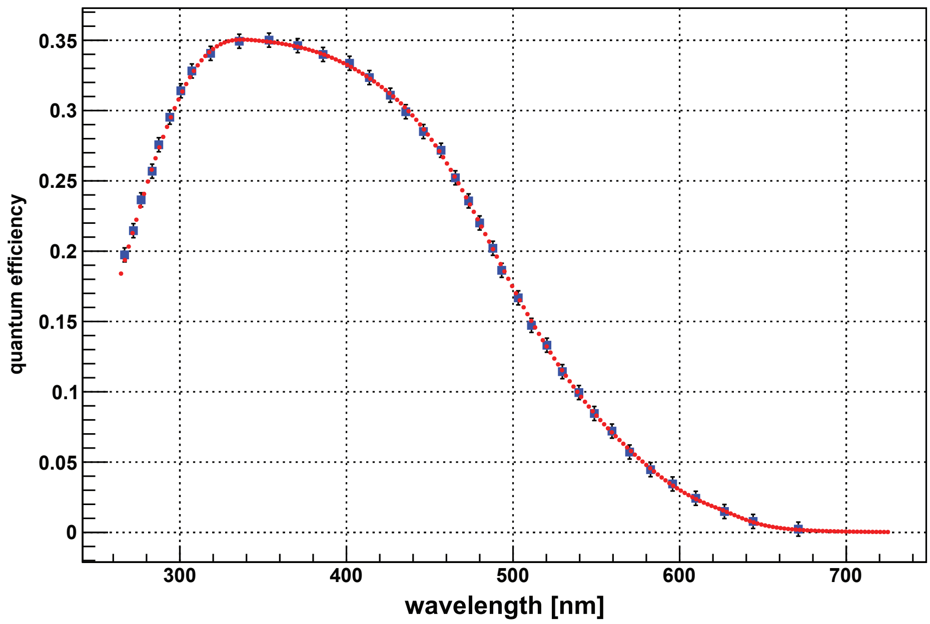

Figure C.2: Quantum efficiency of super bialkali photocathode for R877-100 PMT.

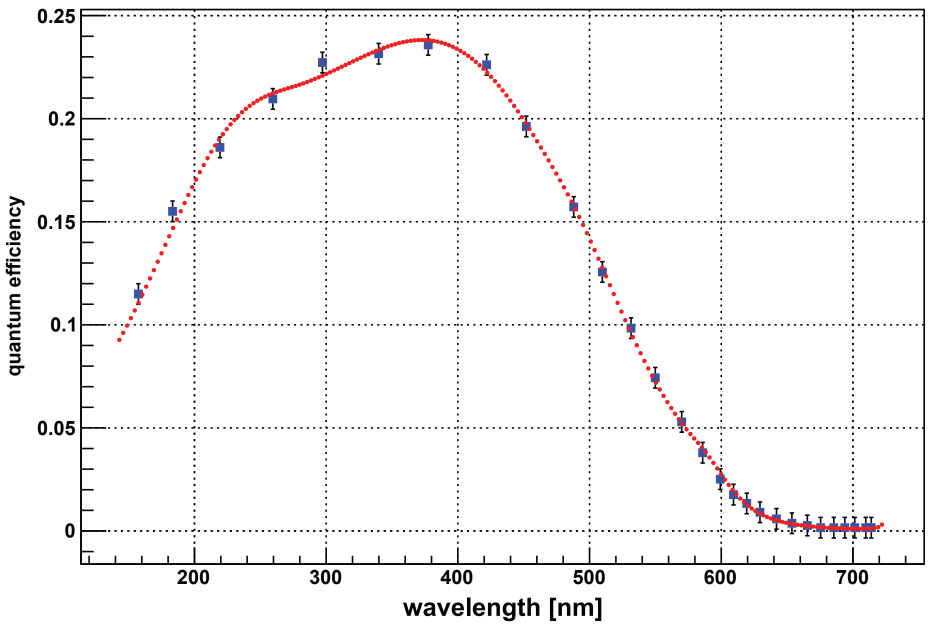

Figure C.3: Quantum efficiency of normal bialkali photocathode for R1250 PMT.

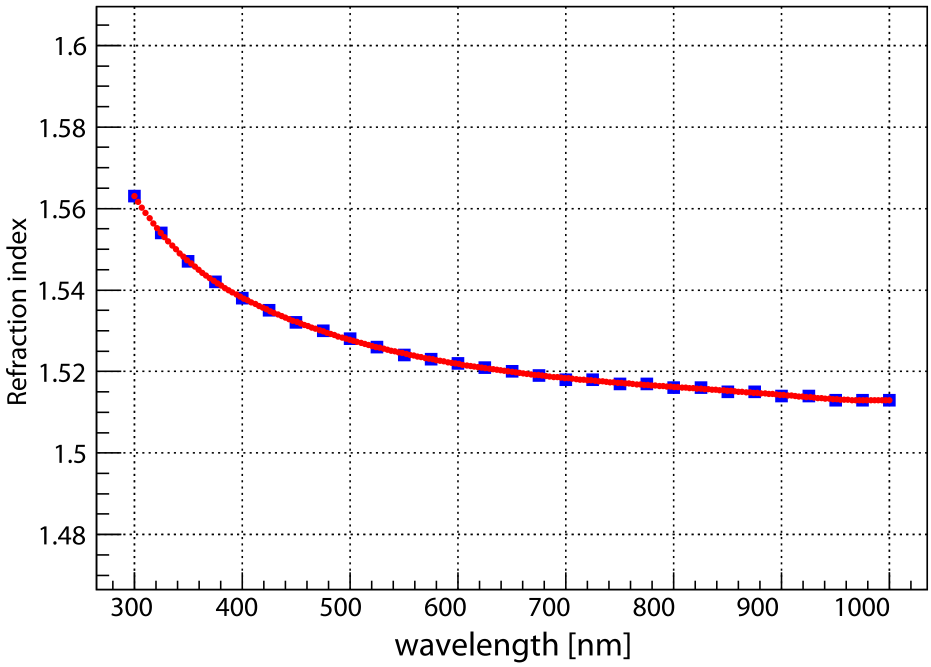

Figure C.4: The refractive index of the PMT window.

APPENDIX D

Arrangement of aerogel

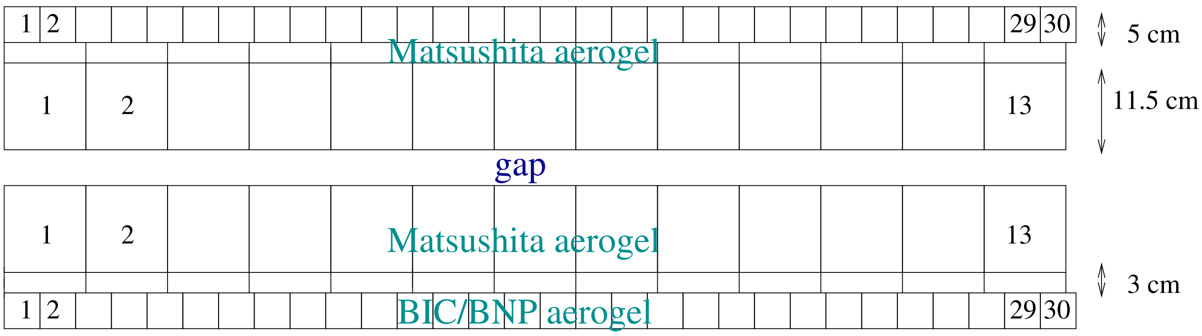

Figure D.1: Drawing of aerogel arrangement in the bottom layer for the beam-time for hypernuclei research via pionic decay: 24.5.-14.6. 2011 and described in Sec. 7.4.

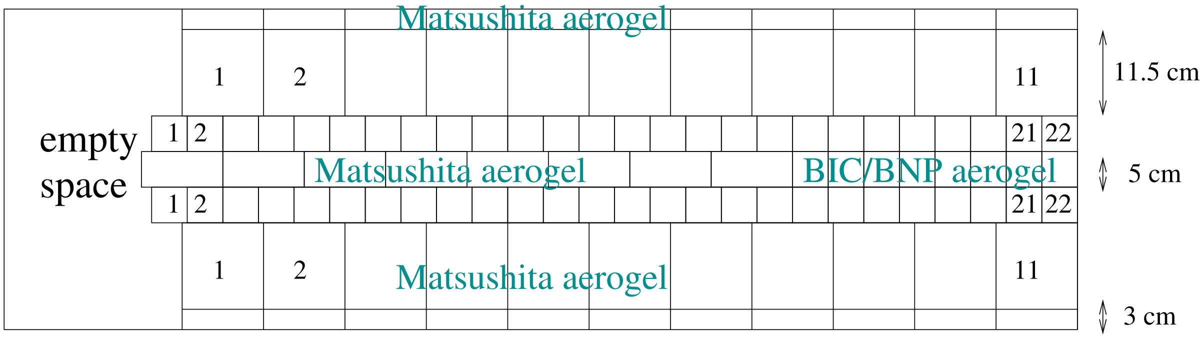

Figure D.2: Drawing of aerogel arrangement in the bottom layer for the kaon electro-production experiment for polarized cross-section measurement: 15.11.-5.12. 2011 and described in Sec. 7.5.

Bibliography

[1] C. N. Brown *et al.*, *Coincidence measurements of single K^+ electroproduction*, Phys. Rev. Lett. **28** (1972) 1086-1089.

[2] C. J. Bebek *et al.*, *Electroproduction of K^+ mesons in the forward direction*, Phys. Rev. Lett. **32** (1974) 21-24.

[3] C. J. Bebek et al., *Scalar-transverse separation of electroproduced $K^+\Lambda$ and $K^+\Sigma$ final states*, Phys. Rev. D **15** 3082 (1977) 3082-3084.

[4] P. Brauel *et al.*, *Electroproduction of π^+n, π^-p and $K^+\Lambda$, $K^+\Sigma^0$ final states above the resonance region*, Zeit. Phys. C **3** (1979) 101.

[5] G. Niculescu *et al.* (E93-018 Collaboration) *Longitudinal and transverse cross sections in the $^1H(e, e'K^+)\Lambda$ reaction.* Phys. Rev. Lett. **81** (1998) 1805-1808.

[6] R. M. Mohring *et al.* (E93-018 Collaboration) *Separation of the longitudinal and transverse cross sections in the $^1H(e, e'K^+)\Lambda$ and $^1H(e, e'K^+)\Sigma^0$ reactions.* Phys. Rev. C **67**, 055205 (2003).

[7] M. Iodice (E98-108 Collaboration), *Kaon electro-production on protons at JLab in Hall A*, Eur. Phys. J. A **17** (2003) 345-348.

[8] P. Markowitz and A. Acha, Proceedings of the Sendai International Symposium Strangeness in Nuclear and Hadronic Systems (SENDAI08) 2008.

[9] T. Gogami, *Study of Light Hypernuclei by the $(e, e'K^+)$ Reaction*, Proceedings of the 20th International IUPAP Conference on Few-Body Problems in Physics (FB20) 2012.

[10] P. Ambrozewicze *et al.* (CLAS Collaboration), *Separated structure functions for the exclusive electroproduction of $K^+\Lambda$ and $K^+\Sigma^0$ final states*, Phys. Rev. C **75**, 045203 (2007).

[11] P. Bydžovský and T. Mart, *Analysis of the data consistency on kaon photoproduction with Λ in the final state*, Phys. Rev. C **76**, 065202 (2007).

[12] R. Heine *et al.*, *Recent Status of the MAMI-C Accelerator and First Experiences with the Energy Upgrade towards 1.6 GeV*, Proc. of the iPAC 2010, Kyoto, Japan, 23.-28.05.2010

[13] G. D. Rochester and C. C. Butler, *Evidence for the existence of new unstable elementary particles*, Nature 160 (1947) 855-857.

[14] C. F. Powell. *Mesons*, Rep. Prog. Phys. **13** (1950) 384.

[15] M. Gell-Mann, *Symmetry and currents in particle physics*, in: *Nobel Lectures, Physics 1963-1970*, Elsevier, Amsterdam, 1972.

[16] A. Zenoni, P. Gianotti, *The physics of hypernuclei*, Europhysics News Vol. 33, No.5 (2002) 157-161.

[17] http://en.wikipedia.org/wiki/Baryon.

[18] J. Mareš, P. Bydžovský, A. Gal, *Topics in Strangeness Nuclear Physics*, Springer (2007).

[19] G. Zweig, *An SU(3) model for strong interaction symmetry and its breaking*, CERN Report 8181/Th 8419, CERN, Geneva, Switzerland (1964).

[20] G. Zweig, *An SU(3) model for strong interaction symmetry and its breaking:II*, CERN Report 8419/Th 8412, CERN, Geneva, Switzerland (1964).

[21] M. Gell-Mann, *A schematic model of baryons and mesons*, Phys. Lett. **8** (1964) 214-215.

[22] Patrick Achenbach, *The Kaos Spectrometer at the Mainz Microtron and First Measurements of Kaon Electro-Production*, Habilitation thesis, Johannes-Gutenberg-Universität, Mainz, 2010.

[23] C. Milner, *et al.*, *Observation of Λ-hypernuclei in the reaction* $^{12}C(\pi^+,K^+)^{12}_{\Lambda}C$, Phys. Rev. Lett. **54** (1985) 1237-1240.

[24] P. H. Pile, *et al.*, *Study of hypernuclei by associated production*, Phys. Rev. Lett. **66** (1991) 2585-2588.

[25] M. Akei, *et al.*, *The* (π^+,K^+) *reaction on* ^{12}C *and* ^{56}Fe, Nucl. Phys. A **534** (1991) 478-492.

[26] T. Hasegawa, *et al.*, *Core-excited states of* $^{12}_{\Lambda}C$ *hypernuclei formed in the* (π^+,K^+) *reaction*, Phys. Rev. Lett. **74** (1995) 224-227.

[27] T. Hasegawa, *et al.*, *Spectroscopic study of* $^{10}_{\Lambda}B$, $^{12}_{\Lambda}C$, $^{28}_{\Lambda}Si$, $^{89}_{\Lambda}Y$, $^{139}_{\Lambda}La$, *and* $^{208}_{\Lambda}Pb$ *by the* (π^+,K^+) *reaction*, Phys. Rev. C **53** (1996) 1210-1220.

[28] S. Ajimura, *et al.*, *The* (π^+,K^+) *reaction and light* Λ *hypernuclear spectroscopy*, Nucl. Phys. A **639** (1998) 93c-102c.

[29] H. Hotchi, *et al.*, *Spectroscopy of medium-heavy Λ hypernuclei via the (π^+, K^+) reaction*, Phys. Rev. C **64**, 044302 (2001).

[30] A.K. Kerman and M. S. Weiss, *Superstrange nuclei*, Phys. Rev. C **8** (1973) 408-410.

[31] P. Achenbach *et al.* (A1 Collaboration), *Strange hadrons - strangeness in strongly interacting particles*, Eur. Phys. J. Special Topics **198** (2011) 307-327.

[32] A.S. Raskin and T.W. Donnelly, *Polarization in coincidence electron scattering from nuclei*, Annals of physics **191** (1989) 78-142.

[33] M. Iodice *et al.*, *High Resolution Spectroscopy of $^{12}_{\Lambda}B$ by electroproduction*, Phys. Rev. Lett. **99**, 052501 (2007).

[34] M. Kawaguchi and M. J. Moravcsik, *Photoproduction of K mesons from single nucleons*, Phys. Rev. **107** (1957) 563-569.

[35] R. A. Adelseck and B. Saghai, *Kaon photoproduction: Data consistency, coupling constants, and polarization observables*, Phys. Rev. C **42** (1990) 108-127.

[36] R. A. Williams, C.-R. Ji, and S. R. Cotanch, *Hyperon electroproduction in a crossing and duality constrained model*, Phys. Rev. C **46** (1992) 1617-1635.

[37] T. Feuster and U. Mosel, *Photon and meson induced reactions on the nucleon*, Phys. Rev. C **59** (1999) 460-491.

[38] T. Mart, C. Bennhold, *Evidence for a missing nucleon resonance in kaon photoproduction*, Phys. Rev. C **61**, 012201 (2000).

[39] T. Mart, C. Bennhold, H. Haberzettl, and L. Tiator, *An effective Lagrangian Model for Kaon Photo- and Electroproduction on the Nucleon*, `http://wwwkph.kph.uni-mainz.de/MAID//kaon/kaonmaid.html`.

[40] T. Mizutani *et al.*, Electromagnetic production of associated strangeness, Phys. Rev. C **58** (1998) 75.

[41] M. Guidal, J. M. Laget and M. Vanderhaeghen, *Pion and kaon photoproduction at high-energies: Forward and intermediate angles*, Nucl. Phys. A **627**, 645678 (1997).

[42] M. Guidal, J. M. Laget and M. Vanderhaeghen, *Electroproduction of strangeness above the resonance region*, Phys. Rev. C **61**, 025204 (2000).

[43] T. Corthals, *Regge-plus-resonance approach to kaon production from the proton*, PhD thesis, Ghent University, Belgium, (2007).

[44] T. Corthals, D.G. Ireland, T. Van Cauteren, J. Ryckebusch, *Regge-plus-resonance treatment of the* $p(\gamma, K^+)\Sigma^0$ *and* $p(\gamma, K^0)\Sigma^+$ *reactions at forward kaon angles*, Phys. Rev. C **75**, 045204 (2007).

[45] L. De Cruz, T. Vrancx, P. Vancraeyveld, J. Ryckebusch, *Bayesian inference of the resonance content of* $p(\gamma, K^+)\Lambda$, arXiv:1111.6511 [nucl-th] (2011).

[46] O. Hashimoto and H. Tamura, *Spectroscopy of* Λ *hypernuclei*, Part. Nucl. Phys. **57** (2006) 564-653.

[47] H. Herminghaus *et al.*, *The Design of a Cascaded 800 MeV Normal Conducting C. W. Race Track Microton*, Nucl. Instr. & Meth. **138** (1976) 1-12.

[48] A. Jankowiak, *The Mainz Microtron MAMI - Past and Future*, Eur. Phys. J. **A 28**, s01, (2006) 149-160, doi 10.1140/epja/i2006-09-016-3.

[49] K.I. Blomqvist *et al.*, *The three-spectrometer facility at the Mainz microtron MAMI*, Nucl. Instr. Meth. A **403** (1998) 263-301.

[50] M. O. Distler, *Aufbau und test einer vertikalen Driftkammer*, Diploma thesis, Johannes Gutenberg-Universität, Mainz, 1990.

[51] P. Sauer, *Entwicklung, Aufbau and Inbetriebnahme der vertikalen Driftkammern der Drei-Spektrometer-Anlage am Mainzer Mikrotron MAMI und Studium der Reaktion* $^{12}C(e, e'p)^{11}B$ *für mittlere und hohe Nukleonenimpulse im Kern*, PhD thesis, Johannes Gutenberg-Universität, Mainz, 1995.

[52] R. Böhm, *Eichtung der Szintillations-Triggerdetektoren des Spektrometers A an MAMI*, Diploma thesis, Johannes Gutenberg-Universität, Mainz, 1993.

[53] A. Richter, *Trennung des longitudinalen, transversalen und longitudinal-transvesal inteferirenden Anteils des Wirkungsquerschnitts der Reaktionen* $H(e, e'\pi)$ *in der Nähe der Pionschwelle*, PhD thesis, Johannes Gutenberg-Universität, Mainz, 1994.

[54] Th. Pospischil, *Aufbau und Inbetriebnahme eines Protonen-Polarimeters an MAMI und Messung der Proton-Polarisation in der Reaktion* $p(\vec{e}, e'\vec{p})\pi^0$ *in paralleler Kinematik im Bereich der* Δ*(1232)-Resonanz*, PhD thesis, Johannes-Gutenberg-Universität, Mainz, 2000.

[55] L. Doria, *Polarization observables in virtual compton scattering*, PhD thesis, Johannes Gutenberg-Universität, Mainz, 2007.

[56] P. Merle, *Entwicklung des programmierbaren Koinzidenztriggersystems und Messung von* A_Y^0 *in der Reaktion* $^3\vec{H}e(\vec{e}, e'n)$, PhD thesis, Johannes Gutenberg-Universität, Mainz, 2002.

[57] P. Achenbach *et al.* (A1 Collaboration), *Associated Λ/Σ^0 electroproduction with the Kaos spectrometer at MAMI*, in: E. Epelbaum, H.-W. Hammer, and U.-G. Meißner (Eds.), *Proceedings of the 19th International IUPAP Conference on Few-Body Problems in Physics (FB19), Rheinische Friedrich-Wilhelms-Universit"at, Bonn, 31 August-5 September 2009*, EPJ Web of Conferences 3, 2010, art. no. 07010.

[58] P. Achenbach *et al* (A1 Collaboration), *First measurements of Λ and Σ^0 hyperons in elementary electroproduction at MAMI*, Nucl. Phys. A **835** (2010) 313-316.

[59] P. Achenbach *et al.* (A1 Collaboration), *Exclusive electroproduction of $K^+\Lambda$ and $K^+\Sigma^0$ final states at $Q^2 = 0.030 - 0.055$ (GeV/c)^2* Eur. Phys. J. A **48** (2012) 14.

[60] P. Achenbach *et al.*, *Strange hadronic physics in electroproduction experiments at the Mainz Microtron*, Nucl. Phys. A *881* (2012) 187-198.

[61] S. Sanchez Majos, *Measurement of the unpolarized $K^+\Lambda$ and $K^+\Sigma^0$ electroproduction cross-section off the proton with the Kaos spectrometer.* PhD thesis, Johannes Gutenberg-Universität, Mainz, 2012.

[62] P. Achenbach *et al.* (A1 Collaboration), *Kaon electroproduction with Kaos at MAMI-C, Proceedings XXXII International Workshop on Gross Properties of Nuclei and Nuclear Excitations, Hirschegg, Austria, 11-17 Januar 2004*, pp. 137-142.

[63] A. Esser, *Teilchennachweis und Triggerung mit dem Faserdetektor im Kaos-Spektrometer am Mainzer Mikrotron*, Diploma thesis, Johannes Gutenberg-Universität, Mainz, 2010.

[64] C. Ayerbe Gayoso, *The scintillating fiber focal plane detector for the use of Kaos as a double arm spectrometer*, PhD thesis, Johannes Gutenberg-Universität, Mainz, 2012.

[65] L. Nungesser, *Aufbau und Simulation des Kaos-Spektrometers fr Koinzidenzmessungen in der assoziierten Kaonproduktion*, PhD thesis, Johannes-Gutenberg-Universität, Mainz, 2009.

[66] M. Gmez Rodrguez de la Paz, *Strahltest und Betrieb von Vieldrahtproportionalkammern für das Kaos-Spektrometer*, Diploma thesis, Johannes-Gutenberg-Universität, Mainz, 2008.

[67] F. Schulz, *Teilchenidentifikation unter kleinen Streuwinkeln in der Pionzerfallsspektroskopie von Hyperkernen*, Diploma thesis, Johannes-Gutenberg-Universität, Mainz, 2011.

[68] P. Achenbach *et al.*, *Particle tracking in kaon electroproduction with cathode-charge sampling in multi-wire proportional chambers*, Nucl. Instr. Meth. Phys. Res. A **641** (2011) 105-113.

[69] M. Bösz, *Datenerfassung und Spurerkennung mit den Vieldrahtproportionalkammern für das Kaos-Spektrometer an MAMI*, Diploma thesis, Johannes-Gutenberg-Universität, Mainz, 2009.

[70] W. Klempt, *Review of particle identification by time of flight techniques*, Nucl. Instr. Meth. Phys. Res. A **433** (1999) 542-553.

[71] `http://en.wikipedia.org/wiki/Cherenkov_radiation`.

[72] W. R. Leo, *Techniques for Nuclear and Particle Physics Experiments*, Springer-Verlag, 1994.

[73] D. W. Higinbotham, *Diffusely reflective aerogel Cherenkov detector simulation techniques.* Nucl. Instr. Meth. Phys. Res. A **414** (1998) 332-339.

[74] T. Ferbel, *Experimental techniques in high energy physics* Menlo Park: Addison-Wesley, 1987.

[75] G.J. Lolos *et at.*, *Performance and design characteristics for the Hall A aerogel Cherenkov counters*, Nucl. Instr. Meth. Phys. Res. A **385** (1997) 403-411.

[76] R. Perrino *et at.*, *Performance of the aerogel threshold Cherenkov counter for the Jefferson Lab Hall A spectrometers in the 1-4 GeV/c momentum range*, Nucl. Instr. Meth. Phys. Res. A **457** (2001) 571-580.

[77] E.J. Brash *et at.*, *Operational performance of the Hall A mirror aerogel Cherenkov counter*, . Instr. Meth. Phys. Res. A **487** (2002) 346-352.

[78] S. Marrone *et at.*, *Performance of the Two Aerogel Cherenkov Counters of the JLab Hall A Hadron Spectrometer*, Il Nuovo Cimento B, Vol. 124, issue 01, 99-114.

[79] R. Asaturyan *et al.*, *The aerogel threshold Cherenkov detector for the High Momentum Spectrometer in Hall C at Jefferson Lab*, Nucl. Instr. Meth. Phys. Res. A **548** (2005) 364-374.

[80] T. Hasegawa *et at.*, *A large silica aerogel Cherenkov counter for SKS*, Nucl. Instr. Meth. Phys. Res. A **342** (1994) 383-388.

[81] B. Tonguc *et al.*, *The BLAST Cherenkov detectors*, Nucl Instr. Meth. Phys. Res. A **553** (2005) 364-369.

[82] T. Iijima *et al.*, *Aerogel Cherenkov counter for the BELLE detector*, Nucl. Instr. Meth. Phys. Res. A **453** (2000) 321-325.

[83] A. Yu. Barnyakov *et at.*, *Results from R&D of Cherenkov detectors at Novosibirsk*, Nucl. Instr. Meth. Phys. Res. A **581** (2007) 410-414.

[84] A. Yu. Barnyakov *et at.*, *Development of aerogel Cherenkov counters at Novosibirsk*, Rad. Phys. Chem. **75** (2006) 862-867.

[85] A. Yu. Barnyakov *et at.*, *Aerogel Cherenkov Counter for the SND Detector, SNIC Symposium, Stanford, California, 3-6 April, 2006.*

[86] Yu. N. Kharzheev, *Use of Silica Aerogels in Cherenkov Counters*, Physics of Particles and Nuclei, Vol. 39, No. 1 (2008), 107-135

[87] M. Cantin *et al.*, *Silica aerogel used as Cherenkov radiators*, Nucl. Instr. Meth. Phys. Res. **118** (1974) 177.

[88] H. Burkhardt *et at.*, *The TASSO gas and aerogel Cherenkov counters*, Nucl. Instr. Meth. **184** (1981) 319-331.

[89] M. Tabata *et at.*, *Development of transparent silica aerogel over a wide range of densities*, Nucl. Instr. Meth. Phys. Res. A **623** (2010) 339-341.

[90] I. Adachi *et at.*, *Study of transparent silica aerogel with high refractive index*, Nucl. Instr. Meth. Phys. Res. A **639** (2011) 222-224.

[91] T. Bellunato *et at.*, *Refractive index of silica aerogel: Uniformity and dispersion law*, Nucl. Instr. Meth. Phys. Res. A **595** (2008) 183-186.

[92] E. Aschenauer *et al.*, *Optical characterization of* $n = 1.03$ *silica aerogel used as radiator in the RICH of HERMES* Nucl. Instr. Meth. Phys. Res. A **440** (2000) 338-347.

[93] L.W. Hrubesh, *Optical characterization of silica aerogel glass*, U.C.R.L. Report no. 53794, 1987.

[94] A.R. Buzykaev *et at.*, *Measurement of optical parameters of aerogel*, Nucl. Instr. Meth. Phys. Res. A **433** (1999) 396-400.

[95] A.F. Danilyuk *et at.*, *Recent results on aerogel development for use in Cherenkov counters*, Nucl. Instr. Metk. Phys. Res. A **494** (2002) 491-494.

[96] L. Lagamba *Silica aerogel threshold Cherenkov counters for the JLab Hall A spectrometers: improvements and proposed modifications* Nucl Instr. Meth. Phy. Res. A 471 (2000) 325-332.

[97] D.L. Perego *Ageing tests and recovery procedures of silica aerogel*, Nucl. Instr. Meth. Phys. Res. A **595** (2008) 224-227.

[98] A. Yu. Barnyakov *et al.*, *Influence of water on optical parameters of aerogel*, Nucl. Instr. Meth. Phys. Res. A **598** (2009) 166-168.

[99] http://en.wikipedia.org/wiki/Thermionic_emission.

[100] http://www.labsphere.com

[101] http://www.labsphere.com/products/reflectance-materials-and-coatings/white-coatings/6080-white-reflectance-coating.aspx.

[102] http://www.fnal.gov/projects/ckm/jlab/2249a-spec.htm.

[103] gentitfx.fr/SLitrani.

[104] F. X. Gentit, *Litrani: a general purpose Monte-Carlo program simulating light propagation in isotropic or anisotropic media*, http://www-dapnia.cea.fr/Phocea/...le.php?class=std&&...le=Doc/Publications/Archives/spp-01-13.pdf.

[105] F. X. Gentit, *Optics inside anisotropic media*, http://gentitfx.fr/litrani/intro/news.html.

[106] www.ppl.phys.chiba-u.jp/research/IceCube/DetectorSim/DOMINANT/index.html.

[107] Gilles Kemener and Serge Kox, *Aerogel Čerenkov counter design for the G^0 Spectrometer*, http://lpsc.in2p3.fr/hadrons/g0/rapports/g0-cerenkov.ps.gz.

[108] Benoît Guillon, *Cherenkov counter for the G^0 backward angle measurements*, Eur. Phys. J. A **24**, s2, (2005) 145, doi 10.1140/epjad/s2005-04-036-8

[109] A. Esser *et al.* (A1 Collaboration), *Pioneering experiment for high resolution decay spectroscopy of light hypernuclei at MAMI*, Proceedings of Science (Bormio2012) 038, 2012.

[110] R. Siudak *et al.*, *A threshold Cherenkov detector for K^+/π^+ separation using silica aerogel*, Nucl. Instr.Meth. Phys. Res. A **596** (2008) 311-316.

[111] P. Achenbach *et al.* (A1 Collaboration), *Unpolarized and polarized elementary kaon electroproduction cross sections measured at MAMI*, Eur. Phys. J. Web of Conferences, to appear in 2012.

[112] B. Povh *et al.*, *Particles and nuclei, An Introduction to the physical concepts*, 4^{th} edition, Springer-Verlag, 2004.

[113] https://ssftrac.ugent.be/strangecalc/wiki/WikiStart.

Razširjen povzetek v slovenskem jeziku

Uvod

Čudnost v hadronskih sistemih ima pomembno vlogo v fiziki, saj leži na presečišču med jedrsko fiziko in fiziko osnovnih delcev. Študij interakcij med hiperoni in nukleoni (YN) ter med hiperoni (YY) nam omogočajo hiperjedra, v katera je vezan eden ali več hiperonov. Obenem nam hiperon ujet v jedro lahko pomaga kot sonda za strukturo jedra in njegove spremembe zaradi prisotnosti hiperona.

S povečanjem energije pospeševalnika za elektrone v Mainzu (MAMI), je mogoče preučevati prav takšna jedra, saj je elektrone možno pospešiti do energije 1.6 GeV [12]. Z novo pospeševalno enoto se je dvignil prag za produkcijo lahkih mezonov (π, η) v območje kaonov. Eden od možnih procesov produkcije kaonov je:

$$e + p \longrightarrow e' + K^+ + \Lambda.$$

V najnižjem redu perturbacije ta proces opišemo kot izmenjavo enega virtualnega fotona med elektronom in protonom. V tem primeru virtualni foton prenese del gibalne količine in energije vpadnega elektrona na proton. V preteklih pedeset letih smo pridobili precej podatkov o foto- in elektroprodukciji kaonov iz različnih mednarodnih fizikalnih institutov, vendar je ostalo še veliko nerešenih vprašanj o interpretaciji teh podatkov. Na primer izmerjeni diferencialni sipalni preseki za fotoprodukcijo kaonov se zelo razlikujejo med različnimi laboratoriji in prav tako teoretične napovedi različnih efektivnih Lagrangevih modelov za opis procesa, kar se še posebej pozna pri majhnih sipalnih kotih kaonov. Da bi odpravili te neskladnosti med rezultati sipalnega preseka, so potrebne dodatne meritve. Primankljaj podatkov o elektroprodukciji kaonov je največji tik nad pragom in pri majhnih četvercih prenosa gibalne količine, Q^2. Območje nizkih Q^2 je zato najzanimivejše za nadaljne meritve sipalnih presekov elektroprodukcije $K^+\Lambda$ in $K^+\Sigma^0$, pri čemer bi novi podatki občutno izboljšali trenutno znanje in interpretacijo omenjenega procesa.

Teoretični opis reakcije $p(e, e'K^+)\Lambda$

Proces elektroprodukcije kaonov v najnižjem redu poteka tako, da vpadni elektron e interagira s protonom, kateremu preda virtualni foton γ^*, sam pa se sipa pod polarnim kotom θ_e glede na začetno smer. Ta potek se dogaja v tako imenovani sipalni ravnini, ki jo definirata vpadni in sipani elektron. Virtualni fotom preda gibalno količino in energijo protonu, kjer kot reakcijski produkt nastaneta nabiti kaon, K^+, in hiperon, Λ ali Σ^0. Kaon se izseva pod polarnim kotom θ_K glede na smer virtualnega fotona. Ravnino, ki jo definirata nastali kaon in hiperon, imenujemo reakcijska ravnina. Azimutalni kot ϕ je kot med sipalno in reakcijsko ravnino. Za mertev takšnega procesa sta potrebna vsaj dva spektrometra: eden za detekcijo sipanih elektronov in drugi za detekcijo nastalih kaonov.

Kinematiko elektroprodukcije kaonov na jedru opišemo kot:

$$N(p^{\mu}_{\rm tar}) + e(k^{\mu}_e) \rightarrow e'(k^{\mu}_{e'}) + K(p^{\mu}_K) + Y(p^{\mu}_Y),$$

kjer N označuje nukleon (proton) in Y hiperon (Λ ali Σ^0). Ker z elektroni obstreljujemo mirujočo tarčo, kjer se nahajajo protoni, z maso $M_{\rm tar}$, zapišemo četverce gibalnih količin delcev pred reakcijo kot:

$$k^{\mu}_e = (E_e, \mathbf{k}_e),\ p^{\mu}_{\rm tar} = (M_{\rm tar}, \mathbf{0})$$

in četverce delcev v končnem stanju (sipani elektron, kaon, hiperon) kot:

$$k^{\mu}_{e'} = (E_{e'}, \mathbf{k}_{e'}),\ p^{\mu}_K = (E_K, \mathbf{p}_K),\ p^{\mu}_Y = (E_Y, \mathbf{p}_Y).$$

Energija, ω, in gibalna količina, $\mathbf{q}$, virtualnega fotona sta definirana kot razlika četvercev vpadnega in izstopajočega elektrona:

$$\omega = E_e - E_{e'},\ \mathbf{q} = \mathbf{k}_e - \mathbf{k}'_e,$$

tako da četverec zapišemo kot $q_\mu = (\omega, \mathbf{q})$. Prenos gibalne količine virtualnega fotona je podan kot:

$$Q^2 = -q_\mu q^\mu = |\mathbf{q}|^2 - \omega^2 \approx 4E_e E_{e'} \sin^2\theta/2,$$

kjer je θ sipalni kot elektrona. Vpeljimo še invariantno energijo W:

$$W^2 = (q^\mu + p^\mu_{\rm tar})^2 = (p^\mu_K + p^\mu_Y)^2.$$

Diferencialni sipalni presek reakcije $p(e,e'K^+)\Lambda$ lahko zapišemo kot produkt virtualnega fotoprodukcijskega sipalnega preseka in fluksa virtualnih fotonov sipanih v fazni prostor $dE_{e'}d\Omega$:

$$\frac{d\sigma}{dE_{e'}d\Omega_{e'}d\Omega^*_K} = \Gamma_{\rm v}\frac{d^2\sigma_{\rm v}}{d\Omega^*_K},$$

kjer je Γ_v fluks fotonov in vsebuje vso informacijo elektromagnetnega vozlišča. Ob dani polarizaciji virtualnih fotonov, ε, se diferencialni sipalni presek v težiščnem sistemu kaona in hiperona zapiše kot:

$$\begin{aligned}\frac{d\sigma_{\rm v}}{d\Omega^*_K} \quad &= \quad \frac{d\sigma_T}{d\Omega^*_K} + \epsilon\frac{d\sigma_L}{d\Omega^*_K} + \sqrt{2\epsilon\,(1+\epsilon)}\frac{d\sigma_{LT}}{d\Omega^*_K}\cos\phi + \epsilon\frac{d\sigma_{TT}}{d\Omega^*_K}\cos(2\phi) + \\ &\quad\ h\sqrt{2\epsilon\,(1-\epsilon)}\frac{d\sigma_{LT'}}{d\Omega^*_K}\sin\phi,\end{aligned}$$

kjer se členi z indeksi T, L, LT, TT, LT' nanašajo na transverzalno in longitudinalno polarizacijo fotona ter interference med njimi. Ti členi so odvisni od kinematičnih spremenljivk Q^2, W in θ_K. Sučnost vpadnega elektrona je označena s simbolom h.

Masa nastalega hiperona, ki ostane vezan v jedru in kasneje razpade najpogosteje po šibki interakciji, se izračuna iz znane energije vpadnih elektronov, mirovne mase protona in energije ter gibalne količine detektiranih delcev. Zaradi zakona o ohranitvi energije in gibalne količine je masa hiperona enaka neizmerjeni, oziroma t.i. mankajoči masi:

$$M_x^2 = ((E_e + M_{\mathrm{tar}} - E_K - E_{e'})^2 - (\mathbf{p}_e - \mathbf{p}_K - \mathbf{p}_{e'})^2).$$

Za opis elektromagnetne produkcije kaonov na jedrih obstaja vrsta različnih modelov, ki se v glavnem razlikujejo v tem, da eni opisujejo procese z elementarnimi gradniki hadronov, kot so kvarki in gluoni, medtem ko drugi obravnavajo hadrone kot osnovne gradnike. Modeli iz druge skupine uporabljajo efektivne Lagrangiane za opis močne interakcije. Oblika takšnih Lagrangianov temelji na simetrijah v fiziki. S prilagajanjem teoretičnih napovedi na eksperimentalne podatke se iščejo prosti parametri in natančna matematična struktura efektivnih Lagrangianov.

Sipalni preseki so izpeljani iz najnižjega reda perturbacije, kjer se interakcija med virtualnim fotonom in protonom opiše s prehodom preko nukleonov, resonance Δ itd., ali z izmenjavo kaonov, hiperonov in njihovih vzbujenih stanj. Vsako takšno vmesno stanje opišemo z njegovo maso in močno ter elektromagnetno sklopitveno konstanto. Različni modeli se med seboj razlikujejo v uprabi nukleonskih, hiperonskih in kaonskih resonanc, vključno z njihovimi efektivnimi sklopitvenimi konstantami.

Spektrometer Kaos

V eksperimentalni hali Kolaboracije A1, na Inštitutu za jedrsko fiziko v Mainzu (Nemčija), so do nedavnega delovali le trije spektrometri, poimenovani A, B in C. Spektrometra A in C sta sestavljena iz kvadrupolnega, sekstupolnega ter dveh dipolnih magnetov, medtem ko je spektrometer B sestavljen samo iz enega dipola. Maksimalne gibalne količine, ki jih dosegajo, so: 735 MeV/c (spektrometer A), 870 MeV/c (spektrometer B) in 551 MeV/c (spektrometer C). Vsak od spektrometrov je opremljen z detekcijskim paketom za določanje položaja delcev, ta pa je sestavljen iz štirih ravnin vertikalnih potovalnih komor, dveh ravnin plastičnih scintilatorjev in pragovnega plinskega detektorja sevanja Čerenkova [49].

Novi pospeševalni stopnji ne ustrezajo omenjeni trije spektrometri, saj ne zajemajo vseh gibalnih količin, ob tem pa imajo pri eksperimentih, ki se bodo nanašali na čudnost, nastali kaoni premajhno verjetnost za detekcijo zaradi kratkega življenskega časa ($c\tau_K = 3.7$ m) in velike potovalne poti skozi spektrometer (okoli 10 m). Zaradi tega se bodo kaoni analizirali pri majhnih sipalnih kotih in majhnimi prenosi gibalnih količin z novim spektrometrom Kaos. Relativno nizka končna energija pospeševalnika MAMI se je izkazala kot prednost, saj takšna kinematika najboljše ustreza meritvam s spektrometrom Kaos.

KAOS je magnetni spektrometer, ki je operativen v Mainzu od leta 2008, načrtovan za simultano detekcijo pozitivnih kaonov na eni strani magneta in negativnih elektronov na drugi strani. Za detekcijo pozitivno nabitih delcev se uporabljata: dve večžični proporcionalni komori za odčitavanje trajektorij in meritve gibalnih količin, dve steni scintilacijskih detektorjev za meritve časa preleta in za proženje. Za detekcijo negativno nabitih delcev se uporabljajo scintilacijska vlakna, ki so trenutno še v fazi testnih meritev.

Za detekcijo kaonov je nujen zelo učinkovit sistem identifikacije oz. ločevanja pionov od kaonov. Za ločevanje redkih kaonov od obilja pionov, se je do nedavnega uporablja metoda merjenja časa njihovega preleta med scintilatorji, vendar postane neuporabna pri višjih gibalnih količinah, $p \geq 800$ MeV/c, saj razlika v času preleta med pioni in kaoni pada kot $\Delta t \propto 1/p^2$. Učinkovito identifikacijo lahko dosežemo s pragovnim Čerenkovim detektorjem.

Načrtovanje in gradnja novega detektorskega sistema za identifikacijo delcev, kateri temelji na pragovnemu Čerenkovemu detektorju je bil glavni del moje doktorske naloge.

Detektor sevanja Čerenkova

Delovanje Čerenkovega detektorja temelji na pojavu, ki ga je prvi opazil Pavel Aleksejevič Čerenkov leta 1943. To sevanje se pojavi, ko nabiti delec prečka prozoren medij, oziroma sevalec, z lomnim količnikom n, pri čemer je hitrost delca v večja od fazne hitrosti svetlobe v tem mediju:

$$v > c/n.$$

V tem primeru se izseva elektromagnetno valovanje pod kotom θ_C v smeri gibanja delca:

$$\cos\theta_C = \frac{1}{\beta n(\omega)} = \frac{c}{v n(\omega)}.$$

Energijski spekter izsevanih fotonov je konstanten dokler je zagotovljen pogoj za Čerenkovo sevanje (do ≈ 10 eV). Energijske izgube delca zaradi sevanja naraščajo s hitrostjo, vendar so zelo majhne, npr. v kondenzirani snovi so reda velikosti $\approx 10^{-3}$ MeV cm^2/g. Spekter Čerenkovih fotonov ima $1/\lambda^2$ odvisnost, kar pomeni da je večina fotonov generiranih v UV delu spektra. Število generiranih fotonov na enoto dolžine je odvisno od naboja delca, ze, njegove hitrosti in lomnega količnika:

$$\frac{dN}{dx} = 475 z^2 \sin^2\theta_C \text{ photons/cm}.$$

Kot vidimo je število generirani fotonov zelo majhno, kar pomeni da potrebuje vsak detektor sevanja Čerenkova dober detekcijski izkoristek [72].

Trije glavni elementi tipičnega detektorja sevanja Čerenkova so: (i) sevalec, katerega prečka nabiti delec, (ii) difuzivni zaboj, kjer se na notranjih stenah Čerenkovi fotoni sipajo difuzivno in (iii) fotopomnoževalke. Za učinkovito detekcijo nastalih fotonov se uporabljajo različni pristopi. Ponavadi so znotraj difuzivnega zaboja ogledala, ali odbojne folije z majhno absorbcijo na katerih se svetloba odbije po odbojnem zakonu in usmerijo fotone proti fotopomnoževalkam, kjer se svetlogni signal pretvori v električnega. Za detektor z notranjimi stenami, ki imajo odbojnost η in fotopomnoževalkami, ki pokrivajo delež notranje površine κ, je povprečno število detektiranih Čerenkovih fotonov, v primeru ko je $z = 1$:

$$N = F_0 L \left(1 - \frac{1}{\beta^2 n^2}\right) \frac{\kappa}{1 - \eta(1-\kappa)},$$

kjer je L debelina sevalca in F_0 t.i. umeritveni parameter, ki vsebuje vse ostale podatke o detektorju, kot so kvantni izkoristek fotopomnoževalk, prepustnost njihovih vstopnih oken in sevalca ter znaša ponavadi $F_0 = 50 - 100$ /cm. Pri načrtovanju takšnih detektorjev je najpomembnejši izziv čim večje število detektiranih fotonov na posamezni dogodek, kar ponavadi znaša manj kot deset fotoelektronov. Ta lastnost vpliva na izkoristek detektorja za detekcijo relativističnih delcev.

Pragovni detektor sevanja Čerenkova je najpreprostejši tip takšnih detektorjev, kjer samo z opazovanjem signala ugotovimo ali je delec pod ali nad pragom za Čerenkov sevanje. Delci z enako gibalno količino in različno maso imajo različne hitrosti. Tako lahko s pravilnim izborom lomnega količnika določimo prag, tako da je en tip delcev pod pragom za sevanje in drugi tip nad njim pri dani kinematiki. Najmanjša gibalna količina delca z maso m, ki ustreza pogoju za Čerenkovo sevanje je:

$$p_t c = \frac{mc^2}{\sqrt{n^2 - 1}}.$$

V našem primeru, kjer želimo da so lažji pioni nad pragom za sevanje in težji kaoni pod njim, smo izbrali sevalec z lomnim količnikom

$$n = 1.055.$$

To pomeni, da je prag za pione $p_t^{\pi^+} \approx 415$ MeV/c in za kaone $p_t^{K^+} \approx 1.47$ MeV/c. Od velikosti gibalne količine je odvisno tudi relativno število detektiranih fotonov:

$$N/N_{\max} = 1 - \frac{m^2}{p^2(n^2 - 1)}.$$

Zaradi zahtev za detektor sevanja Čerenkova kot so: (i) velika površina, ki zajema celotno akceptanco spektrometra Kaos, (ii) dovolj ozek detektor za razpoložljiv prostor v spektrometru in (iii) dobra časovna ločljivost; smo za sevalec izbrali aerogel.

Aerogel je snov, ki bazira na silicijevem oksidu, Si_xO_y, je zelo porozen (več kot 95% njegovege prostornine je zrak), ima majhno gostoto, prepušča svetlobo in je zalo krhek. Razpon lomnih količnikov aerogela, n, sega od $n \approx 1.007$ do $n \approx 1.25$. V detektorju sevanja Čerenkova za Kaos imamo aerogel dveh proizvajalcev: Matsushita Electric Works Ltd. iz Japonske in aerogel narejen skupno med Institutom katalize Boreskov in Institutom za jedrsko fiziko Budker iz Novosibirska (Rusija). Aerogel iz Novosibirska je hidrofilen z dimenzijami $5 \times 5 \times 2$ cm^3, medtem ko je aerogel od Matsushite hidrofobičen z dimenzijami $11.5 \times 11.5 \times 1$ cm^3.

Kritične optične lastnosti aerogela, ki vplivajo na njegovo prepustnost, T, so absorbcijska dolžina, Λ_{abs}, in sipalna dolžina, Λ_{s}. Na območju valovnih dolžin $\lambda > 350$ nm je absorpcijska dolžina aerogela konstantna, sipalna dolžina pa ima λ^4 odvisnost, kar je značilno za Rayleighovo sipanje. Prepustnost zapišemo kot:

$$T = \exp(-d/\Lambda_{\mathrm{abs}} - d/\Lambda_{\mathrm{s}}) = A \exp(-Cd/\lambda^4)|_{\lambda > 350\ \mathrm{nm}},$$

kjer je d debelina aerogela. Parametra A in C, imenovana Huntova parametra, opisujeta absorpcijo oziroma sipanje. Kvaliteten aerogel bo imel A blizu 1 in C blizu 0 [93]. S fitanjem prepustnosti se določita oba Huntova parametra od koder se potem izračunta absorbcijska in sipalna dolžina kot:

$$\begin{aligned} \Lambda_{\mathrm{abs}} &= -d/\ln A, \\ \Lambda_{\mathrm{s}} &= \lambda^4/C. \end{aligned}$$

V območju valovnih dolžin od 200 do 800 nm sem izmeril Λ_{abs} in Λ_{s}. Za aerogel iz Novosibirska sem izmeril, da znaša $\Lambda_{\mathrm{abs}} \approx 10.6$ cm, medtem ko je za aerogel od Matsushite $\Lambda_{\mathrm{abs}} \approx 7.2$ cm. Kar se tiče sipalne dolžine sem za aerogel iz Novosibirska izmeril, da pri valovni dolžini $\lambda = 400$ nm znaša $\Lambda_{\mathrm{s}} \approx 2.8$ cm, medtem ko je za aerogel od Matsushite $\Lambda_{\mathrm{s}} \approx 1.4$ cm.

V hidroskopičnem aerogelu sem opazil padec prepustnosti, kar je posledica absorbcije vlage iz zraka. V letu dni se je absorbcijska dolžina skrajšala za $\approx 7.5\%$ in sipalna dolžina za $\approx 11\%$ pri 400 nm. Optične lastnosti sem povrnil s segrevanjem aerogela v pečici pri visoki temperatur: približno 5 ur pri 500 °C. Prepustnost se je največ izboljšala na območju valovnih dolžin, kjer so fotopomnoževalke najbolj občutljive, in sicer za $\approx 5\%$ pri $\lambda = 400$ nm.

Celotna debelina aerogela v detektorju sevanja Čerenkova je $d = 3$ cm s skupno površino 45 cm $\times$ 150 cm, kar se ujema s površino akceptance spektrometra Kaos. Aerogel je v dveh slojih, pri čemer je v spodnjem sloju pretežno aerogela od Matsushite in debeline 1 cm ter v zgornjem sloju aerogel iz Novosibirska debeline 2 cm. Aerogel je fiksiran v svoji legi z žičkami debeline 10 μm, ki so v razmaku 17 mm paralelno speljane čez celotno površino aerogela. Difuzni zaboj je segmentiran na manjše celice: vsega skupaj je 6 celic, ki so ločene s tankimi predelnimi stenami, ki preprečujejo fotonom, da bi se razširili čez celotni detektor. Vsaka celica je nagnjena pod kotom $\varphi = 35°$ glede na ravnino aerogela, kar sovpada s povprečnim kotom vpadnih delcev. Za boljši izkoristek detektorja so znotraj vsake celice nameščene reflektivne folije, ki odbijajo svetlobo proti fotopomnoževalkam. Na nasprotnih si stranicah sta na vsako celico pritrjeni po dve fotopomnoževalki, kar pomeni da jih je v eksperimentalni hali polovica na spodnji in polovica na zgornji strani detektorja. Fotopomnoževalke so zaščitene pred magnetnim poljem s posebnim kovinskim ohišjem in pritrjene na detektor s pomočjo cilindričnih obročev. Na spodnjih fotografijah je prikazan detektor v fazi izdelave. Aerogel je položen na spodnji ploskvi in fotopomnoževalke na nasprotnih si straneh.

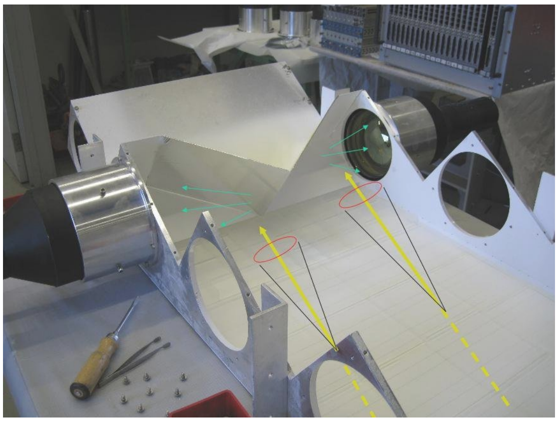

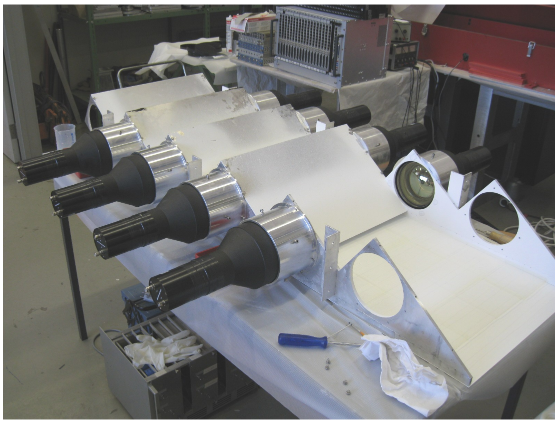

Za detekcijo fotonov sem uporabljal dva različna modela fotopomnoževalk od proizvajalca Hamamatsu: R1250 in R877-100, vendar enakega premera aktivne površine, in sicer 127 mm (5”). Glavna razlika med njima je meterial fotokatode: R1250 ima fotokatodo iz bialkalija, medtem ko R877-100 iz t.i. super bialkalija, kar se pozna v njihovem višjem kvantnem izkoristku, ki lahko doseže vrednosti do 35%. Visok kvantni izkoristek je za naše potrebe ena od bistvenih lastnosti fotopomnoževalk, zaradi manjhega števila generiranih fotonov v primerjavi s številom nastalih fotonov v scintilatorjih. Oba modela sta občutljiva v območju valovnih dolžin, ki se ujema s spektrom izsevane Čerenkove svetlobe, in sicer R1250 ima kvantni izkoristek $\approx$ 23% in R877-100 $\approx$ 33% v območju $350 \lesssim \lambda \lesssim 450$ nm. Oba modela fotopomnoževalk se razlikujeta tudi po številu dinod: R1250 ima 14-stopenjsko strukturo, medtem ko R877-100 10-stopenjsko. To se pozna v različnemu faktorju ojačanja: v R1250 modelu je $\approx 1.4 \times 10^7$ in v R877-100 modelu $\approx 3.1 \times 10^5$ pri nominalnih napajalnih napetostih. Čeprav se ojačanje lahko nastavi z ustrezno napajalno napetostjo, sem za kompenzacijo uporabljal dodatni ojačevalec s faktorjem ojačanja $\approx$ 200, ki je postavljen v elektronski verigi takoj za R877-100 fotopomnoževalkami. Analogni signali so iz fotopomnoževalk speljani po LEMO kablih do ADC pretvornika, kjer se zapiše informacija o zbranem naboju na a- nodi fotopomnoževalke. Za pretvorbo sem uporabljal LeCroy 2294A modul z 12 vhodnimi kanali, kar se točno ujema s številom fotopomnoževalk.

Vse notranje površine difuznega zaboja (razen reflektivnih folij) so prekrite z visoko odbojnim premazom, ki Čerenkovim fotonom preprečuje absorbcijo na stenah ohišja. Odbojnost je med 95% in 98% med 300 in 1200 nm. Za boljši izkoristek smo dodatne t.i. odbojne površine znotrja vsake celice prekrili z aluminiziranimi mylar folijami, z namenom, da odbijajo svetlobo po odbojnem zakonu proti fotopomnoževalkam in skrajšajo povprečno pot fotonom pred detekcijo. Izmeril sem odbojnost teh folij in ugotovil da je med 80% in 90% v območju valovnih dolžin, kjer so fotopomnoževalke najbolj občutljive.

Iz ADC pretvornika dobimo digitalno informacijo o jakosti signala iz fotopomnoževalke, ki se zapiše na računalnik. Po daljšem vzorčevanju teh podatkov lahko izrišemo t.i. ADC spekter, ki ponazarja porazdelitev signalov iz fotopomnoževalk po njihovi velikosti. Čeprav so fotopomnoževalke priključene na enako napajalno napetost, je njihov odziv malenkost različen, kar se pozna po legi eno-fotoelektronskih vrhov v ADC spektrih. To je posledica fluktuacij ojačanja med fotopomnoževalkami.

Da bi bil odziv vseh fotopomnoževalk enak, sem določil njihove napajalne napetosti najprej tako, da sem položil vsako fotopomnoževalko posebej v črno škatlo, jo priklopil na napajalno napetost, na fotokatodo posvetil s šibko lasersko svetlobo s po 3-4 fotoni na pulz in na osciloskopu opazoval njihov odziv v odvisnosti od napajalne napetosti . Napetosti sem nastavil tako, da je bil odziv vseh fotopomnoževalkah približno enak. Natančnejšo umeritev sem naredil v eksperimentalni hali med testnim poskusom, kjer sem opazoval surove ADC spektre vseh fotopomnoževalk. Vsak spe-kter sem pofital z Gaussovo krivuljo in z dodatnim polinomom tretjega reda, da bi našel točno lego eno-fotoelektronskega vrha. Z ustreznimi prilagoditvenemi parametri sem lahko nato umeril vsak ADC spekter po formuli:

$$\mathrm{ADC}_i = (\mathrm{ADC}_i^{\mathrm{raw}} - p_i) * g_i,$$

kjer je i zaporedna številka spektra, $\mathrm{ADC}^{\mathrm{raw}}$ surovi spekter in ADC umerjeni spekter. Prilagoditvena parametra p in g določata za koliko je treba zamakniti posamezen histogram ter njegovo normalizacijo. Po končani umeritvi je v vseh spektrih pedestal postavljen na levi rob spektra in eno-fotoelektronski vrh povsod na točno enako mesto.

Simulacije v programu `SLitrani`

Za namenom, da bi čim bolje razumeli delovanje detektorja sevanja Čerenkova, sem naredil vrsto simulacij v programu `SLitrani`, da bi reproduciral in primerjal rezultate z izmerjenimi podatki. `SLitrani` je objektno orientiran program, napisan v programskem jeziku `ROOT`, kar pomei, da `SLitrani` uporablja njegove razrede [104]. To je program, ki deluje po metodi Monte-Carlo, za simulacijo prenosa svetlobe po anizotropnih optičnih snoveh.

S programom `SLitrani` sem simuliral tako delovanje posamezne celice kot celotnega detektorja. S spreminjanjem geometrijskih, mehanskih in optičnih lastnosti snovi, kot so: velikost aktivne površine fotopomnoževalk z njihovim kvantnim izkoristkom, debelina aerogela, kot med reflektivnimi folijami, višina, širina, kot posamezne celice glede na ravnino aerogela itd., sem poiskal optimalno rešitev za končno obliko detektorja. Za absorbcijsko in sipalno dolžino aerogela sem v simulacijo vključil podatke, izmerjene v laboratoriju.

Iz simulacij sem ugotovil, da ima spekter izsevane svetlobe vrh pri 350 nm - 400 nm. Na podlagi tega smo izbrali fotopomnoževalke z največjim kvantnim izkoristkom na tem območju. Med najzanimivešimi rezultati simulacije je število detektiranih fotonov pri preletu enega delca. Simulacije so pokazale, kako se število detektiranih fotonov veča z debelino aerogela, dokler ne pride do saturacije. Po drugi strani pa je njihov čas preleta skoraj neodvisen od debeline aerogla (na območju med 1 in 10 cm) in znaša $t \approx 2$ ns, kar ustreza povprečni poti preleta ≈ 0.5 m.

S primerjavo simulacij detektorja z reflektivnimi folijami znotraj celic in brez njih sem ugotovil, da je izkoristek detektorja precej boljši (okoli 50%) kadar so takšne folije znotraj celic. Kasneje sem spreminjal tudi kot med odbojnimi površinami, 2α, prekritimi z različnimi reflektivnimi folijami [110]. Izkazalo se je, da je najboljši izkoristek detektorja, kadar so odbojne površine prekrite z aluminizirano mylar folijo in pokrivajo 3/4 spodnje stranice celice, kamor so pritrjene.

Performanso detektorja sem simuliral v okolju kakršnemu je bil izpostavljen detektor v eksperimentalni hali tekom enega od testnih poskusov. V simulacijeh sem detektor obstreljeval z žarkom elektronov (pozironov) in pionov z gibalnimi količinami do 1.6 GeV/c in opazoval relativno število detektoranih fotonov ter reproduciral teoretične napovedi. Za povprečno število fotoelektronov sem dobil $N_{fe} \approx 4.3$ za pione in $N_{fe} \approx 6.8$ za pozitrone pri gibalni količini 720 MeV/c, kar se dobro ujema z meritvami. Na podlagi simulacij je pričakovani izkoristek detektorja, pri detekcijskem pragu 1.5 fotoelektronov, 97% za pozitrone in 86% za pione.

Prav tako sem simuliral število prehodov, odbojev in absorbcij fotonov med in v različnih snoveh in površinah znotraj detektorja. Zaradi totalnega odboja se precej fotonov odbije na notranji površini aerogela, kjer se tudi absorbira večinah fotonov zaradi kratke absorbcijske dožine (v primerjavi z zrakom). Simulacije so tudi pokazale, da lahko nekaj Čerenkovih fotonov pobegne v sosednje celice skozi aerogel. Ta pojav je pogostejši v primerih, ko so fotoni generirani v bližini predelnih sten.

Analiza podatkov in rezultati

Z detektorjem sevanja Čerenkova sem opravil serijo testnih meritev tako s kozmičnimi žarki kot v eksperimentali hali s testnimi žarki.

Prve testne meritve sem naredil s kozmičnimi žarki, tako da je bil detektor postavljen med obe steni scintilacijski steni v spektrometru Kaos. V obdelavo sem zajel le tiste dogodke, ki so ustvarili signal v obeh stenah scintilatorjev hkrati, kar je zaradi konfiguracije detektorjev pomenilo, da je moral kozmični delec prečkati tudi ravnino aerogela. Ker kozmične delce na zemeljski površini sestavljajo pretežno visoko-energijski mioni, so skoraj vsi nad pragom za generiranje Čerenkovih fotonov. Glede na čas preleta med stenami scintilatorjev in njihovih energijskih izgub, sem poskusil čim natančneje ločiti visoko-energijske kozmike od počasnejših in od ozadja.

Izkoristek detektorja se izračuna iz posameznega ADC spektra (če nas zanima izkoristek posamezne celice) ali iz t.i. ADC SUM spektra, ki je vsota vseh ADC spektrov (kadar nas zanima izkoristek celotnega detektorja): ADC SUM $= \sum_i \mathrm{ADC}_i$. Primer ADC SUM spektra je prikazan na naslednji strani. V ADC spektru, ki ima umerjeno skalo v številu fotoelektronov, se določi detekcijski prag (ponavadi 0.5 ali 1.5 fotoelektronov) in nato pogleda razmerje med številom dogodkov nad pragom in številom vseh dogodkov:

$$izk = \frac{\text{Št. dogodkov nad det. pragom v ADC spektru}}{\text{Št. vseh dogodkov v ADC spektru}}.$$

Izmeril sem, da je izkoristek detektorja sevanja Čerenkova s kozmiki, pri detekcijskem pragu 0.5 fotoelektronov, $\approx 95\%$.

Za analizo podatkov iz testnih meritev v eksperimentalni hali, je nujna določitev lege delcev v ravnini aerogela in njihova identifikacija. Koordinate delcev sem v ravnini aerogela določil z linearno ekstrapolacijo iz ene od večžičnih proporcionalnih komor ali iz ene od sten scintilatorjev. Lega delca je pomembna, saj lahko s tem podatkom analiziram izkoristek posamezne celice ali ignoriram tiste delce, ki so leteli mimo aerogela. Za identifikacijo delcev sem si pomagal z izmerjenimi energijskimi izgubami v scintilatorjih in časom preleta med njimi (kar se lahko izrazi tudi kot hitrost, β, če poznamo razdaljo med stenama scintilatorjev).

Preliminaren test v eksperimentalni hali s testnim žarkom je bil narejen pri zelo nizkem toku vpadnih elektronov $I = 300$ nA in centralni gibalni količini spektrometra Kaos 900 MeV/c ter debelini aerogela $d = 2$ cm. Izkoristek celotnega detektorja sem določil iz ADC SUM spektra, ki je prikazan na naslednji strani, in dobil pri pragu 0.5 fotoelektronov $\approx 98\%$. Z izborom koordinat v ravnini aerogela, ki ležijo znotraj območja posamezne delice, in ustreznega ADC spektra sem lahko izračunal tudi izkoristek posamezne celice in dobil $\approx 92\%$.

Naslednji test sem naredil pri višjih tokovih vpadnih elektronov $I = 1.5$ μA, pri čemer je bil detektor izpostavljen fluksu delcev, kjer so prevadovali pozitroni z majhnim deležem protonov. Pri detekcijskem pragu 0.5 fotoelektronov, sem za izkoristek posamezne celice s pozitroni dobil $\approx 90\%$, medtem ko za celoten detektor $\approx 99\%$. Manjši izkoristek posamezne celice je lahko posledica nenatančne rekonstrukcije trajektorij delcev pri visokih števnih hitrostih ali pobega fotonov v

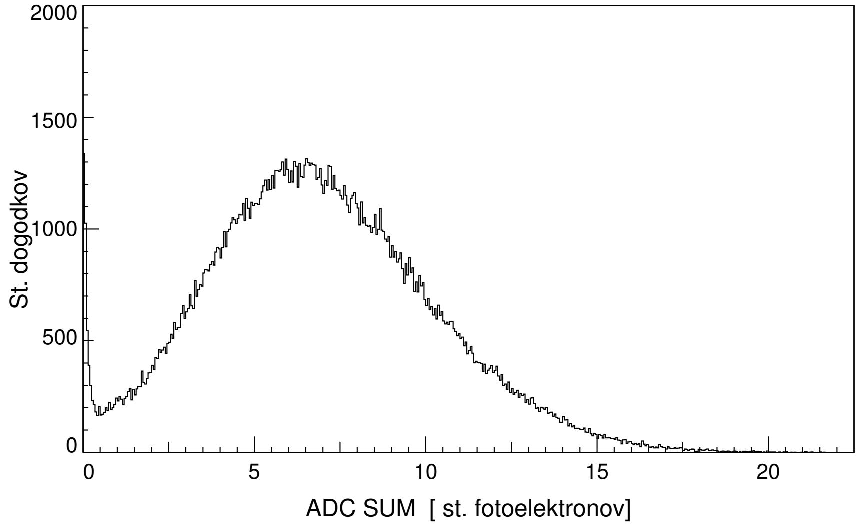

sosednje celice. Izkaže se, da tudi protoni včasih prožijo signale v detektorju, čeprav so zaradi velike mase pod pragom: pri detekcijskem pragu 1.5 fotoelektronov je verjetnost za detekcijo protona v posamezni celici $\approx$ 12%. To se zgodi najverjetneje zaradi δ-elektronv z gibalnimi količinami nad detekcijskim pragom, naključnih koincidenc med šumom v fotopomnoževalkah in prožilcem za zajemanje podatkov ali ustvarjene scintilacijske svetlobe v premazu znotraj detektorja. Izkazalo se je, da lahko z detektorjem sevanja Čerenkova precej dobro ločimo protone od ozadja (pozitroni) pri detekcijskem pragu 1.5 fotoelektronov.

Pri višjem toku vpadnih elektronov $I = 2.0$ μA smo odstranili srednjo vrsto aerogela, kjer je bilo največ pozitronov in jo nadomestili z lahkim podpornikom. S tem smo se znebili ogromnega ozadja, ki je zaradi prevelikega fluksa motilo delovanje R877-100 fotopomnoževalk. Tako se je multipliciteta detektorja (št. detektiranih signalov na en prelet delca) zmanjšala na $\approx$ 0.9, kljub temu, da smo povečali tok vpadnih elektronov iz 1.5 na 2.0 μA. Pri tem toku se je izkoristek posamezne celice s pozitroni zmanjšal pod 90% pri detekcijskemu pragu 0.5 fotoelektronov. Najverjetneje zaradi absorbcije fotonov v lahkem podporniku, ki je nadomeščal aerogel v sredini detektorja, čeprav je bil prekrit z enim slojem miliporja.

Pri R877-100 fotopomnoževalkah sem opazil izrazit premik ADC histograma pri višjih tokovih vpadnih elektronov, oziroma visokih števnostih. Celoten ADC spekter se je zamaknil proti levi, zaradi česar so postali histogrami neuporabni pri višjih števnostih za nadaljno analizo. Ker je števnost delcev na posameno celico bila $\approx$ 500 kHz, kar je še vedno v mejah normale, je do zamika histograma najverjetneje prišlo zaradi DC sklopitve med R877-100 fotopomnoževalko in ojačevalcem. Ta problem bomo rešili tako, da se bodo v uporovno verigo fotopomnoževalk vgradili manjši ojačevalci brez DC-sklopitve.

Dodaten test v eskperimentalni hali sem naredil pri drugačni kinematiki, pri čemer je bil detektor sevanja Čerenkova izpostavljen protonom, pionom in kaonom, ter z debelino aerogela $d = 3$ cm. Test sem naredil pri dveh različnih centralnih gibalnih količinah spektrometra KAOS: 720 MeV/c in 460 MeV/c. Pri 720 MeV/c sem izmeril, da je verjetnost za detekcijo protonov pod 10% pri detekcijskem pragu 0.5 fotoelektronov, vendar večja od nič iz istih razlogov kot v prejšnjem primeru. Izoristek s pioni pa je pri enakem pragu le 82%. Padec izkoristka s pioni je posledica majhnega relativnega pridelka svetlobe pri tej gibalni količini, ki je za pione le $\approx 70\%$. Pri 460 MeV/c je pridelek svetlobe s pioni še manjši, saj so pioni tik nad pragom za sevanje Čerenkovih fotonov, in znaša borih $\approx 30\%$. Padec izkoristka v posamezni celici je zato pri tej izbrani kinematiki še večji, sploh v celicah ki so na strani detektorja z nižjo gibalno količino. Za učinkovito ločevanje med pioni in kaoni je zato nujno potrebna višja centralna gibalna količina.

Pri energijah vpadnih elektronov $E_e = 1.5$ GeV (in centralni gibalni količini 460 MeV/c) sem lahko izmeril izkoristek detektorja s kaoni. Za identifikacijo kaonov sem prav tako uporabil podatke o energijskih izgubah in hitrosti ter koincidenčnemu času med spektrometrom KAOS in spektrometrom s katerim smo detektirali sipane elektrone. in tudi podatke iz detektorja sevanja Čerenkova. Čeprav so kaoni pod pragom za sevanje Čerenkovih fotonov, sem opazil signale nad detekcijskim pragom 1.5 fotoelektronov. Razlog za to je verjetno enak kot pri protonih.

S pravilno identifikacijo kaonov sem lahko izrisal spekter manjkajoče mase, kjer se je pojavil izraziti vrh pri $M_x \approx 1115$ MeV/c^2. Ta vrh ustreza mirovni masi Λ hiperona, kar je bil dokaz, da smo v tarči ustvarili hiperjedra. Tudi v tej testni meritvi sem preveril, ali lahko z detektorjem sevanja Čerenkova ločimo kaone od ozadja (pioni). Izkazalo se je da lahko, kljub majhni centralni gibalni količini, vendar, da se znebim večino ozadja, sem moral upoštevati le tiste dogodke, ki dajo ustrezno manjkajočo maso, in sicer: 1105 MeV/c$^2 < M_x <$ 1125 MeV/c^2.

Z identifikacijo kaonov v spektrometru KAOS in manjkajoče mase, ki ustreza Λ hiperonu, sem identificiral dogodke iz $p(e, e'K^+)\Lambda$ reakcije. Iz podatkov, ki ustrezajo tem dogodkom, sem izračunal sipalni presek elektroprodukcije kaonov. Integrirana luminoznost za ta proces, z upoštevanjem mrtvega časa, je $\int_t \mathcal{L}dt \approx 1930$ fbarn^{-1}. Iz porazdelitve sipalnega kota kaonov, integrirane luminoznosti in akceptance spektrometra sem izračunal diferencialni sipalni presek virtualne fotoprodukcije kaonov pri $\langle Q^2 \rangle = 0.05$ (GeV/c)^2, $\langle \epsilon \rangle = 0.4$, $\langle W \rangle = 1726$ MeV in $\langle \phi \rangle = 40°$. Za povprečni sipalni presek, v težiščnem sistemu kaona in hiperona, pri $\theta^*_K \approx 80°$, sem dobil $d\sigma_v/d\Omega^*_K \approx 0.2$ μbarn/srad. Izmerjeni sipalni presek v odvisnosti od sipalnega kota kaonov lahko primerjamo z različnimi teoretičnimi modeli, kar je prikazano na sliki na naslednji strani.

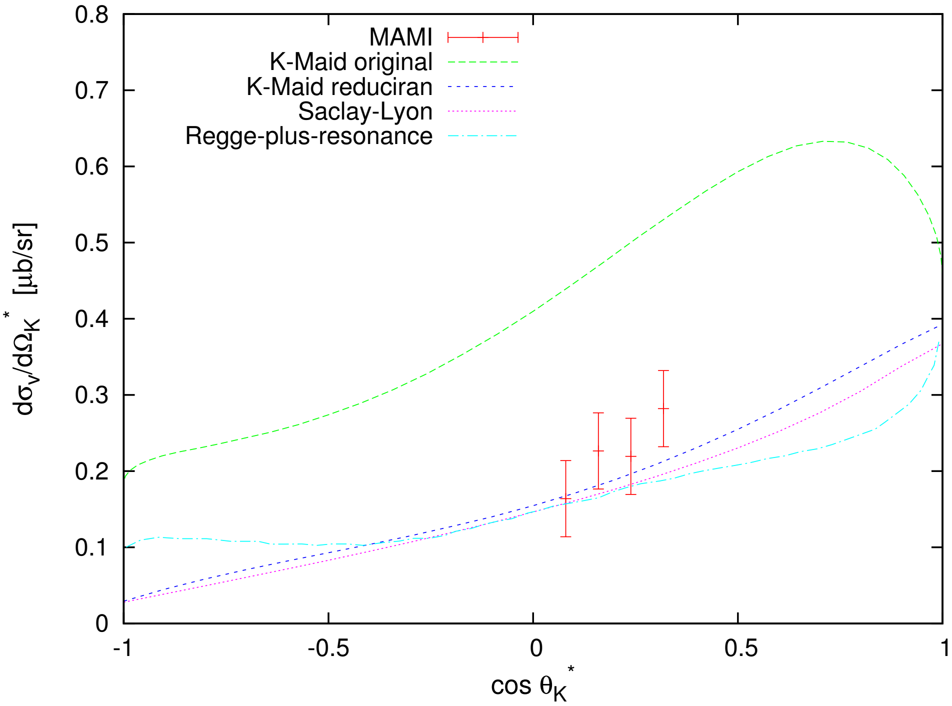
MAMI
K-Maid original
K-Maid reduciran
Saclay-Lyon
Regge-plus-resonance
$d\sigma_v/d\Omega_K^*$ [μb/sr]
$\cos\theta_K^*$
0.8
0.7
0.6
0.5
0.4
0.3
0.2
0.1
0
-1
-0.5
0
0.5
1

Acknowledgements

First of all I would like to thank my supervisor prof. Dr. Simon Širca for giving me the opportunity to work at the Institute for nuclear physics in Mainz, Germany. Many gratitudes for his support, patience and guidance through the challenges of nuclear physics. It is not often that one finds an adviser that always finds the time for listening to the problems.

I would also like to thank Dr. Patrick Achenbach for keeping an eye over my work in the KAOS group and helping me with his knowledge and experiences. Thanks to him I did not waste my time on irrelevances but led me to right direction.

Prof. Dr. Josef Pochodzalla for leading and supervising the experiments in our group.

I would like to thank to all members of KAOS group who helped me during the experiment and data analysis. My particular thanks to Dr. Carlos Ayerbe, Dr. Salvador Sanchez, Anselm Esser and Florain Schulz.

Without outstanding help from Dr. Kyo Tsukada, Toshiyuki Gogami, Sho Nagao, from Tohoku University, during construction of the final detector my work would not have been possible. My great gratitudes to them.

Special thanks to Gerhard Jung for helping me with the technical details and making my stay in Mainz with his whisting even more pleasant.

I appreciate that this operation was part financed by the European Union, European Social Fund.

Finally, it would be impossible to skip the support of my wife, Maja, during all these years.

Spodaj podpisani Luka Debenjak izjavljam, da sem avtor pričujoče doktorske disertacije z naslovom "Izgradnja in umeritev detektorja sevanja Čerenkova za hiperjedrske poskuse pri visokih števnih hitrostih".

Luka Debenjak